Low Resolution Transmission Spectroscopy of Exoplanet Atmospheres using Ground-based and Space Telescopes

by

Eva-Maria Ahrer

Thesis

Submitted to the University of Warwick

for the degree of

Doctor of Philosophy in Physics

University of Warwick, Department of Physics

June 2023

THE UNIVERSITY OF
WARWICK

Contents

List of Tables

List of Figures

Acknowledgments

First and foremost I would like to thank my PhD supervisor Peter Wheatley for his support, advice and guidance at every step of the way.

I am also immensely grateful for all the support, friendship, conversations and paper cakes during my time as part of the Astronomy group at the University of Warwick. Although we did not see each other for almost two years during the Covid-19 pandemic, I always felt connected and knew I could count on all of you, especially Sid, Matt, Catriona, Tom and Marina.

I would also like to thank everyone in the JWST Transiting Exoplanet Community ERS team. For trusting me with this challenge, for believing in me and for all the good friends and support I gained through a very stressful period, including Lili, Adina, Megan, Kevin, Sarah, Zafar, Hannah, Diana, Luis, Anjali and Maria.

I am also grateful for the support from colleagues like James, Matteo, Sebastian, Nathan and Julia.

Of course none of this would have happened without my partner, my parents, my family and my friends.

Lili, Georgina, Fabian, Thomas, Maria, Denis, Johannes, Claudia & Markus – there are not enough words for how much I appreciate your support every day of my life, especially during Covid times when I was not able to physically see some of you for long periods of time.

Daniela, Michael, Karina – Danke, dass ihr immer für mich da seid und ihr mir seit mehreren Jahren geduldig zuhört, wenn ich mal wieder über Astronomie rede.

Mama und Papa – Danke, dass ihr mich immer unterstützt habt, egal ob ich Physik studieren wollte, ohne dass ich in Physik maturiert habe, oder als ich nach England für das Masterstudium bin.

Dan – thanks for believing in me when I was not able to myself. I am incredibly lucky to have you by my side.

I am also grateful for the financial support supplied by the Department of Physics in order for me to complete this research. In addition, I am thankful for the financial support from the Warwick Astronomy Knowledge Exchange (WAKE, organised by Dr Paul Strom and Dr Heather Cegla) to visit my collaborators at the Johns Hopkins University Applied Physics Laboratory to efficiently work on the JWST NIRCam data when it came down.

Declarations

I declare that the work included in this thesis is my own work unless stated otherwise and that it has not been submitted to this or any other academic institution for any other degree or qualification.

Chapters 3 – 5 are mostly reproductions of my published first-author papers Ahrer et al. (2022), Ahrer et al. (2023a) and Ahrer et al. (2023b). Any work completed by collaborators is summarised at the beginning of each chapter as well as explicitly stated within the chapters itself when referring to their contributions.

Abstract

The research on exoplanet atmospheres has expanded rapidly over the last two decades since the first detection of an exoplanet atmosphere. Hot Jupiters – gas giants orbiting their host star on very close-in orbits – have always been at the forefront of exoplanet research as they are the easiest to detect due to their size and short orbits. However, their origins are not fully understood and by studying their atmospheres we aim to gain insight into their formation and evolution.

In this thesis I present spectroscopic observations of three transiting hot Jupiters. For the first two exoplanets I am utilising data from the ground-based telescope NTT (La Silla Observatory), while for the last one data from the space telescope *JWST* is used.

My study of the atmosphere of WASP-94Ab in the optical wavelength range revealed a sodium absorption as well as a scattering slope indicative of Rayleigh scattering.

The optical transmission spectrum of HATS-46b I retrieved using ground-based data showed a fairly featureless spectrum and the atmospheric retrieval analysis provided evidence for clouds in the atmosphere.

The last observations presented in this thesis used *JWST*/NIRCam data of hot Jupiter WASP-39b in the infrared wavelength range, and were part of the *JWST* Early Release Science (ERS) program from the Transiting Exoplanet Community. The retrieved spectrum showed strong water vapour absorption and indicated a low carbon-to-oxygen (C/O) ratio.

I show that the two telescopes provide access to different wavelength ranges and thus different possible scientific findings. Combining data from different telescopes/instruments from both ground-based and space telescopes is becoming more important than ever for our field to help understand degeneracies in both models and data, in order to further our knowledge of exoplanet atmospheres and in turn learn about the origins of hot Jupiter.

Abbreviations

ERS	Early Release Science
ESO	European Southern Observatory
GP	Gaussian Process
HST	Hubble Space Telescope
LRG-BEASTS	Low Resolution Ground-Based Exoplanet Atmosphere Survey using Transmission Spectroscopy
MCMC	Markov-Chain Monte Carlo
MIRI	JWST's Mid-Infrared Instrument
NASA	National Aeronautics and Space Administration
NGTS	Next Generation Transit Survey
NIRCam	JWST's Near-InfraRed Camera
NIRISS	JWST's Near Infrared Imager and Slitless Spectrograph
NIRSpec	JWST's Near InfraRed Spectrograph
NTT	New Technology Telescope
RV	Radial Velocity
TEC	Transiting Exoplanet Community
TESS	Transiting Exoplanet Survey Satellite

Chapter 1

Introduction

In this thesis I present the atmospheric study of three hot gaseous planets orbiting stars other than the Sun, using ground-based and space facilities, based on the publications Ahrer et al. (2022), Ahrer et al. (2023a) and Ahrer et al. (2023b), respectively.

First I describe how extrasolar planets are defined and how they are detected. There have been multiple different techniques used in the literature and while I summarise them all for completeness, the most relevant ones are the transit method and the radial velocity method, detailed at the beginning of this chapter in Sections 1.2.1&1.2.2, respectively.

As I study a specific type of planets, namely hot gas giants, the detection sections are followed by a description of the planet formation and migration mechanisms that play a role when studying this population of planets. They are not fully understood (see Section 1.3.3) and serve as motivation for characterising their atmospheres. Therefore exoplanet atmospheres and their methods of characterisation are summarised in the sections after, concluded by a section on the inferences we can make from the atmosphere, including clouds, hazes, molecular and atomic features, as well as testing for migration mechanisms (see Section 1.4.5).

In Chapter 2 I describe the methods and instruments utilised in my research presented in Chapters 3–5. Finally, I conclude with Chapter 6 where I summarise the findings in my thesis as well as provide an outlook for future work.

1.1 Definition

A planet has been defined by the International Astronomical Union (IAU) as an object that is (1) orbiting the Sun, (2) has sufficient mass to be approximately spherical in shape, and (3) has cleared its orbit from smaller objects (International Astronomical Union, 2006). An extra-solar planet — *exoplanet* — describes a planetary object orbiting a star other than the Sun, however, there is no official definition by the IAU to date. The NASA Exoplanet Archive[1] (see also Akeson et al., 2013) refers to exoplanets as objects with (1) a mass (or minimum mass) of equal to or less than 30 Jupiter masses (based on formation scenarios rather than Deuterium burning), (2) not free-floating, (3) sufficient validation by observations, and (4) published in peer-reviewed publications.

In the last three decades since the first discoveries of exoplanets, the field of exoplanet research has grown immensely. This not only includes the exoplanet detection area but also planetary formation, population studies, as well as exoplanet climate models and atmosphere studies. In this thesis I focus on hot gas giants as the research presented in Chapters 3–5 is centred on the atmosphere of hot gaseous exoplanets.

In the following sections, I first provide an overview and history of exoplanet detection methods. This is followed by motivating atmospheric studies of hot gas giants by discussing planet formation and exoplanet atmospheres with the aim of providing an overview of how theory and observations work hand in hand to improve our understanding of exoplanets and their atmospheres.

1.2 Exoplanet Detection

The field of exoplanets is a relatively recent one, with the first discovery in 1992 by Wolszcan & Frail (1992), where they found two exoplanets orbiting a pulsar using variations in the time of arrival of the pulses. The first unambiguous detection of an exoplanet (51 Pegasi b) around a star on the main sequence was published in 1995 by Mayor & Queloz (1995), using the Radial Velocity (RV) method. The authors went on to win the Nobel Prize in Physics in 2019 for this work where they measured the star's movements that are caused by the gravity of the exoplanet to infer its presence (see Section 1.2.2). 51 Pegasi b is a massive planet similar in mass to Jupiter, orbiting its star at short orbital separation, completing an orbit in 4.23 days — a population now known as *hot Jupiters* — which is unlike any object in our own Solar System.

In the year 1999, the first transit — a dip in the flux of a star due to an object moving across the stellar disk (see Section 1.2.1) — of an exoplanet, HD 209458b, was

---

[1] `https://exoplanetarchive.ipac.caltech.edu/docs/exoplanet_criteria.html`, accessed 04/05/2023

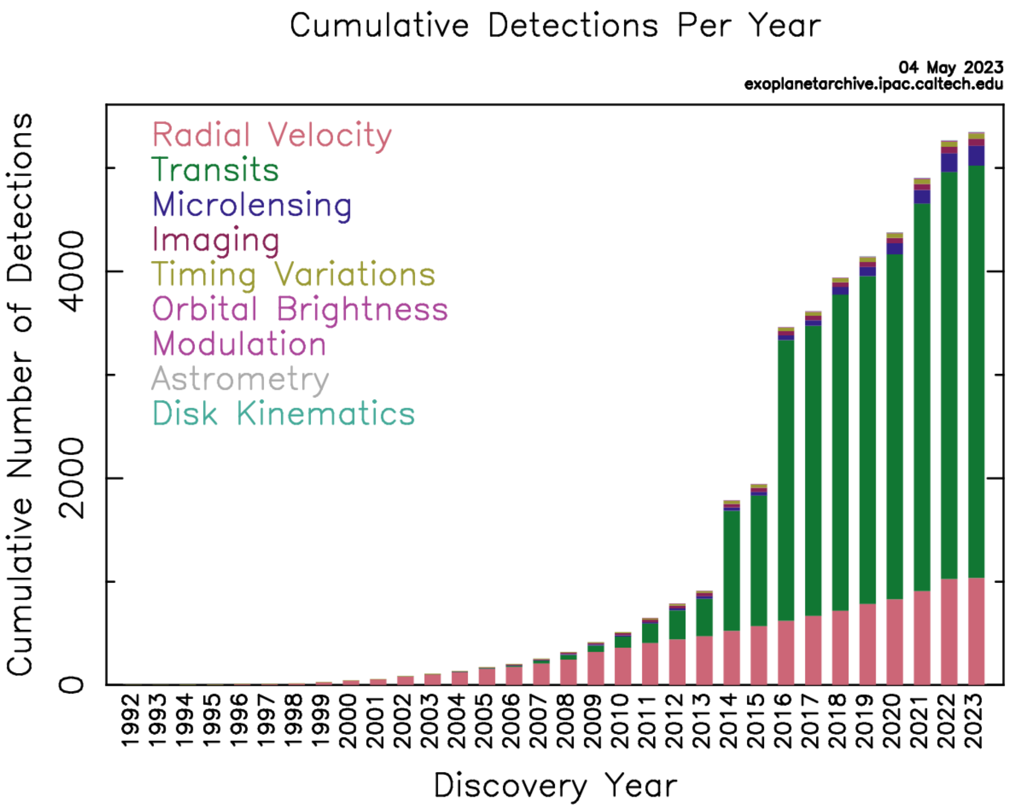

Figure 1.1: Figure from the NASA Exoplanet Archive showing the cumulative number of exoplanets as function of time (accessed 4 May 2023), split up by the individual detection methods. Note that 'Timing Variations' here refers to planets discovered with any timing variations so include both Transit timing variations (TTVs) and pulsar and pulsating timing variations, for further details see text.

observed (Charbonneau et al., 2000), which had previously been discovered using the RV method by Henry et al. (2000) where they also reported photometric variations which might be due to the planet transiting. Surpassing the number of detections by the RV method, the transit method is currently the most successful for discovering exoplanets ($\approx$ 75% of the overall number of detections as of May 2023, see also Fig. 1.1), largely due to ground-based surveys such as WASP (Wide Angle Search for Planets; Pollacco et al., 2006) and HATNet (Hungarian-made Automated Telescope Network; Bakos et al., 2004), as well as space missions such as Kepler (Borucki et al., 2010) and more recently TESS (Transiting Exoplanet Survey Satellite Ricker et al., 2015). The Kepler mission is also the reason for a large jump in the number of detected exoplanets around the year 2016, see Fig. 1.1.

Overall 5437 exoplanets have been detected to date according to the NASA exoplanet archive (as of 4 May 2023), see Fig. 1.1 where all exoplanets are plotted

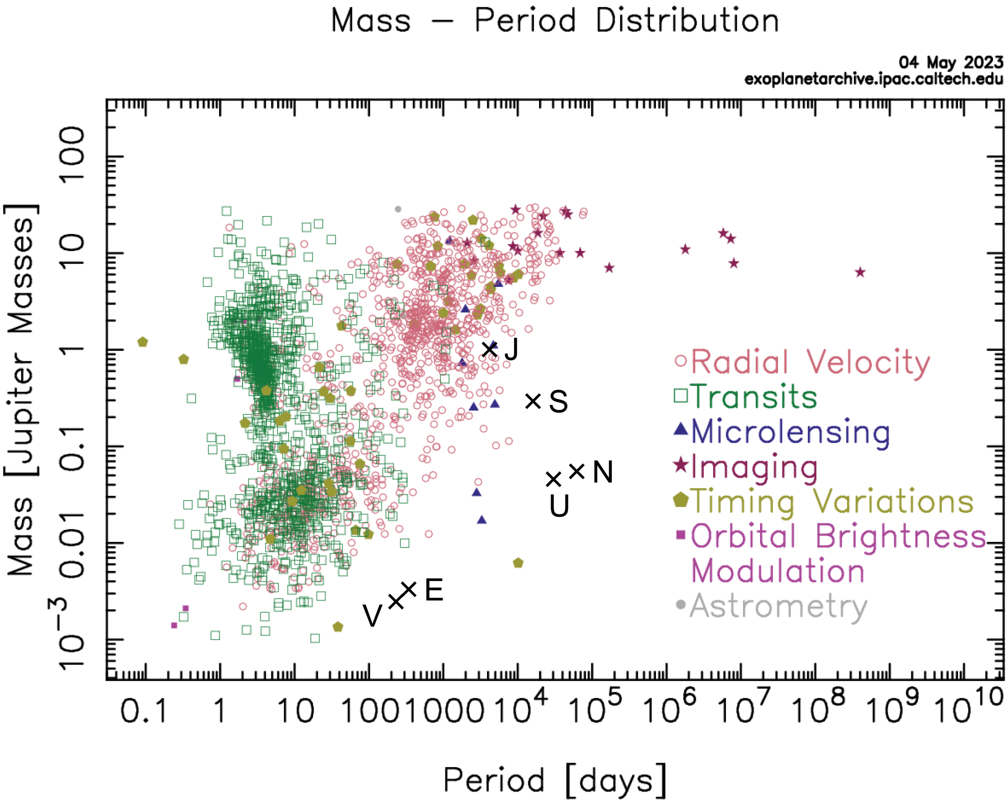

Figure 1.2: Figure from the NASA Exoplanet Archive showing all detected exoplanets to date (4 May 2023) with their mass and period, split up by the individual detection methods. The Solar System planets are marked with their first letter (except for Mercury and Mars which are not massive enough to fit on this figure). Note that 'Timing Variations' here refers to planets discovered with any timing variations so both including Transit timing variations (TTVs) and pulsar and pulsating timing variations, for further details see text.

cumulative since the first discovery, split up by different detection methods. Fig. 1.2 shows all exoplanets' mass and period split up by colour indicating their individual detection method. In the following sections I describe each detection method in more detail, in particular focusing on the transit method which is the basis of the work in this thesis, and RV method which provides the mass measurements essential for accurate atmospheric studies. Exoplanet detection methods using microlensing, imaging, timing variations, orbital brightness modulation, astrometry and disk kinematics are not relevant to the research presented in this thesis and are solely included for completeness.

1.2.1 Transit Method

A *transit* refers to the dip in the brightness of a star caused by an object moving across the face of the star from our point of view. This object most commonly is either another star, referred to as an eclipsing binary, or a planet. To confirm a transit, it is usually necessary to observe the transit of an exoplanet three times, also determining the planet's period P.

The extent of the dip in brightness is called transit depth δ and is usually given in either parts per million (ppm) or in percentage of the star's normalised brightness. These flux measurements of stars as a function of time are referred to as *light curves.* The transit depth is proportional to the ratio $R_\mathrm{p}/R_\mathrm{s}$ of planet R_p to stellar radius R_s squared:

$$\delta \simeq \left(\frac{R_\mathrm{p}}{R_\mathrm{s}}\right)^2 . \tag{1.1}$$

A typical transit observation is shown in Fig. 1.3. The time between contact point 1 and 2 is referred to as ingress, while the time between contact point 3 and 4 is referred to as egress.

Transit observations also allow us to determine the inclination of the system i, as well as the ratio a/R_s of the semi-major axis a of the planet's orbit to the stellar radius. This is possible by comparing the duration where the full planet is in transit T_{23} to the time between start and end of the transit, i.e., including ingress and egress, T_{14}, see also Fig. 1.3. Looking at the transit duration, we can see that it is strongly dependent on the impact parameter b, which is the projected distance between centre of the star and the crossing of the planet, see Fig. 1.4; the closer the planet's transit trajectory is to the stellar centre, the longer the transit. Geometrically (assuming a circular orbit) b can be described as

$$b = \frac{a\cos(i)}{R_\mathrm{s}}, \tag{1.2}$$

whereas the length the planet L has to travel across the disk of the star from point 1 to 4 can be expressed as

$$L_{14} = 2\sqrt{(R_\mathrm{s} + R_\mathrm{p})^2 - (bR_\mathrm{s})^2} = 2R_\mathrm{s}\sqrt{(1+\delta)^2 - b^2}; \tag{1.3}$$

and from point 2 to 3 can be expressed as

$$L_{23} = 2\sqrt{(R_\mathrm{s} - R_\mathrm{p})^2 - (bR_\mathrm{s})^2} = 2R_\mathrm{s}\sqrt{(1-\delta)^2 - b^2}, \tag{1.4}$$

see also Fig. 1.5.

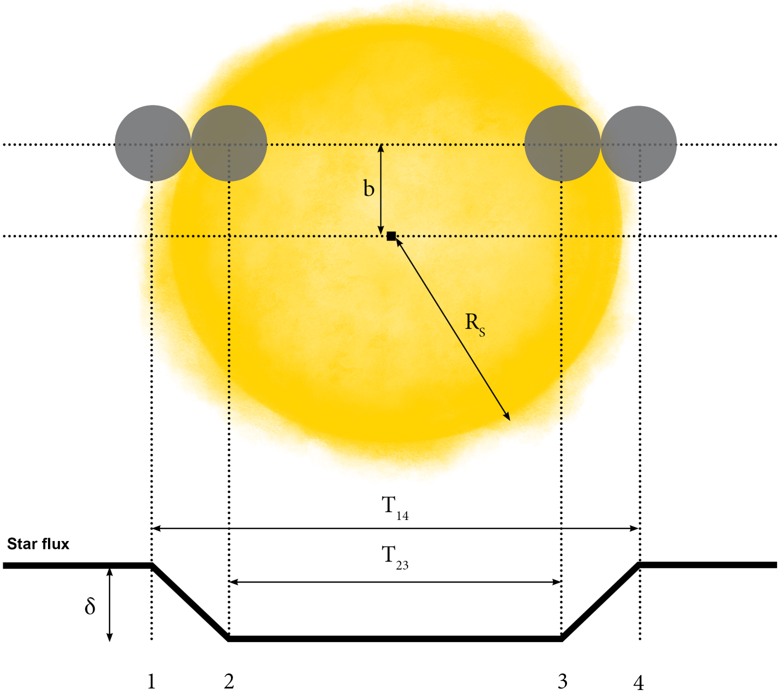

Figure 1.3: A planet transiting its host star, causing a dip in the brightness. The time between contact point 1 and 2 is referred to as ingress, while the time between contact point 3 and 4 is referred to as egress. The total transit duration is the time T_{14}, while the full transit time is T_{23} (as in the time when the planet transits fully). Figure loosely reproduced from `https://www.paulanthonywilson.com/exoplanets/exoplanet-detection-techniques/the-exoplanet-transit-method/`; accessed 02/05/2023.

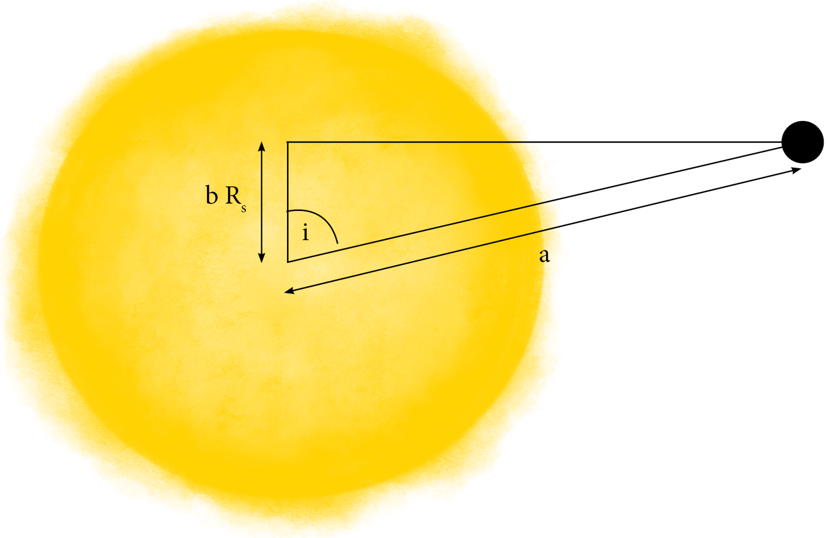

Figure 1.4: Schematic showing the relationship between impact parameter b, system inclination i and semi-major axis of the planetary orbit a. Figure loosely reproduced from https://www.paulanthonywilson.com/exoplanets/exoplanet-detection-techniques/the-exoplanet-transit-method/; accessed 02/05/2023.

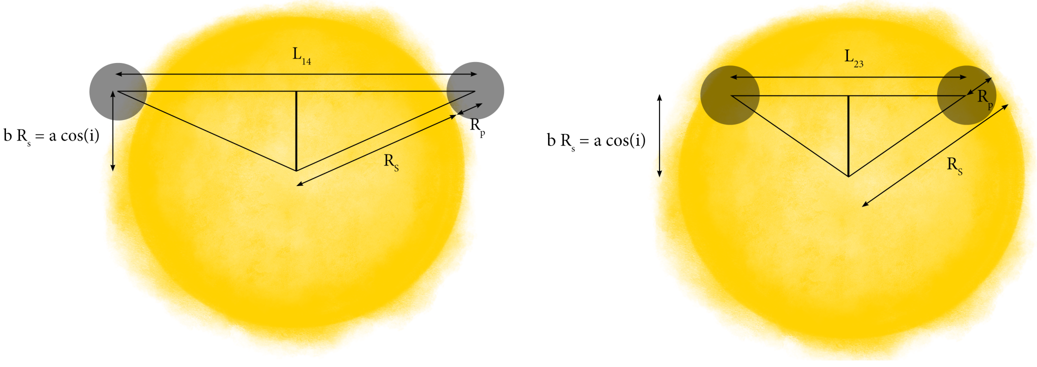

Figure 1.5: Projected transit distance difference between contact point 1 and 4 L_{14} (Left) and 2 and 3 L_{23} (Right), as well as demonstrating the geometric relationships between transit distances, stellar R_s and planetary radius R_p and impact parameter b. Figure loosely reproduced from https://www.paulanthonywilson.com/exoplanets/exoplanet-detection-techniques/the-exoplanet-transit-method/; accessed 02/05/2023.

Continuing to assume a circular orbit, the ratio between the angle α that the planet travels while transiting between points 1 and 4 and the full period 2π is equal to the ratio between the transit duration and the period:

$$\frac{\alpha}{2\pi} = \frac{T_{14}}{P}. \tag{1.5}$$

Using the geometry of the system, the triangle formed between points 1 and 4 and the centre of the star can be used to derive an alternative expression for α

$$\sin\left(\frac{\alpha}{2}\right) = \frac{L_{14}/2}{a}, \tag{1.6}$$

and thus the transit duration $T_{14} = P\frac{\alpha}{2\pi}$ can be changed to

$$T_{14} = \frac{P}{\pi}\arcsin\left(\frac{L_{14}/2}{a}\right) = \frac{P}{\pi}\arcsin\left(\frac{R_{\mathrm{s}}}{a}\sqrt{(1+\delta)^2 - b^2}\right); \tag{1.7}$$

similarly for T_{23}:

$$T_{23} = \frac{P}{\pi}\arcsin\left(\frac{L_{23}/2}{a}\right) = \frac{P}{\pi}\arcsin\left(\frac{R_{\mathrm{s}}}{a}\sqrt{(1-\delta)^2 - b^2}\right). \tag{1.8}$$

Following Winn et al. (2010), solving these two equations and assuming $R_{\mathrm{p}} << R_{\mathrm{s}} << a$, an approximate formula for the scaled stellar radius can be determined

$$a/R_{\mathrm{s}} = \frac{2\delta^{1/4}}{\pi}\frac{P}{\sqrt{T_{14}^2 - T_{23}^2}}, \tag{1.9}$$

which then can be used to determine the inclination using equation (1.2). These calculations are the basis of the transit model that I use when fitting my data, see Section 2.1.2, which also includes limb-darkening discussed in the next paragraphs.

Limb darkening

The shape of the transit is also dependent on the limb darkening of the host star as the star is not uniformly bright across its disk. This is due to the fact that with changing angles between our line of sight and the normal to the stellar atmosphere, the star becomes optically thick at different altitudes. The different heights of the stellar atmosphere are at different temperatures, resulting in different observed blackbody spectra between the limb and the centre of the star. This needs to be taken into account when modelling a transit and fitting transit parameters, especially in the bluer wavelength ranges where the flux differences are larger due to the steeper curve of the black body spectrum. Example light curves are shown in Fig. 1.6 taken from Rustamkulov et al. (2023). In this figure, the spectroscopic light curves of one transit of WASP-39b using *JWST* NIRSpec/PRISM are shown (see more details about *JWST* in Section 2.3.2), ranging from $0.46 - 5.71\,\mu\mathrm{m}$ and clearly showing the changes in limb-darkening between the blue and red end of the wavelength range.

Limb darkening is usually fit using limb-darkening laws and fitted simultaneously with the transit light curve (see Section 2.1.2). The intensity due to limb darkening is often parameterised by (but not limited to) a linear, quadratic, square-root or non-linear (4-parameter) model, from top to bottom (Claret, 2000):

$$I(\theta) = I(0)\,(1 - u_1(1-\mu))\,, \tag{1.10}$$

$$I(\theta) = I(0)\left(1 - u_1(1-\mu) - u_2(1-\mu)^2\right), \tag{1.11}$$

$$I(\theta) = I(0)\,(1 - u_1(1-\mu) - u_2(1-\sqrt{\mu}))\,, \tag{1.12}$$

$$I(\theta) = I(0)\left(1 - u_1(1-\sqrt{\mu}) - u_2(1-\mu) - u_3(1-\mu^{2/3}) - u_4(1-\mu^2)\right), \tag{1.13}$$

where $\mu = \cos\theta$ and $I(\theta)$ is the intensity at angle θ, which is the angle between our line of sight and the normal to the stellar atmosphere. Therefore $I(0)$ is the intensity in the centre of the disk and u_1 to u_4 are the wavelength-dependent limb-darkening coefficients.

When fitting limb-darkening parameters, one of the considerations for choosing one of the above laws is the computational efficiency, e.g. the non-linear law and square-root law will take much longer to compute than the quadratic law. Therefore, the quadratic law is often used for its simplicity and efficiency. Most light curves do not necessitate the use of higher-order laws, however, correlations between limb-darkening laws and values versus transit depth should always be checked.

In practice, it is common to use stellar atmosphere models and generate limb-darkening coefficients which are then used to inform the fitting e.g. by using uniform or Gaussian priors around the generated values, see also Section 3.5. Fixing one or more limb-darkening coefficients to generated values is also common and was done during my studies presented in this thesis, see Chapters 3&4&5. However, fixing all limb-darkening parameters has been shown to be problematic and not accurately represent the data (e.g. see Csizmadia et al., 2013; Espinoza & Jordán, 2015).

Another practical method for fitting for limb-darkening models is using the Kipping parameterisation as introduced by Kipping (2013). They suggest using a different parameterisation of the quadratic law (see equation 1.11), namely to

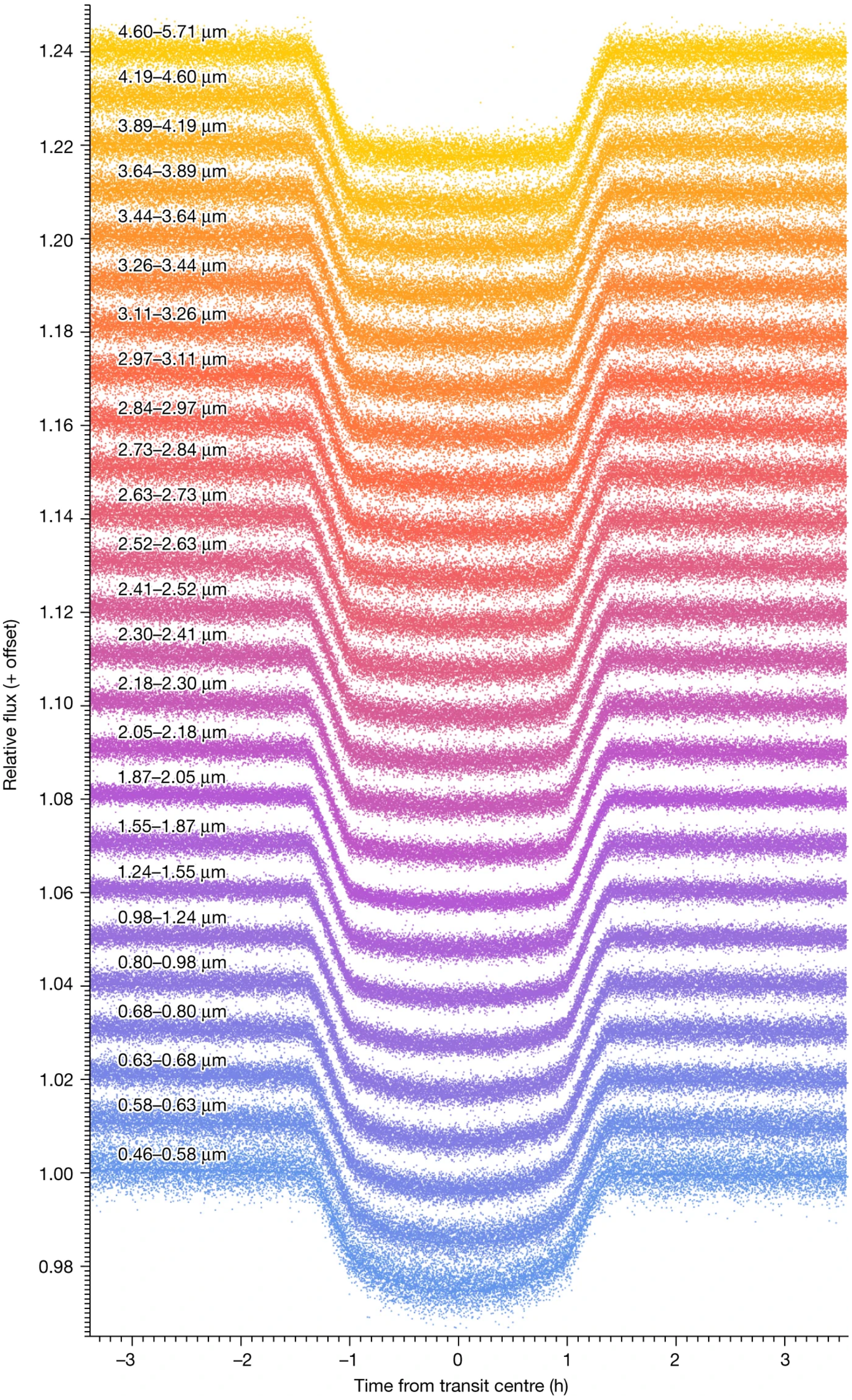

Figure 1.6: Figure 2 from Rustamkulov et al. (2023): Individual light curves in the wavelength range $0.46 - 5.71\,\mu\mathrm{m}$ of one transit of hot Jupiter WASP-39b using the NIRSpec/PRISM instrument on the *JWST*. This nicely demonstrates the difference in flux, in the shape of the ingress and egress, due to limb darkening at the bluer and redder wavelength ranges.

substitute u_1, u_2 by $q_1 = (u_1 + u_2)^2$ and $q_2 = 0.5u_1(u_1 + u_2)$. This parameterisation is suggested to reduce the evaluation of non-physical parameter combinations of u_1 and u_2 and reduce the degeneracy between the two limb-darkening parameters. It was used in the study of exoplanet WASP-39b in Chapter 5.

Transit Timing Variations (TTVs)

While not relevant in this thesis, transits can also be used to determine the mass of exoplanets. Variations in the transit timing, i.e., changes in the period of the transit, can be caused by another planet (possibly non-transiting) due to gravitational interactions. Therefore this can be used to reveal the presence of a planet in a system as these TTV variations are proportional to the mass of the perturbing object (e.g. Holman et al., 2010; Hadden & Lithwick, 2014; Piaulet et al., 2023). This method is particularly advantageous in cases where RV measurements are challenging to take e.g. when the host star is too faint or very active (e.g. Trappist-1; Gillon et al., 2017). An overall of 25 exoplanets have been found using TTVs to date[2].

1.2.2 Radial Velocity (RV) Method

The Radial Velocity method uses the fact that the star and planet system orbit around a common centre of mass, causing a Doppler shift in the observed stellar spectrum with the planet's orbital period, see Fig. 1.7 (Figure 4 from Mayor & Queloz, 1995). The semi-amplitude of this variation K can be described as

$$K = \left(\frac{2\pi G}{P}\right)^{\frac{1}{3}} \frac{M_{\rm p} \sin(i)}{(M_{\rm p} + M_{\rm s})^{\frac{2}{3}}} \frac{1}{\sqrt{1 - e^2}}, \tag{1.14}$$

where G is the gravitational constant, i the inclination of the system, P the period of the planet, $M_{\rm p}$ the mass of the planet, $M_{\rm s}$ the stellar mass and e the eccentricity of the orbit (e.g. see Perryman, 2018). The ability of this method to measure the mass of the planet is complementary to the transit method which can measure the radius of the planet. Both are needed for calculating the density and the surface gravity of the planet, which are crucial parameters for atmospheric characterisation, see Section 1.4.1.

To measure the semi-amplitude $K_{\rm p}$ of a planet, the RVs over time of a star are fitted. The overall RV of a star with $N_{\rm p}$ orbiting planets at time $t_{\rm i}$ is

---

[2] `https://exoplanetarchive.ipac.caltech.edu/docs/exoplanet_criteria.html`, accessed 04/05/2023

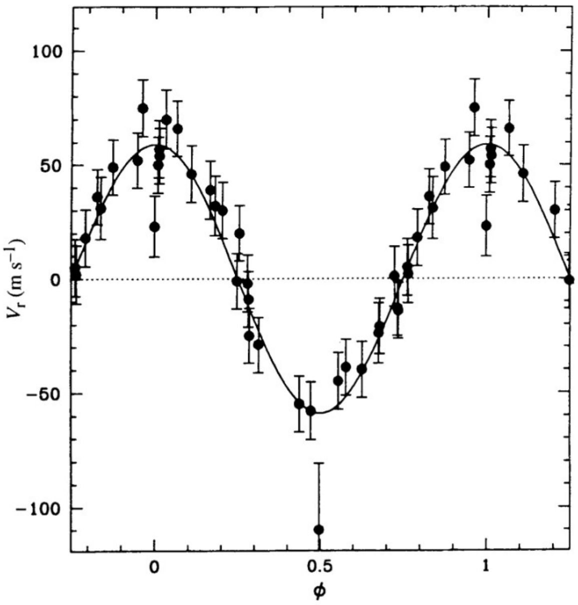

Figure 1.7: Figure 4 from Mayor & Queloz (1995): RV signatures of the exoplanet 51 Peg b, a hot Jupiter orbiting its host star. This figure clearly shows sinusoidal RV variations (here V_r) of several tens of m/s at every phase ϕ of the planet's orbit.

$$RV(t_i) = V_i + \sum_{p=1}^{N_p} K_p \left[\cos(f_{i,p} + \omega_p) + e_p \cos(\omega_p)\right], \tag{1.15}$$

where V_i is the systemic velocity and $f_{i,p}$ the true anomaly, e_p the eccentricity, ω_p the longitude of periastron and K_p the semi-amplitude of the p-th planet in the system (Balan & Lahav, 2009). The longitude of periastron is the angle where the planet is at its periastron but from the observer's point of view, aiding in defining the orientation of the orbital plane with respect to the sky plane.

Note that $f_{i,p}$ is also a function of e_p, ω_p and the period P_p of the planet which links back to the Kepler's equation, which cannot be solved analytically:

$$M_i = E_i - e_p \, \sin(E_i), \tag{1.16}$$

where M_i is the mean anomaly of the system and E_i the eccentric anomaly at time t_i. These angles and geometric definitions are introduced to aid the calculation of the true anomaly $f_{i,p}$ in equation (1.15), which is the angle between the star (which is located in one of the focal points of the elliptic orbit) and the position of the planet at time t_i.

Solving Kepler's equation numerically means that running eccentric RV fitting can become computationally expensive. In the case of hot Jupiters most orbits are circular or circular enough that the eccentricity can be assumed to be equal to zero, then equation (1.16) becomes trivial and equation (1.15) reduces to a sum of sinusoidal planetary signals, see e.g. the signal of hot Jupiter 51 Peg b in Fig. 1.7 (Mayor & Queloz, 1995).

The measured RV variations range from $\approx 10 - 100\,\mathrm{m/s}$ for close-in Jupiter-sized exoplanets down to $\approx 10\,\mathrm{cm/s}$ for Earth-like exoplanets. Highly stable high spectral resolution spectrographs are needed to achieve the precision needed to detect terrestrial exoplanets and it is an ongoing challenge. In particular because periodic variations due to a star's activity can also cause RV shifts up to tens of m/s (depending on the stellar type and age of the star), potentially mimicking planetary signals. In recent years this led to extensive (and challenging) combined analyses of host stars and planets to disentangle stellar and planetary RV signals (e.g. Aigrain et al., 2012; Rajpaul et al., 2015; Barragán et al., 2019; Rajpaul et al., 2021).

Note that while this method can determine the period and eccentricity of the planet's orbit, the mass of the planet M_p can only be fully characterised if the inclination of the system is known, which can be measured with other methods e.g. with the transit method. Until then the RV method gives the value $M_\mathrm{p}\sin(i)$, which is essentially a lower mass limit.

Rossiter-McLaughlin (RM) Effect

In the case where exoplanets are known to be transiting and have RV measurements, one can not only narrow down the mass of the planet but can also measure the change of the RV Doppler shift due to the planet during its transit. This in turn allows us to determine the alignment (or misalignment) of the system and whether the planet is in a prograde or retrograde orbit. As hot Jupiters are thought to have undergone migration (see Section 1.3.3) the information whether the orbit of a hot Jupiter has been flipped or is misaligned can give insight into its migration mechanism, e.g. as is the case for WASP-94Ab in Chapter 3.

As the planet crosses the stellar disk from our point of view, it blocks different areas of the disk. These different areas have different blue and red shifts due to the fact that the star rotates, i.e., part of the stellar disk is moving towards us while the other part is moving away from us. Only in the case when a star's rotational axis is parallel to the line of sight we would not be able to expect a change in Doppler shift while a planet transits.

This change in Doppler shift during the transit is called the Rossiter-McLaughlin (RM) effect (Rossiter, 1924; McLaughlin, 1924). The RM curve is a plot of Doppler change versus time and its shape can be used to determine the projected obliquity (λ) of the system, which is defined as the angle between the planet's orbital plane

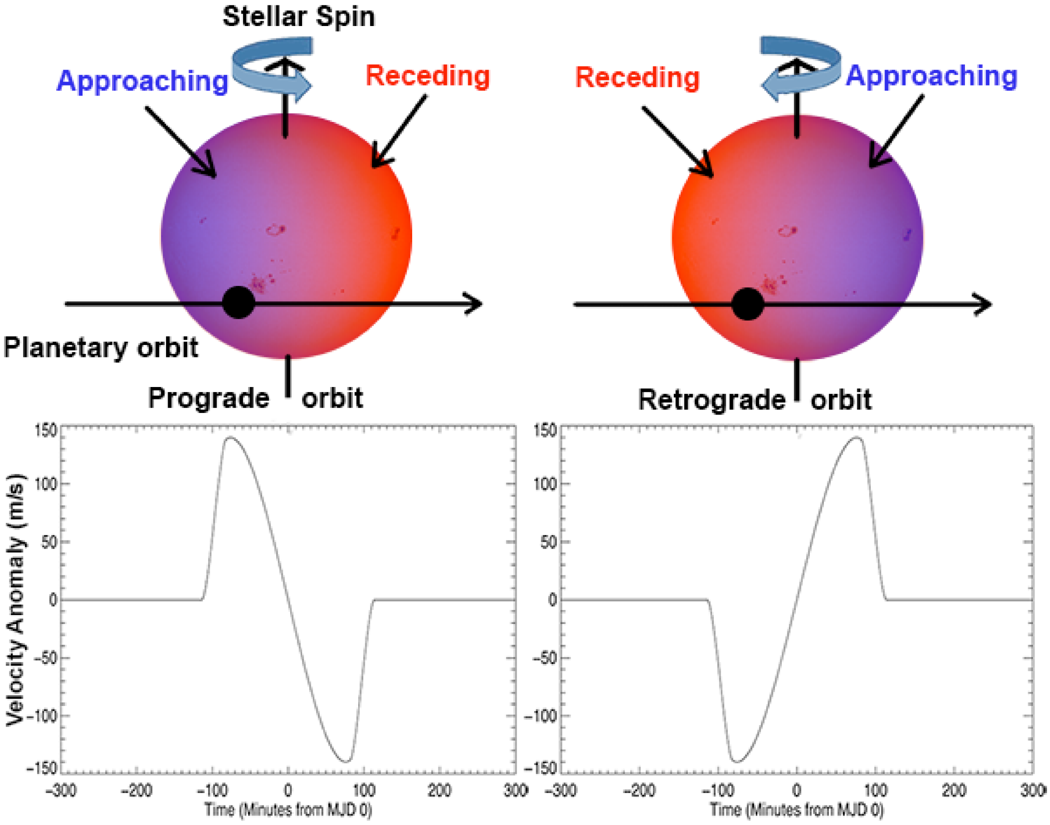

Figure 1.8: Figure 1 from Addison et al. (2014): schematic to illustrate the RM effect. Top row shows the two scenarios of prograde and retrograde orbiting planets transiting their host star. Bottom row shows the respective Doppler shift signals, i.e., the change in the RV measurements due to the blocking of red- and blue-shifted signals from the star. Note that in the case of misaligned orbits the RM curve would not be symmetric as shown here due to the planet travelling across blue- and red-shifted regions for an unequal length of time.

and the stellar equator. Thus if this angle is non-zero the planet is misaligned relative to its host star (it might still be misaligned even if the projected angle is zero). The shape also determines whether the planet orbits its host star in a prograde or retrograde motion, i.e., in which order the planet blocks red-shifted and blue-shifted areas, see Fig. 1.8 (Figure 1 from Addison et al., 2014). The first Rossiter-McLaughlin effect was measured by Queloz et al. (2000), where they used the ELODIE (Baranne et al., 1996) spectrograph to constrain the obliquity for an exoplanet, in this case HD 209458b which was the only known transiting exoplanet at that time.

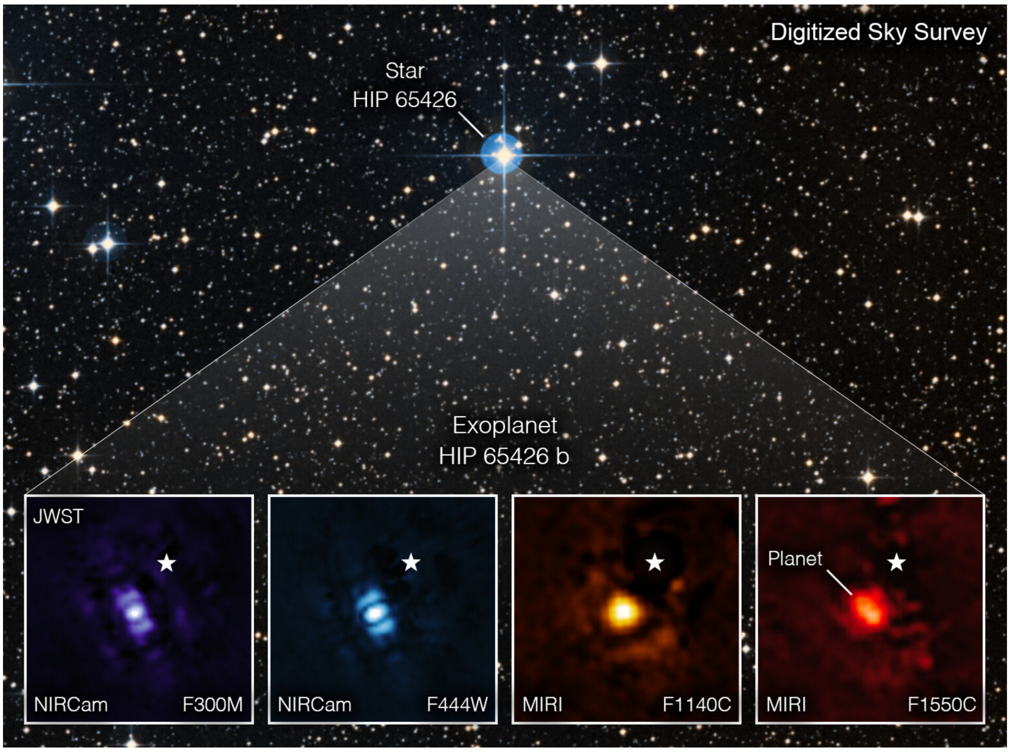

Figure 1.9: Observations of HIP 65426b using the *JWST* instruments NIRCam and MIRI and constraining its mass to 7.1 ± 1.1 Jupiter masses (**?**). Credit: NASA/ESA/CSA, A Carter (UCSC), the ERS 1386 team, and A. Pagan (STScI).

1.2.3 Direct Imaging

The method of detecting exoplanets by directly imaging them has had increased interest in recent years. While it is not relevant to the research discussed in this thesis, I provide a short summarise this method, its history and its effects on upcoming hot Jupiter science.

The method is extremely difficult in practice mainly due to technological limitations in terms of spatially resolving the planet from its star (angular separation), as well as the extreme brightness difference in host star and planetary companion (contrast ratio). In addition, a coronagraph is usually used to block the host star's light, see Fig. 1.9.

A planet's brightness is a sum of its own thermal emission and reflected light which is dependent on the planet's geometric albedo. The thermal emission of an exoplanet can be estimated with the equilibrium temperature of the planet and assuming a black body spectrum. Using Wien's displacement law, the peak for hot Jupiters, assuming $T_{\mathrm{eq}} = 1500\,\mathrm{K}$, is at a wavelength of $1.9\,\mu\mathrm{m}$. Note that younger planets still contain heat from formation so will need different considerations, but those are often targeted deliberately for this reason.

The reflected light component is an echo of the host star's spectrum and thus is brighter in the bluer wavelength ranges due to its higher black body temperature. Therefore the contrast ratio between star and exoplanet due to reflected light is roughly constant over wavelength, while the contrast ratio due to thermal emission is much better in the longer, infrared wavelengths. However, infrared observations are difficult from the ground due to Earth's atmosphere which is why infrared space missions are very amenable for this detection method.

In the ideal case where ground-based observations are not contaminated by the Earth's atmosphere and we have perfect optics, we can get achieve an angular separation equal to the diffraction limit of the telescope. This limits the observable projected distance in the night sky that we can observe an exoplanet orbiting its host star.

Therefore directly imaged exoplanets are technologically challenging, however, 88 exoplanets have been found using this method to date[3] with the first exoplanet imaged by Chauvin et al. (2004). Other examples of planetary systems discovered via direct imaging include HR 8799 with its four planets (Marois et al., 2008), as well as PDS 70 with two planets and a protoplanetary disk (Wang et al., 2020).

Directly imaged planets provide a crucial addition to the other detection methods as it probes long-period planets and non-transiting planets. In addition, as it is a direct flux measurement of the planet it does not have a stellar component to account for during the observations as is the case for transit observations. As soon as it is possible to directly image hot Jupiters we will be able to rule out causes for potential systematics e.g. due to incorrect limb-darkening laws or steller heterogeneities.

1.2.4 Microlensing

The microlensing method uses the fact that light is bent by a gravitational field and therefore an exoplanet — even though not bright enough itself — bends the light from a star behind it due to its mass, which can be measured by observing this bending(Einstein, 1936). This method is included due to completeness but is not relevant to the work in this thesis. Its concept and history, as well as advantages and disadvantages are summarised below.

---

[3] `https://exoplanetarchive.ipac.caltech.edu/docs/exoplanet_criteria.html`, accessed 04/05/2023

Assume that we observe the light of a source which is bent by a star in front from our point of view. If a planet orbits the lens star it can create an additional, relatively short change in the flux of the source (e.g. Mao & Paczynski, 1991), see Fig. 1.10. This flux change depends on the mass of the planet, proper motion and angular radius of the source star.

The first exoplanet to be discovered by this method was OGLE 2003-BLG-235/MOA 2003-BLG-53, an object with 1.5 Jupiter masses orbiting its host star at a distance of ~ 3 AU (Bond et al., 2004). To date 187 planets have been confirmed via the microlensing method[4], mostly due to collaborations such as OGLE (Optical Gravitational Lensing Experiment) and MOA (Microlensing Observations in Astrophysics) (e.g. Bond et al., 2004; Udalski et al., 2005; Beaulieu et al., 2006; Bennett et al., 2014; Bond et al., 2017; Olmschenk et al., 2022). In addition, there are major space missions planned which will provide the continuous photometric monitoring needed to find exoplanets via gravitational microlensing, such as the *Nancy Grace Roman Space Telescope* (formerly known as *WFIRST*, Wide Field Infrared Survey Telescope) and the *Euclid* (launch in July 2023) mission (e.g. see Bachelet & Penny, 2019).

One major advantage of detecting exoplanets using gravitational lensing is that it is probing for planets with semi-major axes of $1-5$ AU (e.g. Beaulieu et al., 2006), which is a difficult range to access for more effective detection methods such as transits or RVs. However, planet parameters tend to be degenerate with other parameters when fitting the gravitational lensing event and gravitational lensing events do not repeat, thus making follow-up observations close to impossible.

1.2.5 Other Detection Methods

Here I shortly summarise other methods for discovering exoplanets that do not attribute a large number to the current known exoplanets and are also not essential to this thesis.

Astrometry

Using astrometry for detecting exoplanets is based on the same idea as the RV method. While the RV method (Section 1.2.2) uses spectroscopy to identify the periodic 'wobble' of the star introduced by an exoplanet, astrometry uses the change in position of the star on sky to measure it.

---

[4] `https://exoplanetarchive.ipac.caltech.edu/docs/exoplanet_criteria.html`, accessed 04/05/2023

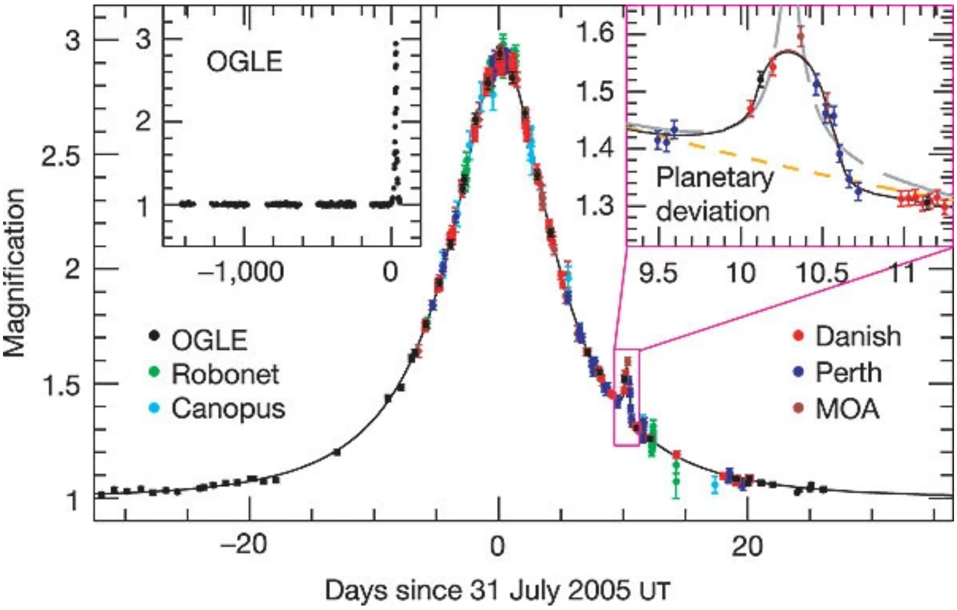

Figure 1.10: Figure 1 from Beaulieu et al. (2006): gravitational microlensing of OGLE-2005-BLG-390 using flux measurements from the Danish telescope (ESO La Silla, red), Perth (blue), Canopus (Hobart, cyan), RoboNet Faulkes North (Hawaii, green), OGLE (Las Campanas, black) and MOA (Mt John Observatory, brown). The yellow dashed line refers to a model without a planetary companion, the grey dashed line fits a binary companion, while the solid line is the best-fitting model with a planetary companion of $5.5^{+5.5}_{-2.7}$ Earth masses at a distance of $2.6^{+1.5}_{-0.6}$ AU.

Only two planets have been discovered with this method to date[5], however, it has very successfully been used to support other detections, e.g. to measure the inclination of the system to retrieve accurate mass measurements for planets detected using the RV method (e.g. Benedict et al., 2002; McArthur et al., 2004; Benedict et al., 2006; McArthur et al., 2014; Snellen & Brown, 2018; Benedict et al., 2022).

It is expected that we will detect many more exoplanets with the astrometry method, with *Gaia* for example predicted to detect thousands of exoplanets out to distances of ~ 500 parsec during the nominal 5-year mission (Perryman et al., 2014). *Gaia* DR2 (Data Release 2 Gaia Collaboration et al., 2018) astrometry has already been used to refine exoplanet properties in combination with previous RV measurements (e.g. Llop-Sayson et al., 2021).

Pulsars and pulsating stars: Timing Variations and Orbital Brightness Modulation

A handful of exoplanets around pulsars and pulsating stars have been revealed by studying changes in the stars' brightness and/or frequency (e.g. Konacki & Wolszczan, 2003; Silvotti et al., 2007), or even directly detecting g-mode pulsations tidally excited by a planetary companion (Orbital Brightness Modulation) (e.g. Silvotti et al., 2014).

Disk Kinematics

Recently, using ALMA (Atacama Large Millimeter/submillimeter Array) observations Pinte et al. (2019) reported a gap in the dust disk around a star, as well as the detection of CO lines and perturbed disk kinematics which all are best explained by an exoplanet in the disk.

1.3 Planet Formation

Planets form in the protoplanetary disk of a star. Thus the atmospheric composition of exoplanets is inherently linked to the composition of the disk and on its formation location and evolution.

In this section I summarise the current theories regarding formation of planets: the leading ones suggest a planet can form either via core accretion or gravitational instability. This is followed by a specific discussion on the origins of hot Jupiters where I provide context for the unsolved mysteries in their formation.

---

[5] `https://exoplanetarchive.ipac.caltech.edu/docs/exoplanet_criteria.html`, accessed 04/05/2023

1.3.1 Core accretion

Core accretion describes the planet formation scenario where planets are built bottom-up, by accreting smaller planetesimals in the protoplanetary disk. A large enough mass is needed ($\sim$ 10 Earth masses) to form a gas envelope through runaway gas accretion where gas accretion continues until it either clears the accessible surrounding gas or the disk dissipates. (e.g. Pollack et al., 1996; Ikoma et al., 2000; Inaba et al., 2003).

Planet formation via core accretion can explain the order of the planets in our solar system as the smaller planets are closer and big gaseous planets are further away (e.g. Pollack et al., 1996). However, due to its large time scales, core accretion theory struggles to explain some observations, e.g. rings and gaps in a protoplanetary disk of a very young system (IRS 63 system, Segura-Cox et al., 2020).

1.3.2 Gravitational Instability

Gravitational instability or the self-gravitating disk scenario is a proposed mechanism where parts of the protoplanetary disk fragment (based on the disk stability criterion by Toomre, 1964) and allows for the formation of planets. This is only possible when the disk is massive enough (Boss, 1997). One of the major advantages is that it works on much shorter timescales (a few thousand years) as there is no build-up phase needed to accrete gas before the gas disk dissipates (a few Myr, e.g. Cieza et al., 2007; Mamajek, 2009) like in the core accretion models (Gammie, 2001).

1.3.3 Origins of hot Jupiters

Hot Jupiters are gaseous exoplanets similar in size to Jupiter but orbiting their host star in a much closer $\lesssim$ 10-day orbit; thus they are much hotter versions of the gas giants we see in our Solar System.

Since hot Jupiters are relatively easy to detect due to their short close-in periods and large size, which leads to large RV signatures and transit depths, there is now a significantly large known population of them. Though note that the occurrence rate of hot Jupiters is relatively low, with recent estimates between 0.2 – 0.7% around AFGKM stars (Grunblatt et al., 2019; Zhou et al., 2019; Temmink & Snellen, 2023).

Hot Jupiters have been a surprise since our understanding of planet formation had previously been based on our Solar System. There was no prediction that gas giants could be found in such close-in orbits, even though planet migration has

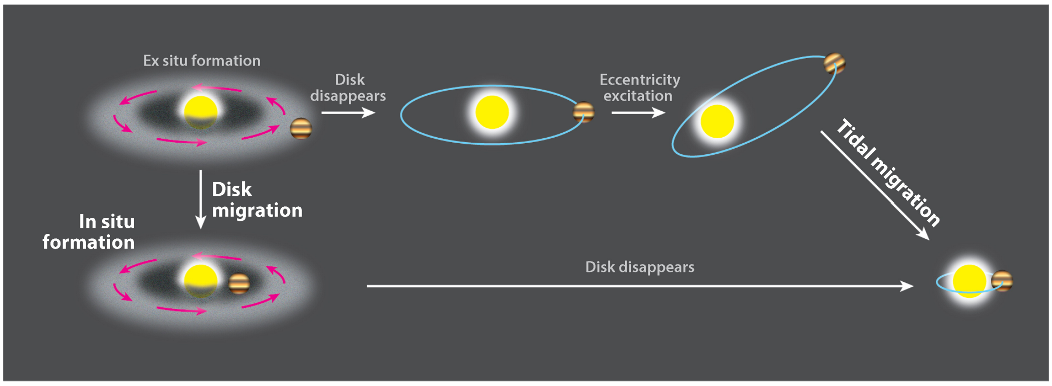

Dawson RI, Johnson JA. 2018.
Annu. Rev. Astron. Astrophys. 56:175–221

Figure 1.11: Figure 1 from Dawson & Johnson (2018), a schematic of the three hypotheses for hot Jupiters: in-situ formation, disk migration and high-eccentricity (also referred to as tidal or disk-free) migration.

already been suggested as a general theoretical concept for planetary objects before the first discovery of a hot Jupiter (Goldreich & Tremaine, 1980; Lin & Papaloizou, 1986).

Over the past almost 30 years since the discovery of the first hot Jupiter, there has been a lot of progress to further our understanding of the mechanisms that explain their close-in orbits (e.g. see review articles of Dawson & Johnson, 2018; Fortney et al., 2021) and at the current time there are three leading theories for the origins of hot Jupiters: in-situ formation, disk migration or high-eccentricity (or disk-free) migration. The first describes the formation of the hot Jupiters at their current observed, short close-in orbit, while the latter two theories assume that the giant planets formed much further out in the protoplanetary disk and migrated inwards either through the disk or through an external body that disturbed the orbit. Fig. 1.11 illustrates those three origin scenarios for hot Jupiters.

In-situ Formation

In-situ formation describes the formation of the hot Jupiters at their current observed, short close-in orbit.

While theoretically core accretion is able to explain in-situ formation (e.g. Lee et al., 2014; Batygin et al., 2016), it requires a large build-up of material for the core and this has been proven to be challenging as it is much easier to form solids out in the disk, beyond the slowline(s) (Schlichting, 2014; Lee & Chiang, 2016). There is no clear consensus on whether hot Jupiters can form in-situ by core accretion.

A better understanding of solids within the planetary disk may resolve this open question (for more details see review by Dawson & Johnson, 2018).

On the other hand, the conditions for gravitational instability cannot be met at such close-in orbits as (at such short periods) it would also require meeting the criterion for fragments to cool before they are rotationally sheared (Rafikov, 2005). This, however, is only possible with implausible high temperatures and gas surface densities, and Rafikov (2005) has shown that the gas would be unbound from the star at these temperatures.

Disk Migration

Assuming that a Jupiter-sized planet has formed further out in the disk by either core accretion or gravitational instability, the planet may have migrated towards the star through torques from the nonuniform gaseous disk (Goldreich & Tremaine, 1980; Lin & Papaloizou, 1986). It also must have come to a halt in the hot Jupiter region, i.e., before it was too close to the star and risked being either tidally destroyed or completely absorbed by the star. It has been suggested that this could be achieved via angular momentum transfer through tides from the star (e.g. Lin et al., 1996; Trilling et al., 1998) or through a magnetocavity mechanism due to the stellar magnetic field (e.g. Rice et al., 2007; Chang et al., 2009). Either way, if disk migration had taken place, the final location is likely highly sensitive to disk conditions (e.g. viscosity, scale height), mass loss, the magnetic field and tidal interactions (e.g. Faber et al., 2005; Chang et al., 2009).

High-eccentricity Migration

This mechanism was proposed to take place after the disk has dissipated and the giant planet has formed further out in the disk either via core accretion or gravitational instability. The planet's orbit gets disturbed by a third object and ends up in a highly eccentric orbit. This process is also referred to as the Kozai-Lidov mechanism (Kozai, 1962; Lidov, 1962). Over time this orbit becomes circular due to tidal decay and the hot Jupiter ends up in a narrow orbit around the star. This mechanism can also explain misaligned orbits and flipped orbits (e.g. see Fabrycky & Winn, 2009; Albrecht et al., 2012; Li et al., 2014; Albrecht et al., 2022) as identified using the RM effect (see Section 1.2.2 for more details) in several hot Jupiters. Observations have identified exoplanets on aligned and misaligned as well as prograde and retrograde orbits (e.g. Queloz et al., 2000; Triaud et al., 2010; Delrez et al., 2016; Santerne et al., 2016; Dorval et al., 2020; Knudstrup & Albrecht, 2022), including hot Jupiter WASP-94Ab (Neveu-Vanmalle et al., 2014) which is the focus of my atmospheric characterisation study in Chapter 3 and future studies as described in Chapter 3.8.

1.4 Exoplanet Atmospheres

In order to better understand hot Jupiters we can determine their atmospheric composition in an attempt to inform our conclusions about their formation and migration history. However, exoplanet atmospheres including hot Jupiters are not solely based on the protoplanetary disk they originated from. For example they could have undergone impacts but also effects from stellar irradiation and/or chemistry can influence a planet's atmospheric composition.

In the following sections I first describe how we can measure exoplanet atmospheres, with a focus on low resolution transmission spectroscopy which is the method used throughout this thesis. In general, for transiting exoplanets there are three techniques for characterising their atmospheres: (i) transmission spectra, where absorption by atoms and molecules in the atmosphere are identified by their imprints in the transit light curve at different wavelengths, (ii) emission spectra, where the day side of a planet is separated from the star during secondary eclipse of the planet, and (iii) phase curves, which is the detailed phase-resolved study of the modulation of planetary emission and reflection during its orbit (e.g. Perryman, 2018). I summarise these three methods at the beginning of this section.

For non-transiting planets, their atmospheres can only be characterised spectroscopically if they can be separated from their host star which is summarised shortly afterwards for completeness. A detailed discussion about the atmospheric inferences we can make from an exoplanet's transmission spectrum follows and I conclude this chapter with a description of the focus of the thesis.

1.4.1 Transmission Spectroscopy

Transmission spectroscopy is the spectroscopic study of the atmosphere of an exoplanet as it transits its host star, probing the day-night terminator region. There are different approaches how to extract a transmission spectrum, mainly dependent on the spectral resolution of the spectrograph. In this thesis I use low (spectral) resolution transmission spectroscopy for studying the atmospheres of three hot Jupiters (Chapters 3–5) and is described in detail below. For completeness I also include high (spectral) resolution transmission here as it complements low resolution observations and has been very successful in detecting molecules and atomic species in the atmosphere of hot Jupiters.

Low resolution transmission spectroscopy

In low spectral resolution (here $R \leqslant 10000$) observations of exoplanet atmospheres we study the transit depth of an exoplanet versus wavelength, i.e., we analyse transit light curves as a function of wavelength, e.g. see Fig. 1.6. Atmospheric opacities absorb the starlight and make it optically thick at wavelengths dependent on the opacity source, resulting in changes in transit depth.

Low resolution transmission spectra led to the first detection of sodium (Charbonneau et al., 2002), which was predicted previously by Seager & Sasselov (2000) and now identified in multiple other hot Jupiters (e.g. Redfield et al., 2008; Sing et al., 2012; Nikolov et al., 2016; Alderson et al., 2020). Other features detected include K (e.g. Sing et al., 2011; Nikolov et al., 2015; Sing et al., 2015; Feinstein et al., 2023), H_2O (e.g. McCullough et al., 2014; Wakeford et al., 2017a; Kreidberg et al., 2018; Carone et al., 2021; Ahrer et al., 2023b), as well as clouds and hazes (e.g. Pont et al., 2008; Kreidberg et al., 2014a; Sing et al., 2016; Louden et al., 2017; Spyratos et al., 2021, 2023), using ground-based telescopes such as the VLT (Very Large Telescope), the GTC (Gran Telescopio Canarias) and WHT (William Herschel Telescope) and space telescopes such as *Hubble* and *JWST*. Fig. 1.12 shows a sample of low resolution transmission spectra of 10 hot Jupiters using *Hubble* and *Spitzer* observations, indicating Na, K and H_2O features and cloud/haze structures (Sing et al., 2016).

High resolution transmission spectroscopy

In the high spectral resolution regime one is not sensitive to the continuum and broad molecular bands in the atmosphere, instead, one can resolve individual and a large number of spectral lines of an atom or molecule. Spectral lines of planetary origin will Doppler shift according to the planet's orbital velocity and can be identified using cross-correlation techniques. With this method narrow spectral lines can be identified and higher altitudes in the atmosphere are probed.

Stellar lines as well as telluric lines (spectral lines due to the Earth's atmosphere) contaminate the observed spectra in both low and high-spectral resolution data. In high resolution spectroscopy they need to be identified and removed as much as possible to accurately and robustly determine absorption from planetary atmospheres. This is often challenging, especially in the infrared as the Earth's atmosphere absorbs more flux largely due to water and this results in higher telluric

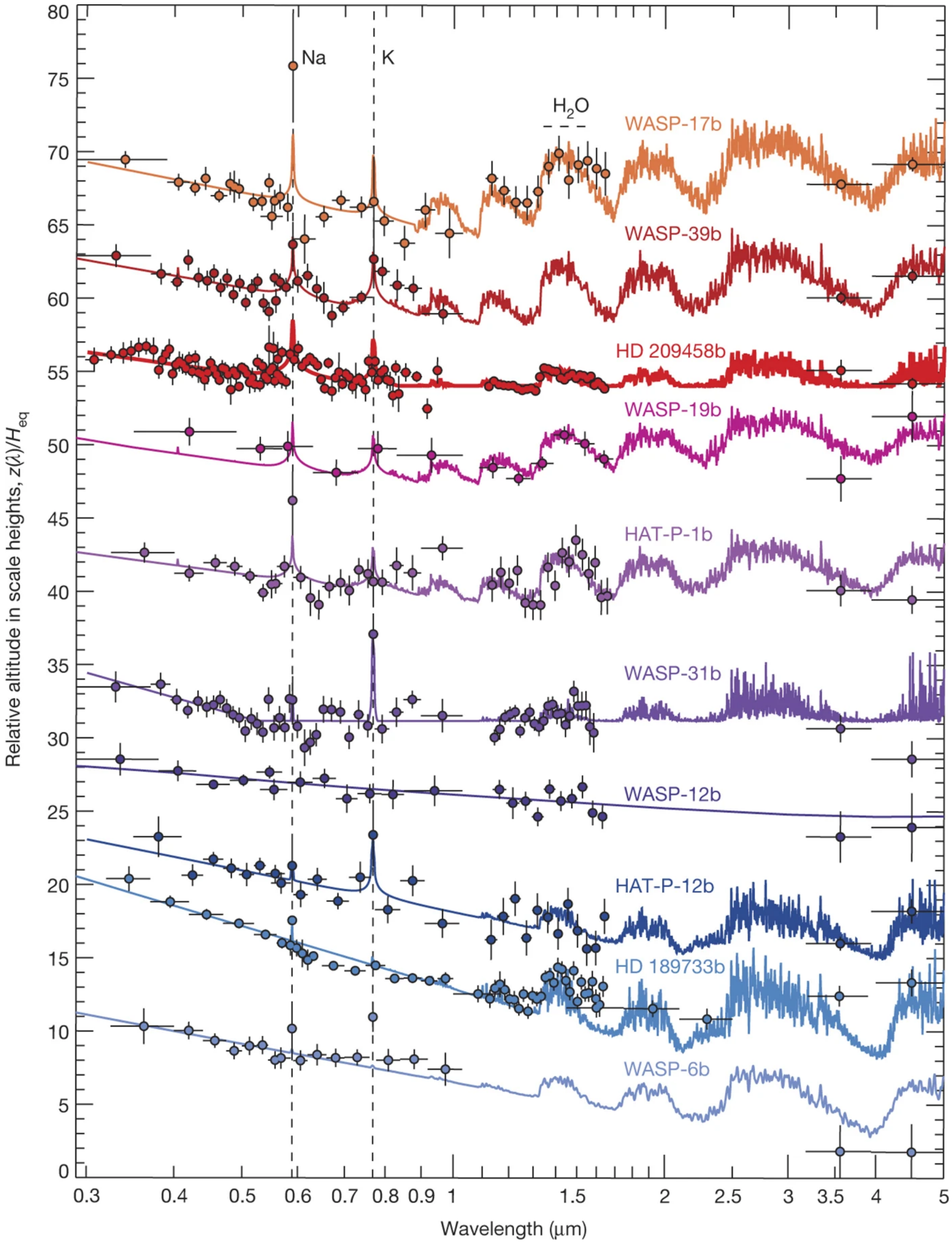

Figure 1.12: Figure 1 from Sing et al. (2016): transmission spectra of 10 hot Jupiters with *Hubble* and *Spitzer* observations. Solid lines refer to the best-fit model. This figure nicely demonstrates the different shapes that transmission spectra of hot Jupiters can take by absorption of alkali metals (dashed lines), water vapour bands (dashed region), scattering slopes towards the blue end and/or clouds which act to mute or mask entirely any absorption features (as seen with WASP-12b).

contamination.

High resolution transmission studies have made a variety and large number of molecular and atomic detections in the atmosphere of exoplanets, e.g. CO, Na, Ti, Fe, CO_2, CH_4 among others (e.g. Snellen et al., 2010; Wyttenbach et al., 2015; Hoeijmakers et al., 2018a; Seidel et al., 2019; Ehrenreich et al., 2020; Gibson et al., 2020; Giacobbe et al., 2021; Prinoth et al., 2022) using state-of-the-art spectrographs such as HARPS (High Accuracy Radial velocity Planet Searcher; Mayor et al., 2003), ESPRESSO (Echelle SPectrograph for Rocky Exoplanets and Stable Spectroscopic Observations; Pepe et al., 2014), CRIRES (CRyogenic InfraRed Echelle Spectrograph; Kaeufl et al., 2004) and IGRINS (Immersion GRating INfrared Spectrometer; Park et al., 2014) to name a few.

As my PhD work is focused on low spectral resolution transmission spectroscopy I do not describe the methods used in high resolution transmission spectroscopy in more detail here, but I do want to emphasise that high resolution is an important complementary method to low resolution spectroscopy as they probe different layers of the atmosphere and together provide a better understanding of the complete exoplanet atmosphere (e.g. Pino et al., 2018; Khalafinejad et al., 2021).

Atmospheric scale height

Studying the transmission spectrum of an exoplanet requires high photometric precision and a high enough cadence to resolve the transit. The aim is to measure the transit depth as a function of wavelength as precisely as possible so choosing as good of a star as possible is recommended. Exoplanets orbiting bright stars are good targets (e.g. HD 209458 in Charbonneau et al., 2002), as well as larger close-in planets and planets orbiting smaller stars.

Following Sing (2018) and Brown (2001), in addition to the obvious photometric precision and wavelength resolution requirement, one also has to consider the expected atmospheric signal, i.e., whether an atmosphere can be detected with the precision of the observing setup. The pressure or atmospheric scale height H is commonly used as an indicator for this purpose. It reflects the distance over which the pressure decreases by a factor of e, derived from the equation for hydrostatic equilibrium and the ideal gas law (assuming the atmosphere is isothermal). It is defined as

$$H = \frac{k_{\mathrm{B}}\, T}{\mu\, g}, \tag{1.17}$$

where k_{B} is the Boltzmann constant, T the temperature of the atmosphere, μ the mean mass of the atmospheric molecules and g the planet's surface gravity. The mean mass of the atmospheric molecules is usually estimated to be $\mu = 2.3$ atomic mass units (e.g. Sing, 2018) for giant exoplanets, which have an atmosphere dominated by H/He. The temperature of the atmosphere T is usually approximated to be equal to the equilibrium temperature of the planet, referring to the temperature expected from a balance of heating and cooling. The equilibrium of an exoplanet T_{eq} (assuming zero albedo). is calculated by

$$T_{\mathrm{eq}} = (1/4)^{1/4}\, T_{\mathrm{eff}} \sqrt{\frac{R_{\mathrm{s}}}{a}}, \tag{1.18}$$

where T_{eff} is the effective temperature of the host star, R_{s} the radius of the star and a the semi-major axis of the planet's orbit. The effective temperature of the host star is defined as the temperature of a blackbody of the same size as the star. It can be estimated by fitting a blackbody curve to the star's spectral energy distribution or by using empirical relation to determine a star's effective temperature, e.g. the NASA Exoplanet Archive uses the difference in magnitude in the B and V bands, $B - V$, for O through mid-K dwarfs and the relation derived by Flower et al. (1996).

The larger the atmospheric scale height H, the larger the expected absorption signal from the exoplanet's atmosphere. As an example, more massive exoplanets have high surface gravity which results in smaller atmospheric scale heights and thus in smaller signals in the transmission spectrum of the planet. But there is also a fairly large sample of hot Jupiters that have low densities due to inflated radii, have low surface gravities and high temperatures and as result have large atmospheric scale heights (e.g. Brown, 2001).

It is often convenient to refer to the atmospheric scale height as a change in transit depth i.e. the difference D_{sh} between the transit depth with and without the additional opacity from 1 atmospheric scale height. D_{sh} is the predicted signal, which is expressed following Bento et al. (2014) as

$$D_{\mathrm{sh}} = \frac{\pi (R_{\mathrm{p}} + H)^2}{\pi R_{\mathrm{s}}^2} - \frac{\pi R_{\mathrm{p}}^2}{\pi R_{\mathrm{s}}^2} = \frac{2HR_{\mathrm{p}} + H^2}{R_{\mathrm{s}}^2}, \tag{1.19}$$

where R_{p} and R_{s} are the radii of the planet and the star, respectively. Assuming that $R_{\mathrm{p}} >> H$, the predicted signal is given by

$$D_{\mathrm{sh}} \simeq \frac{2HR_{\mathrm{p}}}{R_{\mathrm{s}}^2}. \tag{1.20}$$

This value can then be used for target selection and is also quoted in Chapters 3&4 to show that the telescope and instrument setup is able to reach the precision needed to detect atmospheric signatures.

While I primarily use $D_{\rm sh}$ for target selection, another common value to calculate the Transmission Spectroscopy Metric (TSM) introduced by Kempton et al. (2018). The TSM is also based on the transmission signal being proportional to $\frac{HR_{\rm p}}{R_{\rm s}^2}$ as $D_{\rm sh}$, but absorbs parameters that are a constant (see equation 1.17), including semi-constant parameters that vary depending on the population of exoplanets you consider (specifically μ, the mean mass of the planet's atmospheric molecules), into a normalisation factor. It also considers the brightness of the planet's host star.

The TSM is given by

$$\mathrm{TSM} = \frac{R_{\rm p}^3 \, T_{\rm eq}}{M_{\rm p} \, R_{\rm s}^2} \times 10^{-m_J/5} \times \text{normalisation factor}, \tag{1.21}$$

where m_J is the apparent magnitude of the exoplanet's host star in the J band, but this can be of course changed to any bandpass magnitude. Note that $R_{\rm p}$ and $M_{\rm p}$ are in Earth radii ($R_\oplus$) and Earth masses ($M_\oplus$). In Kempton et al. (2018) the normalisation constant has also been utilised to scale the TSMs to give near-realistic values for the expected S/N for transit observations using *JWST* NIRISS/SOSS.

The fact that the TSM value depends on the magnitude of the star (which affects the S/N) is complementary to the predicted signal $D_{\rm sh}$ in ppm when generating target samples to observe.

1.4.2 Emission spectroscopy

Emission spectroscopy follows a similar concept to transmission spectroscopy, but instead of the transit this focuses on the secondary eclipse of the planet, i.e., the planet moving behind the host star. This allows us to observe the stellar spectrum without the planetary component. This is then used to identify the planet's dayside spectrum which consists of the planet's thermal spectrum and the star-reflected spectrum.

With the thermal and star-reflected spectrum varying in wavelength, this method follows a similar concept to direct imaging, see Section 1.2.3. Longer infrared wavelengths are more suitable for these observations as the emitted light from exoplanets is relatively large, peaking between 1–3 µm for hot Jupiters and with a long, almost constant tail towards longer wavelengths. An example emission spectrum of HD 149026b using *JWST* NIRCam observations is shown in Fig. 1.13, Figure 1 from Bean et al. (2023).

Using low resolution emission spectroscopy observations, molecules such as water vapour (both in absorption and emission) (e.g. Kreidberg et al., 2014b; Evans

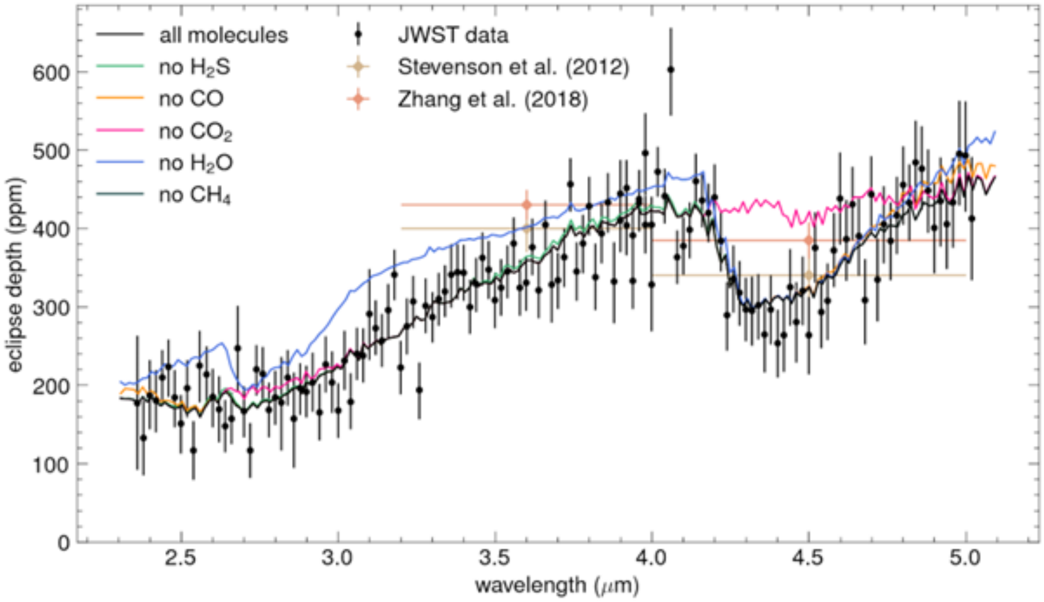

Figure 1.13: Figure 1 from Bean et al. (2023): The thermal emission spectrum of HD 149026b using *JWST* NIRCam observations (black points). Previous photometric observations from the *Spitzer* telescope (Stevenson et al., 2012; Zhang et al., 2018) are shown as diamonds, the horizontal error bar corresponding to the full width of the bandpasses. The solid black line refers to the best-fit model, while the coloured lines refer to models where the opacities of individual species are removed thus demonstrating their contributions to the emission spectrum, e.g. carbon dioxide in the area around 4.4 µm.

et al., 2017a; Fu et al., 2022) and CO_2 (shown in Fig. 1.13; Bean et al., 2023) have been successfully detected in exoplanet atmospheres and there has been evidence for other species such as CO, TiO and VO (Haynes et al., 2015; Evans et al., 2017a; Sheppard et al., 2017; Fu et al., 2022).

High resolution emission spectra have led to detections in exoplanet atmospheres such as CO, H_2O, OH (e.g. Brogi et al., 2012; Birkby et al., 2013; De Kok et al., 2013; Nugroho et al., 2021; Brogi et al., 2023; van Sluijs et al., 2023).

JWST is expected to be extremely beneficial for observing dayside exoplanet spectra due to its infrared observing capabilities. Science operations started in July 2022 and as of May 2023 *JWST* has already robustly detected three water emission features and found evidence for optical opacity in the dayside emission spectrum of WASP-18b using NIRISS/SOSS (Coulombe et al., 2023). The previously mentioned study by Bean et al. (2023) using *JWST* NIRCam has found carbon dioxide and water vapour absorption in the emission spectrum of Saturn-mass planet HD 149026b. For further details about *JWST*, its instruments and capabilities see Section 2.3.2.

The improved precision and high time cadence of *JWST* will also allow us to extract eclipse maps (Williams et al., 2006; Rauscher et al., 2006; De Wit et al., 2012; Majeau et al., 2012). The idea is to accurately resolve spectral slices during ingress and egress, probing different areas of the planet disk as it disappears behind and reappears at the side of the star. This is a challenging endeavour as any noise effects need to be well understood as well as any baseline trends in the light curve (e.g. Mansfield et al., 2020; Schlawin et al., 2023).

1.4.3 Phase curves

Observing the full phase curve of an exoplanet refers to the study of the planet for a full orbit as it transits and eclipses its host star, see example in Fig. 1.14. As the planet moves along its orbit it will contribute varying amounts to the flux received from the planetary system mainly due to the changes of observing different sides of the planet and the resulting temperature differences (day to night). This method assumes that we cannot resolve the star and planet on the sky (in contrast to direct imaging methods). Observations usually consist of two secondary eclipses and one primary eclipse and need almost continuous observations over a long period of time (up to days) or multiple shorter observations over months to cover a full phase.

Similar to eclipses, phase curves in different wavelength bands provide different information, i.e., in the optical wavelength range the light from the planet is dominated by reflected light so the phase curve can provide information about the planet's albedo (linking to its cloudiness) while the infrared wavelength passes

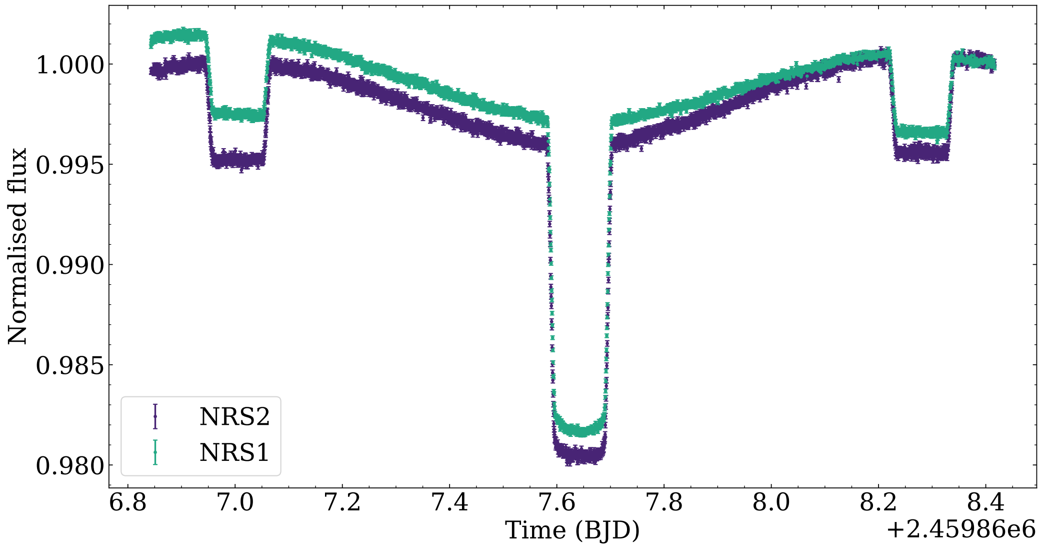

Figure 1.14: Phase curve observation of Jupiter-sized planet WASP-121b with the transit in the centre and two secondary eclipses at either ends of the observation. This figure uses *JWST* NIRSpec/G395H data from Mikal-Evans et al. (2023) taken over 37.8 hours and shows the white-light phase curves from the two detectors NRS1 and NRS2 (more details on *JWST* instruments in Chapter 2.3.2) which cover different wavelength ranges and exhibit different noise properties. The latter of which is assumed to be the cause for the offset between the two light curves. The authors have found that the peaks in both phase curves are minimally shifted prior to mid-eclipse ($\sim 3^{\circ}$).

through the clouds, allow us to access the planet's temperature structure and atmospheric composition.

The first phase curve observations by Knutson et al. (2007) of hot Jupiter HD 189733b using the *Spitzer* space telescope showed that hot gas giants can have an offset in their hottest spot from the substellar point, subsequently seen in other phase curves (e.g. Knutson et al., 2012; Stevenson et al., 2016b; Arcangeli et al., 2019; Mikal-Evans et al., 2023). This was predicted before from circulation models due to strong winds ('jets') along the equator caused by the large temperature differences on day and night side on tidally locked exoplanets (Showman & Guillot, 2002).

Phase curves are extremely challenging due to the fact that high precision is needed and any noise trends must be well understood (e.g. Crossfield et al., 2012), as well as model parameters (e.g. Bell et al., 2021). Recently Lally & Vanderburg (2022) also demonstrated that the observed variability in phase curve of a hot Jupiter in the optical wavelength range can also be explained by stellar activity, namely supergranulation on the star.

1.4.4 Non-transiting Exoplanets

High resolution spectrographs can also be used to characterise atmospheres of non-transiting planets by identifying their planetary trace, i.e., atomic or molecular signatures that are moving at the exoplanet's orbital velocity. Examples include Snellen et al. (2014) who detected CO in the atmosphere of β Pic b, as well as water vapour and CO in other non-transiting planets (e.g. Brogi et al., 2014; Hoeijmakers et al., 2018b; Petit Dit De La Roche et al., 2018; Wang et al., 2021).

While it is not relevant to the work in this thesis, looking ahead, upcoming telescopes such as the ELT (Extremely Large Telescope) are expected to play a large role in future atmospheric characterisation using direct imaging and high resolution spectroscopy due to its high angular resolution and sensitivity. This also includes very promising capabilities in both visible and infrared wavelength ranges (e.g. see Bowens et al., 2021).

1.4.5 Atmospheric Properties and Inferences

After observing exoplanet atmospheres with the various methods discussed in the previous sections, the retrieved results have to be interpreted. In this section I describe the atmospheric properties we can retrieve from transit observations of hot Jupiters. Different phenomena and atmospheric composition of an exoplanet leave different types of imprints on the retrieved planetary spectra which are detailed in the following paragraphs, starting with the most important properties: clouds and hazes and atomic and molecular absorption features (as shown in Fig. 1.12). Stellar activity can also induce observable variations in transmission spectra, often referred to as stellar contamination (e.g. McCullough et al., 2014; Rackham et al., 2017, 2019) and is summarised afterwards, followed by other instrumental or systematical contamination which can also occur e.g. due to the Earth's atmosphere. I conclude with a description on how measurements of molecular and atomic abundances allow us to infer constraints on planet formation and migration mechanisms.

Molecules and atoms

Molecular and atomic species in the exoplanet atmosphere absorb (and emit) light and leave imprints in the planetary spectrum. Shortly after the first exoplanets were confirmed, models predicted that the alkali metals sodium and potassium were likely to be detected using transmission spectroscopy of giant close-in exoplanets (Seager & Sasselov, 2000). This and other studies also suggested the presence of molecular bands in the infrared wavelength ranges such as water vapour and methane as well as Rayleigh scattering and clouds (e.g. Brown, 2001; Hubbard et al., 2001). They also predicted that line profiles (such as sodium and potassium) can show pressure-broadening, i.e., strong broadening of absorption lines due to collisions with deuterium in the atmosphere (Seager & Sasselov, 2000), which can be described using a Lorentz profile.

Sodium has now been detected in several hot Jupiters using both high- and low-resolution spectroscopy and both space and ground-based telescopes (e.g. Charbonneau et al., 2002; Redfield et al., 2008; Snellen et al., 2008; Huitson et al., 2012; Sing et al., 2015; Casasayas-Barris et al., 2017; Hoeijmakers et al., 2019; Alderson et al., 2020; Carter et al., 2020; Seidel et al., 2020; Ahrer et al., 2022; Langeveld et al., 2022). This also includes a small number of observations with evidence for the wings of pressure-broadened sodium in the low spectral resolution regime (Fischer et al., 2016; Nikolov et al., 2018; Alam et al., 2021; Ahrer et al., 2022). Potassium has also been observed in a few exoplanet atmospheres (e.g. Sing et al., 2011; Nikolov et al., 2015; Sing et al., 2015, 2016; Borsa et al., 2021; Chen et al., 2022; Feinstein et al., 2023).

Water vapour has been identified in many hot Jupiters, mainly using *HST* observations of the band centred on 1.4 µm (e.g. Huitson et al., 2013; Kreidberg et al., 2014b; Wakeford & Sing, 2015; Evans et al., 2016; Wakeford et al., 2017b; Kreidberg et al., 2018; Tsiaras et al., 2018; Carone et al., 2021) but also using high-resolution spectroscopy (e.g. Birkby et al., 2013; Brogi et al., 2014; Birkby et al., 2017; Hawker et al., 2018; Maimone et al., 2022). Oxygen-bearing species such as water vapour are particularly useful to constrain the metallicity and the carbon-to-oxygen ratio which in turn are used for studying trends and gathering insights into the formation and migration mechanisms in place, which are described later in this section.

Other atomic and molecular species detected using high spectral resolution data include ionised and atomic lines such as Fe, Fe+, Ti+, Ca, Ca+ in the atmosphere of ultra-hot Jupiters (e.g. Hoeijmakers et al., 2018a, 2019; Ehrenreich et al., 2020; Hoeijmakers et al., 2020; Borsato et al., 2023), as well as carbon-bearing species (e.g. Brogi et al., 2012, 2014; Giacobbe et al., 2021; Carleo et al., 2022; Guilluy et al., 2022). However, species such as CO_2 and CH_4 are challenging for low resolution observations as they exhibit features in the infrared wavelengths. With *JWST* we are now able to observe bands from carbon-bearing species such as carbon dioxide and carbon monoxide (e.g. The JWST Transiting Exoplanet Community Early Release Science Team et al., 2023; Alderson et al., 2023; Bean et al., 2023; Rustamkulov et al., 2023), however, surprisingly methane has not yet been detected using low resolution transmission spectroscopy. Possible causes are chemical disequilibrium processes that result in methane depletion (e.g. Cooper & Showman, 2006; Moses et al., 2011; Steinrueck et al., 2019; Tsai et al., 2021), and formation and migration mechanisms resulting in a low abundance of carbon-bearing species (e.g. Madhusudhan et al., 2014; Ali-Dib & Ali-Dib, 2017; Cridland et al., 2019). This is also relevant later in this section where I summarise formation and migration inferences and is mentioned in Chapter 5 as part of the discussion about the absence of methane absorption in the atmosphere of WASP-39b (Section 5.6.3).

Clouds/hazes and scattering

Understanding clouds and hazes in the atmospheres of exoplanets is essential for accurately identifying molecular and atomic abundances as clouds can mute or mask features entirely, while hazes and cloud layers can cause a slope in the observed transmission spectrum (e.g. Lecavelier Des Etangs et al., 2008a,b; Helling et al., 2016; Ohno & Kawashima, 2020). Note that I use aerosols as a term combining hazes and cloud layers (i.e. patchy clouds) that can cause scattering slopes, while I refer to clouds as a simplified case with no wavelength dependence; definitions and terminologies within the exoplanet community are not yet established. The composition of aerosols in a hot Jupiter depends heavily on its temperature but can still vary, as shown in Fig. 1.15.

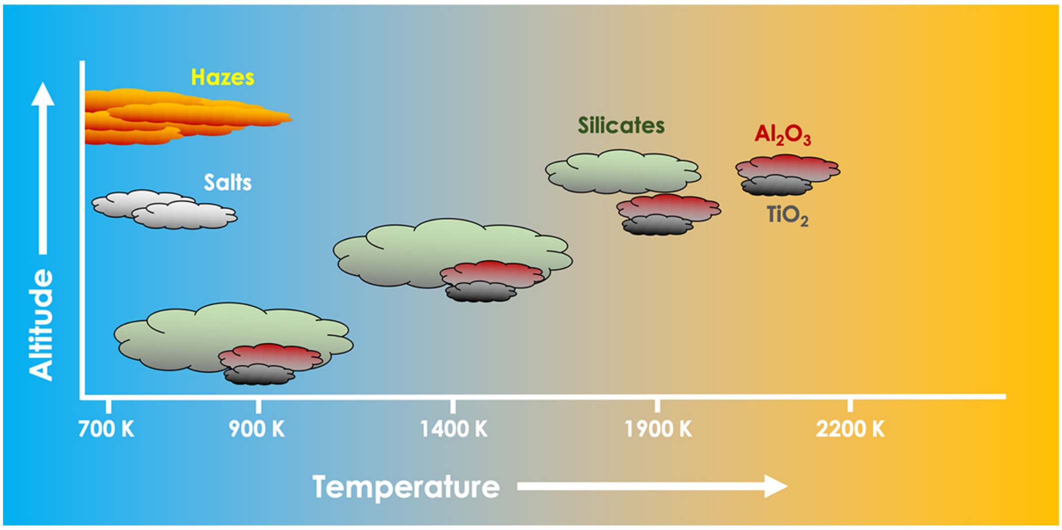

Figure 1.15: Schematic of cloud compositions and altitudes in hot Jupiter atmospheres as a function of temperature.
Figure Credit: Peter Gao, UC Berkeley

The first atmospherically studied exoplanet HD 209458b has shown a shallower absorption feature than expected (Charbonneau et al., 2002), suggesting high altitude clouds obscuring the pressure-broadened sodium wings (Fortney et al., 2003). A larger sample of observations shows that nearly every exoplanet gas giant contains some amount of cloudiness, see Fig. 1.12, as their features are muted or entirely obscured, the latter leaving a relatively flat transmission spectrum. Examples of flat transmission spectra include hot Jupiters (e.g. Kirk et al., 2016; Louden et al., 2017; Spyratos et al., 2021; Panwar et al., 2022b), as well as Neptune-size (e.g. Kreidberg et al., 2014a; Chachan et al., 2019) and Earth-sized planets (e.g. Crossfield et al., 2022; Damiano et al., 2022; Garcia et al., 2022). Note that the latter studies of smaller, Earth-sized planets generally conclude that a cloudy atmosphere is indistinguishable from no significant atmosphere at all.

However, modelling and retrieving clouds/hazes from spectra is not trivial as a lot of processes influence the composition, formation and evolution of aerosols in exoplanet atmospheres. This includes but is not limited to the temperature of the planet and stellar irradiation, the surface gravity, formation and migration history, as well as the multitude of microphysical interactions and chemical reactions that are not fully understood.

Rayleigh scattering in the atmosphere of an exoplanet results in an increase in transit depth in the bluer end of the spectrum. Rayleigh scattering describes scattering of light by particles in the atmosphere (main constituent is H_2) much smaller than the wavelength of the radiation, and thus is more prominent in the bluer end of the electromagnetic spectrum. In fact, the intensity of the scattering is proportional to wavelength λ^{-4} and a slope in the transmission spectrum due to Rayleigh scattering can be described as

$$-4H = \frac{d \ln R_\mathrm{p}}{d \ln \lambda}, \tag{1.22}$$

where H is the atmospheric scale height (see Section 1.4.1) and R_p the radius of the planet. The derivation of this and first discussions of Rayleigh scattering in hot Jupiter atmospheres and measurements in transmission spectra can be found in Lecavelier Des Etangs et al. (2008a,b).

In the literature, steep slopes in the transmission spectrum are often referred to as 'super-Rayleigh', i.e., gradients that are steeper than λ^{-4}. They cannot be explained by Rayleigh scattering and it has been suggested that they are a combination of Rayleigh scattering and opacity sources varying in altitude (e.g. Lecavelier Des Etangs et al., 2008a; Pont et al., 2013), photochemical hazes (Ohno & Kawashima, 2020) or contamination by stellar activity (e.g. McCullough et al., 2014; Espinoza et al., 2019). The steep scattering slope of HD 189733b (Pont et al., 2008; Lecavelier Des Etangs et al., 2008a; Sing et al., 2011; Huitson et al., 2012; Pont et al., 2013; Sing et al., 2016), second transmission spectrum from the bottom in Fig 1.12, is the most studied one and there is no clear consensus on its origin. It is generally attributed to high altitude hazes (Sing et al., 2016; Barstow, 2020), but other explanations include small mineral particles in the form of clouds (Lecavelier Des Etangs et al., 2008a; Pont et al., 2013; Helling et al., 2016; Lee et al., 2016) and a combination of clouds and haze layers (Pont et al., 2013; Pinhas et al., 2019). Distinguishing between different cloud species is difficult with current observations, but could be more accessible using mid-infrared wavelength ranges with *JWST*/MIRI, e.g. mineral aerosols (Wakeford & Sing, 2015)

There have been studies and comparisons to test for empirical correlations between the presence of clouds/hazes and planetary properties such as temperature (e.g. Stevenson, 2016; Crossfield & Kreidberg, 2017; Fu et al., 2017; Pinhas & Madhusudhan, 2017; Fisher & Heng, 2018; Taylor et al., 2021). However, they have mainly been inconclusive or contradicting each other so more research is needed.

In the last decade there has also been a major effort in the theory and modelling side of clouds and hazes in exoplanet atmospheres e.g. 1D cloud modelling (e.g. Mollière et al., 2017; Pinhas et al., 2018; Mollière et al., 2019), 3D cloud modelling (e.g. Parmentier et al., 2013; Lee et al., 2016; Lines et al., 2018; Steinrueck

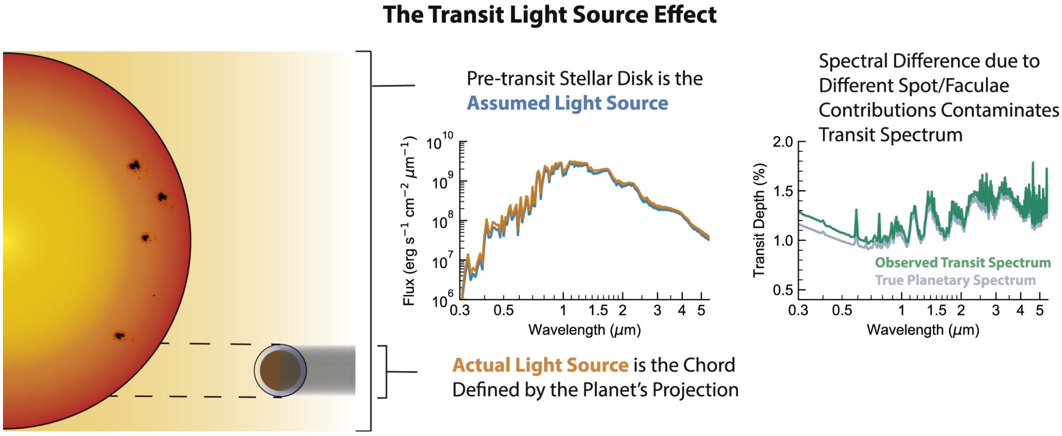

Figure 1.16: Figure 1 from Rackham et al. (2018): Schematic of stellar heterogeneities effecting the observed transmission spectrum, also referred to as the transit light source effect. The stellar light passing through the atmosphere of the exoplanet from our point of view varies as the planet crosses the stellar disk (left). Thus our assumed light source (disk-integrated) is not equal to the actual light source (middle) and can cement in differences in the transmission spectrum, particularly in the optical wavelength ranges (right).

et al., 2019; Roman & Rauscher, 2019) but also studies of cloud microphysics (e.g. Helling et al., 2016; Powell et al., 2018; Gao et al., 2020) and laboratory tests (He et al., 2018; Hörst et al., 2018; Yu et al., 2021), the latter remains challenging for high-temperature planets.

Stellar contamination

Opacity sources in the atmosphere of an exoplanet are not the only possible origin for a slope in the bluer wavelength range. Stellar activity can also cause a systematic rise in the measured transit depth due to spots and plage occurring on the stellar disk, e.g. as suggested for the case of HD 189733b's steep slope (McCullough et al., 2014; Oshagh et al., 2014). Recent simulations have shown that active FGK stars and nearly all M stars are expected to induce measurable features in transmission spectra, also referred to as the transit light source effect (e.g. Rackham et al., 2018, 2019), see Fig. 1.16.

In practice stellar heterogeneities are fitted at the atmospheric retrieval stage, i.e., parameters including spot coverage fraction and spot temperature are marginalised over (e.g. Pinhas et al., 2018; Mollière et al., 2019; Zhang et al., 2020; Welbanks & Madhusudhan, 2021). But fully accounting for stellar contamination is difficult as it is more complex than that, e.g. discrepancies between state-of-the-art models and measured stellar spectra exist (e.g. seen with *JWST* Rackham & de Wit, 2023; Moran et al., 2023) and there are degeneracies between the parameters describing the stellar heterogeneities and those defining the properties of the planetary atmosphere (e.g. Pinhas et al., 2018; Wakeford et al., 2019; Barclay et al., 2021).

Another issue that can arise was also demonstrated recently by Moran et al. (2023) where the authors were not able to constrain whether a water feature in the transmission spectrum originated from the planet's atmosphere or from water contained in cool spots on the M star. This is due to the models being degenerate at this wavelength range, bluer wavelength range in the right panel in Fig. 1.16).

Systematical contamination

Non-astrophysical effects can also imprint features in the retrieved exoplanet spectrum. This includes systematics such as absorptions from the Earth's atmosphere that were not fully accounted for (see Chapter 4) and changes in cloud cover, weather, airmass etc. during ground-based observations (Chapters 3&4). Instrumental effects, for both ground-based and space observations, can also introduce systematics e.g. due to instrumental settling time at the beginning of an observation, intrapixel effects due to detector pixels not having perfectly uniform spatial sensitivity (e.g. with *Spitzer*, see Stevenson et al., 2012; Deming et al., 2015), target position shifts over the course of the observation, fringing effects (Chapter 4, specifically Section 4.3), etc. These effects are removed as much as possible during data processing and data fitting, e.g. changes in weather are accounted for at the time of transit light curve fitting (Section 2.1.2) as well as during background subtraction at the data reduction stage (Section 2.1.1).

Other issues may arise when there are gaps in the observations due to scheduling or bad weather as it can cause differences in the retrieved transit depths, e.g. in the case of *Hubble* observations where the orbit limits the observations. In addition, systematics can also be introduced by inaccurate fitting during the data reduction and fitting stages, or when using inaccurate calibration e.g. see Chapter 5 where the wavelength calibration provided by the *JWST* Calibration Reference Data System (CRDS) was inaccurate.

In the past, systematical noise caused several early results to be disputed at a later stage, e.g. the detections of water vapour and methane in the atmosphere of HD 189733b (Tinetti et al., 2007; Swain et al., 2008) were not reproduced when modelling systematics in a more complex analysis (Gibson et al., 2011). Therefore any noise sources have to be treated carefully to ensure accurate and robust detections (or non-detections) of atomic and molecular features, as well as clouds/hazes. It is also common for data processing to be conducted by two or more independent pipelines to guarantee that any results are reliable and reproducible, e.g. as done by the Early Release Science Transiting Exoplanet Community (ERS TEC) in the case of the first *JWST* transmission spectra, see Chapter 5 and the ERS TEC papers to date (Ahrer et al., 2023b; Alderson et al., 2023; Coulombe et al., 2023; Feinstein et al., 2023; Rustamkulov et al., 2023; The JWST Transiting Exoplanet Community Early Release Science Team et al., 2023).

Carbon-to-oxygen (C/O) ratio and mass-metallicity relationship

Since the origins of hot Jupiters are not fully understood (see Section 1.3.3), the compositions of their atmospheres have been suggested as a way to constrain their formation and migration mechanisms. However, constraining planet formation processes from the atmospheric composition is a complex goal due to multiple processes taking place at the same time while the planet is forming, growing and accreting, as the disk is also evolving. It is especially challenging to provide hypotheses that are testable with current observations of atmospheric compositions, but the carbon-to-oxygen (C/O) ratio and metallicity are the best indicators so far and summarised below.

The C/O ratio of hot Jupiters has become important in recent years due to the difference in the radial distance of the snow lines for H_2O, CO_2 and CO in the protoplanetary disk (Öberg et al., 2011), see Fig. 1.17. Madhusudhan et al. (2014) showed that the C/O ratio and metallicity are expected to be influenced by the formation location but also by the migration mechanism. Other studies followed investigating a variation of scenarios e.g. the effect of pebble accretion during/after migration or chemically evolving disks, mainly focused on hot Jupiters (e.g. Kama et al., 2015; Cridland et al., 2016; Mordasini et al., 2016; Booth et al., 2017; Madhusudhan et al., 2017; Eistrup et al., 2018; Cridland et al., 2019; Keyte et al., 2023), see also review in Madhusudhan (2019).

Note that the value of the C/O ratio observed through the exoplanet's transmission spectrum is not only influenced by its formation and migration or the unknown ratio of oxygen sequestered in clouds, disequilibrium chemistry processes can also alter the C/O ratio. For example, processes induced by the presence of light (photochemistry) (e.g. Moses et al., 2011; Baeyens et al., 2022) or processes due to the transport of chemical species within the atmosphere (e.g. Steinrueck et al., 2019; Drummond et al., 2020; Zamyatina et al., 2023).

Another hypothesis that can be tested is the mass-metallicity relationship

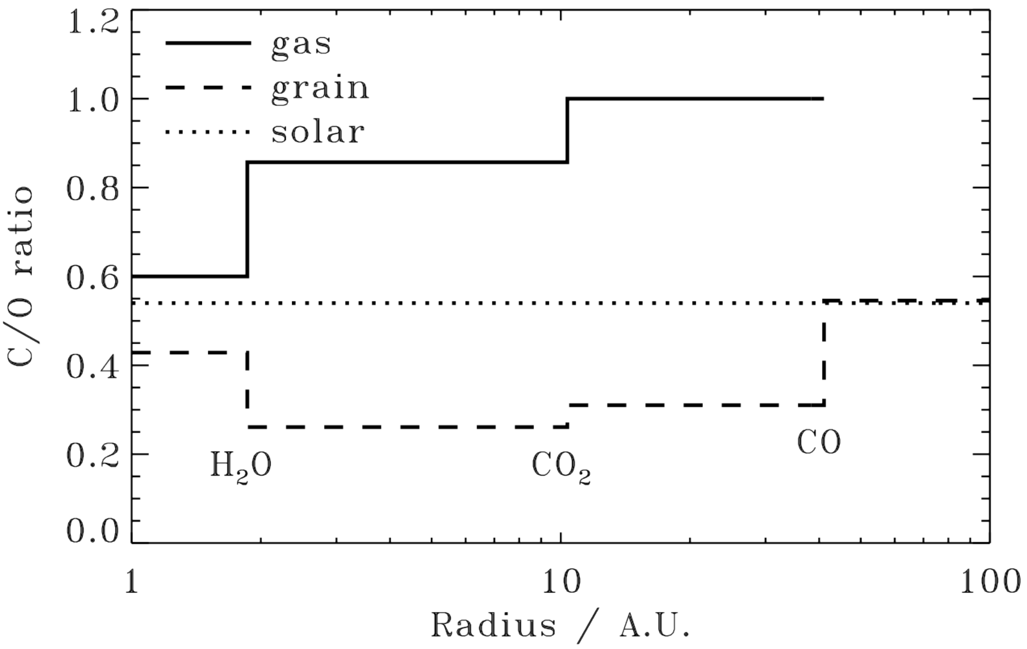

Figure 1.17: Figure 1 from Öberg et al. (2011): The C/O ratio of gas and grains as a function of radius within the protoplanetary disk around a solar-type star. The snowlines of H_2O, CO_2 and CO are annotated for reference.

and whether it is also present in exoplanets or rather in populations of exoplanets. The solar system's giant planets demonstrate an increase in atmospheric metallicity with decreasing mass, a hypothesis supported by core accretion formation (e.g. Pollack et al., 1996). There have been studies using samples of transmission spectroscopy observations of hot gaseous exoplanets aimed at using water vapour abundance as a proxy to estimate the atmospheric metallicity (e.g. Barstow et al., 2017; Pinhas et al., 2019; Welbanks et al., 2019), as shown in Fig. 1.18 using 19 data sets from *HST* and ground-based telescopes. However, there are a lot of caveats that need to be understood further as there are multiple processes involved that result in an observed water vapour abundance, linking back to the variations in C/O ratio (e.g. Madhusudhan et al., 2014). For example, H_2O is not reflecting the full inventory of oxygen, e.g. CO might be as abundant in some cases (e.g. Baeyens et al., 2021, 2022). Another caveat is that oxygen is thought to be a key component of clouds in hot Jupiter atmospheres (e.g. Visscher et al., 2010; Gao et al., 2020; Gao & Powell, 2021; Christie et al., 2021), but how much gaseous oxygen is exactly confined in clouds is not fully understood yet (e.g. Lee et al., 2016; Chachan et al., 2023).

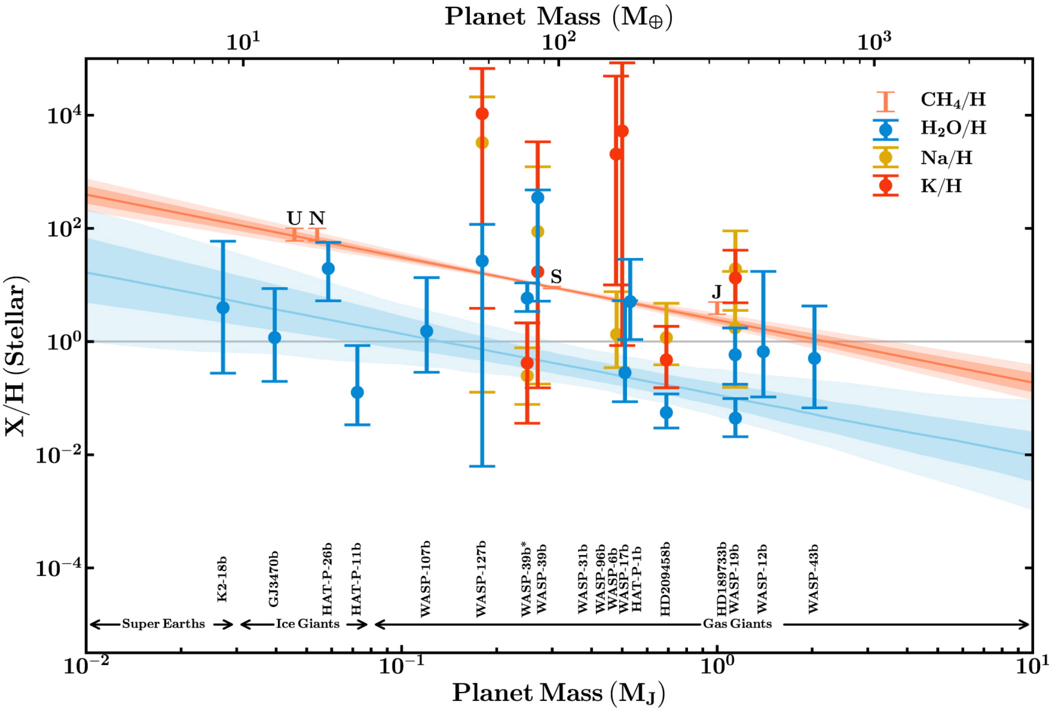

Figure 1.18: Figure 3 from Welbanks et al. (2019): Mass-metallicity relationship for exoplanets. Detection of H_2O, Na and K above 2σ using both space and ground-based transmission spectroscopy data are included for exoplanets, CH_4 abundances are used for the solar system planets from Atreya et al. (2022). The orange line and shaded region shows the trend for the solar system planets, while the blue line and shaded region correspond to the fit of the H_2O abundances.

1.5 Summary and thesis focus

Hot Jupiters, hot gaseous exoplanets, can be detected using a multitude of detection methods. In particular the transit method and the RV method were able to detect a large sample of hot Jupiters, see Sections 1.2.1&1.2.2, respectively.

As the origins of hot Jupiters regarding their formation and migration are not fully understood, characterising their atmosphere can shed light on this mystery. The current leading theories and mechanisms favour formation in the outer disk area followed by either disk-driven or high-eccentricity migration towards the host star. By characterising the composition of hot Jupiter atmospheres — linking theory with observations — we aim to further our understanding of the origins of hot Jupiters.

At the minute the most promising testable cases focus on constraining the C/O ratio and metallicity of hot Jupiters. To determine the C/O ratio and metallicity of an exoplanet atmosphere, observations of carbon- and oxygen-bearing species are required. They have large absorption signatures in the infrared and have been detected with high resolution spectroscopy as well as with telescopes such as *HST* and *JWST*. However, clouds/hazes and stellar contamination effects need to be understood in order to accurately determine atmospheric abundances. In addition, other processes like disequilibrium chemistry can also influence the C/O ratio of an exoplanet atmosphere. This is discussed in detail in the previous section, Section 1.4.5.

In summary, in order to further our understanding of hot Jupiters and the processes that are at play leading to their current orbital separation, they need to be characterised atmospherically e.g. by methods described in Section 1.4 as well as understood chemically and sources of contamination must be identified (see Section 1.4.5).

In the following chapters I present the atmospheric study of three hot Jupiters, WASP-94Ab, HATS-46b and WASP-39b, using ground-based and space facilities.

The first two exoplanets, WASP-94Ab and HATS-46b, have been observed as part of a ground-based transmission spectroscopy survey in the optical wavelengths. The first one, WASP-94Ab, showed a relatively cloud-free atmosphere with a slope in the bluer wavelength range suggesting aerosols in the atmosphere and a detection of Na. The transit observations of the latter planet, HATS-46b, produced a flat transmission spectrum suggesting the presence of clouds in its atmosphere.

The observations of the third exoplanet, WASP-39b, were part of the JWST Early Release Science (ERS) program of the transiting exoplanet community. I present the observations using the NIRCam instrument which allow the detection of water in the atmosphere, as well as the presence of clouds. We were also able to constrain the C/O ratio and metallicity, mainly due to the non-detection of methane.

Before presenting the individual observations in Chapters 3–5, in the next chapter (Chapter 2) I describe the methods and instruments used. I also provide a summary of the advantages of combining ground-based and space observations.

Chapter 2

Methods and Instruments

Transmission spectroscopy requires time-series observations of stellar spectra. In this thesis I use data from a ground-based telescope, as well as data from a space observatory to study the atmosphere of exoplanets in the optical and infrared wavelength range. In this chapter I first describe the workflow and data reduction and analysis details regarding the pipelines used for the ground-based and space observations. This is followed by a description of the computational and statistical methods used in the work in this thesis, and I conclude with a summary of the differences between ground-based and space observations.

2.1 Workflow

Analysing time-series data for exoplanet low-resolution spectroscopy is often split into data reduction and light curve fitting. The first is somewhat unique to the instrument (e.g. handling of raw frames or wavelength calibration) while the latter step is rather similar between all instruments. Here I will give a concise overview of the differences and steps between the two and then explain in detail the data reduction and fitting methods used for both the ground-based and the space observations, as well as their differences.

Note that another critical part of studying exoplanet transmission spectra is the interpretation of the atmospheric features, which is carried out using atmospheric retrieval software as well as forward model grids. I have conducted the atmospheric retrievals in one of the ground-based studies presented in this thesis (Chapter 3) so I will describe the process in Section 2.2.1. In the other chapters more complex and/or more flexible atmospheric retrieval codes were needed and my collaborators conducted those. I will not describe them here but in the individual chapters.

2.1.1 Data Reduction

Data reduction includes all steps from the raw frames to the extraction of light curves: cosmic ray effect removal, bias subtraction, as well as extracting the stellar spectra by identifying the spectral trace and fitting the background to subtract. It also includes wavelength calibration if the instruments' internal wavelength calibration is not accurate enough or offset.

When the stellar spectra are cleaned and wavelength calibrated, they are binned up and the flux — the spectroscopic light curves — are extracted. A white-light light curve is also generated, i.e., a light curve summing over the whole wavelength range. Light curves are usually also normalised to the out-of-transit flux or less frequently to the mean flux.

2.1.2 Light curve fitting

To retrieve a transmission spectrum the spectroscopic light curves have to be fitted, e.g. see Fig. 1.6, to get the transit depth for each bin. This can include a simple transit model and a systematics model. For an overview of the sampling methods used to fit the light curves, see Section 2.4.

Transit model with `batman`

`batman` is a PYTHON package for modelling exoplanet transit and eclipse light curves (Kreidberg, 2015) by inputting the time of mid-transit, the ratio of the planet to the star, the semi-major axis, the inclination and eccentricity of the system and the limb-darkening law (based on the equations in Section 1.2.1). The output is the transit light curve, i.e., flux versus time. `batman` is commonly used in the exoplanet community for transit light curve fitting as it is easy to use and optimised using C extension modules and parallelised using OPENMP.

`batman` uses the Mandel & Agol (2002) light curve formalism in combination with the input limb-darkening law (for details on limb-darkening see Section 1.2.1) to generate the transit light curve either analytically in the case of using the uniform, linear and quadratic limb-darkening laws or numerically for all other laws (including custom-defined limb-darkening laws). The accuracy of the output light curve is stated as better than 0.001 ppm (Kreidberg, 2015).

In this thesis, during my studies of both ground-based and space data I used `batman` for the transit model to fit my exoplanet transit light curves.

Systematics model

Systematic noise is commonly modelled at the light curve fitting stage e.g. using a linear slope if there are only long-term trends in the light curve, but it can get complex in the case of strong noise properties. For example, the systematics model might have to handle stellar spot crossings, instrumental systematics, bad observing conditions and/or hitting saturation. In ground-based observations more often than not the exact origin of the noise cannot be modelled/fitted in a sufficient way and Gaussian Processes (GPs) are used to model systematics in light curves. A description of GPs can be found at the end of this chapter, Section 2.5.

2.2 Exoplanet Observations with NTT

The Low Resolution Ground-Based Exoplanet Atmosphere Survey using Transmission Spectroscopy (LRG-BEASTS; 'large beasts') was initiated in 2016 with the goal to gather a large sample of transmission spectra of exoplanet atmospheres, mainly focused on hot Jupiters at optical wavelengths. The published data from LRG-BEASTS are shown in Fig. 2.1.

For this purpose LRG-BEASTS uses observations with the low-resolution spectrographs on two 4m-class telescopes: the ACAM instrument on the William Herschel Telescope (WHT) in La Palma and the EFOSC2 instrument on the New Technology Telescope (NTT) at La Silla Observatory in Chile. The LRG-BEASTS transmission spectra in this thesis are the first studies of exoplanet atmospheres using NTT/EFOSC2 (ESO Faint Object Spectrograph and Camera 2).

In my work described in this thesis I used LRG-BEASTS data from the EFOSC2 spectrograph in the long-slit spectroscopy mode. This mode allows us to place a target and comparison star in a 4.1-arcmin-long and 27-arcsecond-wide slit. ESO kindly manufactured this slit that is 27 arcseconds wide after a request from my collaborators. The larger slit width avoids differential slit losses (part of the light not being passed through the grism) which can cause systematics in the light curves as the telescope tracks the star throughout the night. The detector used is a Loral/Lesser CCD with a size of 2048 × 2048 pixels.

The light from the target and comparison star is dispersed using a grism of our choosing. The ones with the largest wavelength coverage and sufficient resolution have been found to be Gr#11 (3380 – 7520 Å, R$\sim$250), and Gr#13 (3685 – 9315 Å, R$\sim$380). While Gr#11 allows for spectra further to the blue end of the spectrum, Gr#13's range is wider and provides coverage for the K doublet in the redder end. However, EFOSC2 observations with grisms that cover wavelengths > 7200 Å are

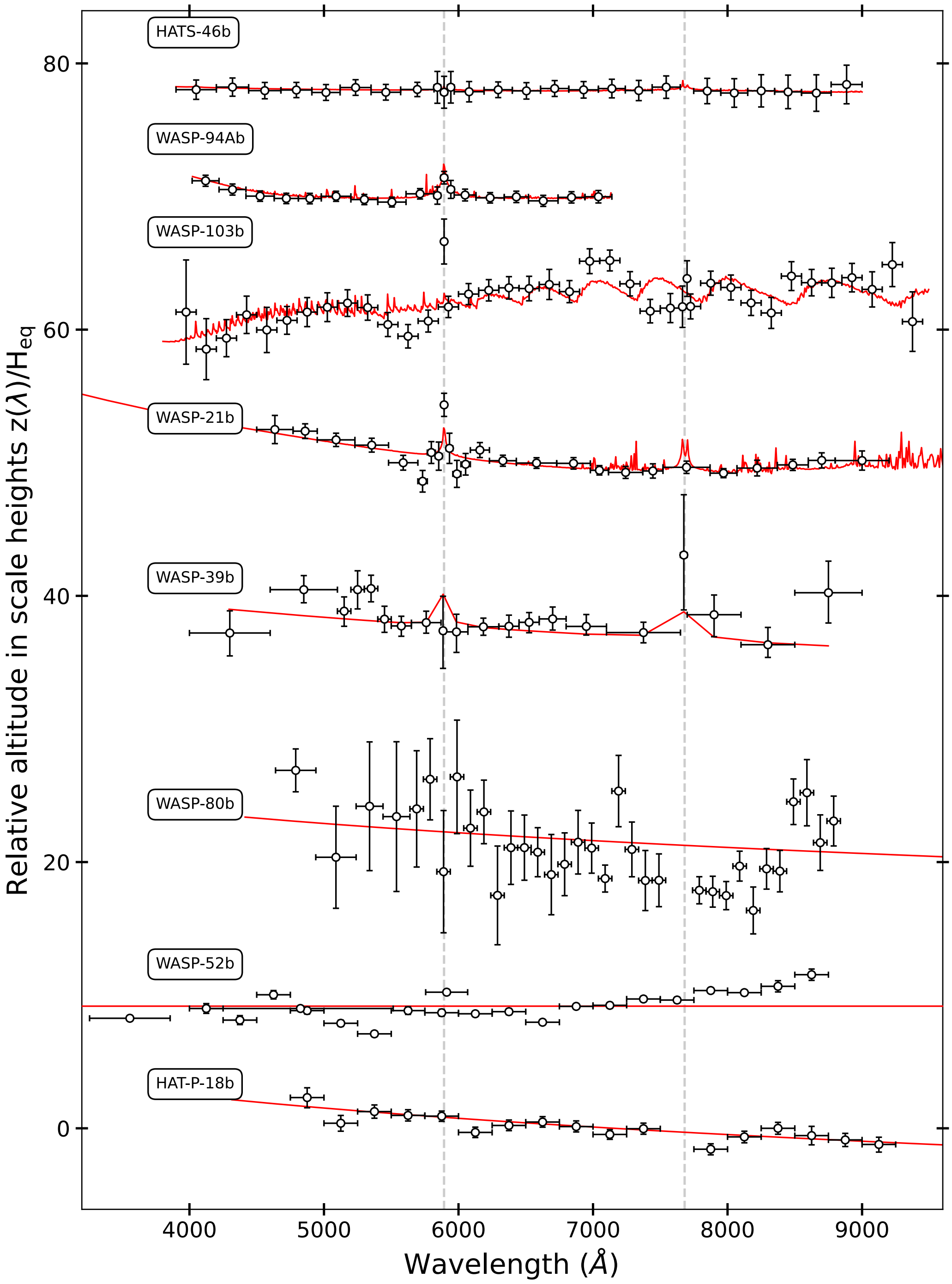

Figure 2.1: Exoplanet transmission spectra published as part of the LRG-BEASTS survey, most recent at the top (Kirk et al., 2016; Louden et al., 2017; Kirk et al., 2017, 2018, 2019; Alderson et al., 2020; Ahrer et al., 2022, 2023a), demonstrating the capabilities of 4m-class telescopes with precisions of around one atmospheric scale height. The red line denotes the best-fitting model.

significantly affected by fringing which turned out to be problematic for data taken with Gr#13. Further details can be found in Chapter 4, specifically Section 4.3 discusses the problems with fitting the fringing.

The LRG-BEASTS pipeline is described in Kirk et al. (2018) and in full detail in Kirk (2018), and consists of a series of PYTHON scripts. They follow the following structure. First, the raw data files are sorted into science frames, bias frames, flat frames and arc frames. Bias frames are combined in a master bias and subtracted from the raw files, while flat frames are combined into a master flat and used for correction at this stage if proved to be necessary (see Chapter 3 & 4).

In the next step, the spectra of both the target and comparison star are extracted using the user-defined aperture size, background window and background fitting method e.g. a polynomial. Figures and descriptions of the raw frames and spectral extraction can be found in Section 3.4. In practice, multiple extractions are computed using a variation of aperture size and background fitting methods in order to minimise the noise.

The data is further reduced by utilising several individual Jupyter notebook scripts to (1) remove cosmic ray effects, (2) calculate the wavelength solution of arc spectra (calibration spectra using lamps), (3) resample stellar spectra if necessary (e.g. due to shifts through the course of the night), (4) refine the wavelength solution using spectral lines, (5) bin the spectra into spectroscopic light curves, and (6) conduct other preparations for fitting e.g. normalise the light curves.

Finally, the light curves are fitted using separate scripts with choices of different systematic models, limb-darkening parameters and laws as well as different sampling methods.

While this summarises the LRG-BEASTS pipeline steps in general, individual steps have been adapted as part of the work in this thesis e.g. using nested sampling for parameter estimation and allowing for cosmic ray effects to be removed at the raw science frame stage (before spectral extraction). Any changes to the LRG-BEASTS pipeline applied in this thesis are described in detail in the individual chapters.

2.2.1 PLATON atmospheric retrievals

Atmospheric retrieval analysis refers to parameter estimation by fitting an atmospheric model to the retrieved transmission spectrum of an exoplanet and in turn retrieving the probability distributions of the model parameters. This is different to forward modelling where an atmospheric model is generated based on input parameters and grid model fitting where a set of forward models are fitted (e.g. using least-squares) to determine the best-fit model.

For the atmospheric retrieval analysis in Chapter 3 I have used the PYTHON retrieval code PLATON (PLanetary Atmospheric Transmission for Observer Noobs) (Zhang et al., 2019, 2020), previously used in other LRG-BEASTS analyses (Kirk et al., 2019; Alderson et al., 2020).

PLATON is a tool for atmospheric forward modelling and retrieval for transmission and emission spectra. It includes gas absorption, clouds and scattering as well as the functionality to account for spot coverage and spot temperature (Zhang et al., 2019, 2020). The retrieval uses the nested sampling algorithm DYNESTY (Speagle, 2020) for parameter exploration.

It is an ideal tool for quick forward modelling and retrieval analysis, however, atomic and molecular abundances are combined in single parameters for metallicity and C/O. This can create problems in case of unexpected features, e.g. when we tried to constrain the cloud level of HATS-46b in Chapter 4 and we were concerned about the influence of a telluric band mimicking K absorption, or when the fitted model does not account for the observed molecule e.g. in the case of the photochemical product SO_2 in the atmosphere of WASP-39b (Alderson et al., 2023; Rustamkulov et al., 2023; Tsai et al., 2023).

More details about the PLATON retrieval analysis can be found in the relevant part of this thesis, specifically Section 3.6.2.

2.3 Exoplanet Observations with *JWST*

In this thesis I use *JWST* observations (Gardner et al., 2006); *JWST* is a space telescope, launched on Christmas Day, 25 December 2021. It then travelled to its current position, Lagrange point 2, where it is now in orbit around the Sun, parallel to the Earth, at a distance of 1.5 million kilometers.

2.3.1 Detectors and ramp-fitting

The *JWST* detectors are commonly used infrared detectors where the photo-electrons are measured during an exposure as they are accumulated. It is called non-destructive reading or sampling up-the-ramp. The ramp refers to the linear (if incident flux is constant) increase in charge calculated for every pixel during an exposure. The intercept of this slope is the bias level, while the slope itself is the flux in counts (ADUs; analog-to-digital units) per second.

Each non-destructive read/measurement on this slope is called a frame which is combined into a group following a chosen readout pattern. The first step in each

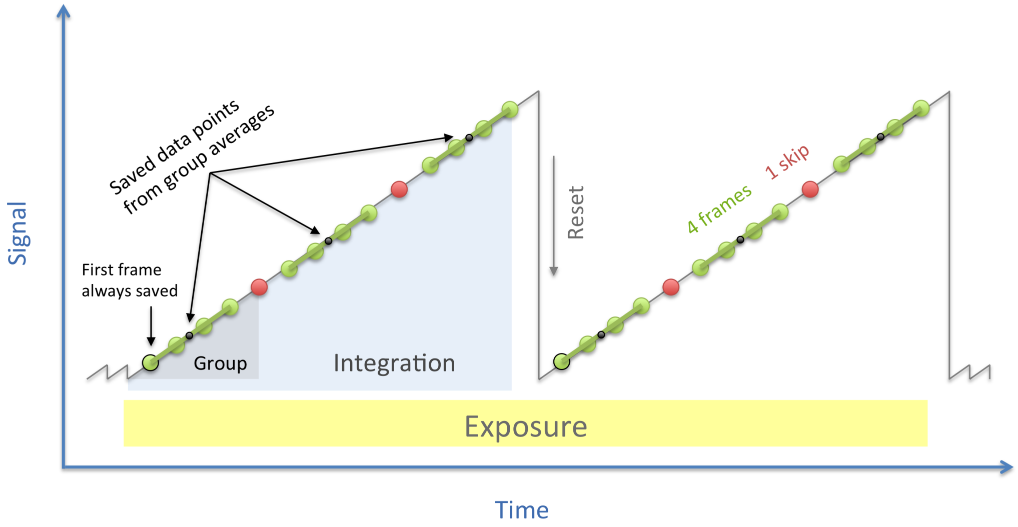

Figure 2.2: Schematic of two integrations with their individual groups and showing an example readout pattern where four frames are averaged into one group and one frame is skipped (to cause a delay between groups) (e.g. see also Robberto, 2009). Figure Credit: *JWST* User Documentation[1].

reduction pipeline is to convert these groups into an integration by fitting this slope, see Fig. 2.2[1]. This figure also shows an example of a readout pattern (SHALLOW4) which defines how many and in which way frames will be combined into groups to be used for the ramp-fitting step.

2.3.2 Instruments and Modes for Transmission Spectroscopy

JWST has four instruments on board: the Mid-Infrared Instrument (MIRI), the Near-InfraRed Camera (NIRCam), the Near Infrared Imager and Slitless Spectrograph (NIRISS) and the Near InfraRed Spectrograph (NIRSpec). In the following paragraphs I will describe the modes that can be used for time-series, spectroscopic observations and thus for transmission spectroscopy.

MIRI (e.g. see Kendrew et al., 2015; Rieke et al., 2015) allows for spectra in the mid-infrared wavelength range. The Low Resolution Spectroscopy (LRS) mode provides spectra from 5 – 14 µm at a resolution of $R \simeq 40$ at 5µm to $R \simeq 160$ at 10µm. For higher resolution ($R \simeq 1500 - 3500$) and longer wavelength ranges there is the option of using the Medium Resolution Spectroscopy (MRS) mode. However,

---

[1] JWST User Documentation, `https://jwst-docs.stsci.edu/jwst-near-infrared-camera/nircam-instrumentation/nircam-detector-overview/nircam-detector-readout-patterns`, accessed 07/06/2023.

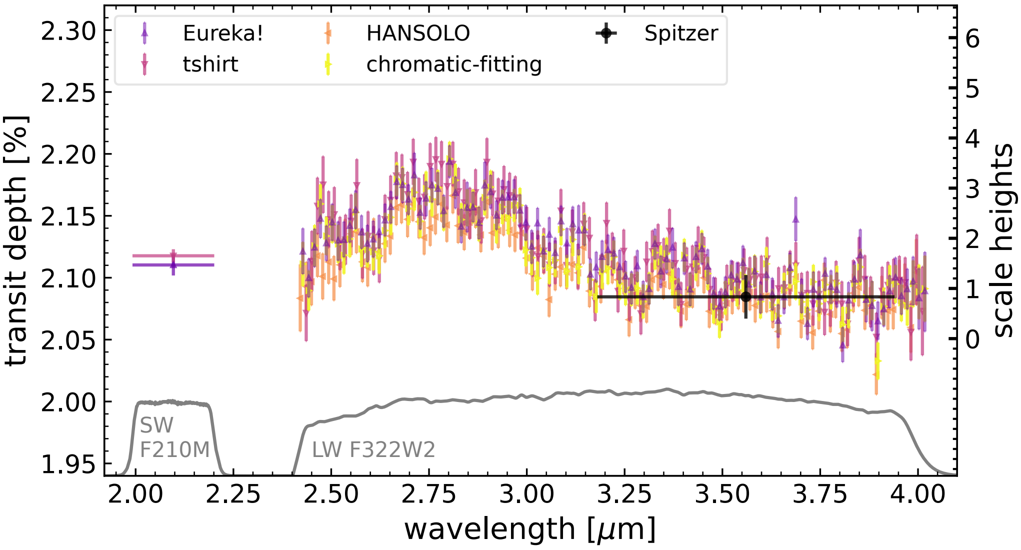

Figure 2.3: First transmission spectrum of an exoplanet using *JWST*'s NIRCam instrument from Ahrer et al. (2023b) and Chapter 5. This shows the four retrieved transmission spectra using independent analyses, as well as previous *Spitzer* observations (Wakeford et al., 2018). The throughput of the photometric (SW) and spectroscopic (LW) filters used are shown in grey at the bottom of the figure.

four observations are necessary to cover the whole possible wavelength range, i.e. observe in each of these channels: Channel 1 (4.90 – 7.65 µm), Channel 2 (7.51 – 11.7 µm), Channel 3 (11.55 – 17.98 µm) and Channel 4 (17.7 – 27.9 µm). The first transmission spectrum of an exoplanet using MIRI has not been published yet at the time of writing of this thesis, but there have been observations taken, including a phase curve of WASP-43b as part of the *JWST* Transiting Exoplanet Community (TEC) Early Release Science (ERS) team, e.g. see first-look summary pre-print by Bell et al. (2023).

NIRCam (e.g. see Rieke et al., 2005; Greene et al., 2007) has a grism time series mode that can be used for transmission spectroscopy. The overall wavelength range is 2.4 – 5.1 µm with a spectral resolution of $R \simeq 1600$. Four filters are available to choose from for time-series observations: F277W (2.4 – 3.2 µm), F322W2 (2.4 – 4.1 µm), F356W (3.1 – 4.0 µm) or F444W (3.8 – 5.1 µm). NIRCam is unique in a way that it can obtain simultaneous photometry using a weak lens to defocus the image. There are multiple filters available for this purpose, ranging from 0.6 – 2.3 µm. The first transmission of an exoplanet using NIRCam, see Fig. 2.3, has been published by Ahrer et al. (2023b) as part of the *JWST* Transiting Exoplanet Community ERS team and further discussed in Chapter 5.

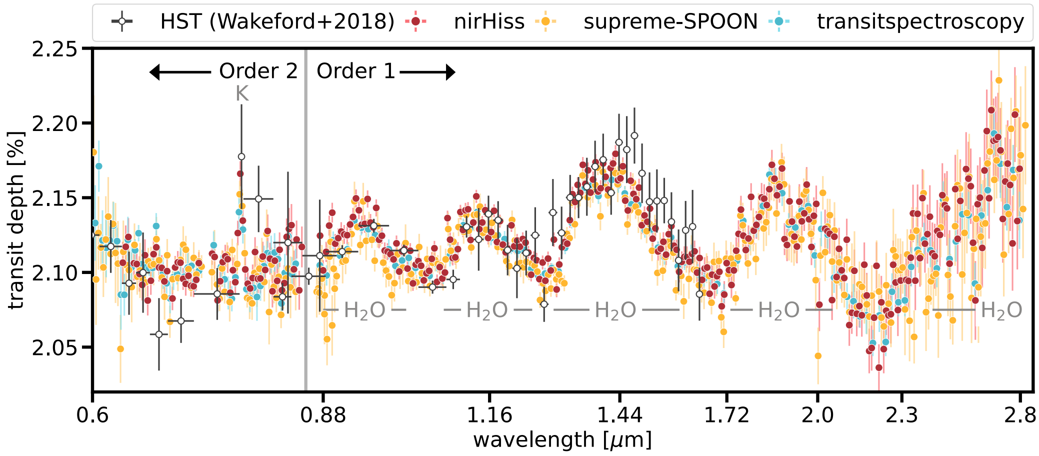

Figure 2.4: First published transmission spectrum of an exoplanet using *JWST*'s NIRISS instrument, Figure 2 from Feinstein et al. (2023). Three independent data reductions are shown in colours, as well as previous *Hubble* observations (Wakeford et al., 2018). The grey line displays the border between orders 1 and 2 of the spectrum.

NIRISS (e.g. see Doyon et al., 2012) can be used for time-series spectroscopy in its single Object Slitless Spectroscopy (SOSS) mode. It produces spectra at a resolution of $R \simeq 700$ (in the first order) over a wavelength range of $0.6 - 2.8\,\mu\text{m}$ in three cross-dispersed orders. Due to the orders being spread over the detector it results in unique spectral traces in the science images. The result is that the usage of NIRISS/SOSS is limited by its surrounding stars which can contaminate the spectrum. The first transmission spectrum of an exoplanet using NIRISS was shown as part of the *JWST* Early Release Observations (ERO) which were revealed in July 2021. The first published result was by Feinstein et al. (2023) as part of the *JWST* TEC ERS program, see Fig. 2.4.

NIRSpec (e.g. see Plate et al., 2005; Ferruit et al., 2014) uses its Bright Object Time-Series (BOTS) mode to do transmission spectroscopy. It has multiple options in terms of wavelength ranges and spectral resolution. There are four dispersers and filter combinations with a medium (M, $R \simeq 1000$) and high (H, $R \simeq 2700$) resolution option: G140(H or M)/F070LP ($0.70 - 1.27\,\mu\text{m}$), G140(H or M)/F100LP ($0.97 - 1.84\,\mu\text{m}$), G235(H or M)/F170LP ($1.66 - 3.07\,\mu\text{m}$) and G395(H or M)/F290LP ($2.87 - 5.10\,\mu\text{m}$). In addition, there is the PRISM/CLEAR mode which has the lowest resolution of $R \simeq 100$, but the largest wavelength range possible of $0.60 - 5.30\,\mu\text{m}$. However, this mode also has the tightest constraint on the brightness of the target due to saturation at a maximum brightness of ≈ 10.5 in the

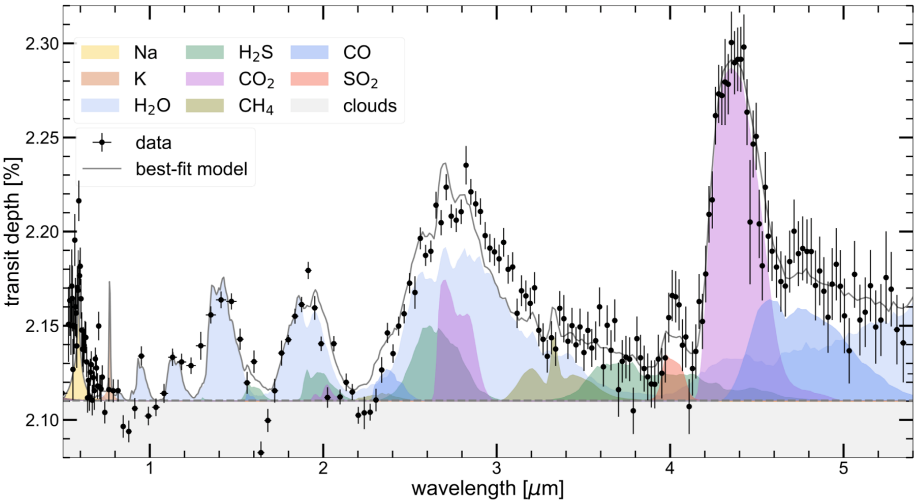

Figure 2.5: First published transmission spectrum of an exoplanet using the full range of PRISM on *JWST*'s NIRSpec instrument, Figure 4 from Rustamkulov et al. (2023). Here the authors also show the key atomic and molecular species that contribute to the feature in the transmission spectrum and the best-fit model.

J band (depending on the stellar type and subarray settings). The first transmission of an exoplanet using NIRSpec was published in The JWST Transiting Exoplanet Community Early Release Science Team et al. (2023) and only showed the CO_2 detection using part of a PRISM spectrum. The full PRISM spectrum was published by Rustamkulov et al. (2023), see Fig. 2.5, at the same time as the first NIRSpec G395H transmission spectrum of WASP-39b by Alderson et al. (2023) see Fig. 2.6, which were also part of the *JWST* TEC ERS.

2.3.3 Data Analysis with `Eureka!`

To prepare for the upcoming *JWST* observations, the TEC ERS team hosted a hackathon and a data challenge using simulated data of WASP-39b observations. The first of which happened during June 2021 as an online format where `Eureka!` was first introduced by L. Kreidberg and K. B. Stevenson. The idea was to build one pipeline that is able to reduce *JWST* data from all instruments and analyse the data of transiting exoplanets, with the final outputs corresponding to the planet's transmission spectrum, emission spectrum or phase curve. It was also adapted to

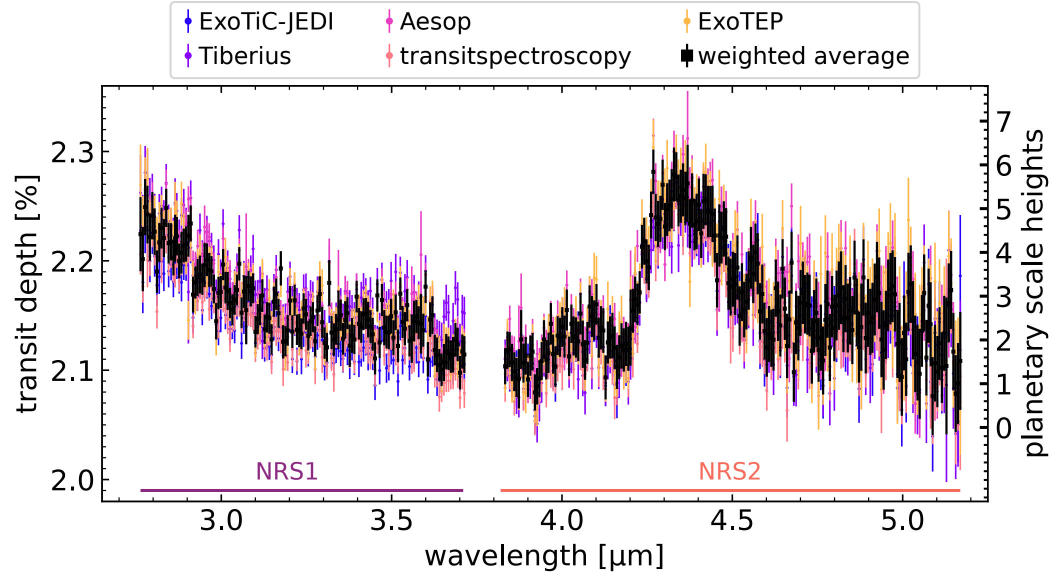

Figure 2.6: First published transmission spectrum of an exoplanet using G395H on *JWST*'s NIRSpec instrument, Figure 2 from Alderson et al. (2023). It shows the independent data reduction and analysis from the community in different colours and the weighted average transmission spectrum in black. NRS1 and NRS2 denotes the two different NIRSpec detectors over which the spectrum is spread out.

extract photometric light curves (e.g. for NIRCam or MIRI) and not just spectroscopic data. `Eureka!` is an open-source PYTHON package and has been published in the Journal of Open Source Software (JOSS) in Bell et al. (2022).

I have been part of the development team of `Eureka!` since the hackathon in June 2021 and in particular have contributed significantly to Stages 1 and 5 (in particular the full Gaussian Process functionality), as well as to Stage 4. Here I will summarise the Stages of `Eureka!` which is then used in Chapter 5.

Stages 1 and 2

`Eureka!` is split into six stages. Stages 1 and 2 are wrapped around the *JWST* Science Calibration Pipeline (`jwst`)[2]. Stages 3 to 6 are independently written by the `Eureka!` team. An overview of the Stages is also demonstrated in Fig. 2.7, from Bell et al. (2022). Each Stage requires the definition of a `Eureka!` Control File (ECF) which is a simple text file which reads in the relevant parameters when running the individual stages, e.g. the aperture width for the spectral extraction in Stage 3. Note that Stage 5 also requires a `Eureka!` Parameter File (EPF) that

---

[2] https://jwst-pipeline.readthedocs.io/

contains the planetary system parameters as well as the fitting parameters and their respective priors if applicable. Examples of these files for each instrument are of course supplied in the `Eureka!` installation directory and also described further in our documentation online[3].

`jwst` is `Python` software for processing data from all *JWST* instruments and observing modes. It is organised into three stages: Stage 1 takes the raw `*uncal.fits` files and performs detector-level corrections which include data quality initialisation, detection of saturated pixels, bias subtraction, reference pixel and linearity correction, dark current subtraction, jump (cosmic ray) detection, and gain scale correction. Most importantly, it conducts ramp fitting for each frame. `Eureka!` allows you to define whether to skip steps in the reduction, change the jump detection threshold, and also allows for changing the weighting of the ramp fitting.

`jwst` Stage 2 takes in slope images (ramps) from Stage 1 and performs an assignment of the world coordinate system, flat fielding, and assignment of a wavelength solution. Similar to Stage 1, `Eureka!` allows the user in Stage 2 to select which `jwst` reduction steps to conduct, as well as manually define the edges of a slit (for NIRSpec).

Stage 3

In Stage 3 the stellar spectra are extracted. The user can define parameters at this stage that control the aperture width, the background subtraction region and extraction method, the threshold for outlier rejection and whether to use optimal extraction (Horne, 1986). It also allows for defining how much output (Tables, Figures, etc.) is created by `Eureka!` at this stage.

This stage is often repeated with different sets of parameters to optimise the reduction and minimise the scatter in the light curves. Similar to the ground-based data, the treatment of background subtraction matters, as well as the aperture size and rejection thresholds.

Stage 4

In Stage 4 the light curves are extracted by binning to the user-given number of bins in the specified wavelength region. There is an option to apply a drift correction of the 1D spectra. Parameters for sigma clipping can be specified here for both the unbinned and binned light curves.

---

[3] `https://https://eurekadocs.readthedocs.io/`

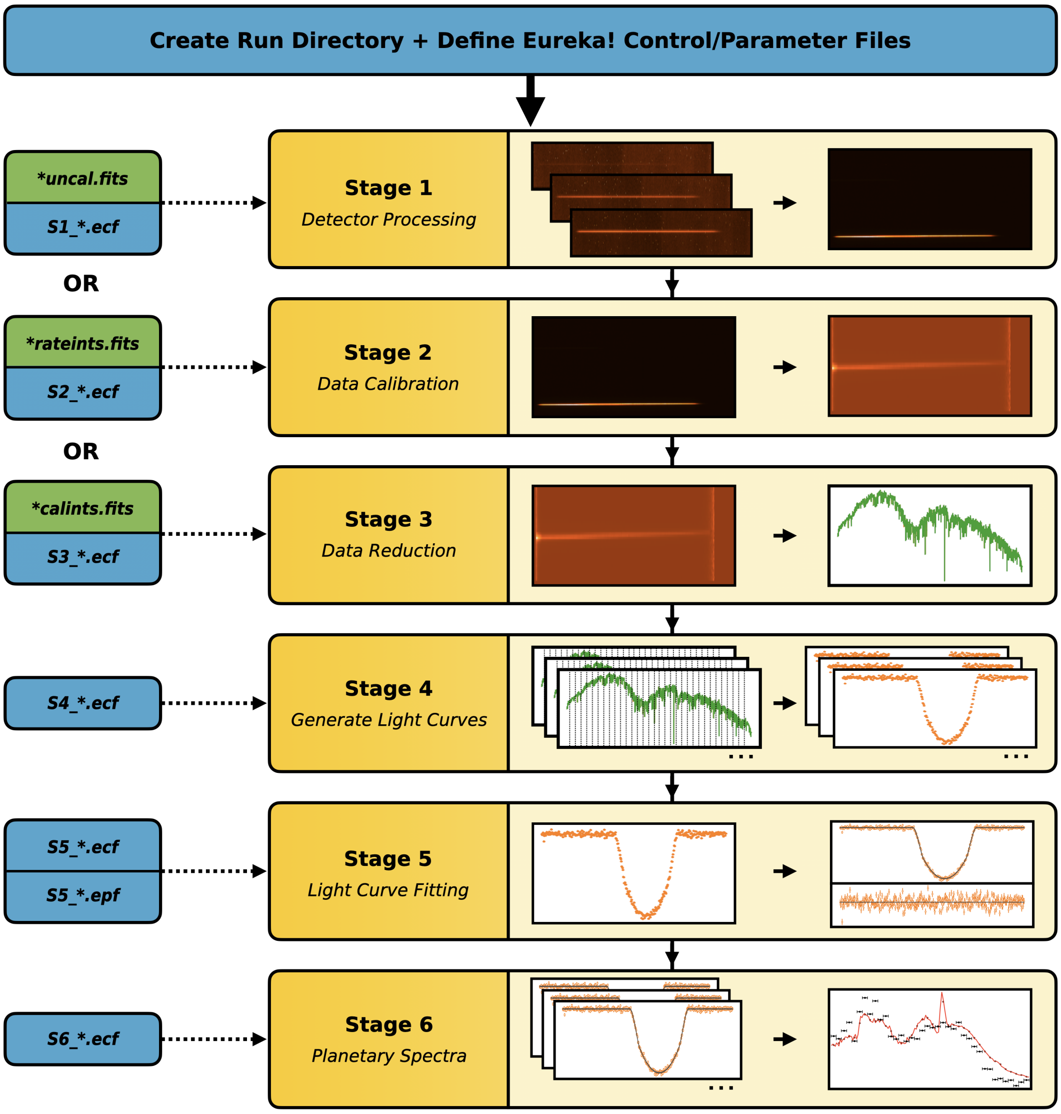

Figure 2.7: Figure from Bell et al. (2022) showing an overview of the Stages in `Eureka!`. The green boxes with `*uncal.fits`, `*rateints.fits` and `*calints.fits` show the individual names of files from the `jwst` pipeline, which can be used as starting points for running `Eureka!`. The `*.ecf` denotes the individual `Eureka!` Control File (ECF) and in Stage 5 the user also needs to define a `Eureka!` Parameter File (EPF) that contains the system and fitting parameters and priors if applicable.

In addition, the ExoTiC-LD code (Laginja & Wakeford, 2020a,b; Wakeford & Grant, 2022) can be utilised to compute limb-darkening coefficients that can be used for light curve fitting in Stage 5. It requires the download of *JWST* instrument throughput data to accurately determine the limb-darkening parameters using either 1D (Kurucz & Bell, 1995) or 3D stellar models (Magic et al., 2015).

Stage 5

In Stage 5 the light curves are fitted, both the white-light as well as the spectroscopic light curves. The user can choose between different fitters (least-squares, Markov Chain Monte Carlo or nested sampling algorithms, see also Section 2.4), choose the physical model (transit model, eclipse model, phase curve) as well as systematic models to use (Gaussian Process as described in Section 3.5.3, polynomial, step function, exponential ramps, etc.). Integrations can be clipped and limb-darkening parameters custom-defined or used from Stage 4. It is common to spend some time studying and testing different options to check which models fit the data best.

Stage 6

In Stage 6 the transmission spectrum, dayside spectrum or phase curve is assembled by using the fitted values from Stage 5. It is particularly useful to generate figures and check whether fitted parameter values are in the expected range e.g. by plotting the limb-darkening coefficients and systematic model parameters as a function of wavelength.

2.4 Data Fitting Methods

In the following research chapters I will use both Markov Chain Monte Carlo (MCMC) sampling as well as nested sampling algorithms to fit models to observations and retrieve posterior distributions and thus uncertainties. Note that in Chapter 5 my collaborators also use a χ^2 analysis for finding their best-fit model due to the nature of the program (see chapter for further details). This method compares models by simply computing the squared differences in data and model relative to the data, giving an estimate of goodness-of-fit. It is not described further in this chapter, instead, the focus is on MCMC and nested sampling as it incorporates prior knowledge about the parameters, takes the data uncertainties into account and provides posterior probabilities for the fitted parameters.

The main advantage of MCMC over nested sampling is that it is computationally faster and it is simple in determining fitted parameter values, while nested sampling has the advantage of exploring the whole parameter space more thoroughly and being able to do model comparison directly with the Bayesian evidence values.

2.4.1 Bayesian statistics

Both MCMC and nested sampling use Bayesian inference to sample and fit a model to data. Both require prior functions or definitions and a likelihood function and will produce a best-fit model along with posterior distributions of the fitted parameters. Nested sampling will also provide a Bayesian evidence value for Bayesian model comparison, while MCMC computes a Bayesian Information Criterion (BIC) for model comparison.

Here I will summarise the concepts of Bayesian inference, including Bayes' Theorem, prior distributions, likelihood, posterior distributions, Bayesian evidence and Bayesian model comparison.

Bayes' Theorem

Using Bayesian inference in a sampling algorithm means that it is based on Bayes' Theorem to estimate the probability of a model. Bayes' Theorem is an important relation in Bayesian probability theory and describes the probability of an event based on our prior/current knowledge of conditions related to this event. It is written as

$$\mathrm{Pr}(\Theta|\mathrm{D},\mathrm{M}) = \frac{\mathrm{Pr}(\mathrm{D}|\Theta,\mathrm{M})\ \mathrm{Pr}(\Theta|\mathrm{M})}{\mathrm{Pr}(\mathrm{D}|\mathrm{M})}, \tag{2.1}$$

where $\mathrm{Pr}(\mathrm{D}|\mathrm{M})$ is the probability of data D given that a model M is true, $\mathrm{Pr}(\Theta|D,M)$ the probability of the parameters Θ given D and M, $\mathrm{Pr}(\Theta|M)$ the probability of Θ given M, and $\mathrm{Pr}(D|\Theta,M)$ the probability of D given Θ and M.

Following the notation used by Feroz et al. (2009), this can also be written in Bayesian terminology using prior distribution $\pi(\Theta) = \mathrm{Pr}(\Theta|M)$, Bayesian evidence $\mathcal{Z}(\Theta) = \mathrm{Pr}(\mathrm{D}|\mathrm{M})$, posterior distribution $\mathcal{P}(\Theta) = \mathrm{Pr}(\Theta|D,M)$ and likelihood $\mathcal{L}(\Theta) = \mathrm{Pr}(D|\Theta,M)$ as:

$$\mathcal{P}(\Theta) = \frac{\mathcal{L}(\Theta)\ \pi(\Theta)}{\mathcal{Z}(\Theta)}. \tag{2.2}$$

Prior distribution

Prior distributions correspond to the sampling range and the distribution of the free parameters. They are independent of the data and can be informed or uninformed, i.e., constrained by prior knowledge of the parameters.

Likelihood

The description of the likelihood defines the value that is going to be maximised by the nested sampling algorithm or MCMC. It is the probability of the data given, fitted with a current model and current parameter values.

The likelihood is commonly described in a logarithmic scale as

$$\ln \mathcal{L}(\Theta) = \sum_{i} - \ln \sqrt{2\pi\sigma_{\mathrm{i}}^{2}} - \frac{1}{2\sigma_{\mathrm{i}}^{2}} [m(t_{\mathrm{i}};\Theta) - d_{\mathrm{i}}]^{2}, \tag{2.3}$$

where the variable $m(t_{\mathrm{i}};\Theta)$ describes the model with parameters Θ, while d_{i} describes the data with their corresponding observational error estimate σ_{i} at a time t_{i}.

Posterior distribution

Posterior distributions describe the distribution of all fitted parameters from where the best-fit value and their confidence intervals can be computed. They can be any shape, e.g. symmetric/Gaussian-shaped or with long asymmetric tails.

Bayesian evidence

The Bayesian evidence value determines the quality of the model fitted to the given data, penalising large numbers of parameters when not justified by the data, and allowing for model comparison. It is not relevant for computing fitted values and their confidence intervals.

It is computed by integrating the prior distributions over the whole parameter space

$$\mathcal{Z}(\Theta) = \int \pi(\Theta)\ \mathcal{L}(\Theta)\ d\Theta, \tag{2.4}$$

which results in numerical computation of high-dimensional integrals and is computationally expensive, especially in comparison to MCMC. MCMC does not compute the Bayesian evidence, but we can compute the Bayesian Information Criterion (BIC) (Schwarz, 1978) which is an approximation of the Bayesian evidence, derived from the Bayesian approach for model comparison with simplifications. It is defined as

$$\mathrm{BIC} = k \ln(N) - 2 \ln \mathcal{L}(\Theta_{\mathrm{best}}), \tag{2.5}$$

where k is the number of parameters fitted, N the number of data points fitted and $\mathcal{L}(\Theta_{\mathrm{best}})$ the likelihood of the best-fitting model (e.g. Kass & Raftery, 1995). The term $k \ln(N)$ punishes models with larger numbers of parameters, while the

$\lvert\Delta \ln \mathcal{Z}\rvert$	Odds	Probability	Remark
< 1.0	$\lesssim$ 3:1	< 0.750	Inconclusive
1.0	$\sim$ 3:1	0.750	Weak evidence
2.5	$\sim$12:1	0.923	Moderate evidence
5.0	$\sim$150:1	0.993	Strong evidence

Table 2.1: Jeffreys scale, as introduced by Jeffreys (1983), for estimating the significance of the evidence difference of two models. This means the model with a lower number of parameters is favoured unless a model with additional parameters has a higher evidence of $\geqslant 5.0$ in logarithmic scale. As a reference, 1σ and 3σ are equal to probabilities of 0.6827 and 0.9973, respectively.

term $-2 \ln \mathcal{L}$ rewards models that fit the data well. Lower BIC values are generally preferred, however, it is only an approximation of the Bayesian evidence.

Bayesian model comparison

Bayesian evidence values are required to compare two or more models. The ratio between two Bayesian evidence values, also called Bayes' factor $\Delta \ln \mathcal{Z}$, is indicative of how much one model is favoured over the other. As this is usually done in logarithmic scale, the Bayes' factor becomes a simple subtraction:

$$\Delta \ln(\mathcal{Z}) = \ln \left(\frac{\mathcal{Z}_1}{\mathcal{Z}_2} \right) = \ln \mathcal{Z}_1 - \ln \mathcal{Z}_2, \tag{2.6}$$

where $\mathcal{Z}_1$ and $\mathcal{Z}_2$ are the respective evidence values for two competing models 1 and 2.

The Jeffreys scale (Jeffreys, 1983), as seen in Table 2.1, can then be used to estimate the significance of the differences in Bayesian evidence value, i.e., the confidence which you can favour one model above the other. Note that it cannot tell you the 'correct' model, instead it can inform your decision on which one of your tested – though all potentially 'wrong' – models is favoured given your data and uncertainties and prior information.

2.4.2 Nested sampling

A nested sampling algorithm randomly generates a uniformly distributed hypercube ranging from 0 to 1, where the number of generated samples is defined by a parameter defining the number of live points. The user will define prior functions to convert these numbers into the ranges and distributions required for each of the parameters of the model. The parameter slices will then be evaluated in terms of likelihood and the lowest likelihood will be rejected and new parameters generated.

This will be continued until a local maximum is found, defined by a criterion that is a specific fraction of posterior to prior distribution.

The global maximum is found by reiterating the process. The outcome of a nested sampling algorithm is the weighted samples of the posterior distributions, including their individual likelihoods, and the Bayesian evidence value of the model fit to the data (because it fully sampled the prior ranges and can integrate over the set of live points).

2.4.3 Markov Chain Monte Carlo (MCMC)

MCMC is an algorithm based on Monte Carlo methods and using Markov chains and is generally used to sample a parameter space and find the best-fitting model and generate posterior distributions of the parameters, similar to nested sampling algorithms.

Markov chains are a stochastic process where the next step in the chain solely depends on the current step, i.e., the sample is built up instead of generated at the beginning as in the nested sampling case.

An MCMC algorithm starts with the initialisation values for each parameter and then explores the parameter space using Markov chains. This is the burn-in stage where the sample explored does not account for the posterior in the end. The user defines the number of steps in the chain, the number of samples in the burn-in stage and the number of simultaneous random walkers in the parameter space.

Finally, there is no convergence criterion for MCMC since it is defined by steps and the number of walkers. Depending on the data set and model those two values need to be adapted and the chains inspected.

2.5 Gaussian Process (GP)

Gaussian processes or GPs have been increasingly used in all areas of exoplanet science to describe data that cannot be described (or not easily described) using parametric functions, likely due to a lack of information about the intrinsic nature of the signal.

Practically, GPs are based on a non-parametric approach, using a sample of functions described by the correlation between the individual data points (the covariance) instead of a set of parameters to fit a specific function to the data.

Examples of where GPs have successfully been used in exoplanet science include identifying stellar activity variations in RV measurements by pinning down semi-periodic signals in both the RVs and stellar activity indicators (e.g. Haywood et al., 2014a; Rajpaul et al., 2015; Barragán et al., 2019), some of which have been previously falsely reported to be of planetary nature (see e.g. Rajpaul et al., 2016). Aside from that, GPs are also commonly being used to capture correlated photometric noise when identifying transits (e.g. Carter & Winn, 2009; Aigrain et al., 2012; Lienhard et al., 2020) and subsequently in transmission spectroscopy (e.g. Gibson et al., 2012a,b; Evans et al., 2015; Cartier et al., 2016; Kirk et al., 2017, 2021).

2.5.1 Covariance and kernels

The term covariance refers to the correlation between the data. It is mathematically described as a matrix K_{ij} acting on the input data.

In the case of white, Gaussian, uncorrelated noise this kernel matrix is a diagonal matrix where the diagonal values are equal to the variance of the white noise σ^2. Correlated noise is then described by the off-diagonal elements in the matrix. Technically every element can be described individually, however, that is not practical and instead the covariance is modelled using a covariance function or kernel k.

Kernel

Commonly used kernels include the exponential and squared exponential kernel, the Matern 3/2 and Matern 5/2 kernel, as well as sine or cosine kernels. A covariance function can also be a sum of multiple kernels, e.g. see Chapter 3 and in particular Section 3.5.3.

While every kernel is different, common parameters that describe them are amplitude A (or signal variance) and a scale length l which refers to how long the correlation between data points carries on (see also Fig. 2.8). These parameters are also known as the GP's hyperparameters and are fitted for.

For example, in this thesis I used the squared exponential kernel in Chapters 3&4 for light curve fitting, described as

$$k_{\mathrm{SE}}(r) = A^2 \exp\left(-\frac{r^2}{l^2}\right), \tag{2.7}$$

where $r = x_{\mathrm{i}} - x_{\mathrm{j}}$ of two data points at position i and j. An example of drawn functions with the squared exponential kernel is shown in Fig. 2.8.

The Matern 3/2 kernel is described as

$$k_{\mathrm{M32}}(r) = A^2 \left(1 + \frac{\sqrt{3r^2}}{l^2}\right) \exp\left(-\frac{\sqrt{3r^2}}{l^2}\right), \tag{2.8}$$

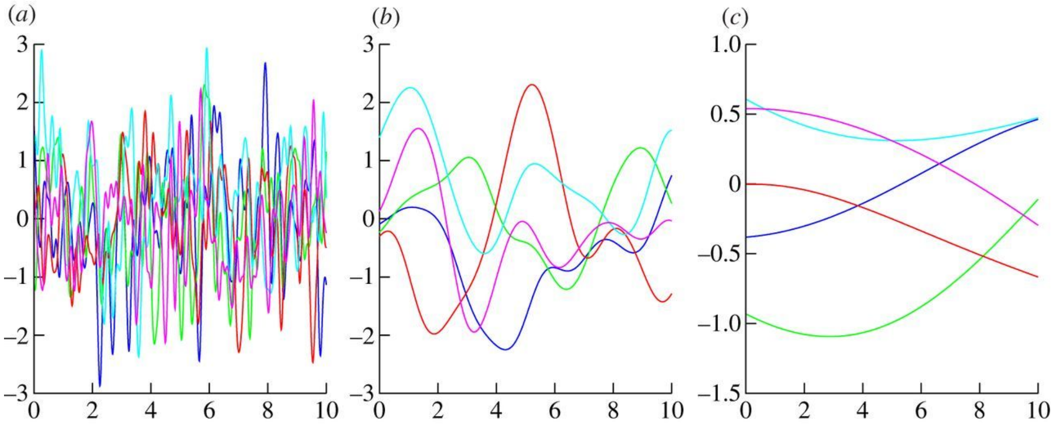

Figure 2.8: Figure 5 from Roberts et al. (2013): Example functions drawn from a GP using the squared exponential kernel with different scale lengths, (a) to (c) from low to high values. X and y axes are arbitrary in this example case; in the transit light curve cases discussed in this thesis the x and y axes would refer to time and flux, respectively, e.g. see Fig. 2.9.

which is used by my collaborator in Chapter 5 to fit light curves and I have also tested for it in Chapters 3&4 to make sure that the resulting transmission spectrum is not correlated with the choice of kernel(s).

Other kernels I have used in this thesis, not for the purpose of fitting light curves but instead for modelling fringing effects, are the exponential kernel in combination with the sinusoidal kernel as follows

$$k_{\mathrm{E}}(r) = A^2 \exp\left(-\frac{r}{l^2}\right), \tag{2.9}$$

$$k_{\mathrm{S}}(r) = A^2 \sin\left(\frac{2\pi r}{P}\right), \tag{2.10}$$

where P refers to the period of the oscillation.

Computation for transmission spectroscopy

In practice, the GP model is constructed using the transit model and a GP with one or more kernels. The kernel(s) captures the detrending of the light curve and either the time is used as an input or other quantities such as the Full Width Half Maximum (FWHM) of the extracted spectra, the airmass or the telescope derotator among others. Note that the kernel input changes the structure of the detrending since the GP uses it to compute the covariance matrix, as shown in Fig. 2.9.

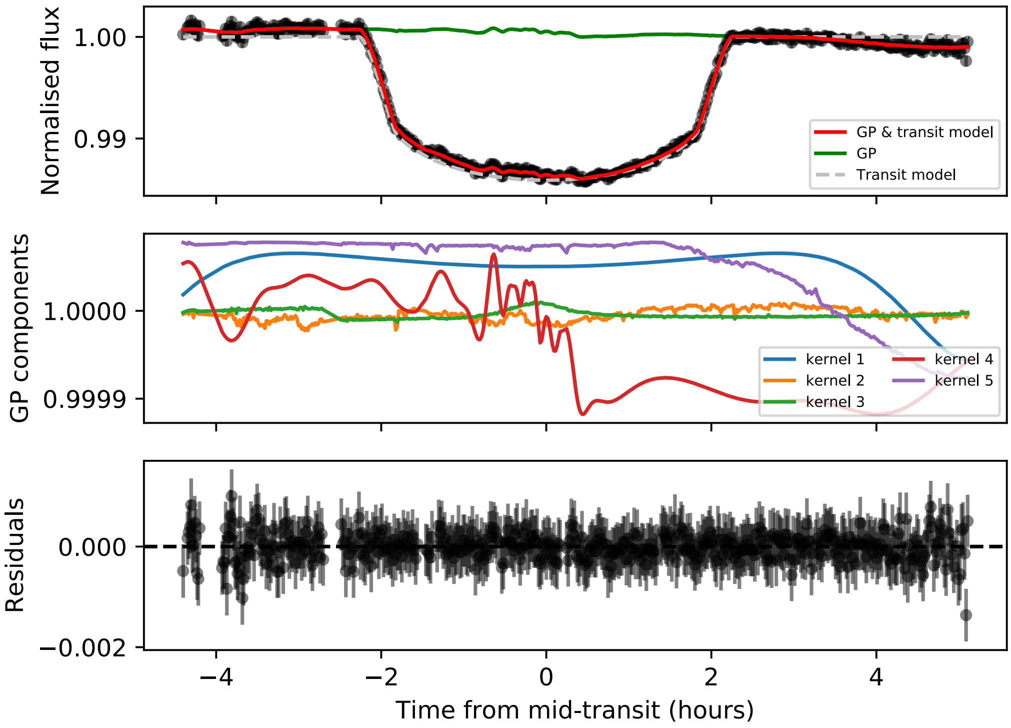

Figure 2.9: White-light light curve of observations of WASP-94Ab (see Chapter 3) fitted with a transit model and a GP (top). The GP included five different kernel inputs (middle) showing the different structures depending on kernel input quantity, with 1 - 5 referring to time (blue), airmass (orange), FWHM (green), derotator angle (red) and sky background (violet), respectively. The bottom panel shows the residuals of the fit.

2.6 Ground-based versus space observations

In the previous sections, I have discussed the various steps in data reduction and fitting when reducing and fitting low-resolution transmission spectroscopy data from the ground and from space. But there are also other differences that need to be taken into account when analysing data from ground-based and space telescopes. In this section I will give an overview of those, but conclude this chapter with the advantages and atmospheric constraints we can gain from combining space and ground-based observations.

2.6.1 Differences

Raw Data

Every telescope and every instrument has its own systematics and every detector is different. Thus this is also true when dealing with space versus ground-based observations. More details about individual instrumental differences can be found in the previous sections of this chapter and in the individual science chapters.

Observability and Visibility

One of the most obvious differences between ground-based and space observations is the difference in observing as a whole, i.e., the observing strategy and planning of observations.

For ground-based observations, the presence of the Earth's atmosphere as well as any clouds within is the main cause for noise in the transit light curves. Using one (or more) comparison stars to monitor changes in the Earth's atmosphere is common practice in low resolution transmission spectroscopy from the ground (as well as in transit surveys). However, finding a good comparison star (similar brightness, similar colour) within the field of view can be challenging. Recently there has been a push to develop methods where a comparison star is not needed e.g. by using Gaussian Process (Panwar et al., 2022a,b; Spyratos et al., 2023), which sounds promising for future ground-based observations of exoplanet atmospheres.

Ground-based observations are further limited by the Earth's atmosphere when it comes to observable wavelength ranges. For example, in the infrared water vapour makes low resolution transmission spectroscopy observations nearly impossible from the ground.

In addition to Earth's atmosphere, the fact that there is limited nighttime also means that exoplanet transits are required to fall in that time window, including sufficient out-of-transit time to get enough baseline. Similarly, ground-based observations are also limited by the seasons, i.e., targets are only visible during specific months of the year due to the Earth's orbit around the Sun and some targets are only visible from the northern or southern hemisphere.

On the other side, while space observations do not require comparison stars and are not limited by night time, they are also limited in target visibility, e.g. *Hubble* due to its orbit around the Earth or *JWST* due to its orbit around the Sun leading to seasonal variations in visibility and dependent on the position in the sky.

2.6.2 Combining Observations

Confirming detections and atmospheric variability

It is essential to repeat observations and tune instruments so that we can identify the origins of any differences between them; Non-agreeing transmission spectra have been an issue in the literature (e.g. WASP-127; Palle et al., 2017; Chen et al., 2018; Spake et al., 2021) (e.g. WASP-121; Evans et al., 2018; Wilson et al., 2021) and it is an ongoing challenge to identify the source(s). Repeat observations with the same and with different instruments (also high-resolution spectroscopy) will be crucial to resolve any discrepancies in the future.

This is needed in the hope that in the future we will be able to detect variability in exoplanet atmospheres, e.g. due to weather or climate changes or stellar activity, as suggested by 3D models (Parmentier et al., 2013; Komacek & Showman, 2020).

Wavelength coverage

The main advantage of combining ground-based and space observations comes from the fact that you can cover a wider wavelength range. As an example see Fig. 2.10, showing an example transmission spectrum and the respective wavelength coverages of NTT/EFOSC2 as well as the individual *JWST* instruments.

For example, the optical wavelength range allows us to study slopes due to hazes (e.g. Sing et al., 2016; Kirk et al., 2018; Parviainen, 2018; Palle et al., 2017), as well as probe for stellar activity (e.g. Espinoza et al., 2019; Weaver et al., 2020; Rackham & de Wit, 2023). Detections or non-detections of atomic features such as sodium or potassium doublet are also able to constrain the metallicity of an exoplanet atmosphere (e.g. Kirk et al., 2019; Alderson et al., 2020; McGruder et al., 2020). The lack of features also provides evidence for clouds (e.g. Kirk et al.,

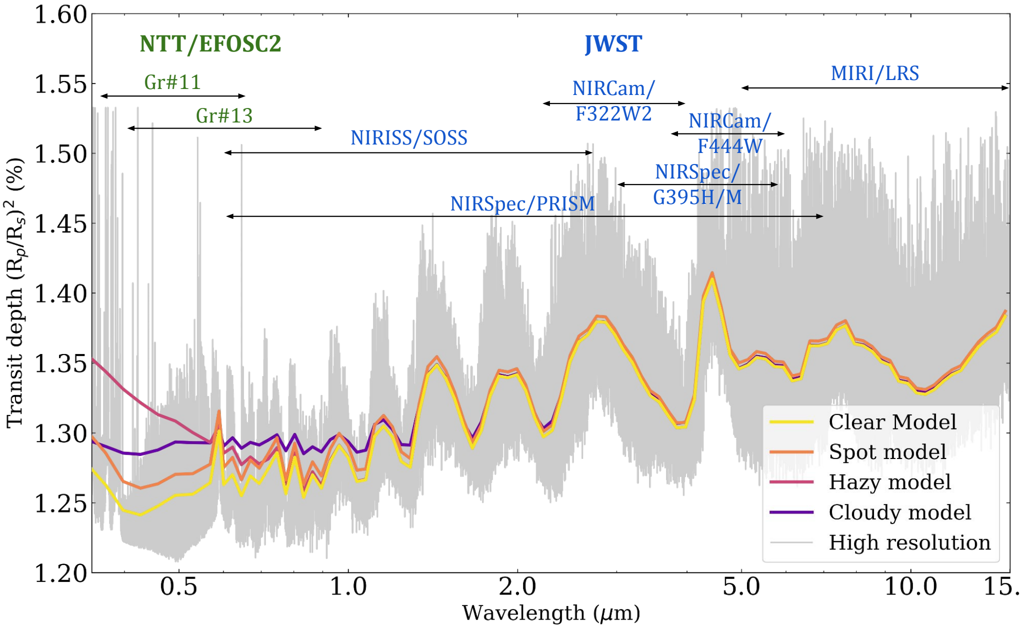

Figure 2.10: Generated transmission spectra of a typical hot Jupiter (using WASP-94Ab parameters) using PLATON models for a hazy atmosphere, a cloudy atmosphere and a clear atmosphere with and without stellar contamination. The unbinned, high-resolution model is shown in grey. The wavelength ranges of NTT/EFOSC2 Gr#11 and Gr#13 are indicated in green, as well as the coverage of *JWST*'s individual instrument and modes in blue. This demonstrates the capability of optical transmission spectroscopy in being able to distinguish between different atmospheric models that can cause degeneracies in the infrared wavelength ranges.

2016; Louden et al., 2017; Espinoza et al., 2019; Spyratos et al., 2021; Panwar et al., 2022b).

On the low-resolution infrared side of the spectrum you have the advantage of being able to observe molecular bands from species such as water vapour (e.g. Huitson et al., 2013; Wakeford et al., 2013; McCullough et al., 2014; Wakeford et al., 2018; Wong et al., 2022) and carbon dioxide (e.g. The JWST Transiting Exoplanet Community Early Release Science Team et al., 2023; Alderson et al., 2023; Rustamkulov et al., 2023). In this wavelength range, however, the sensitivity for stellar contamination is not as prominent and hard to distinguish (e.g. Moran et al., 2023), see Fig. 2.10. Similarly, clouds/hazes and scattering features are not easily identifiable and can cause degeneracies in abundance determinations, e.g. in the case of hot Jupiter WASP-101b (Wakeford et al., 2017b).

2.7 Summary and Conclusions

Low-resolution transmission spectroscopy from the ground and from space are conceptionally identical but provide different challenges when it comes to data reduction and analysis, while also sharing some steps e.g. light curve fitting.

While ground-based observations are heavily influenced by the Earth's atmosphere and weather conditions and are constrained in visibility, space observations have their own challenges due to their unique orbits and instrumental effects and are limited in their mission durations with no chance of updating or intervening.

Most importantly though they are complementary in many ways. Ground-based observations allow for samples of optical transmission spectra that provide key information about clouds/hazes, features like sodium and potassium, as well as scattering slopes and/or constraints on the stellar contamination. These measurements are crucial for infrared observations to break degeneracies e.g. between molecular abundances and cloud continuum level or stellar contamination. In addition, ground-based observations can be used to choose targets and justify infrared (or other) space observations.

In addition, comparing ground-based and space observations of the same target in the same wavelength range is beneficial to confirm findings and identify instrumental offsets and/or noise, in order to be able to robustly confirm atmospheric variability.

In summary, both ground-based and space observations of exoplanet atmospheres in transmission provide unique information and are not exchangeable. Both are needed to understand the effects of systematic noise, stellar contamination and identify atomic and molecular features together with clouds/hazes. All to get closer to the end goal, to fully extract all information possible from an exoplanet's transmission spectrum: from the chemical composition to the atmospheric processes taking place in an exoplanet's atmosphere as well as its formation and migration history.

Chapter 3

Transmission Spectroscopy of WASP-94Ab

Declaration

This chapter is based on the paper published as Ahrer et al. (2022), but adapted to make my contributions clear and additional context was added e.g. regarding the WASP-94 system. I have led all reduction and analysis within this chapter. Specific contributions from my collaborators were from James Kirk who took the observations prior to the start of my thesis and wrote large parts of the pipeline software used in this work using the same technique and a similar telescope.

3.1 Introduction

In this chapter, I present the first transmission spectrum for the highly-inflated hot Jupiter WASP-94Ab (Neveu-Vanmalle et al., 2014). This is also the first exoplanet transmission spectrum using long-slit spectroscopy with the EFOSC2 instrument at the New Technology Telescope (NTT).

This work is part of the Low Resolution Ground-Based Exoplanet Atmosphere Survey using Transmission Spectroscopy (LRG-BEASTS; 'large beasts'), initiated in 2016 with the aim to gather a large sample of transmission spectra of exoplanet atmospheres, mainly focused on hot Jupiters at optical wavelengths. LRG-BEASTS has shown it is possible to achieve precisions on 4-m class telescopes that are comparable to those obtained with 8- to 10-m class telescopes and HST. Characterisations within LRG-BEASTS include the detection of hazes, Rayleigh scattering and grey clouds in atmospheres of the exoplanets WASP-52b (Kirk et al., 2016; Louden et al., 2017), HAT-P-18b (Kirk et al., 2017), WASP-80b (Kirk et al., 2018) and WASP-21b (Alderson et al., 2020), as well as sodium absorption in the atmosphere of WASP-21b (Alderson et al., 2020). An analysis of the atmosphere of WASP-39b revealed supersolar metallicity (Kirk et al., 2019), and evidence for TiO was found in the atmosphere of the ultrahot Jupiter WASP-103b (Kirk et al., 2021).

3.2 The WASP-94 system

WASP-94Ab was detected in 2014 within the Wide Angle Search for Planets survey (WASP, Pollacco et al., 2006). WASP-94 is a binary star system with each star hosting one known exoplanet. WASP-94A is a star of spectral type F8 with a transiting hot Jupiter orbiting with a period of 3.95 days, while WASP-94B is a system consisting of a F9 type star and a non-transiting hot Jupiter with an orbital period of 2.008 days characterised solely by radial velocity measurements so far (Neveu-Vanmalle et al., 2014). The stellar parameters for the WASP-94 system are summarised in Table 3.1. GAIA DR2 determined the distance of the system to be 212.46 ± 2.50 pc (GAIA DR2, Bailer-Jones et al., 2018).

WASP-94A and its companion star WASP-94B are of almost identical spectral type with F8 and F9 and of similar V magnitude with 10.1 and 10.5 respectively, and they have an angular separation of 15.03 ± 0.01 arcseconds. This makes them excellent comparison stars for each other, which is highly favourable for ground-based transmission spectroscopy. The two stars have a physical separation of at least 2700 AU (Neveu-Vanmalle et al., 2014).

WASP-94Ab has an inflated radius with $1.72^{+0.06}_{-0.05}$ $\mathrm{R_{Jup}}$ (Neveu-Vanmalle et al., 2014) and a mass of $0.456^{+0.034}_{-0.036}$ $\mathrm{M_{Jup}}$ (Bonomo et al., 2017). The orbital and planetary parameters for WASP-94Ab are summarised in Table 3.2.

By measuring the Rossiter-McLaughlin effect, Neveu-Vanmalle et al. (2014) found that the orbit of WASP-94Ab is misaligned and likely retrograde with a spin-orbit obliquity of $\lambda = 151^\circ \pm 20^\circ$. Without external influence a migrating planet cannot have its orbit flipped, which is a theoretical prediction backed up by observations (see Fig. A1 of Albrecht et al., 2022) and WASP-94Ab is too close within the gravitational pull of WASP-94A to have been influenced by stellar flybys in any considerable way. However, the 3-body scattering Kozai-Lidov mechanism (Kozai, 1962; Lidov, 1962) is capable of flipping WASP-94Ab into a retrograde orbit (Li et al., 2014; Neveu-Vanmalle et al., 2014; Teske et al., 2016). Since there is no other planet known in the WASP-94A system, this suggests that WASP-94Ab's orbit has been perturbed by WASP-94B and that migration took place via the

Table 3.1: Stellar parameters for the binary star system WASP-94 as found by [1] Neveu-Vanmalle et al. (2014), [2] Teske et al. (2016), [3] Bonomo et al. (2017) and [4] Bailer-Jones et al. (GAIA DR2, 2018).

Parameter	WASP-94A	WASP-94B	Reference
V_{mag}	10.1	10.5	[1]
Spectral type	F8	F9	[1]
T_{eff} (K)	6194 ± 5	6112 ± 6	[2]
Age (Gyr)	2.55 ± 0.25	2.55 ± 0.25	[2]
log g ($\log_{10}(\mathrm{cm/s}^2)$)	4.210 ± 0.011	4.300 ± 0.015	[2]
[Fe/H]	0.320 ± 0.004	0.305 ± 0.005	[2]
Mass ($M_{\odot}$)	1.450 ± 0.090	1.24 ± 0.09	[3], [1]
Radius ($R_{\odot}$)	$1.653^{+0.087}_{-0.081}$	$1.438^{+0.067}_{-0.240}$	[4]

high-eccentricity tidal migration or disk-free mechanism.

In addition, WASP-94Ab is an interesting target as it is one out of only nine exoplanets [1] that are orbiting a star with a binary companion in a misaligned retrograde orbit[2]. Only three of these are hot Jupiters, with masses $<1.5\mathrm{M}_{\mathrm{Jup}}$, periods <10 days and radii $<3\mathrm{R}_{\mathrm{Jup}}$.

With its low density and an equilibrium temperature of 1508±75 K (Garhart et al., 2020), one atmospheric scale height of WASP-94Ab corresponds to a transit depth of 262 ppm, making it an attractive target for atmospheric studies. Thus it has one of the highest transmission spectroscopy metrics (TSM of 590 in K band; Kempton et al., 2018) of all known exoplanets (top 14 of all exoplanets considering both K mag and V mag) and by far the highest of the three hot Jupiters that are known to orbit its binary host star in a misaligned retrograde way.

No transmission spectrum has been published of WASP-94Ab before this work, making this the first atmospheric characterisation for this highly-inflated hot Jupiter.

3.3 Observations

Observations of WASP-94A took place on the night of the 14 of August 2017, using the EFOSC2 instrument (Buzzoni et al., 1984) mounted at the Nasmyth B focus of the ESO NTT, La Silla, Chile[3]. The detector is a Loral/Lesser CCD with a size of 2048 x 2048 pixels, a resolution of 0.12 arcseconds per pixel and an overall field of

---

[1] Using the NASA Exoplanet Archive, as of January 2023.

[2] Here misaligned and retrograde is defined as an obliquity of $|\lambda| > 90^{\circ}$ by at least 3σ, using the TEPCat exoplanet catalogue.

[3] Based on observations collected at the European Southern Observatory under ESO programme 099.C-0390(A).

Table 3.2: Orbital and planetary parameters for the hot Jupiter WASP-94Ab and the corresponding references. [1] Neveu-Vanmalle et al. (2014); [2] Bonomo et al. (2017); [3] Garhart et al. (2020)

Parameter	Value	Reference
Period, P (days)	3.9501907^{+44}_{-30}	[1]
Semi-major axis, a (AU)	$0.0554^{+0.0012}_{-0.0011}$	[2]
Mass, $M_{\rm p}$ ($M_{\rm Jup}$)	$0.456^{+0.034}_{-0.036}$	[2]
Radius, $R_{\rm p}$ ($R_{\rm Jup}$)	$1.72^{+0.06}_{-0.05}$	[1]
Inclination, i (°)	88.7 ± 0.7	[1]
Surface gravity, log g ($\log_{10}$(cm/s^2))	$2.590^{+0.044}_{-0.042}$	[2]
Equilibrium temperature, $T_{\rm eq}$ (K)	1508 ± 75	[3]
Spin-orbit obliquity λ (°)	151 ± 20	[1]

view of 4.1 arcmin, see also Section 2.2. The fast readout mode was used and 2 × 2 pixel binning was applied, resulting in a readout time of 22 s.

For the spectroscopic measurements a slit was chosen with a width of 27 arcseconds to avoid differential slit losses between target and comparison star. Grism #11 was used for these observations, which provides a spectrum from $3750 - 7520$ Å at resolution of $R \simeq 200$.

477 spectral frames were acquired with airmass ranging from 1.70 to 1.00 to 2.41. An exposure time of 30 s was used at the beginning of the night for 33 frames, afterwards it was changed to a 45 s exposure to increase the Signal to Noise Ratio (SNR). The moon was illuminated 48% and rose during the second half of the night having a distance of at least 102° to the target at all times. 39 bias frames were taken, as well as 127 flat frames with different settings (91 dome flats, 25 sky flats, 11 lamp flats) and 15 HeAr arc frames for wavelength calibration, which were taken in the morning after the transit observations. Note that I did not use any of the flat frames during my final data reduction as using flat-fielding resulted in an increase in noise. This has been seen previously in the analysis of low-resolution spectra in LRG-BEASTS observations (e.g. Kirk et al., 2017; Alderson et al., 2020; Kirk et al., 2021), and has also been found with ACCESS data (Rackham et al., 2017; Bixel et al., 2019; Espinoza et al., 2019; Weaver et al., 2020; Kirk et al., 2021).

WASP-94B served as a comparison star during the observations of WASP-94Ab in order to perform differential spectrophotometry to reduce the effects of the Earth's atmosphere. WASP-94A and WASP-94B have similar spectral types and their angular separation of 15 arcseconds (Neveu-Vanmalle et al., 2014) is low enough to ensure very similar perturbations due to the Earth's atmosphere for both stars, but large enough so that their respective signals are uniquely identified (see

Figure 3.1). This makes the system an ideal target for long-slit transmission spectroscopy.

3.4 Data Reduction

I reduced the data using a custom-built `python` pipeline developed for the LRG-BEASTS survey and described in detail by Kirk et al. (2018) and used by Kirk et al. (2017, 2019, 2021) and Alderson et al. (2020). For this analysis I modified the methods for cosmic ray rejection and wavelength calibration, as described below.

First, a master bias was constructed by median-combining 39 individual bias frames, and this was subtracted from each science frame. In contrast to previous LRG-BEASTS analyses, I did not remove cosmic rays after the spectra were extracted, but at the raw science frame level. The change of method was chosen to increase the reliability and sensitivity of cosmic ray detection, and to minimise the risk of introducing spurious features into 1D spectra by mistakenly classifying real spectral features as cosmic rays.

By dividing each science image by the previous frame (in the case of the first frame the subsequent frame was used) I identified affected pixels and replaced them with the median of the surrounding pixels. For this I used a criterion of 16 σ with σ being the standard deviation of the divided image, resulting in ≈ 50 pixels being replaced per frame. The median of the surrounding pixels as a replacement value for outliers was chosen instead of the average as the latter can be biased towards a higher value as the rise in flux due to cosmic rays commonly spreads over several pixels.

To extract the spectra I used an aperture width of 33 pixels, as shown in Figure 3.1, and spectral counts were summed within the aperture. The sky background was fitted using a quadratic polynomial on a region of 150 pixels on either side of the trace, separated by 20 pixels from the edge of the source aperture. I experimented with several different values for aperture width, background width, offset and polynomial order for the background fit; the numbers stated here were found to be optimal for minimising the noise. Errors were calculated based on photon and read noise.

The target and comparison stars are ≈ 70 pixels apart and thus would disturb the sky background fit, and so the star not being fitted had to be masked (see Figure 3.1). Outliers of at least three standard deviations were also masked from the fit. Diagnostics of the spectral extraction and observing conditions are plotted in Figure 3.2.

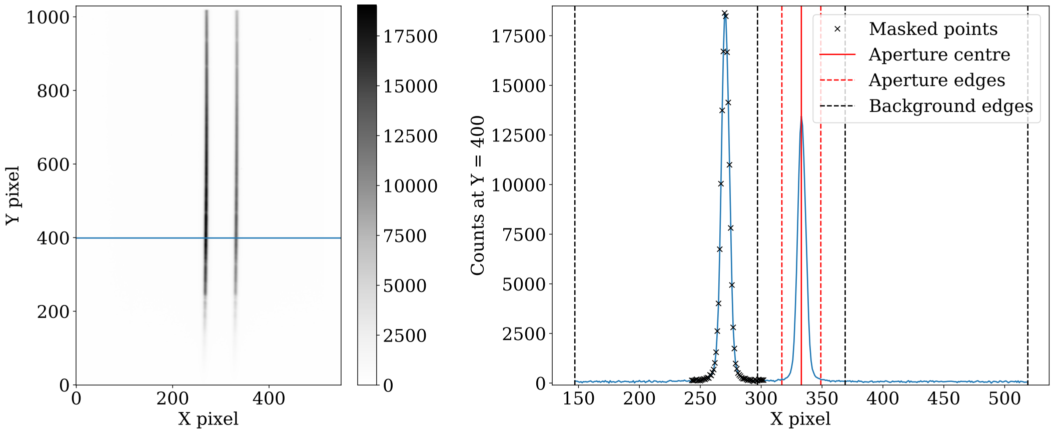

Figure 3.1: Left: Example science frame with the target WASP-94A (left) and comparison star WASP-94B (right). The horizontal and vertical axis correspond to the position along the slit and the wavelength, respectively. Note that this is a cropped frame (full frame in 2×2 binning is 1030×1030 pixels). The ADU counts are shown with the colourbar. The blue line indicates the position of the cut corresponding to the righthand figure.
Right: A cut along spatial direction at row 400 showing the flux of the two stars in blue. In this example the right star was fitted with the red lines indicating the aperture: dashed lines representing the edges and the solid one the centre. The background regions are indicated with dashed black lines, while the black crosses mark the mask for the non-fitted star.

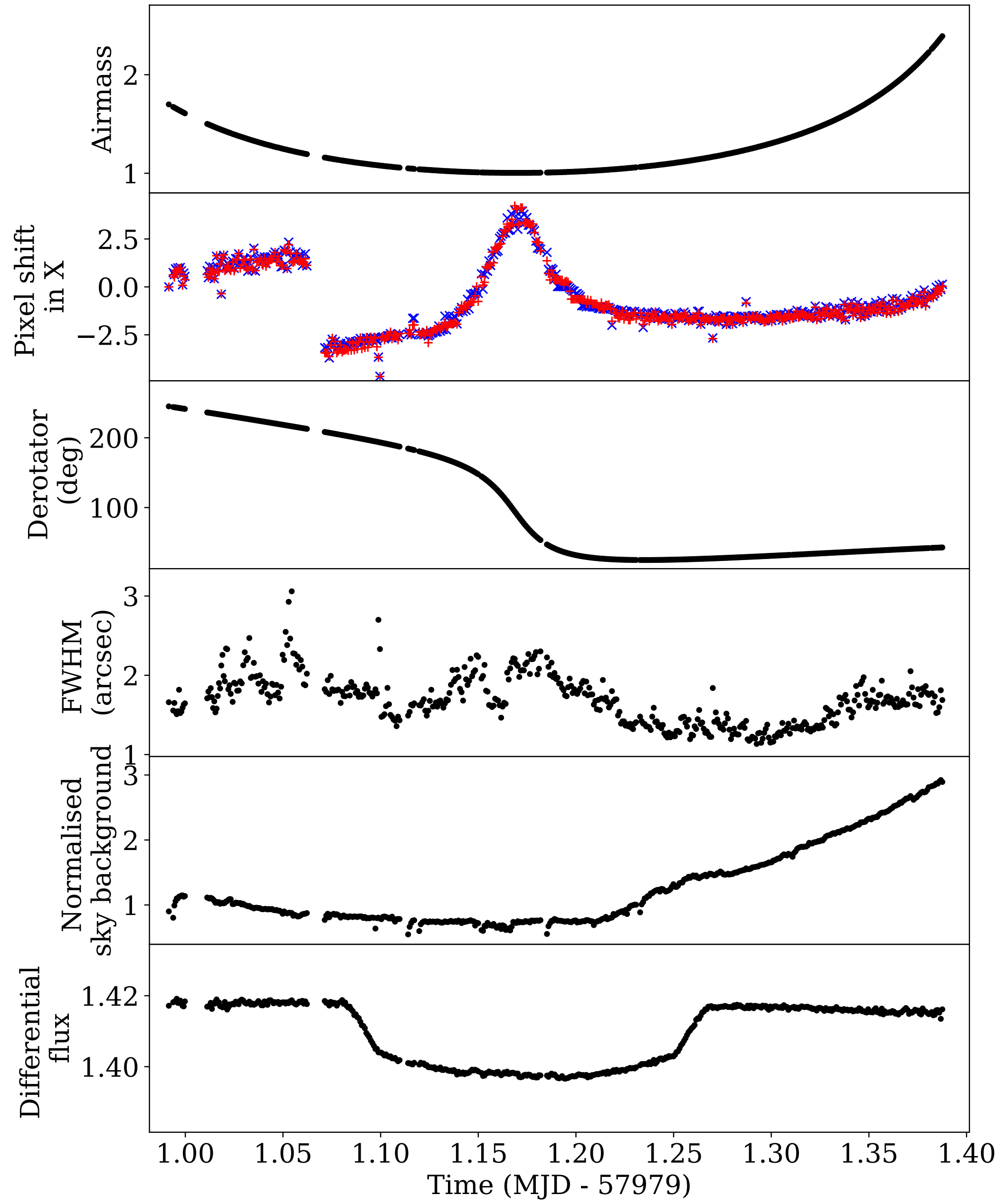

Figure 3.2: Ancillary data for the transit of WASP-94Ab, with the colours blue and red corresponding to the target star WASP-94A and comparison star WASP-94B respectively. From top to bottom: airmass, pixel shift along the slit, derotator angle (peaking at zenith), full width half maximum (FWHM) of the stellar profile, normalised sky background (increasing as the moon rises in the second half of the night) and the differential flux (white light curve).

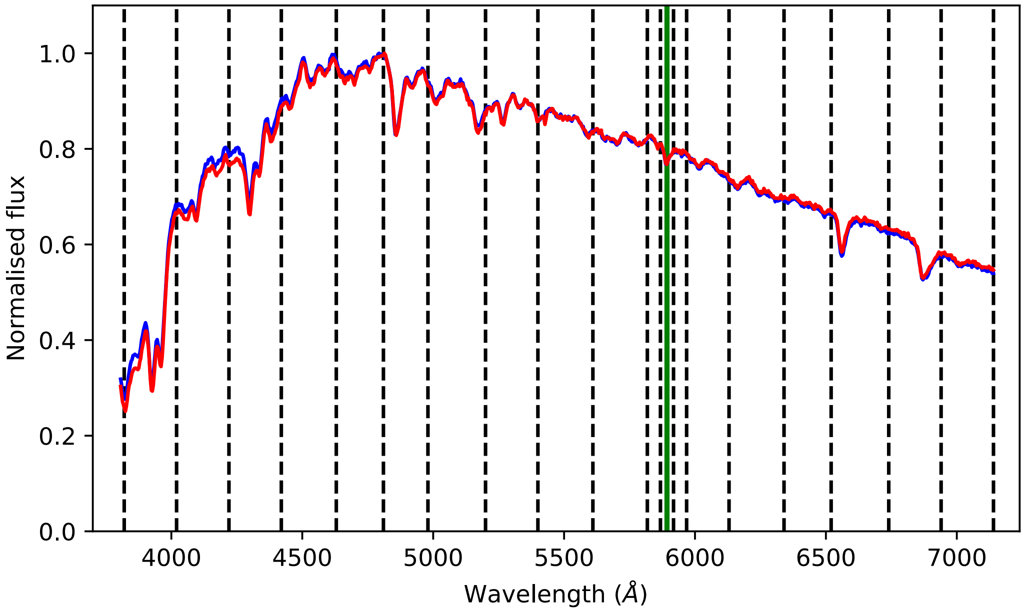

Figure 3.3: The blue and red line correspond to the flux of WASP-94A and the comparison star. The dashed black lines indicate the edges of the wavelength bins, the green line shows the central wavelength of the sodium doublet line.

Following the extraction of each spectrum, wavelength solutions were found for each individual frame. Unlike in previous LRG-BEASTS studies, I used RASCAL (Veitch-Michaelis & Lam, 2019) to make an initial wavelength calibration using the gathered HeAr arc frames. For improved accuracy throughout the time series, I combined the arc calibration with a solution based on absorption lines in the extracted stellar spectra. Note that this wavelength calibration step was computed for each frame individually to account for wavelength drifts throughout the night (on the order of ≈ 5 pixels or ≈ 25 Å).

For my main analysis, the spectra were binned into 19 wavelength bins. Of these, 16 have a width in the range $160-220$ Å, with the wavelength ranges chosen to avoid bin edges falling on spectral absorption lines. The remaining three bins have a width of 50 Å centred on the sodium doublet. The wavelength bins are shown in Figure 3.3. I also extracted higher-resolution data around the sodium doublet for analysis of the line width in Section 3.6.3 (35 bins with a width of 14 Å). The light curves for each bin were computed by summing the flux within the corresponding wavelength range of each frame. To correct for the affects of the Earth's atmosphere each light curve was divided by the comparison star's light curve. A white-light light curve was also computed by defining the whole spectrum as a single wavelength bin.

Table 3.3: Parameter values obtained from the white-light light curve fitting, for both the polynomial and Gaussian Processes detrending. The respective priors placed on these parameters are listed in Table 3.4. The values for the parameters for a/R_s, i and T_C listed here were fixed for during the spectroscopic light curve fitting.

Parameter	Polynomial detrending	GP detrending
a/R_s	$7.368^{+0.028}_{-0.021}$	$7.436^{+0.020}_{-0.029}$
i (°)	$89.25^{+0.20}_{-0.37}$	89.42 ± 0.38
T_C (BJD)	$2457980.681061 \pm 0.000038$	$2457980.68093 \pm 0.00019$
$R_\mathrm{p}/R_\mathrm{s}$	0.10827 ± 0.00017	$0.10544^{+0.00040}_{-0.00039}$
$u1$	0.5326 ± 0.0049	$0.529^{+0.021}_{-0.018}$
$u2$	0.0862	0.0862

3.5 Data Analysis

3.5.1 Transit model

In order to fit the individual transit light curves I used the nested sampling algorithm `PolyChord` (Handley et al., 2015a,b) in `python` in combination with the `batman` package (Kreidberg, 2015) and the analytic light curves from Mandel & Agol (2002).

The fitting parameters included the ratio of planet to star radius, $R_\mathrm{p}/R_\mathrm{s}$, the inclination i of the system, the quadratic limb-darkening coefficients $u1$ and $u2$, the scaled stellar radius a/R_s and the time of mid-transit T_C. Additional parameters were used to describe detrending functions, as explained below.

First, the system parameters a/R_s, i and T_C were fitted for using the white-light light curve (see Tables 3.3 & 3.4). All priors for system parameters were chosen to be wide and uniform, with lower and upper limits corresponding to the respective literature values (Table 3.2) subtracting and adding three times the respective error. The limb-darkening coefficients and respective uncertainties were generated using the Limb-Darkening Toolkit (`LDTk`) package (Parviainen & Aigrain, 2015). A quadratic limb-darkening law was applied and one coefficient held fixed to avoid degeneracies ($u2$). The prior for $u1$ was uniform, centered at the generated value with a range corresponding to the generated error inflated by a factor of four. All priors are summarised in Table 3.4.

The parameter values determined from the white-light light curve were then used as fixed parameters for the binned light curve fits to ensure the errors in the transmission spectrum reflected the uncertainties in the wavelength-dependence of the planet radius, and not the uncertainty in the absolute radius.

To model systematic trends in the light curves I took two different approaches

Table 3.4: Parameter used in the white-light light curve fitting, for both the polynomial and Gaussian Processes detrending and the respective priors placed on these parameters. Values for semi-major axis a, radius of the star R_s and radius of the planet R_p and inclination i are listed in Table 3.2.

Parameter	Prior distribution and range	
Scaled stellar radius a/R_s	Uniform	$a/R_\mathrm{s} \pm 3\sigma_{a/R_\mathrm{s}}$
Inclination i ($^\circ$)	Uniform	$i \pm 3\sigma_i$
Time of mid-transit T_C (BJD)	Uniform	$0.9 \times\ T_\mathrm{C}$, $1.1 \times\ T_\mathrm{C}$
Transit depth $R_\mathrm{p}/R_\mathrm{s}$	Uniform	$R_\mathrm{p}/R_\mathrm{s} \pm 3\sigma_{R_\mathrm{p}/R_\mathrm{s}}$
Limb-darkening coefficient $u1$	Uniform	$u1 \pm 4\sigma_{u1}$
Limb-darkening coefficient $u2$	Fixed	–

for detrending in order to demonstrate that the retrieved transmission spectrum is not sensitive to the treatment of systematics.

3.5.2 Polynomial Detrending

I fitted a low-order polynomial model in combination with the transit model to remove a small overall trend (see Figs. 3.4 & 3.5). The best fitting model for the white-light light curve was quadratic in time (Figure 3.4), while the light curves for the individual wavelength bins were found to be fitted best by a linear model (Figure 3.5).

I experimented with several variations of polynomial functions and different input files e.g. polynomials of different order with airmass, sky background, telescope derotator angle or two or more linear in time and airmass models simultaneously. However, the linear polynomial in time showed the highest Bayesian evidences with strong statistical significance i.e. at least a difference in logarithmic evidence of > 5 corresponding to a 99.3 % probability (Jeffreys, 1983).

The system parameters a/R_s, i and T_C obtained from the white-light light curve are shown in Table 3.3, while the parameters $R_\mathrm{p}/R_\mathrm{s}$, $u1$, $u2$ for each individual wavelength bin are shown in Table 3.5.

The first wavelength bin showed features in the light curve that are distinct from the other bins, potentially related to increased extinction in the Earth's atmosphere and the much lower flux in this bin (see Figure 3.3). While experimenting with different detrending methods as well as bin sizes I found that the transit depth for this particular bin changed significantly with the type of detrending used. Because of this poorly defined behaviour I conducted further analysis without considering this first wavelength bin and it is excluded from the white light fit, as well as Figs. 3.5 & 3.8.

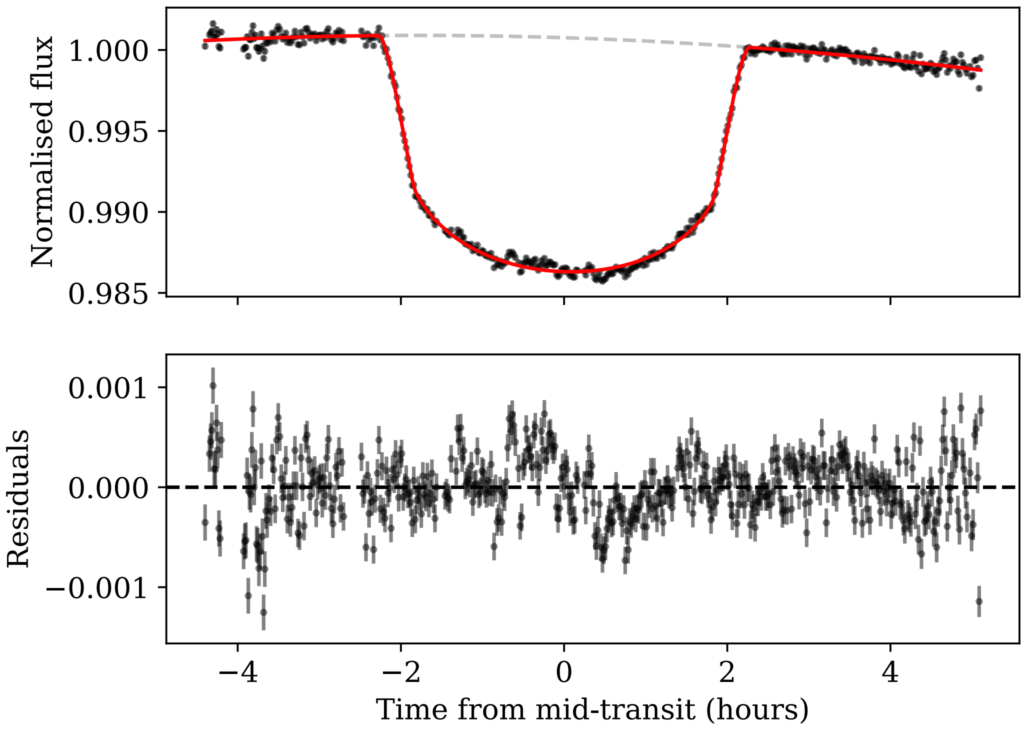

Figure 3.4: The white-light transit light curve of WASP-94Ab fitted using a quadratic in time detrending function. The top panel shows the fitted light curve; bottom panel shows residuals to the fit. The red line shows the best fitting model, while the dashed grey line represents the transit model including the quadratic detrending model.

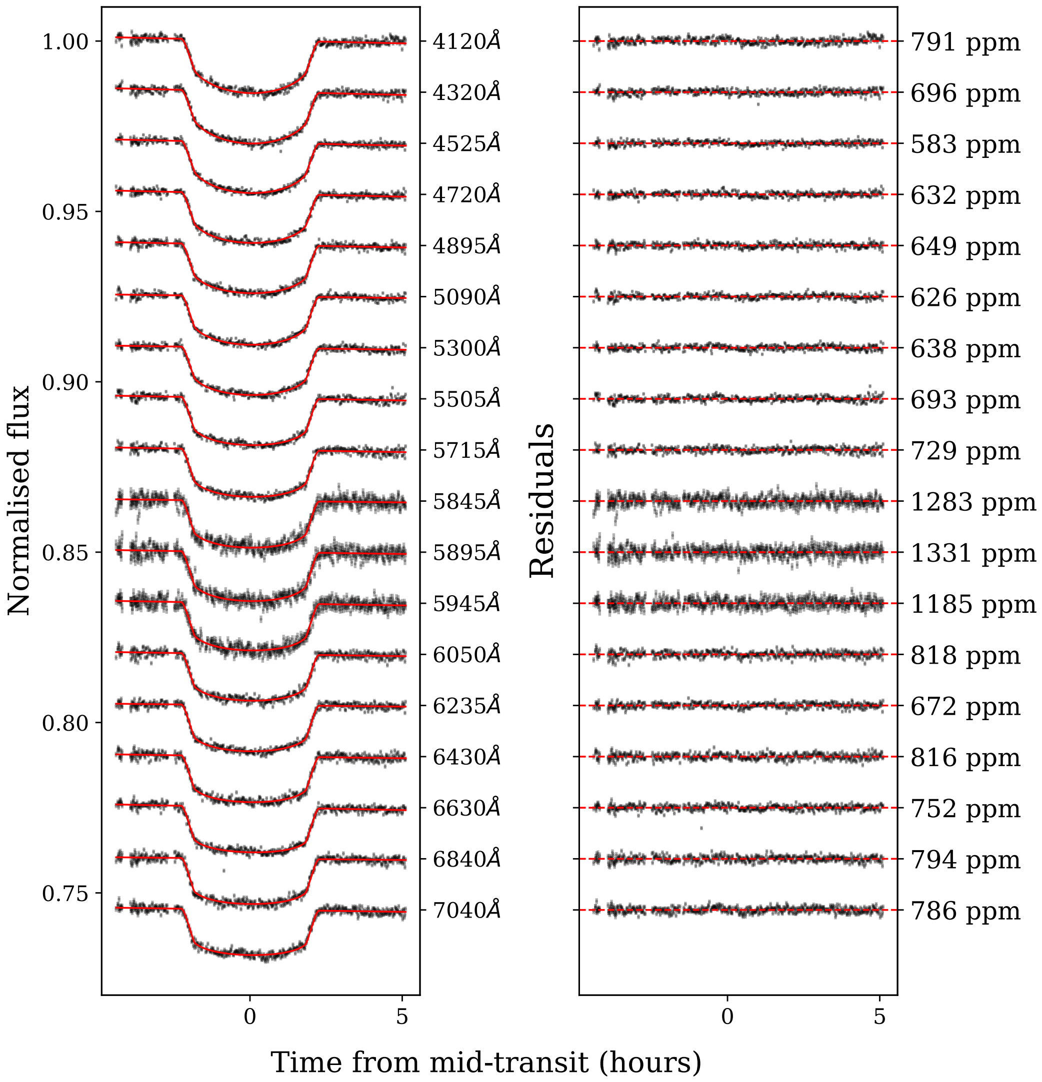

Figure 3.5: Left: Light curves for each individual wavelength bin fitted with a transit model and a linear in time detrending model. The wavelength increases from blue to red from top to bottom. The red lines correspond to the fitted transit models including the linear trend. Right: Respective RMS amplitude of the residuals for the individual fitted spectroscopic light curves on the left.

Table 3.5: Transmission spectrum of WASP-94Ab in tabulated form using a linear in time detrending, as plotted in Figure 3.9

Bins (Å)	$R_\mathrm{p}/R_\mathrm{s}$	u1	u2
3800 - 4020	$0.10790^{+0.00045}_{-0.00067}$	$0.87^{+0.02}_{-0.03}$	-0.0639
4020 - 4220	$0.10965^{+0.00036}_{-0.00061}$	$0.70^{+0.03}_{-0.02}$	-0.0109
4220 - 4420	$0.10831^{+0.00033}_{-0.00064}$	$0.72^{+0.03}_{-0.02}$	-0.0275
4420 - 4630	$0.10774^{+0.00027}_{-0.00059}$	$0.64^{+0.03}_{-0.01}$	0.0460
4630 - 4810	$0.10766^{+0.00025}_{-0.00070}$	$0.58^{+0.03}_{-0.01}$	0.0736
4810 - 4980	$0.10740^{+0.00031}_{-0.00067}$	$0.53^{+0.03}_{-0.02}$	0.1032
4980 - 5200	$0.10709^{+0.00028}_{-0.00065}$	$0.55^{+0.03}_{-0.01}$	0.0884
5200 - 5400	$0.10636^{+0.00029}_{-0.00072}$	$0.51^{+0.03}_{-0.01}$	0.1080
5400 - 5610	$0.10724^{+0.00023}_{-0.00079}$	$0.46^{+0.05}_{-0.01}$	0.1134
5610 - 5818	$0.10734^{+0.00025}_{-0.00076}$	$0.45^{+0.04}_{-0.01}$	0.1265
5818 - 5868	$0.10757^{+0.00033}_{-0.0015}$	$0.41^{+0.08}_{-0.01}$	0.1348
5868 - 5918	$0.10975^{+0.00038}_{-0.0015}$	$0.43^{+0.07}_{-0.01}$	0.1269
5918 - 5968	$0.10810^{+0.00037}_{-0.0018}$	$0.42^{+0.08}_{-0.01}$	0.1315
5968 - 6130	$0.10741^{+0.00021}_{-0.0011}$	$0.41^{+0.06}_{-0.01}$	0.1334
6130 - 6340	$0.10700^{+0.00025}_{-0.00092}$	$0.41^{+0.05}_{-0.01}$	0.1337
6340 - 6520	$0.10745^{+0.00016}_{-0.0011}$	$0.36^{+0.06}_{-0.01}$	0.1404
6520 - 6740	$0.10725^{+0.00017}_{-0.0011}$	$0.32^{+0.07}_{-0.01}$	0.1565
6740 - 6940	$0.10710^{+0.00030}_{-0.00091}$	$0.35^{+0.06}_{-0.01}$	0.1429
6940 - 7140	$0.10710^{+0.00029}_{-0.00093}$	$0.35^{+0.06}_{-0.01}$	0.1434

3.5.3 Detrending with Gaussian Process (GP) Regression

Using Gaussian Processes (GPs) is a common technique in exoplanet research to model correlated noise (Rasmussen & Williams, 2006), see Section 2.5. It has been used in detrending photometric data (e.g. Carter & Winn, 2009; Aigrain et al., 2016; Santerne et al., 2018; Nowak et al., 2020; Leleu et al., 2021), in disentangling planetary signals from stellar activity in radial velocity signals (e.g. Haywood et al., 2014b; Rajpaul et al., 2015; Faria et al., 2016; Suárez Mascareño et al., 2018; Barragán et al., 2019; Damasso et al., 2020) and in transmission spectroscopy (e.g. Gibson et al., 2012a; Evans et al., 2015; Hirano et al., 2016; Kirk et al., 2017, 2021).

For detrending the retrieved light curves with GP regression, I used the `george` package (Ambikasaran et al., 2014) in combination with `PolyChord`. GPs use hyperparameters which describe functions modelling the covariance between the data points (see Section 2.5). In this case, the hyperparameters take the form of a length scale and an amplitude of the noise correlation. Note that I did not apply a common noise model or any other detrending method before fitting the spectroscopic light curves.

For my fitting I used a combined kernel, a sum of the following basic kernels: a white noise kernel capturing random Gaussian noise and two squared-exponential kernels, one with sky background as an input variable, and the other using telescope derotator angle (see Figure 3.2). I note that systematics based on the derotator are not expected to be very large for the NTT as there is no Atmospheric Dispersion Corrector (ADC), which has been known to cause large rotation-induced systematics in some VLT/FORS data (Moehler et al., 2010).

As with previous LRG-BEASTS papers, each input for the GP was standardised by subtracting the mean and dividing by the standard deviation, as previously also used by e.g. Evans et al. (2017b). I experimented with different combinations of kernel inputs which included up to five (airmass, FWHM, position of stars along the slit, telescope derotator angle, mean sky background). I found that two kernel inputs (sky and derotator angle) were sufficient to remove the red noise in the data (Figure 3.6). The use of additional kernel inputs resulted in a lower Bayesian evidence value ($\Delta \log \mathcal{Z} > 2$), it did not improve the noise in the residuals and also led to degeneracies between kernel components. For this reason, I used two kernel inputs (sky and derotator angle) for my final analysis.

The white-light light curve fit is shown in Figure 3.6 where the GP component contributions of the sky and derotator as inputs are shown in orange and blue, respectively. The distributions of the posteriors of the white-light light curve fit including the GP hyperparameters is shown in Figure 3.7.

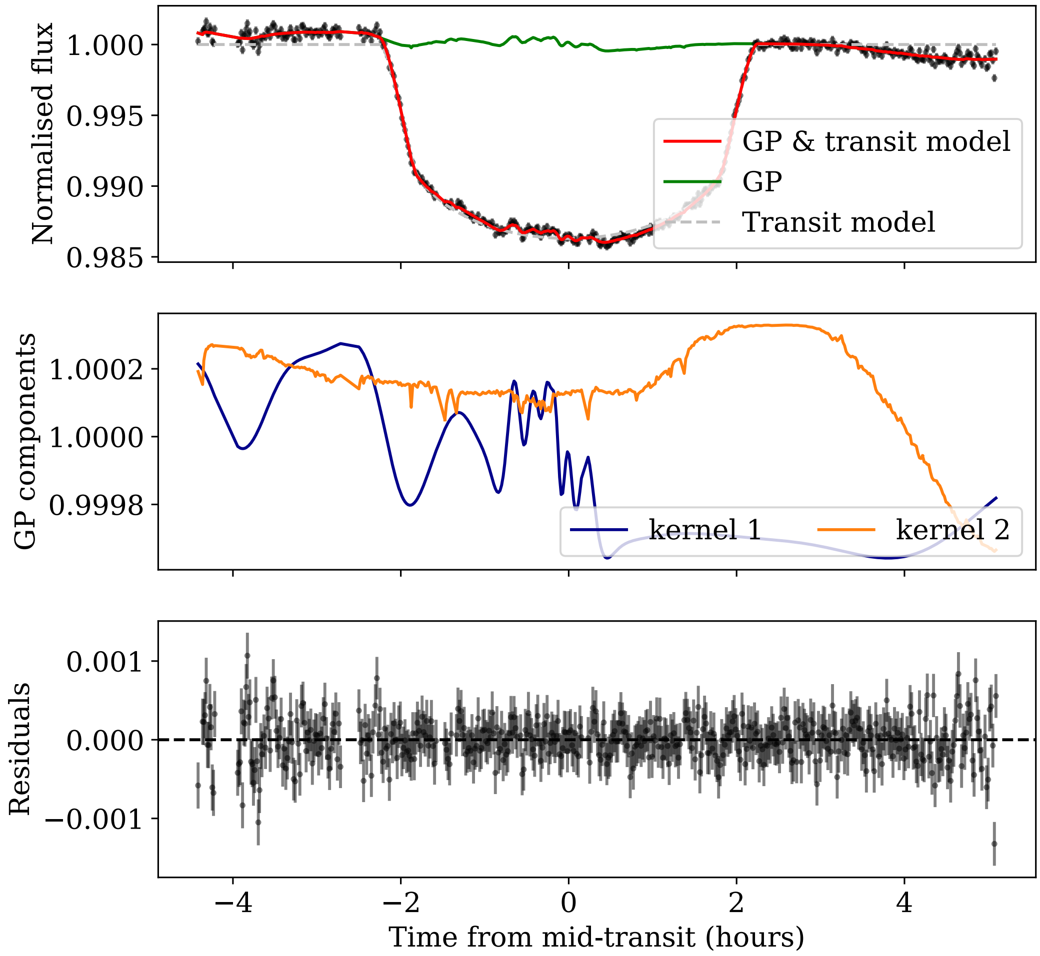

Figure 3.6: The white-light transit light curve of WASP-94Ab fitted using a GP. The top panel shows the fitted light curve; middle panel shows the contributions fromt the two GP kernel inputs: sky (orange) and derotator (blue); bottom panel shows residuals to the fit. The red line shows the best fitting model, while the dashed grey line represents the transit model and the green line refers to the overall GP model.

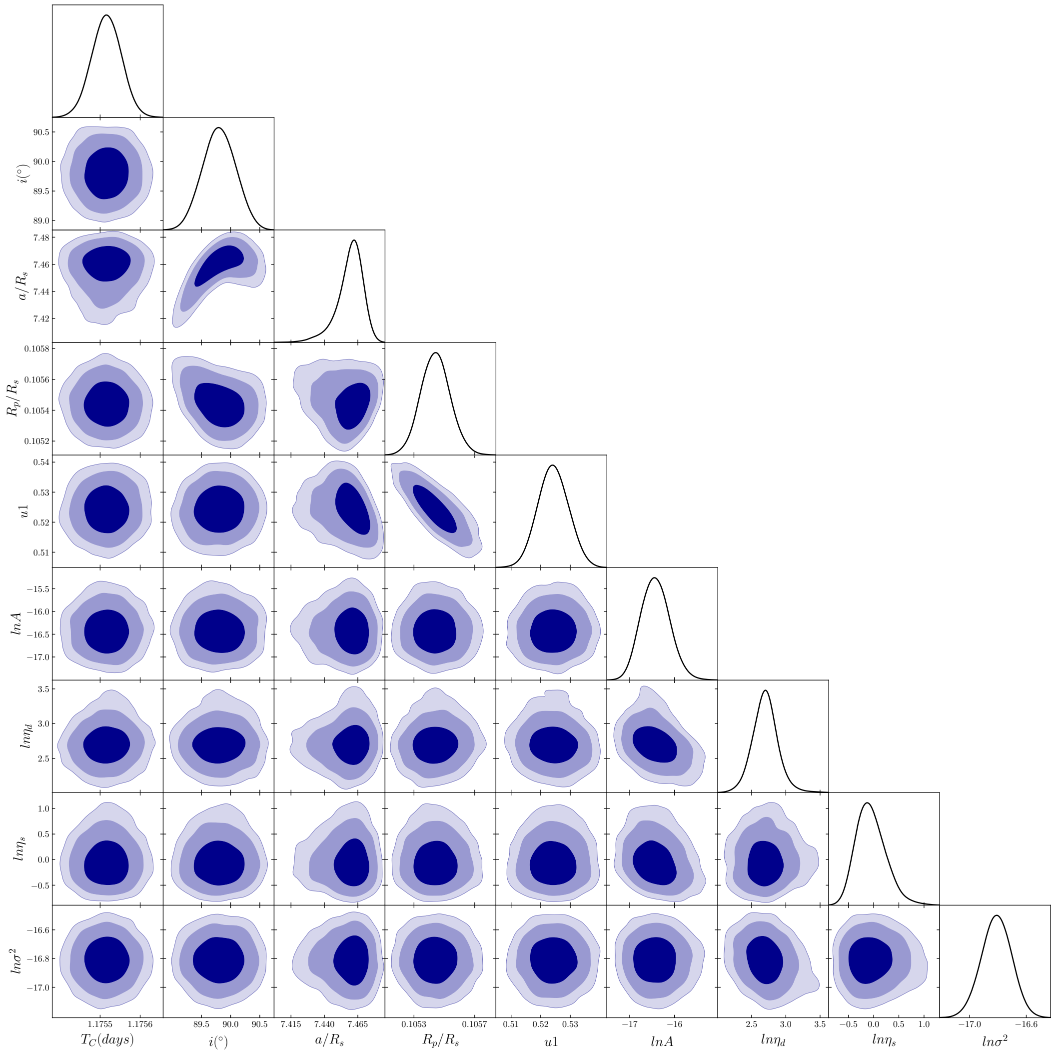

Figure 3.7: Corner plot of the posterior distributions of parameter values as determined by the white-light light curve fit using a GP to model systematics. Some of the parameters describe the transit: time of mid-transit T_C, inclination i, scaled stellar radius a/R_s, transit depth $R_\mathrm{p}/R_\mathrm{s}$ and limb-darkening coefficient $u1$; while the GP is described by the amplitude A, the logarithmic inverse length scales $\ln\eta_\mathrm{d}$ and $\ln\eta_\mathrm{s}$ and the variance of the white noise kernel $\ln\sigma^2$. All retrieved parameters and their prior distributions are summarised in Table 3.3 and further described in the main text of the paper.

The final GP kernel function k is then described as the sum of two exponential-squared basic kernel functions and a white noise kernel function:

$$\begin{aligned} k_{\mathrm{sd}}(s_i, d_i, s_j, d_j) = {} & A\left(\exp\left(-\eta_{\mathrm{s}}(s_{\mathrm{i}} - s_{\mathrm{j}})^2\right) + \exp\left(-\eta_{\mathrm{d}}(d_{\mathrm{i}} - d_{\mathrm{j}})^2\right)\right) \\ & + \sigma^2 \delta_{\mathrm{ij}}, \end{aligned} \tag{3.1}$$

where A is the amplitude of the covariance, s and d are the sky and derotator inputs, η_{s} and η_{d} are the sky and derotator inverse length scales, σ^2 is the variance of the white noise, and δ is the Kronecker delta. In practice, I fit for the natural logarithm of A, η_{s}, η_{d}, and σ^2 since these vary over orders of magnitude.

In contrast to previous LRG-BEASTS analyses, I fit all spectroscopic bins simultaneously, sharing the GP hyperparameters for length scale to capture the common noise shape, while allowing the amplitude and the white noise to be independently fitted for each spectroscopic light curve. This was computationally expensive, but resulted in more consistent detrending between neighbouring wavelength bins. The two shared parameters across all 18 bins are the natural logarithm of the inverse length scale of the kernel inputs sky and derotator angle $\ln \eta_s$ and $\ln \eta_d$. Each spectroscopic light curve j had four individual parameters: transit depth $(R_{\mathrm{p}}/R_{\mathrm{s}})_{\mathrm{j}}$, limb darkening coefficient $u1_{\mathrm{j}}$, logarithm of white noise variance $\ln \sigma_{\mathrm{j}}^2$ and GP amplitude A_{j}. In total 74 parameters were fitted simultaneously.

The fitted spectroscopic light curves are shown in Figure 3.8 and the resulting transmission spectrum in tabular form is displayed in Table 3.6, including the retrieved GP hyperparameters.

3.6 Transmission Spectrum

Following the light curve fitting, the transmission spectra for both detrending methods were constructed as shown in Figure 3.9. While the transmission spectrum inferred with parametric detrending shows less uncertainty, the GP noise modelling provided a slightly better fit, showing less residual noise (see Figs. 3.5 & 3.8). The overall shape of both transmission spectra are very similar, with a slope towards the blue end of the spectrum and excess absorption at 5893 Å (the centre of the NaI doublet). The detection of the sodium absorption feature in both spectra demonstrates that the presence of the signal is not sensitive to my treatment of the systematics.

Table 3.6: Retrieved transmission spectrum of WASP-94Ab in tabulated form using GP detrending, as plotted in Figure 3.9, and the individual retrieved GP hyperparameters amplitude A and the white noise kernel variance parameter $\ln \sigma^2$. The shared hyperparameters are determined to be $\ln \eta_s = -1.21^{+0.90}_{-1.9}$ and $\ln \eta_d = 0.26^{+0.44}_{-0.58}$. The fixed values for the limb-darkening parameter $u2$ are equal to the ones used in the linear detrending and displayed in Table 3.5.

Bins (Å)	$R_\mathrm{p}/R_\mathrm{s}$	u1	ln A	$\ln \sigma^2$
4020 - 4220	$0.10825^{+0.00062}_{-0.00067}$	0.71 ± 0.03	$-14.1^{+3.5}_{-2.1}$	$-17.0^{+1.6}_{-6.8}$
4220 - 4420	$0.10728^{+0.00062}_{-0.00066}$	0.73 ± 0.03	$-14.9^{+3.7}_{-2.1}$	$-18.4^{+2.6}_{-6.2}$
4420 - 4630	$0.10656^{+0.00057}_{-0.00057}$	0.65 ± 0.03	$-15.3^{+3.5}_{-1.8}$	$-21.0^{+3.9}_{-4.6}$
4630 - 4810	$0.10630^{+0.00058}_{-0.00058}$	0.59 ± 0.03	$-14.8^{+3.5}_{-2.0}$	$-20.4^{+3.8}_{-5.0}$
4810 - 4980	$0.10629^{+0.00058}_{-0.00060}$	0.53 ± 0.03	$-15.4^{+3.5}_{-2.1}$	$-20.3^{+3.8}_{-5.0}$
4980 - 5200	$0.10654^{+0.00056}_{-0.00058}$	0.55 ± 0.03	$-15.5^{+3.8}_{-2.4}$	$-19.3^{+3.1}_{-5.7}$
5200 - 5400	$0.10618^{+0.00056}_{-0.00056}$	0.51 ± 0.03	$-15.4^{+3.7}_{-2.3}$	$-19.6^{+3.4}_{-5.4}$
5400 - 5610	$0.10590^{+0.00054}_{-0.00050}$	0.48 ± 0.03	$-14.8^{+3.6}_{-2.3}$	$-16.8^{+1.3}_{-6.5}$
5610 - 5818	$0.10681^{+0.00058}_{-0.00061}$	0.46 ± 0.03	$-15.4^{+3.7}_{-2.3}$	$-16.0^{+0.8}_{-5.5}$
5818 - 5868	$0.10662^{+0.00096}_{-0.00088}$	0.45 ± 0.04	$-17.7^{+4.2}_{-8.6}$	$-20.0^{+4.6}_{-5.2}$
5868 - 5918	$0.10859^{+0.00070}_{-0.0011}$	0.48 ± 0.04	$-17.7^{+4.0}_{-8.1}$	$-19.0^{+4.2}_{-5.9}$
5918 - 5968	$0.1073^{+0.0010}_{-0.0011}$	0.46 ± 0.04	$-16.8^{+3.7}_{-6.5}$	$-20.9^{+4.6}_{-4.6}$
5968 - 6130	$0.10668^{+0.00066}_{-0.00068}$	0.43 ± 0.03	$-16.0^{+3.7}_{-2.5}$	$-17.0^{+1.8}_{-6.9}$
6130 - 6340	$0.10637^{+0.00058}_{-0.00059}$	0.42 ± 0.02	$-17.3^{+3.5}_{-2.6}$	$-20.6^{+4.0}_{-4.8}$
6340 - 6520	$0.10647^{+0.00063}_{-0.00065}$	0.40 ± 0.03	$-15.9^{+3.7}_{-2.7}$	$-16.6^{+1.5}_{-6.9}$
6520 - 6740	$0.10603^{+0.00061}_{-0.00057}$	0.36 ± 0.03	$-14.7^{+3.6}_{-2.1}$	$-17.6^{+2.1}_{-6.7}$
6740 - 6940	$0.10642^{+0.00063}_{-0.00064}$	0.38 ± 0.03	$-17.0^{+3.8}_{-6.0}$	$-19.1^{+3.4}_{-5.8}$
6940 - 7140	$0.10649^{+0.00069}_{-0.00070}$	0.38 ± 0.03	$-14.5^{+3.7}_{-2.4}$	$-21.0^{+4.2}_{-4.6}$

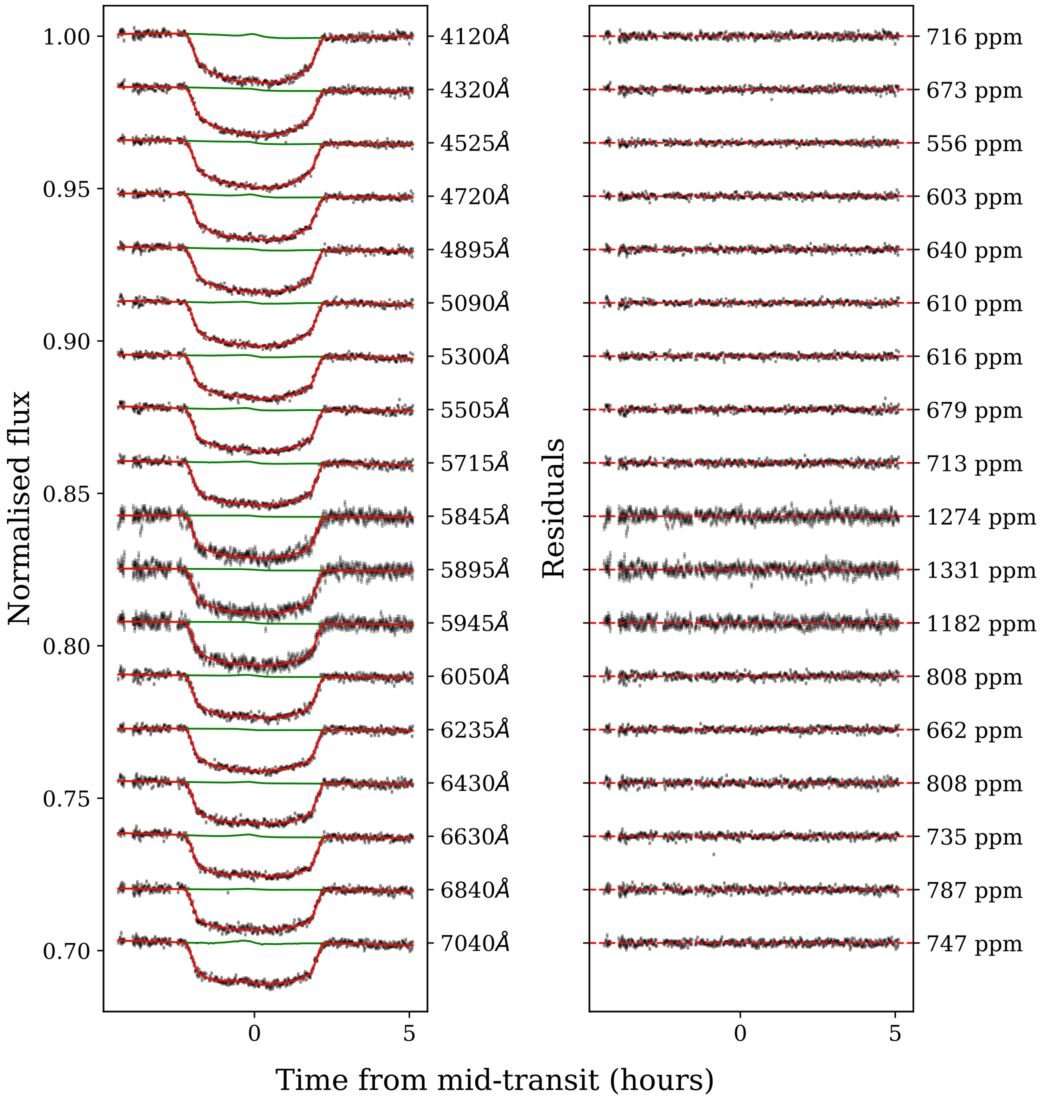

Figure 3.8: Left: Light curves for each individual wavelength bin fitted with the transit model and the GP detrending model (red line). The GP detrending model is also plotted on its own in green. Wavelength increases from top to bottom. Right: Corresponding residuals for the spectroscopic light curves.

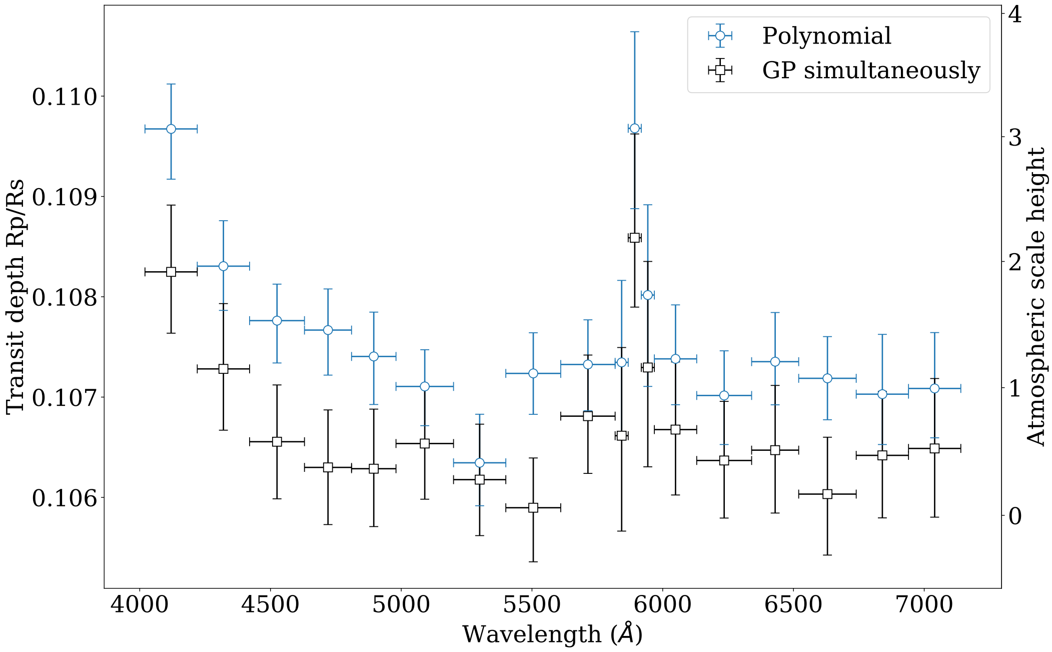

Figure 3.9: Transmission spectrum for WASP-94Ab determined using two detrending models: a linear trend in time (blue), and using Gaussian Process with kernel inputs based on sky background and telescope derotator angle (black). Note that the offset between the transmission spectra is a natural consequence of fixing the values of system parameters, which is necessary in order to accurately assess the relative uncertainties between different wavelengths.

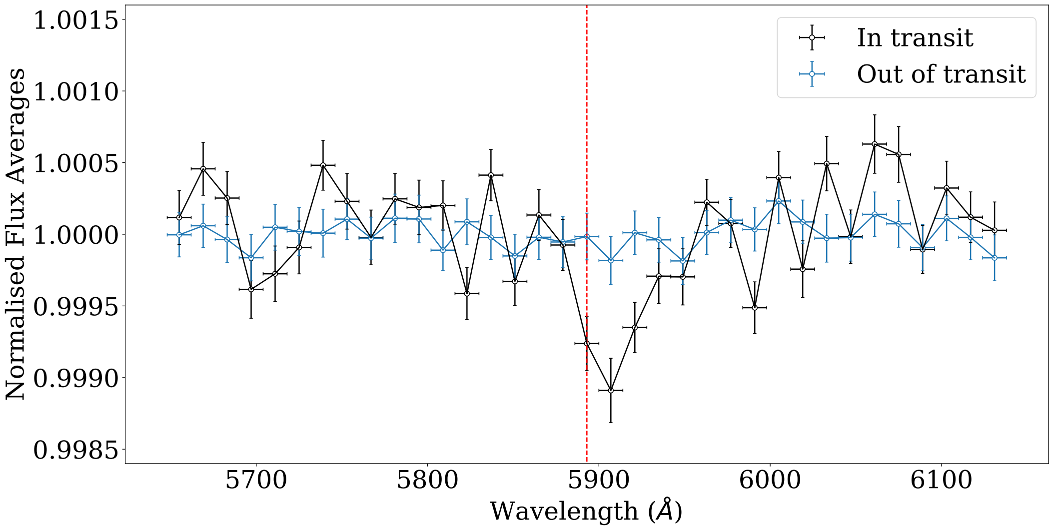

Figure 3.10: Direct ratio of the spectra of the target star (WASP-94A) and comparison star (WASP-94B) made separately for in-transit (black) and out-of-transit (blue) times. This shows excess absorption during transit at the wavelength of the sodium doublet (dashed red line).

3.6.1 Testing the sodium signal

As an independent test of the significance of the sodium absorption, I extracted average spectra for WASP-94A and WASP-94B for in-transit (between 2nd and 3rd contact) and out-of-transit times, and calculated the direct ratio of the two spectra. These are plotted in Figure 3.10. Because the two stars have such similar spectral types, stellar absorption features cancel, and the out-of-transit ratio spectrum is featureless (blue points in Figure 3.10). In contrast, a strong absorption feature is seen at the expected wavelength of sodium in the ratio spectrum for the in-transit data (black points). This excess absorption during transit must presumably arise in the atmosphere of WASP-94Ab. Due to the similarity of target and comparison star, this simple approach allows me to verify the presence of the sodium absorption without any light curve fitting or detrending.

To estimate the significance of the absorption signal seen in Figure 3.10, I fitted a Gaussian to determine the in-transit flux ratio at the peak absorption and compare it to the continuum, resulting in a significance of 4.9σ.

The spectra in Figure 3.10 are binned to 14 Å wavelength bins, which is half the inherent resolution of the spectrum of 27.24 ± 0.17 Å. This value was calculated from the FWHM of target and comparison stars, as well as the instrument/grism resolution with 2×2 binning of 4.08 Å/pixel. In Figure 3.10 I see an offset of the ab-

Table 3.7: Priors for the parameters in the atmospheric retrieval analysis with `PLATON`. Values for T_{eff} and R_{p}, M_{p}, T_{eq} are listed in Table 3.1 and Table 3.2, respectively.

	Priors	
Parameter	Distribution	Limits
Planet mass M_{p} (M_{Jup})	Gaussian	$\mu = M_{\mathrm{p}}$, $\sigma = 0.036$
Planet radius R_{p} (R_{Jup})	Uniform	$0.9 \times \mathrm{R_p}$, $1.1 \times \mathrm{R_p}$
Limb Temperature T_{limb} (K)	Uniform	$0.5 \times T_{\mathrm{eq}}$, $1.5 \times T_{\mathrm{eq}}$
Metallicity ($\log Z/Z_{\odot}$)	Uniform	-1, 3
Cloud-top pressure $\log P_{\mathrm{cloud}}$ (Pa)	Uniform	-0.99, 5
Scattering factor $\log S$	Uniform	-10, 10
Scattering gradient α	Uniform	-4, 20

sorption from the wavelength of the sodium doublet by one bin i.e. half the inherent resolution which is within the uncertainty of my wavelength solution.

3.6.2 Atmospheric Retrieval

In order to aid interpretation of the transmission spectrum shown in Figure 3.9 I performed atmospheric retrievals using the `PLATON` `python` tool by Zhang et al. (2019, 2020), an open-source package assuming equilibrium chemistry.

To account for clouds and hazes `PLATON` uses three parameters: the logarithm of cloud-top pressure, $\log P_{\mathrm{cloud}}$; the power-law index of the wavelength dependence of the scattering cross-section, α (with value 4 for Rayleigh scattering); and the logarithm of a scattering slope multiplying factor, $\log S$. The atmospheric opacity is thus given by $S \times \lambda^{-\alpha}$ with λ equal to the wavelength.

For my retrieval I considered two different models, one where the gradient of the scattering slope is fixed to Rayleigh scattering ($\alpha = 4$) and one where this parameter is free. Parameters retrieved in all models are mass of the planet (M_{p}), radius of the planet at 1 bar ($\mathrm{R_{p,\,1bar}}$), the limb temperature (T_{limb}), metallicity ($\log Z/Z_{\odot}$), cloud-top pressure ($\log P_{\mathrm{cloud}}$) and the scattering factor ($\log S$), which are shown along with their corresponding priors in Tables 3.7 & 3.8. The ranges for the priors were mostly chosen to be wide and uniform, with the exception of the mass of the planet which was described by a Gaussian prior centred on the measured mass of the planet with standard deviation of the error (Table 3.2). The C/O ratio was fixed to the solar value of 0.53 as I cannot constrain this value due to the lack of sensitivity to carbon and oxygen bearing species such as water or carbon monoxide in the optical wavelength range.

I chose to run the `PLATON` retrieval with a nested sampling algorithm, which

Table 3.8: Retrieved parameters for the atmospheric retrieval analysis with `PLATON` for the two models, one including the scattering as a free gradient and one fixed to the Rayleigh scattering ($\alpha = 4$), and their respective Bayesian evidence values $\log \mathcal{Z}$. For both models, the C/O ratio is fixed to solar at 0.53 and the stellar radius is fixed to 1.36 $R_\odot$ (see Table 3.1). Prior distributions are listed in Table 3.7 and posterior distributions of both models in the form of a corner plot are displayed in Figure 3.12.

	fixed to Rayleigh scattering		free scattering gradient	
Parameter	Median	Best Fit	Median	Best Fit
M_p (M_Jup)	$0.457^{+0.030}_{-0.031}$	0.465	0.458 ± 0.030	0.455
R_p (R_Jup)	$1.639^{+0.032}_{-0.050}$	1.672	$1.645^{+0.030}_{-0.037}$	1.624
T_limb (K)	1070^{+230}_{-180}	930	1110^{+220}_{-200}	1300
$(\log Z/Z_\odot)$	$1.5^{+1.0}_{-1.6}$	1.7	$1.46^{+0.93}_{-1.4}$	1.61
$\log P_\mathrm{cloud}$ (Pa)	$2.6^{+1.4}_{-1.7}$	4.1	$2.6^{+1.1}_{-1.3}$	2.3
$\log S$	$0.8^{+3.6}_{-5.5}$	0.2	$-2.8^{+2.9}_{-2.1}$	-3.9
α	fixed to 4		$13.5^{+4.4}_{-8.7}$	18.8
$\log \mathcal{Z}$	131.40 ± 0.26		131.93 ± 0.29	

is implemented in `PLATON` using the `python` package `dynesty` (Speagle, 2020). Using nested sampling allows us to compare Bayesian evidence values for the two models, describing their statistical significance, see Section 2.4. The higher the Bayesian evidence value, the better description of the data, where a difference in logarithmic evidence $\Delta \log \mathcal{Z}$ of > 5 between two models corresponds to a 99.3 % probability (Jeffreys, 1983), i.e. strongly favouring one model over the other.

The two resulting retrieved models are plotted in Figure 3.11 and their posterior distribution in the form of a corner plot in Figure 3.12. They are both dominated by an overall scattering slope and a prominent sodium line that exhibits significant pressure broadening. The corresponding parameter values for these retrievals are presented in Table 3.8, which also includes the values for the Bayesian evidence. These results show that while the model including a free scattering slope resulted in a higher Bayesian evidence value, the difference of $\Delta \log \mathcal{Z} = 0.53 \pm 0.33$ does not equate to strong enough evidence to rule out the model where the gradient is fixed to Rayleigh scattering ($\alpha = 4$). It is interesting to note that all fitted parameters are consistent between the two models to within 1σ, except for the scattering gradient where the fitted value deviates from the Rayleigh slope by 1.1σ.

I note that the retrieved limb temperatures of $\approx$ 1100 K are lower than the equilibrium temperature of 1500 K obtained by Garhart et al. (2020). This is consistent with the expected terminator temperatures for such hot Jupiters (Kataria et al., 2016). In addition, such differences between retrieved limb temperatures and

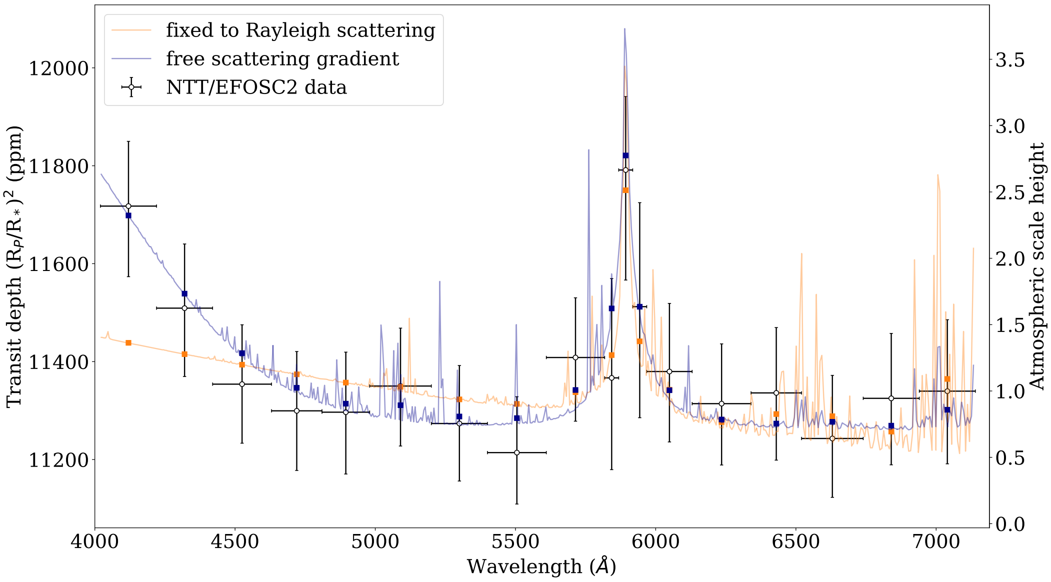

Figure 3.11: Obtained transmission spectrum for WASP-94Ab using the GP simultaneous detrending method (black) and the two `PLATON` models, one where the scattering gradient is fixed to Rayleigh scattering (orange) and one where the gradient of the scattering slope is a free parameter (blue). Note that based on the Bayesian evidence, neither of the models is significantly preferred over the other.

equilibrium temperatures can also be explained by the single-temperature retrieval being applied to the differing temperatures and compositions of morning and evening terminators in the exoplanet's atmosphere (MacDonald et al., 2020).

3.6.3 The width of the sodium line

My atmospheric retrieval shows significant broadening in the sodium line, corresponding to pressure broadening in a relatively cloud-free atmosphere (Figure 3.11). The two wide data points neighbouring the three narrow bins around the sodium line are also elevated, suggesting the pressure broadening may be significantly detected in the observed transmission spectrum. To investigate the sodium line profile further, I split the spectrum between 5600 − 6200 Å into 35 wavelength bins, each with a width of 14 Å (the Nyquist sampling, see the beginning of this section). The middle bin was centred on the sodium doublet. The spectroscopic light curves were then fitted using linear detrending, resulting in a higher-resolution transmission spectrum that is plotted in Figure 3.13.

The sodium line remains clearly visible in this higher-resolution transmission spectrum, and the line profile was fitted with two different models: a Gaussian with

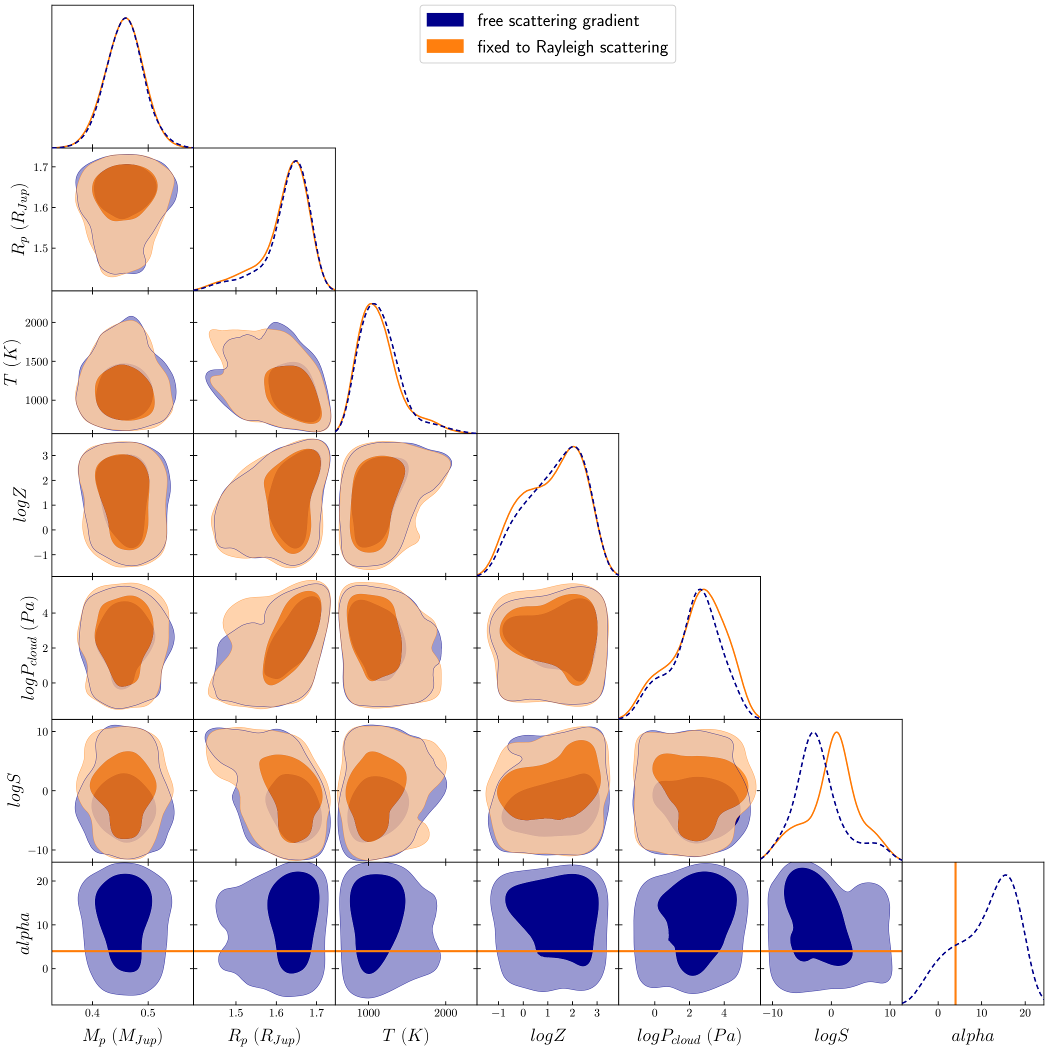

Figure 3.12: Posterior distributions of the parameters fitted by the two atmospheric retrieval models using `PLATON` as shown in Figure 3.11 with all retrieved values and uncertainties displayed in Table 3.8. Following the same colour code, blue represents the retrieved parameters fitted by the free scattering gradient model and orange describes the distributions of the parameters when the gradient was fixed at Rayleigh scattering i.e. $\alpha = 4$.

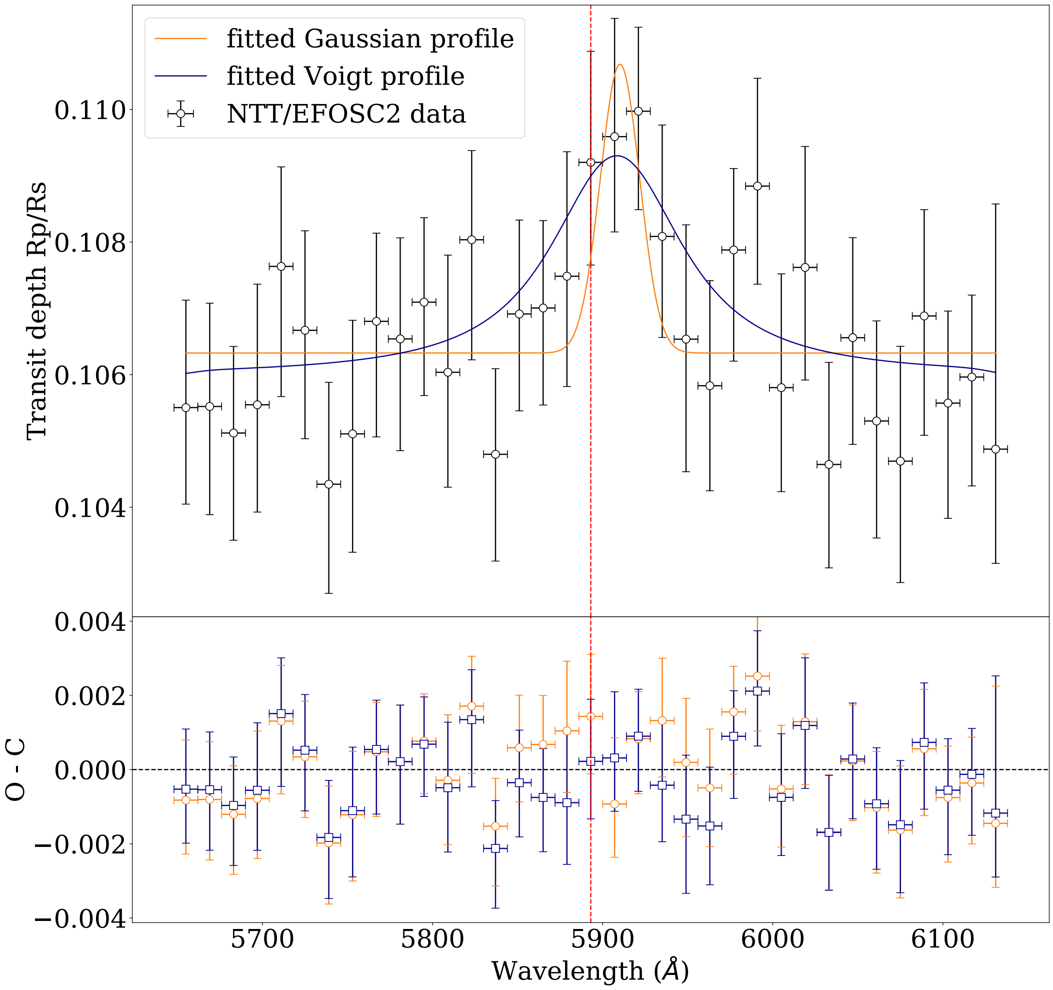

Figure 3.13: Transmission spectrum of WASP-94Ab when sampling at Nyquist rate (14 Å bin width) between 5600 − 6200 Å with two competing models and corresponding residuals. The orange line corresponds to the model solely considering instrumental inherent broadening, while the blue one fits for an extra width equal to a Voigt profile (convolution of the instrumental profile with a Lorentzian profile i.e. the pressure-broadened sodium absorption). The expected central wavelength of the Na I doublet is indicated with the red dashed line.

FWHM fixed to the instrumental resolution (27.24 Å) and a Voigt profile with an unconstrained additional width. The latter model is a convolution of the former, instrumental model, with a Lorentzian describing the pressure-broadened sodium described by the fitting parameter γ. The FWHM of the Lorentzian profile is 2γ. To account for uncertainties in my wavelength solution I allowed both models to fit for the centre of the sodium absorption. The two model fits are included in Figure 3.13.

The instrumental width does not fit the sodium line well and suggests broadening is needed. I find a best fitting FWHM for the Voigt profile of 78^{+67}_{-32} Å, where the FWHM of the Lorentzian component is 68^{+72}_{-38} Å, which is inconsistent with zero at the 1.8σ level. The Bayesian evidence for the Voigt model, however, is lower than the value for the instrument-only broadening model by $\Delta\mathcal{Z} = 1.69 \pm 0.15$.

3.7 Discussion

3.7.1 Precision of observations

In this chapter I presented the first transmission spectroscopy measurements with ESO's EFOSC2 instrument on the 3.6 m NTT. EFOSC2 is a grism spectrograph, with a simple optical design, which is favourable for high precision observations. My wavelength-dependent light curves shown in Figs. 3.5 & 3.8 are relatively free of systematic noise, with the RMS amplitude of residuals only 1.1× and 1.4× above the expected photon noise for each of the detrending approaches (Sections 3.5.2 & 3.5.3). This is better than typically seen with larger 8–10 m class telescopes, where the improved photon noise often cannot be exploited because the precision is limited by systematics. Consequently, transmission spectroscopy with medium-sized telescopes such as the NTT can achieve comparable precision.

In the retrieved transmission spectra using the simultaneous GP fitting method, shown in Figs. 3.9 & 3.11, I achieve an average absolute precision of 128 ppm in 200Å bins, which is less than half the atmospheric scale height of the target planet WASP-94Ab. This precision compares very favourably with single-transit transmission spectroscopy in low-resolution carried out with much larger telescopes such as the 8.2 m VLT using the FORS2 instrument (e.g. 200 ppm for 150Å wide bins in Wilson et al., 2020), as well as from space with HST using the STIS instrument (e.g. 221 ppm for ≈ 175Å wide bins with grism G750L or 175 ppm for ≈ 55Å wide bins with grism G430L in Sheppard et al., 2021).

In part, the very high precision of this single-transit observations arises from the binary nature of the system, with WASP-94B providing an ideal comparison star of very similar brightness and spectral type at an ideal separation of just 15 arcsec from the target (similar to the situation for XO-2b, e.g. Pearson et al., 2019). I want to note that this makes WASP-94Ab particularly well suited to a future intensive ground-based programme of atmospheric characterisation.

I also found the absolute precision in the transmission spectrum with the GP detrending was improved by fitting all light curves simultaneously while linking the GP hyper-parameters for length-scale. This allowed us to account for systematic features in the light curves while imposing similar detrending. The precision is significantly lower when fitting the light curves with GPs individually, with an average precision of 181 ppm compared to 128 ppm for bins $\approx$ 200 Å wide. I illustrate this in Figure 3.14, where I show the different transmission spectra with the three different detrending methods, from top to bottom with increasing uncertainties.

3.7.2 Sodium absorption

My analysis reveals sodium to be present in the atmosphere of WASP-94Ab at a significance of 4.9σ. The absorption feature is visible in transmission spectra measured with each of my detrending models (linear polynomial and GP; Figure 3.9). I also confirmed the detection and significance of sodium absorption independently of my light curve fitting using a direct comparison of average spectra in and out of transit (Figure 3.10). This was possible because of the very close match between the stellar spectra of the target star WASP-94A and its binary companion, WASP-94B (Figure 3.3)

My measured transmission spectrum and its retrieval models using `PLATON` in Figure 3.11 suggest a pressure-broadened sodium absorption line arising in a relatively cloud-free atmosphere. To investigate the sodium line profile further, I extracted a second transmission spectrum using the full spectral resolution available from the data (extracted with the Nyquist sampling of 14 Å bins; Figure 3.13). My best-fitting line profile is indeed broader than the instrumental resolution, with a FWHM of 78^{+67}_{-32}Å (see Section 3.6.3 and Figure 3.13), although at this spectral resolution the signal-to-noise ratio of this single-transit observation is low and Bayesian model comparison does not support the additional free parameter of the broadened model. Further observations are required to determine whether sodium absorption in the transmission spectrum of WASP-94Ab is indeed significantly pressure-broadened.

Detections of sodium absorption in hot Jupiters remain relatively rare, especially in the low-resolution regime, with less than ten cases from HST and only a handful measured from the ground (e.g. Sing et al., 2012; Nikolov et al., 2016, 2018;

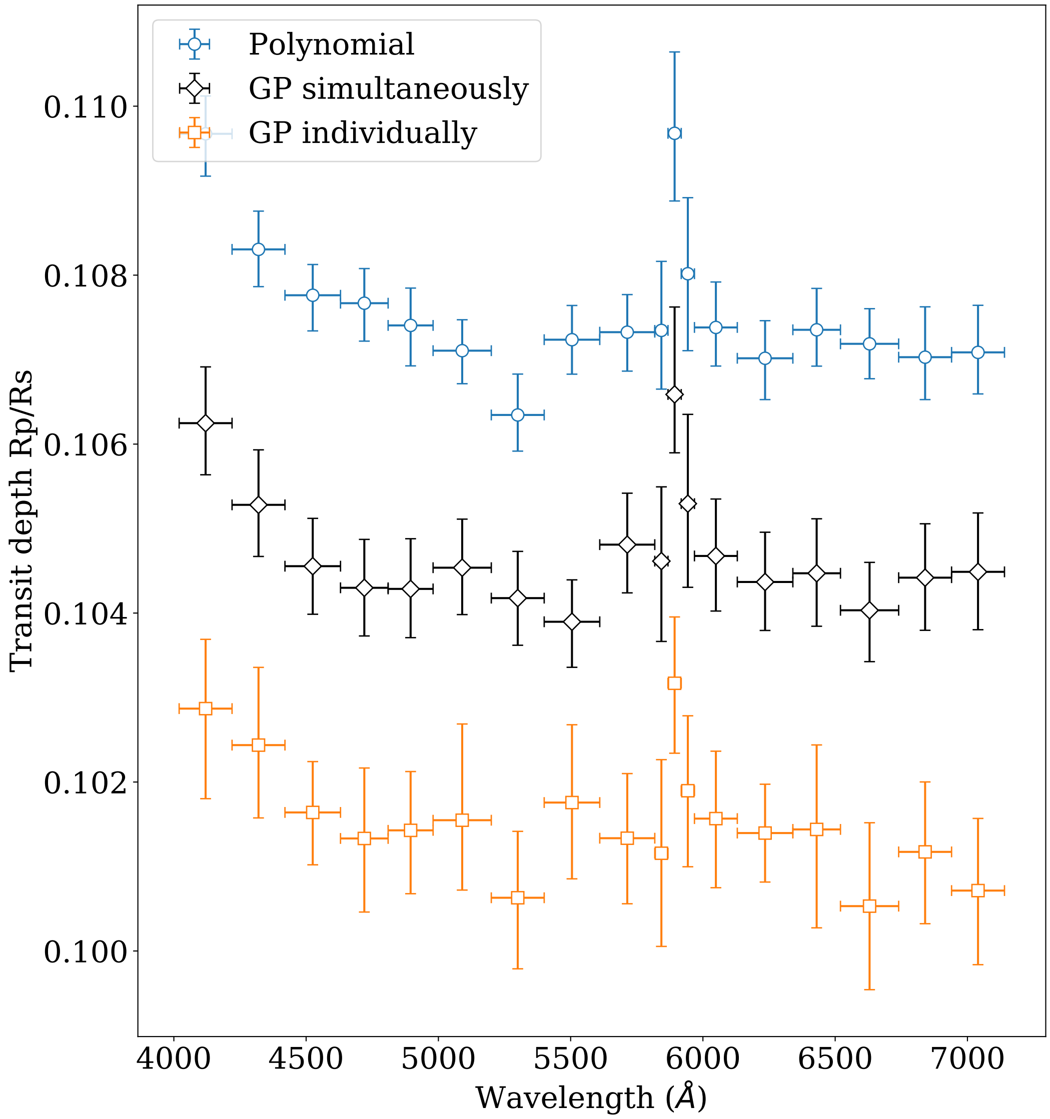

Figure 3.14: WASP-94Ab transmission spectra comparing the precision achieved with three different detrending methods (with an artificial offset for clarity). From top to bottom: first order polynomial detrending is used for the individual light curves (98 ± 3 ppm precision in 200 Å wide bins); GP detrending simultaneously on all spectroscopic light curves with shared GP hyperparameters for length scales (128 ± 2 ppm precision); GP detrending with all bins fitted independently (181 ± 6 ppm precision).

Chen et al., 2020). In some cases the detections are disputed, for instance in the original case of HD 209458b (Casasayas-Barris et al., 2020, 2021). In most cases the detected sodium lines are consistent with being narrow, and arising from relatively high in the planetary atmosphere, with the pressure-broadened absorption from the lower atmosphere being masked by condensates (e.g. Nikolov et al., 2014; Sing et al., 2016). Only in a few exoplanet atmospheres the pressure-broadening has been observed so far, such as WASP-39b (Fischer et al., 2016), WASP-96b (Nikolov et al., 2018) and WASP-62b (Alam et al., 2021). If confirmed with higher signal-to-noise observations, my tentative detection of pressure-broadened sodium absorption in WASP-94Ab would indicate a relatively cloud-free atmosphere, making it a priority target for infrared observations aiming to detect molecular bands and measure atmospheric abundances.

3.7.3 Scattering slope

My transmission spectra show a clear and steep upward slope at the blue end of the spectrum (Figs. 3.9 & 3.11), which is indicative of Rayleigh scattering in the planetary atmosphere. Similar slopes have been observed for alike planets such as HD 209458b (Sing et al., 2016) and HAT-P-1b (Nikolov et al., 2014), demonstrated in Figure 3.15. Both exoplanets possess close resemblance to WASP-94Ab in physical properties, while also orbiting similar stars (G0 type stars). HD 209458b has a 3.52-day period, with a mass of 0.69 M_{Jup}, a radius of 1.38 R_{Jup} (Bonomo et al., 2017) and equilibrium temperature of 1480 K (e.g. Evans et al., 2015), while HAT-P-1b orbits its host star every 4.47 days, with a mass of 0.53 M_{Jup}, a radius of 1.32 R_{Jup} and equilibrium temperature of 1320 K (Nikolov et al., 2014).

I find evidence for a super-Rayleigh slope in the transmission spectrum (see Section 3.6.2). The strength of this evidence depends of the choice of detrending method, which in turn sets the precision of the transmission spectrum (Figure 3.14). With the smaller uncertainties estimated with linear detrending, I find reasonably strong evidence of a super-Rayleigh slope ($\Delta \log \mathcal{Z} = 3.70 \pm 0.71$ which corresponds to $2 - 2.5\sigma$ significance). However, using the more conservative uncertainties from the Gaussian Process detrending I find the evidence for a super-Rayleigh slope is weaker ($\Delta \log \mathcal{Z} = 0.54 \pm 0.38$ which is $\lesssim 1\sigma$).

Super-Rayleigh slopes have been observed in several exoplanet atmospheres before (e.g. HD189733b, WASP-127b, WASP-21b, WASP-74b, WASP-104b; Sing et al., 2011; Palle et al., 2017; Alderson et al., 2020; Luque et al., 2020; Chen et al., 2021). Several explanations have been suggested for this, including based on additional opacity sources such as mineral clouds (e.g. Lecavelier Des Etangs et al.,

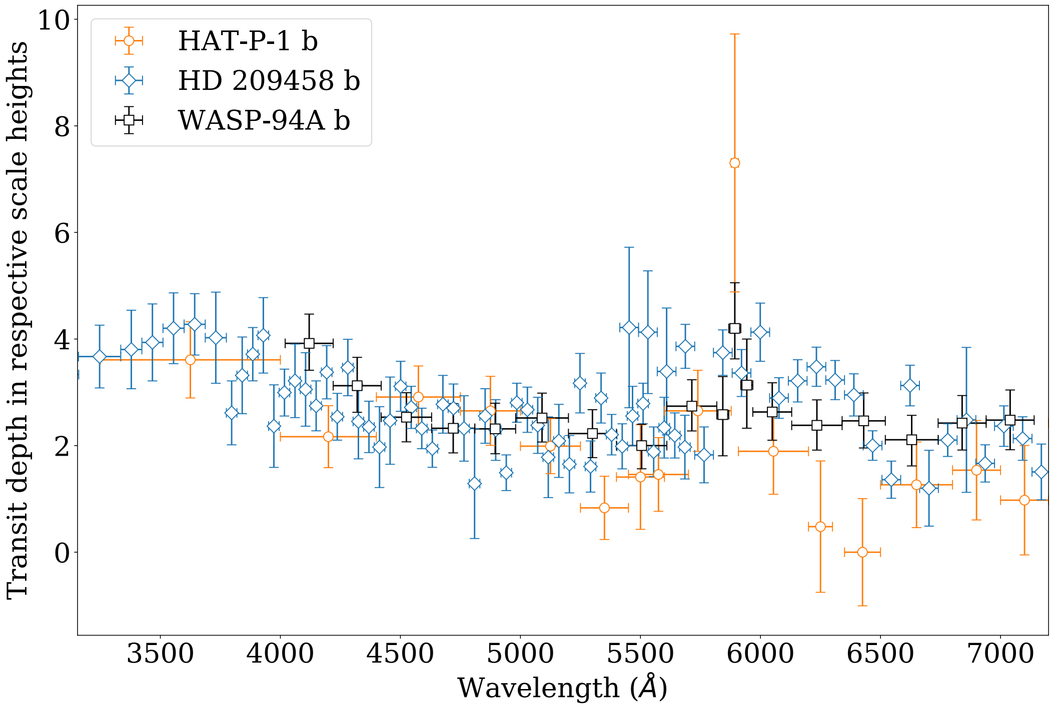

Figure 3.15: Transmission spectrum of WASP-94Ab (black) in comparison to the transmission spectra of HD 209458b (blue) (Sing et al., 2016) and HAT-P-1b (orange) (Nikolov et al., 2014) as a function of scale height. One atmospheric scale height corresponds to 262 ppm for WASP-94Ab, 166 ppm for HD 209458b and 146 ppm for HAT-P-1b. Both HD 209458b and HAT-P-1b have similar properties to WASP-94Ab and orbit stars with similar spectral type (see text for details).

2008a), photochemical hazes — especially for exoplanets like WASP-94Ab with equilibrium temperatures around 1000 – 1500 K (Kawashima & Ikoma, 2019; Ohno & Kawashima, 2020), a combination of clouds and haze layers (e.g. Pont et al., 2013) or alternatively stellar activity (e.g. McCullough et al., 2014; Espinoza et al., 2019; Weaver et al., 2020). Thermal inversion could potentially push a H_2 Rayleigh scattering opacity source to a steeper slope (Fortney et al., 2008), however, planets below $\simeq 2000$ K are less likely to have thermal inversions due to species such as TiO and VO as they are not expected to be in the gas phase at these temperatures (e.g. Gandhi & Madhusudhan, 2019). Given the WASP-94Ab's equilibrium temperature of 1500 K, a thermal inversion on the dayside atmosphere is unlikely.

In the case of WASP-94A I do not expect stellar activity to play a significant role as the effects of spots and faculae were estimated to be < 30 ppm for F8-type stars assuming 1% transit depth (Rackham et al., 2019), which is not detectable with the precision achieved and cannot account for the detected slope. In addition, in the discovery paper by Neveu-Vanmalle et al. (2014) there was no mention of any photometric variations in the lightcurve of WASP-94Ab. Nevertheless, I tested this case by running retrieval models with `PLATON` including stellar activity instead of the gradient of the scattering slope. These retrievals included fitting for spot temperature and spot coverage fraction, which was limited to <7% as estimated for F8-type stars by Rackham et al. (2019). These retrievals confirmed that the stellar activity was not able to account for the observed blueward slope.

3.7.4 Evidence for atmospheric escape

As part of my investigation into stellar activity as a potential explanation of the steep scattering slope (Section 3.7.3) I checked whether there is chromospheric emission in the CaII H&K lines using high-resolution observations with the HARPS spectrograph (Mayor et al., 2003) of WASP-94A[4].

Following Lovis et al. (2011) and using calibrations by Noyes et al. (1984) and Middelkoop (1982) I calculated the $\log R'_{\mathrm{HK}}$ of WASP-94A to be $\log R'_{\mathrm{HK}} = -5.18 \pm 0.27$. This value is below -5.1 which corresponds to a basal level exhibited by inactive FGK stars and I found that the H&K lines do not show emission in the core. Instead, the H&K lines appear to have excess narrow absorption in their core, which can be seen in Figure 3.16.

This excess absorption is similar to that seen in WASP-12b and a number of other hot Jupiters (Fossati et al., 2013), where it is interpreted as absorption

---

[4] Based on observations collected at the European Southern Observatory under ESO programme 097.C-1025(B).

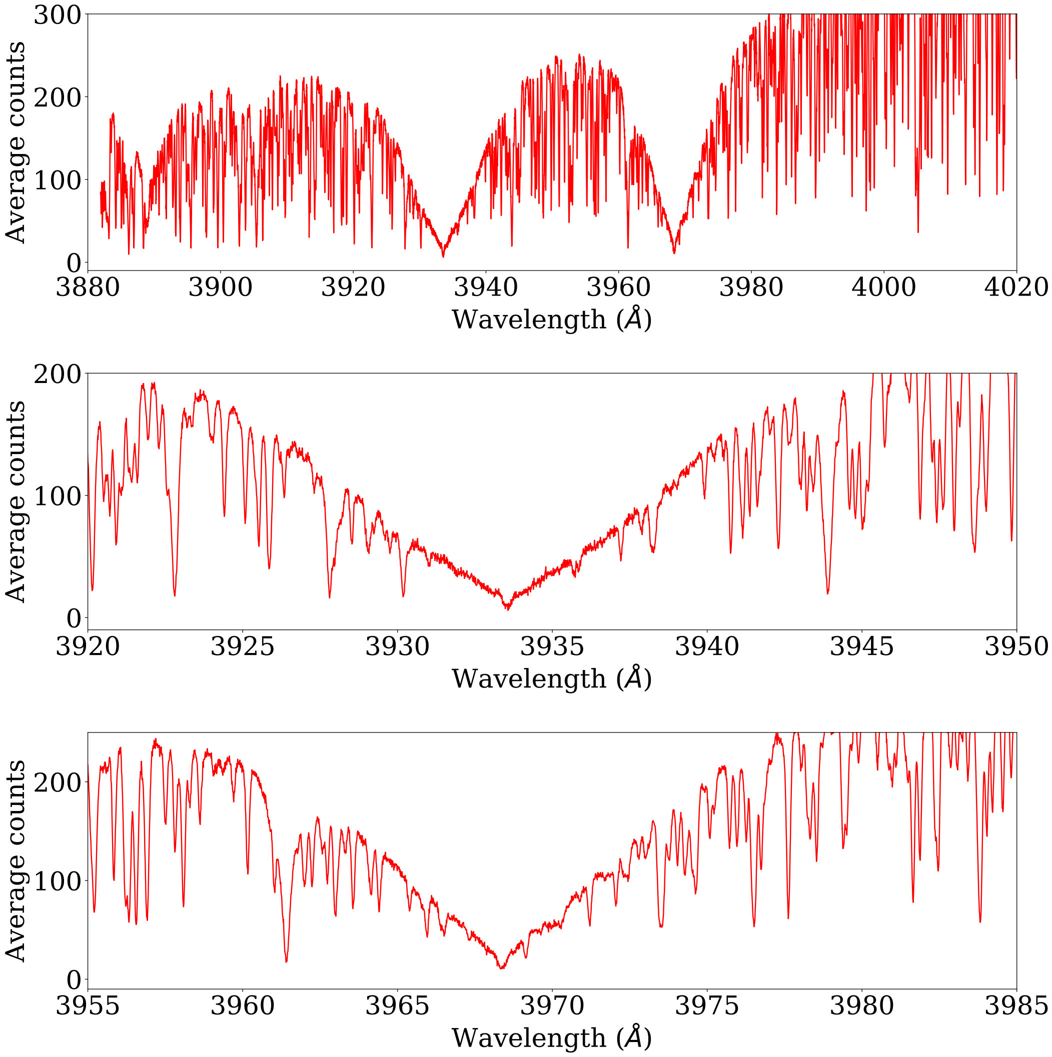

Figure 3.16: High-resolution HARPS spectrum of WASP-94A: Both CaII H&K lines (top) and zoomed in on the two lines (middle: K line with centre at 3933.66 Å, bottom: H line with centre at 3968.47 Å). There is no emission seen in either of the core lines, instead there is a dip visible, resulting in a $\log R'_{\mathrm{HK}}$ value of -5.18 ± 0.27.

by circumstellar material escaping the hot Jupiter atmosphere and absorbing the stellar emission of CaII in the H&K lines. This interpretation is supported by the statistical analysis of a larger sample of stars by Haswell et al. (2020). It is also supported by the fact that a $\log R'_{\mathrm{HK}}$ value this low (and in combination with the colour of the star $B-V = 0.69$) would suggest a rotation period of 40 days and a high age of 8 Gyr (Mamajek & Hillenbrand, 2008). The rotation period was determined by Neveu-Vanmalle et al. (2014) to be 19.5 days, based on their measurement of $v \sin i_*$, the projected stellar rotational velocity. This leads to the conclusion that WASP-94A is most likely enshrouded in gas escaping from its hot Jupiter.

3.8 Conclusions

I have presented a low-resolution optical transmission spectrum of the hot Jupiter WASP-94Ab: the first atmospheric characterisation of this highly-inflated exoplanet. These observations form part of the LRG-BEASTS survey and made use of the EFOSC2 instrument at the ESO NTT, which has not been utilised for transmission spectroscopy previously. The retrieved transmission spectrum from one full transit of WASP-94A covers the wavelength range $4020 - 7140$ Å, with an average transit-depth precision of 128 ppm for ≈ 200 Å wide bins. This corresponds to less than half a scale height in the planetary atmosphere. The binary companion WASP-94B served as an ideal comparison star with very similar brightness and spectral type to WASP-94A, resulting in an average RMS-noise to expected photon noise ratio of 1.15.

I compared two methods for accounting for systematic trends in the light curves, in order to show that my results are insensitive to the choice of detrending model. In the first case I utilised a simple linear detrending approach, while in the second I modelled the noise using a Gaussian Process. For the Gaussian Process, I employed a kernel using sky background and telescope derotator angle as kernel inputs. I also simultaneously fitted all spectroscopic light curves, linking the Gaussian Process hyperparameters for length scales. While this was computationally expensive, I found this approach provided more consistent detrending between wavelength bins and an overall improvement in the precision of the transmission spectrum (from an average of 181 ppm to 128 ppm).

My subsequent analysis of the transmission spectrum reveals sodium absorption in the atmosphere of WASP-94Ab with a significance of 4.9σ. The sodium absorption is visible even in a direct ratio of in- and out-of-transit spectra, and I find evidence for substantial pressure broadening. The detection of strong sodium absorption with probable pressure broadening indicates a clear atmosphere.

In addition, my retrieved transmission spectrum of WASP-94Ab shows a steep blueward slope at short wavelengths. Although my retrievals are consistent with Rayleigh scattering, the best-fitting slope is much steeper. A super-Rayleigh slope might be caused by mineral clouds or photochemical hazes.

Finally, I note that the relatively clear atmosphere of WASP-94Ab combined with the availability of an ideal comparison star makes it a prime target for further atmospheric characterisation, especially abundance measurements in the infrared.

Chapter 4

Transmission Spectroscopy of HATS-46b

Declaration

This chapter is based on the paper published as Ahrer et al. (2023a), but adapted to make my contributions clear and with an additional section on the fringing effects in the stellar spectra and the investigated corrections, Section 4.3. I have led all reduction and analysis within this chapter. Specific contributions from my collaborators were from James Kirk who took the observations prior to the start of my thesis and wrote large parts of the pipeline used in this work (as part of his PhD using a similar technique and telescope). In addition, my collaborators Siddharth Gandhi and Luis Welbanks conducted the atmospheric retrieval analysis, Section 4.4.3.

4.1 The HATS-46 system

This chapter presents the first transmission spectrum of the hot Jupiter HATS-46b as part of the LRG-BEASTS survey. The observations were made using the EFOSC2 instrument on the New Technology Telescope (NTT). HATS-46b was discovered within the HATSouth survey (Bakos et al., 2013) by Brahm et al. (2018). Their photometric observations, together with follow-up Radial Velocity (RV) measurements, confirm HATS-46b, which orbits its G type host star in 4.74 days. Using TESS and *Gaia* data, HATS-46b has been re-characterised by Louden & Hartman (2021) who provided revised planetary and orbital parameters: HATS-46b has a mass of $0.158 \pm 0.042\,\mathrm{M_{Jup}}$ and a radius of $0.951 \pm 0.029\,\mathrm{R_{Jup}}$, orbiting at a distance of 0.05272 ± 0.00045 au; the equilibrium temperature was determined to 1082.1 ± 8.2 K.

Table 4.1: Parameters for the star HATS-46 and its planet HATS-46b, with V_{mag} and spectral type as determined by Brahm et al. (2018) and all other parameters as revised by Louden & Hartman (2021).

Parameter	**Value**
Stellar parameters	
V_{mag}	13.634 ± 0.050
Spectral type	G
Temperature T_{eff} (K)	5451 ± 19
Age (Gyr)	8.4 ± 1.9
Surface gravity $\log g$ ($\log_{10}(\mathrm{cm\,s^{-2}})$)	4.474 ± 0.019
Metallicity [Fe/H]	-0.029 ± 0.039
Mass ($M_{\odot}$)	0.869 ± 0.023
Radius ($R_{\odot}$)	0.894 ± 0.010
Planetary parameters	
Period (d)	4.7423749 ± 0.0000043
Mass (M_{Jup})	0.158 ± 0.042
Radius (R_{Jup})	0.951 ± 0.029
Semi-major axis (au)	0.05272 ± 0.00045
Equilibrium temperature T_{eq} (K)	1082.1 ± 8.2
Inclination (°)	86.97 ± 0.10
Surface gravity log g ($\log_{10}(\mathrm{cm\,s^{-2}})$)	2.64 ± 0.14

Stellar and planet parameters are summarised in Table 4.1. The star HATS-46 does not appear to be active as the RV measurements by Brahm et al. (2018) did not show any evidence for stellar activity. Unfortunately, the signal-to-noise of the RV spectra was not sufficient to place any constraints on the chromospheric activity from the Ca II H&K lines (Brahm et al., 2018). The TESS light curves showed variability, however, these were significantly higher in amplitude in comparison to the HATSouth light curves and thus regarded as not real stellar activity-related variations (Louden & Hartman, 2021).

4.2 Observations

Observations took place with the EFOSC2 instrument (Buzzoni et al., 1984) on the night of 17 August 2017[1]. This is the same telescope and instrument setup as in the previous chapter (Chapter 3). However, a different grism, Grism #13, was used for the HATS-46 spectroscopic measurements, providing a low-resolution ($R \simeq 380$) spectrum from $3900 - 9000$ Å. For further details see also the description

---

[1] Based on observations collected at the European Southern Observatory under ESO programme 099.C-0390(A) (PI: Kirk).

in Section 2.2.

In total, 93 spectral frames were acquired, each with a relatively long exposure time of 240 s due to the relatively faint magnitude of both target ($V_{\mathrm{mag}} = 13.6$) and comparison star ($V_{\mathrm{mag}} = 12.7$). The readout time was 22 seconds. The observations were taken at an airmass ranging from 1.60 to 1.12 to 1.26. The illumination of the moon was at 16% and it only rose towards the very end of the observation night at a distance to the target of 108°.

For calibration, 67 bias frames were acquired, as well as 112 flat frames (54 lamp, 53 sky, 5 dome) and 3 HeAr arc frames, taken at the beginning of the night. While I experimented with using flat frames in my data reduction, I did not use any in my final reduction as I found it to increase the noise in the data. This is in line with previous reports of similar analyses, for example by the LRG-BEASTS and ACCESS surveys (e.g. Rackham et al., 2017; Bixel et al., 2019; Weaver et al., 2020; Kirk et al., 2021), see also discussion in Kirk (2018).

A nearby star (UCAC4 169-000364) at a distance of 1 arcmin to the target star HATS-46 served as a comparison star and is not known to be a variable star. The two stars are a good match in both magnitude ($\Delta V_{\mathrm{mag}} = 0.87$) and colour ($\Delta(B - V) = 0.09$), thus well-suited for differential spectrophotometry. HATS-46 is the less bright and slightly bluer star.

4.3 Data Reduction

LRG-BEASTS observations are commonly reduced using a custom-built `Python` pipeline, which is described in detail by Kirk et al. (2018). The data for HATS-46 have been reduced following this pipeline, but with modifications to the cosmic ray removal and wavelength calibration, introduced in Ahrer et al. (2022) which is described in the previous chapter in Section 3.4. In the following I summarise the reduction steps.

First, the biases were median-combined to produce a master bias. When executing the `Python` script for extracting the spectra from each science frame the master bias is subtracted from each science frame. However, before extracting the spectra from the individual frames, pixels affected by cosmic rays were identified and replaced with the median of the surrounding pixels.

An aperture width of 32 pixels was applied to extract the spectral counts from each star. To fit the sky background I used a second order polynomial, which was fitted to regions of 50 pixels either side of the stars at a distance of 5 pixels from the edge of the aperture. Outliers of more than three standard deviations were masked from the fit. Extracted properties such as airmass, pixel shift along the slit, Full Width Half Maximum (FWHM), normalised sky background and differential white-light flux and their changes throughout the night are displayed in Fig. 4.1. Example spectra are plotted in Fig. 4.2.

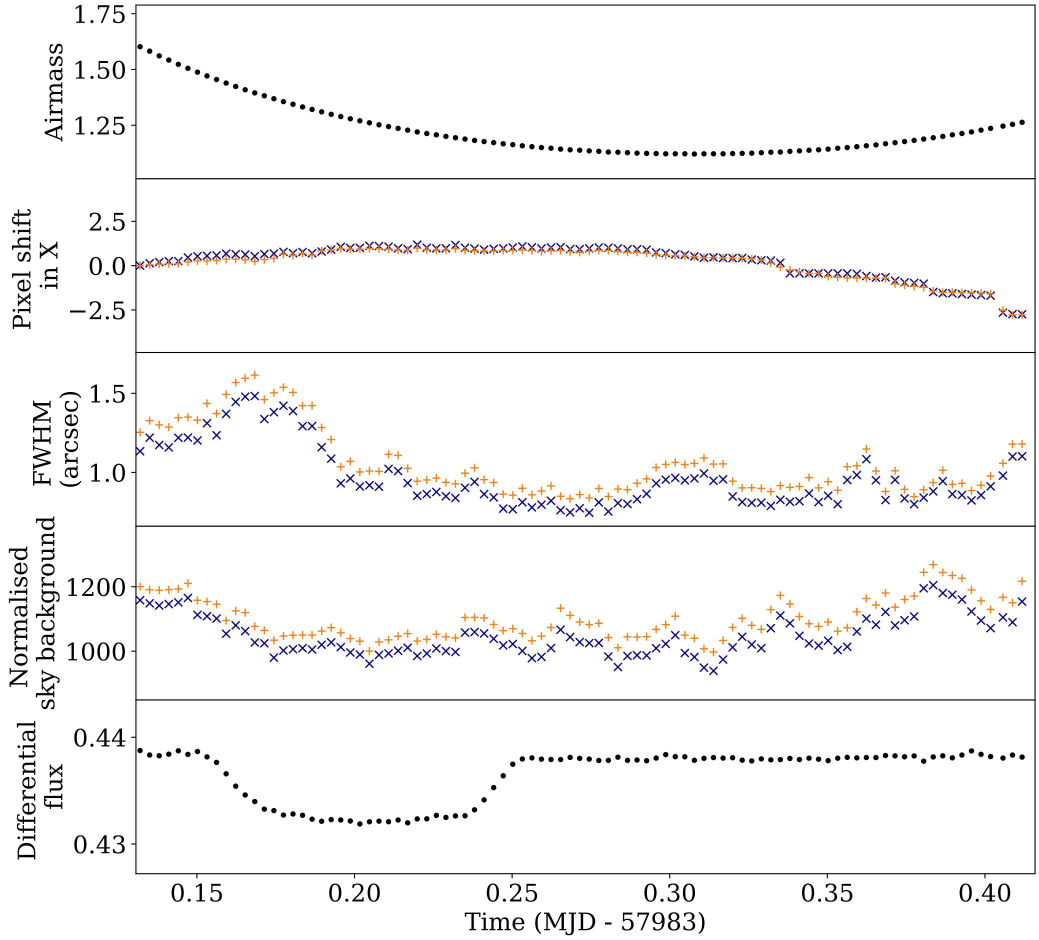

Figure 4.1: From top to bottom: variations of airmass, pixel shift along the X axis, FWHM, sky background and differential flux across the night. In the middle panels, the target is indicated with dark blue X symbols, and the comparison star with orange + symbols.

Wavelength calibration follows the spectral extractions and is a two-step process. First, `RASCAL` (Veitch-Michaelis & Lam, 2019) was utilised to find a wavelength solution using the HeAr arc frames. The second step is to optimise the wavelength calibration by fitting the positions of the stellar absorption lines in each frame, adjusting the solution, and then saving the wavelength solution for each frame individually. This allowed me to account for wavelength drifts between the frames throughout the night, which were of the order of ≈ 5 pixels or ≈ 20 Å.

Lastly, the spectra were binned into 26 wavelength bins, computed by summing the flux within the corresponding wavelength range of each frame and dividing by the comparison star's flux in the same wavelength bin to correct for the effects of the Earth's atmosphere. Similarly, a white-light light curve was computed by defining one single bin across the whole wavelength range. Bin widths of ≈ 200 Å (avoiding edges of strong stellar absorption lines) were applied across the whole spectral range, with the exception of two small ranges where I searched for absorption by sodium and potassium, see Fig. 4.2.

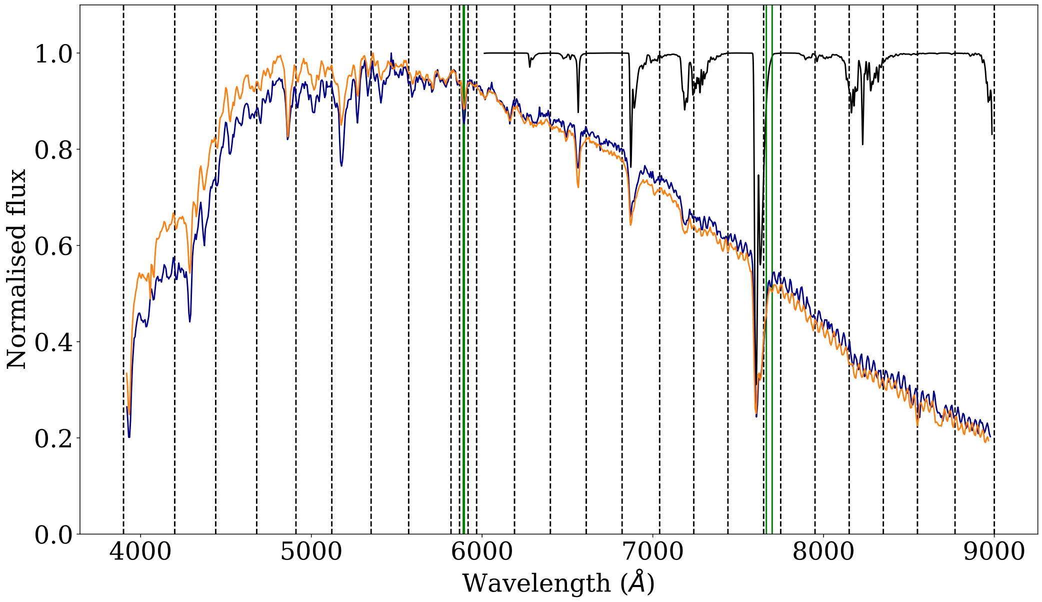

Figure 4.2: Normalised spectra of comparison star (orange) and target star (dark blue), as well as the expected strong telluric lines (black) in the redder part of the wavelength range. Wavelength bin edges are indicated with dashed black lines. Green lines indicate the position of the sodium doublet (5890, 5895 Å) and potassium doublet (7665, 7699 Å).

Fringing effects

Observations with EFOSC2 at wavelengths > 7200 Å are subject to fringing effects, see Fig. 4.3. I found that correcting for these effects in the individual spectra using flat fields was not possible as the fringing changed in amplitude and phase during the night, see Fig. 4.3, and the acquired flat frames were taken before the observations started.

I investigated whether the fringing effects could be modelled using Gaussian

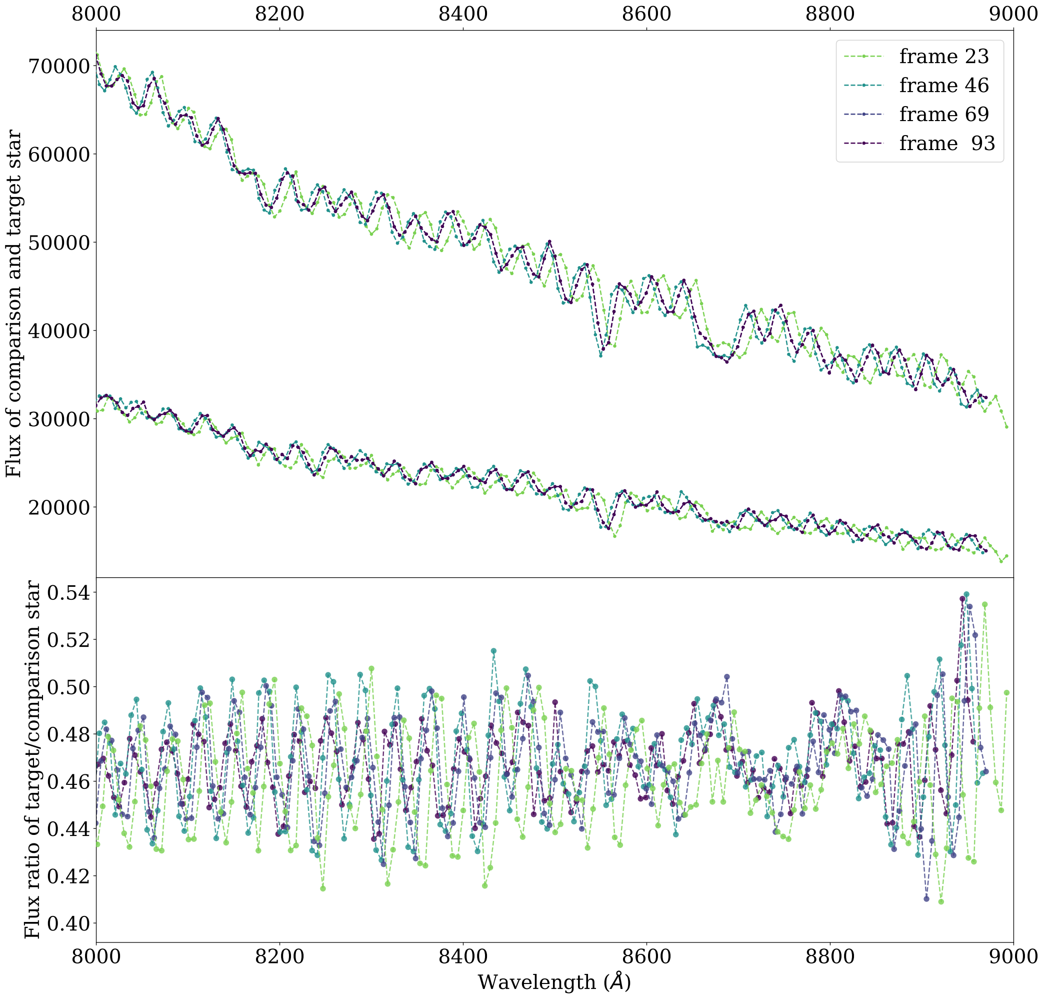

Figure 4.3: Example stellar spectra of comparison (higher flux) and target star HATS-46 over the course of the night (top panel) demonstrating the changes in the fringing effect behaviour.The bottom panel shows the individual frames' respective flux ratios between the two stars, showing that the fringing is still visible after the division of the comparison star is performed (differential spectroscopy) and also varies over time, particularly in the red end of the spectrum.

Process (GP), i.e., by fitting a linear function to the spectra and a GP model for capturing the fringing and other trends, and removing the fringing component from the spectra before binning and light curve extraction.

The GP models I used were sinusoidal kernel for the fringing combined with an exponential kernel for the almost but not quite linear trend. I investigated multiple variations of fitting: (1) fitting a simultaneous linear model instead of a GP trend, (2) fit the slope of the spectrum first and fix it, then fit the fringing variations on top, (3) different combinations of GP kernels, (4) including vs excluding the telluric feature in the middle. An example spectrum of the affected region and the fringing-corrected flux is shown in Fig. 4.4, as well as the removed GP component. In this case, the telluric was cut out so it would not be fitted by the GP and influence the GP fitting to the rest of the spectrum.

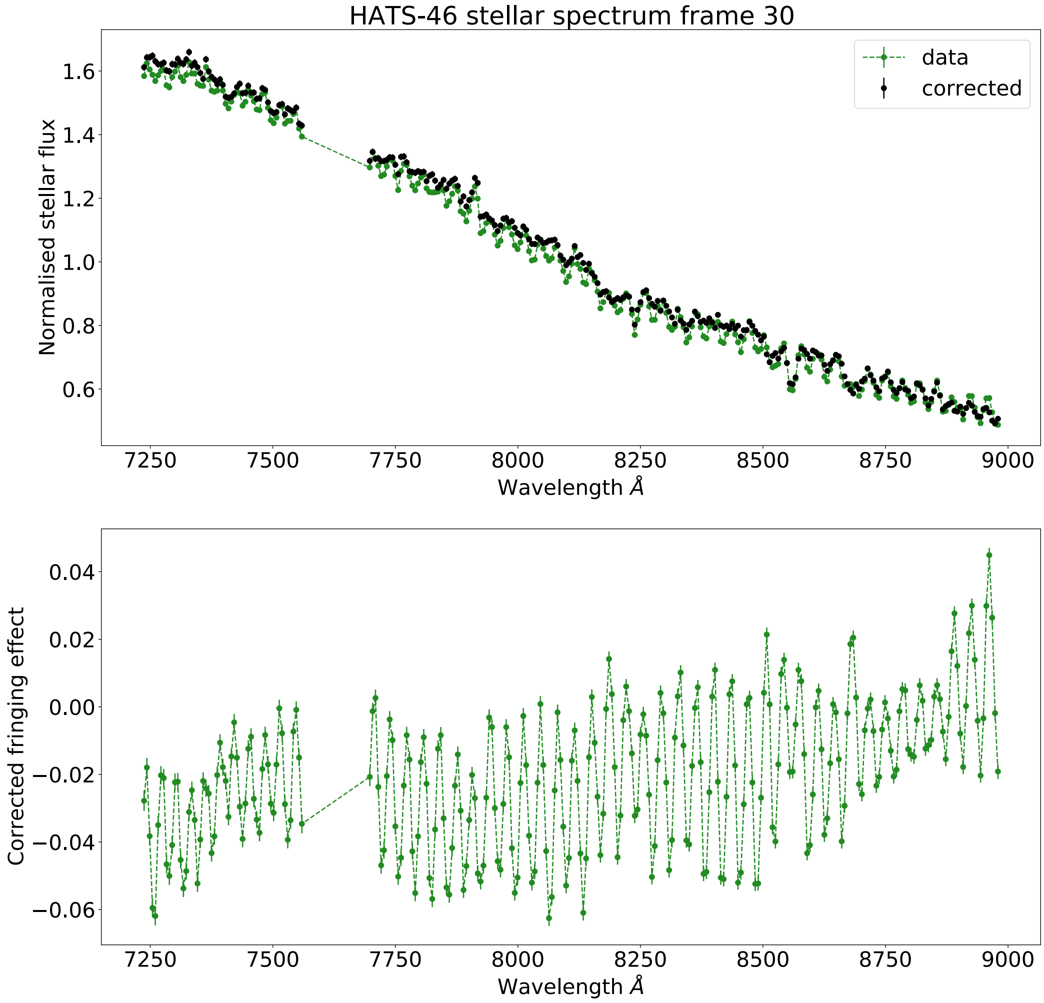

Figure 4.4: Stellar spectrum of HATS-46 in the redder part of the wavelength range of NTT/EFOSC2 grism #13. Top: the raw stellar spectrum (black) and the fringing-corrected data (green) using a sinusoidal GP kernel. Bottom: the corrected fringing effect, i.e. equal to the difference between the two spectra in the top panel.

Even though the fitting seemed to work well in fitting and removing the fringing effects, there was an added uncertainty due to the removal of the GP component which in turn meant that the transmission spectrum and the light curve fitting was not improved. In addition the fringing effect removal introduced systematic noise that was individual to the star's stellar spectrum and to the frame. In turn the transmission spectrum of HATS-46b looked different in these wavelength ranges, see Fig. 4.5

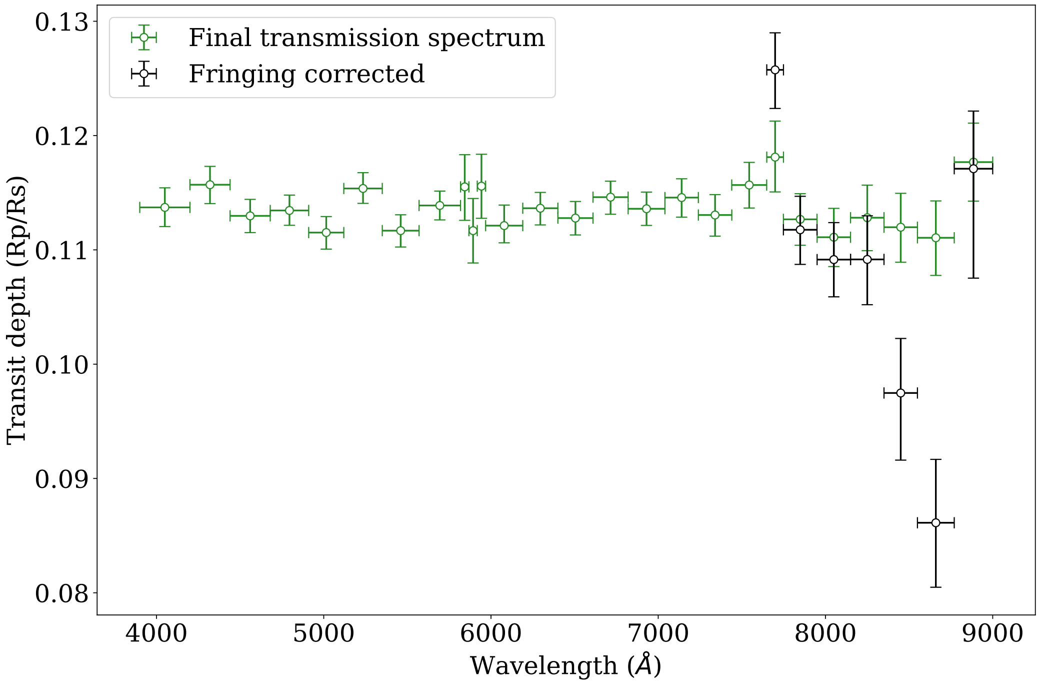

Figure 4.5: Transmission spectrum with and without fringing effects using a GP, with identical light curve fitting parameters. This clearly suggests some introduced systematic noise due to the fringing correction, potentially due to changes in stellar and/or telluric lines throughout the night that are not fully capture. This supports the decision to not move forward with the corrected spectrum.

This method may potentially be further improved by fitting all affected stellar areas at the same time and quantifying the correlations between them. However, I decided to not utilise the fringing-corrected spectra for the final analysis of HATS-46b.

4.4 Data Analysis

4.4.1 Transit model

Each transit light curve was described using the `batman` `Python` package (Kreidberg, 2015) in combination with the analytic light curves from Mandel & Agol (2002) and fitted using the nested sampling algorithm `PolyChord` (Handley et al., 2015b). First, the white-light light curve was fitted using the ratio of planet to star radius

$R_\mathrm{p}/R_\mathrm{s}$, the inclination of the system i, the scaled stellar radius a/R_s, the time of mid-transit T_C and the two limb-darkening coefficients $u1$ and $u2$. I computed the quadratic limb-darkening coefficients with the Limb-Darkening Toolkit (`LDTk`) package (Parviainen & Aigrain, 2015), which uses `phoenix` models (Husser et al., 2013) based on the stellar parameters to determine $u1$ and $u2$ and their errors. One of them ($u2$) was held fixed to the generated value to avoid degeneracy, while the other one was fitted for ($u1$) using a uniform prior with four times the generated error (see Table 4.2) to allow for small inconsistencies between the stellar model and the observation. This quadratic limb-darkening law provides a good fit to the data, see Section 4.4.2, and the fitted values for $u1$ were consistent with the model prediction, see Fig. 4.6. The Kipping parameterisation (Kipping, 2013) was also tested to check for potential effects in the transmission spectrum due to the chosen limb-darkening parameterisation, but I can confirm that this is not the case.

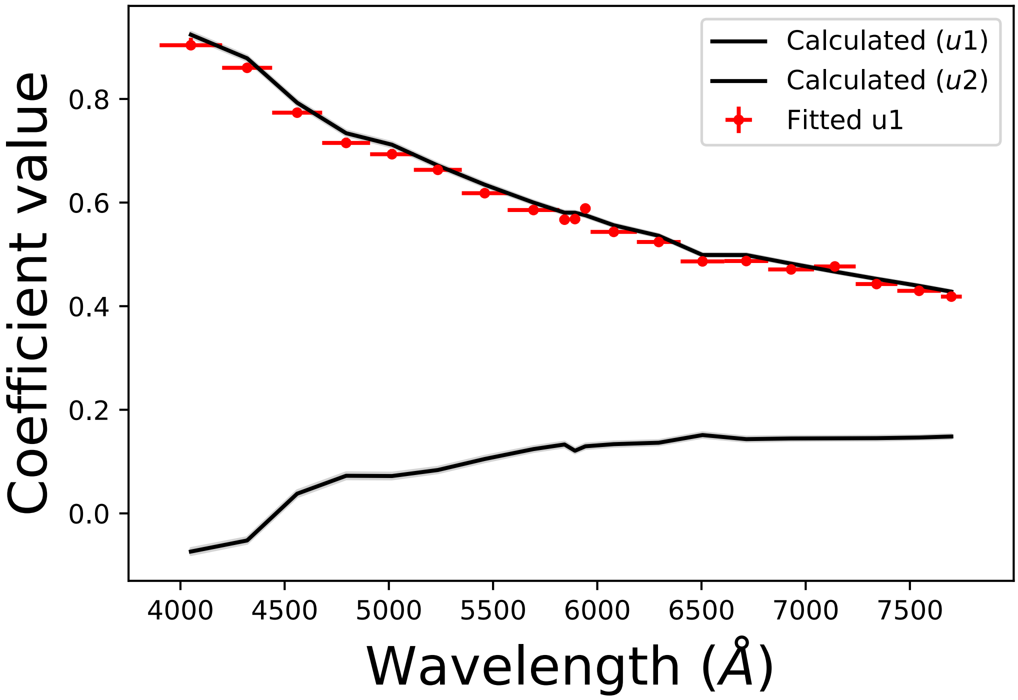

Figure 4.6: Calculated quadratic limb-darkening coefficients $u1, u2$ in black, while the fitted $u1$ are shown in red to demonstrate the overlap.

All priors for the system parameters can be found in Table 4.2, which were chosen to be uniform and wide ($\pm 5\sigma$) centred on the previously reported literature values (Table 4.1; Louden & Hartman, 2021). Depending on the detrending method, additional parameters were added to the fitting (introduced in the following section).

Table 4.2: Parameters for the white-light curve fitting and their respective priors. Values for semi-major axis a, radius of the star R_{s} and radius of the planet R_{p} and inclination i are listed in Table 4.1.

Parameter	Prior distribution and range	
Scaled stellar radius a/R_{s}	Uniform	$a/R_{\mathrm{s}} \pm 5\sigma_{a/R_{\mathrm{s}}}$
Inclination i (°)	Uniform	$i \pm 5\sigma_i$
Time of mid-transit T_{C} (BJD)	Uniform	$0.9 \times\ T_{\mathrm{C}}$, $1.1 \times\ T_{\mathrm{C}}$
Transit depth $R_{\mathrm{p}}/R_{\mathrm{s}}$	Uniform	$R_{\mathrm{p}}/R_{\mathrm{s}} \pm 5\sigma_{R_{\mathrm{p}}/R_{\mathrm{s}}}$
Limb-darkening coefficient $u1$	Uniform	$u1 \pm 4\sigma_{u1}$
Limb-darkening coefficient $u2$	Fixed	–

Table 4.3: Parameter values obtained from the white-light curve fitting. The retrieved values for the parameters a/R_{s}, i and T_{C} listed here were fixed for the spectroscopic light curve fitting.

Parameter	Fitted values
Scaled stellar radius a/R_{s}	$13.94^{+0.24}_{-0.65}$
Inclination i (°)	$87.60^{+0.12}_{-0.33}$
Time of mid-transit T_{C} (BJD)	$2457983.70725^{+0.00046}_{-0.00033}$
Transit depth $R_{\mathrm{p}}/R_{\mathrm{s}}$	$0.11250^{+0.0.0018}_{-0.00083}$
Limb-darkening coefficient $u1$	0.547 ± 0.014
Limb-darkening coefficient $u2$	0.1171

The determined values for a/R_{s}, i and T_{C} from the white-light light curve fitting (Table 4.3) were then held fixed for the spectroscopic light curve fitting, which allowed us to fit for relative changes in transit depths over the wavelength range. Thus the fitting parameters for each of the 26 binned light curves were transit depth $R_{\mathrm{p}}/R_{\mathrm{s}}$, limb-darkening coefficient $u1$ and additional noise modelling parameters.

4.4.2 Light curve fitting

For detrending the white-light light curve, various different approaches were investigated e.g. different combinations of kernels and kernel inputs for a GP, 1st and 2nd order polynomials using airmass, FWHM, derotator angle, etc. However, all of these models retrieved very low amplitudes for their respective noise modelling, e.g. see amplitude of the best-fitting GP model in top panel in Fig. 4.7 which is 0.062 % compared to the transit depth of 1.287 %. In addition, the Bayesian evidence values for each of these fits did not statistically favour a particular GP model or parametric fitting model. The differences across all wavelengths in Bayesian evidences averaged at 0.5 (0.67σ) and never exceeded 1 ($< 1.15\sigma$). Consequently, I opted to use only a linear dependence on the FWHM for detrending the white-light light curve, see bottom panel in Fig. 4.8.

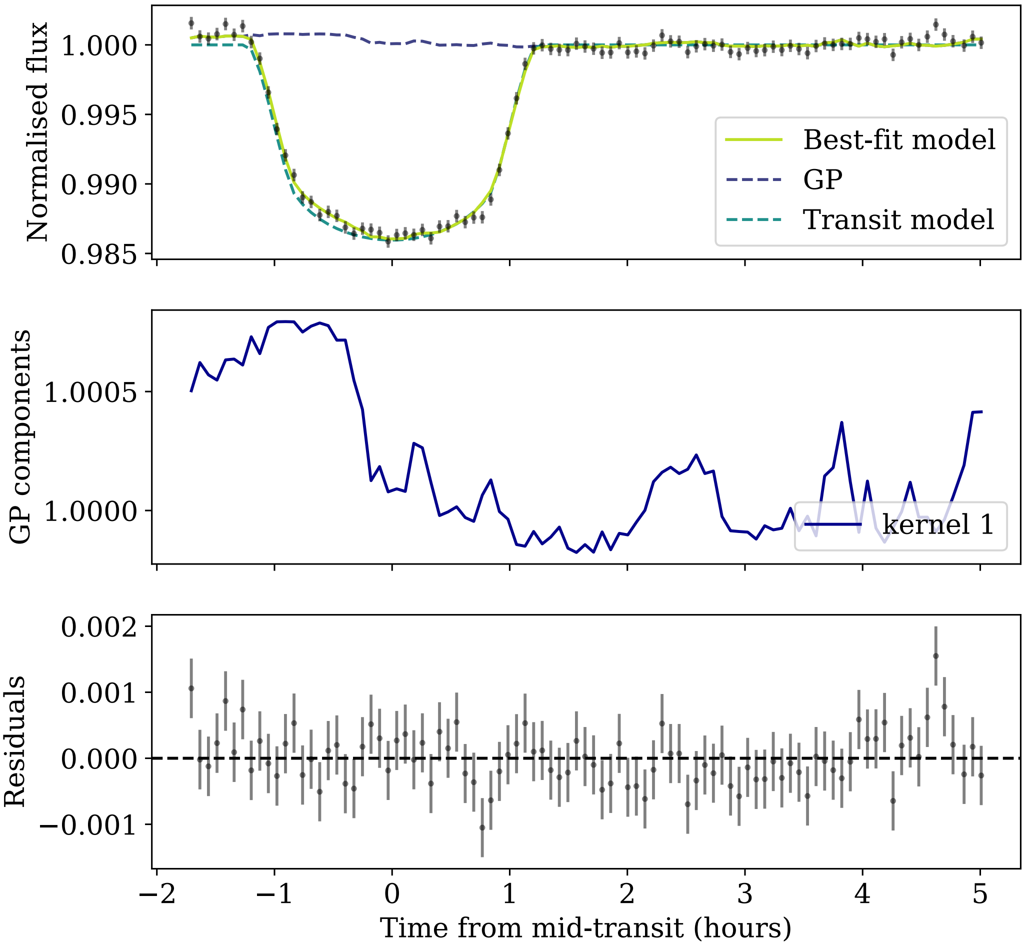

Figure 4.7: White-light light curve fitted with a transit model and a GP to account for systematics. The top panel shows the fitted light curve in red, the data in black and the GP systematics model in green. The middle panel in displays the GP components of the systematics model in blue, while the bottom panel shows the residuals of the fit.

To determine the transit depths for each wavelength bin, I fitted the individual light curves of the 26 bins with a transit model and a detrending model. I conducted an investigation of the systematics modelling, similar to the one done for the white-light light curve fit. This was to ensure that the transmission spectrum is independent of the choice of noise modelling, and to provide the best estimate of the uncertainties.

The light curves show exceptionally little systematic noise such as drifts or correlated noise, see left panel in Fig. 4.9 for the raw light curves. I experimented

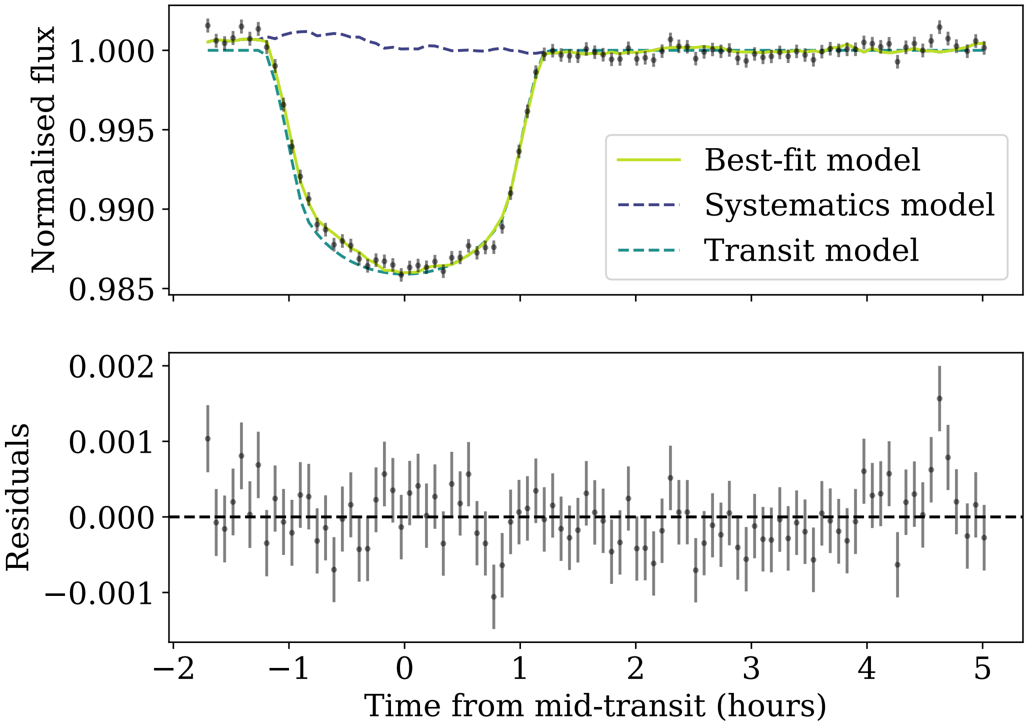

Figure 4.8: White-light light curve fitted with a transit model and a linear in FWHM to account for systematics. The top panel shows the fitted light curve in red, the data in black and the systematics model in dashed gray. Bottom panel: the residuals of the fit.

with simple models to account for the small noise amplitudes, as well as using a transit model without any systematic modelling at all. First, linear models in time, airmass and FWHM were investigated, with the linear in FWHM performing the best according to the Bayesian evidence value of each spectroscopic light curve fit and an average fitted noise amplitude of 0.06% or 600 ppm. In addition, I looked into GP models and sampled different types of kernels and kernel input, out of which the exponential-squared model with FWHM as input resulted in the best choice, with an average fitted GP amplitude of 0.03% or 300 ppm. As both the linear in FWHM and GP model resulted in similar transit depths and small noise amplitudes, I chose the first, parametric model over the GP model due to its lower uncertainties in the transit depths. This results in an average precision of transit depth error equal to 1.03 × photon noise. The light curves and respective fits are shown in Fig. 4.9, as well as the residual scatter of the fits and their respective Root Mean Square (RMS) values.

The previously described models all favoured only small variations and FHWM

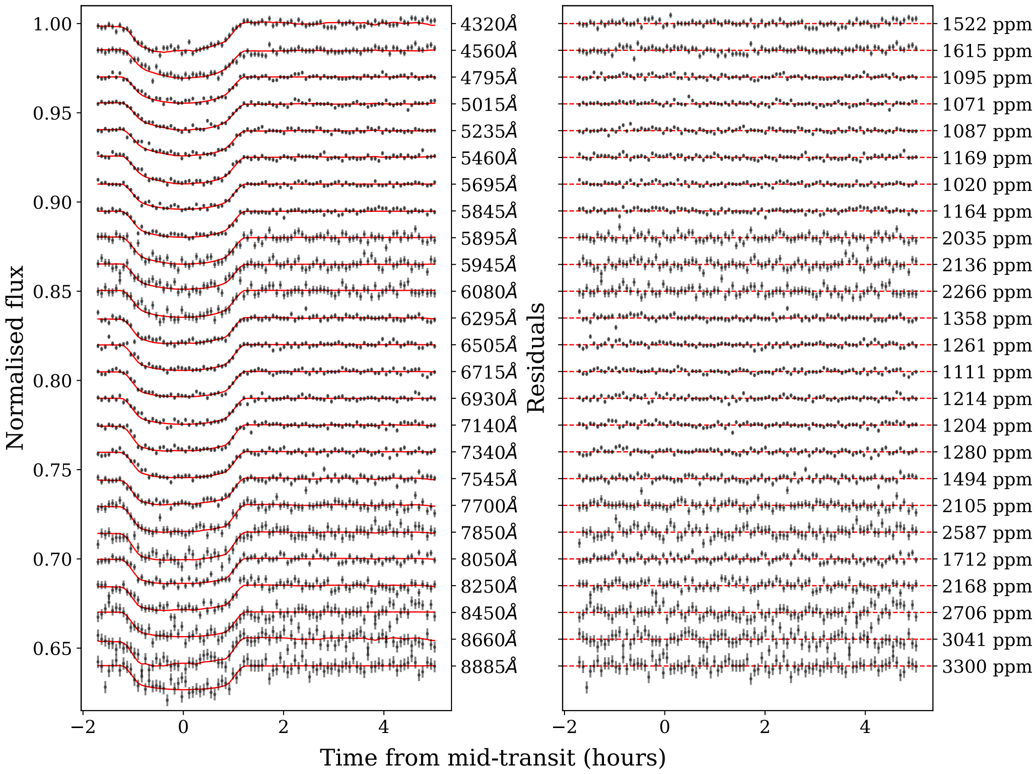

Figure 4.9: Left: My fits (red) of the undetrended spectroscopic light curves (black) using a transit model and a linear in FWHM for detrending to the data with their respective centre wavelengths (blue end at the top) displayed on the right vertical axis. Right: Residuals of the corresponding light curve fitting. The scatter is quantified in the form of the RMS on the right vertical axis.

as the detrending source for all spectroscopic bins. This led us to investigate using a common noise model (e.g. as used in Sing et al., 2012; Gibson et al., 2013; Lendl et al., 2016; Nikolov et al., 2016; Nortmann et al., 2016; Huitson et al., 2017; Todorov et al., 2019; Wilson et al., 2020; Kirk et al., 2021; McGruder et al., 2022) in the hope of reducing the uncertainties and getting rid of common noise structures potentially dominating the systematics. In this method the GP component from the white-light light curve fit is subtracted from the spectroscopic light curves before fitting them individually. However, this did not have the desired effect of improving the noise modelling and on average resulted in larger uncertainties. Therefore I did not pursue this method further.

All computed transmission spectra using the GP model, the polynomial model, the common noise model and one without any detrending at all i.e. solely a transit model, are shown in Fig. 4.10. This demonstrates that my resulting transmission spectrum is independent of my choice of noise modelling. Following the points made above about each detrending approach, I selected a simple polynomial model, 'Linear in FWHM', as the preferred detrending method. The final transmission spectrum in tabular form is displayed in Table 4.4. Note that for my final spectrum I chose to dismiss the relatively large transit depth of the bin centred on the potassium doublet due the high chance of it being affected by the nearby strong telluric signal (O_2 A-band). Other studies in the past have come to similar conclusions when probing for potassium absorption with ground-based instruments (e.g. Kirk et al., 2017; McGruder et al., 2022).

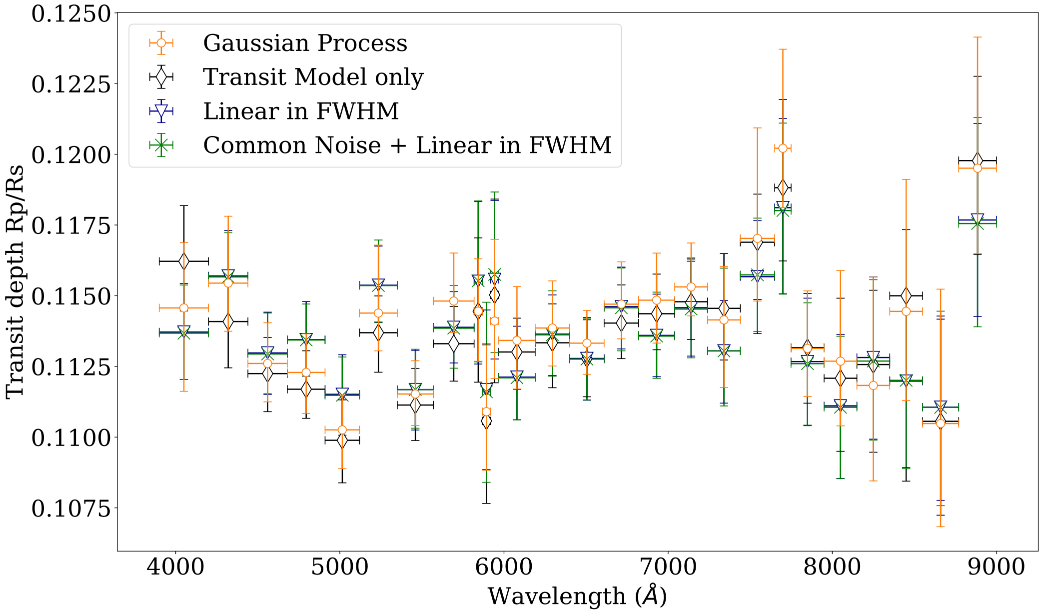

Figure 4.10: Transmission spectra of HATS-46b using NTT/EFOSC2 observations. Median precisions of transit depths for ≈ 200 Å wide bins are quoted in brackets in the description respectively. The orange and blue colours represent the resulting transmission spectrum using Gaussian Process (387 ppm) and a linear in FWHM (357 ppm) to account for systematics modelling, respectively. The black represents the case for when not using any noise modelling i.e. solely a transit model (326 ppm). The green indicates a model where the GP component fitted to the white-light light curve was subtracted (common noise model) from the spectroscopic light curves and then a linear in FWHM was used to fit residual systematics (358 ppm). The 'Linear in FWHM' transmission spectrum is used for the retrieval analysis (see text for further details), but note that the bin centred on the potassium doublet (7665, 7699 Å) is not included as it is affected by the close-by strong telluric O_2 line.

Table 4.4: Retrieved transmission spectrum of HATS-46b in tabulated form using the 'Linear in FWHM' detrending approach, as plotted in Fig. 4.10, excluding the bin centred on the K doublet.

Bins (Å)	$R_\mathrm{p}/R_\mathrm{s}$	u1	u2 (fixed)
3900 - 4200	$0.1137^{+0.0018}_{-0.0017}$	0.92 ± 0.02	-0.0737
4200 - 4440	0.1157 ± 0.0017	0.87 ± 0.02	-0.0523
4420 - 4680	0.1130 ± 0.0015	0.79 ± 0.02	0.0380
4680 - 4910	$0.1134^{+0.0014}_{-0.0013}$	0.73 ± 0.02	0.0726
4910 - 5120	$0.1115^{+0.0014}_{-0.0015}$	0.71 ± 0.02	0.0721
5120 - 5350	0.1154 ± 0.0014	0.67 ± 0.02	0.0837
5350 - 5570	$0.1117^{+0.0014}_{-0.0015}$	0.63 ± 0.01	0.1050
5570 - 5818	0.1139 ± 0.0013	0.59 ± 0.01	0.1241
5818 - 5868	$0.1155^{+0.0029}_{-0.0030}$	0.58 ± 0.01	0.1330
5868 - 5918	0.1117 ± 0.0029	0.58 ± 0.01	0.1209
5918 - 5968	$0.1156^{+0.0028}_{-0.0029}$	0.58 ± 0.01	0.1295
5968 - 6190	$0.1121^{+0.0018}_{-0.0016}$	0.55 ± 0.01	0.1336
6190 - 6400	$0.1136^{+0.0014}_{-0.0015}$	0.53 ± 0.01	0.1364
6400 - 6610	0.1128 ± 0.0015	0.50 ± 0.01	0.1512
6610 - 6820	0.1146 ± 0.0015	0.50 ± 0.01	0.1433
6820 - 7040	0.1136 ± 0.0015	0.48 ± 0.01	0.1446
7040 - 7240	$0.1146^{+0.0017}_{-0.0018}$	0.47 ± 0.01	0.1449
7240 - 7440	$0.1130^{+0.0018}_{-0.0019}$	0.45 ± 0.01	0.1452
7440 - 7649	$0.1157^{+0.0020}_{-0.0021}$	0.44 ± 0.01	0.1464
7749 - 7950	0.1127 ± 0.0023	0.42 ± 0.01	0.147
7950 - 8150	0.1111 ± 0.0026	0.42 ± 0.01	0.1476
8150 - 8350	0.1128 ± 0.0029	0.40 ± 0.01	0.1482
8350 - 8550	$0.1120^{+0.0030}_{-0.0031}$	0.38 ± 0.01	0.1474
8550 - 8770	0.1111 ± 0.0033	0.37 ± 0.01	0.1488
8770 - 9000	0.1177 ± 0.0035	0.37 ± 0.01	0.1494

4.4.3 Atmospheric Retrieval

My collaborators retrieved the transmission spectrum of HATS-46b using the HyDRA (Gandhi & Madhusudhan, 2018) and Aurora (Welbanks & Madhusudhan, 2021) atmospheric retrieval codes. Their model uses 14 free parameters which describe the atmospheric composition, thermal profile and cloud/haze properties (shown in Table 4.5) to generate spectra of HATS-46b to compare against the observations. They used high temperature molecular line lists to compute the cross sections and hence opacity for the spectrally active species, utilising the Kurucz line list for the atomic species Na and K (Kurucz & Bell, 1995), and the ExoMol POKAZATEL line list for H_2O (Tennyson et al., 2016; Polyansky et al., 2018). They spectrally broaden each line in the line list with both pressure and temperature, resulting in a Voigt profile (see e.g. Gandhi et al., 2020). They also include collisionally induced absorption from H_2-H_2 and H_2-He interactions (Richard et al., 2012), as well as Rayleigh scattering due to H_2.

In addition to these sources of opacity we also include 4 free parameters to model and fit for a partially cloudy and/or hazy atmosphere, as any clouds/hazes can have a strong influence on the overall spectrum. We include a grey (wavelength independent) cloud deck, P_{cl}, and two parameters which determine a wavelength dependent haze, with α_{haze} the strength and γ_{haze} the wavelength dependence of the haze (see e.g., Pinhas et al., 2018). Finally, we include the cloud/haze fraction, ϕ_{cl}, as a free parameter, with the prior ranging from 0, representing a clear atmosphere, to 1, a fully cloudy/hazy atmosphere (see Table 4.5).

My collaborators model the temperature profile of the atmosphere using the method described in Madhusudhan & Seager (2009). This parametrisation breaks the atmosphere into three distinct layers, with the temperature at the top of the model atmosphere included as a free parameter. They also retrieve the transition pressures P_1 between the top layers 1 and 2 and P_3 between layers 2 and 3. The top two layers have temperature-pressure gradients α_1 and α_2 as free parameters. The final deepest layer of the atmosphere is fixed to an isotherm, and continuity of the temperature between these layers results in 6 free parameters for the temperature profile. We restrict our parametrisation to only allow non-inverted or isothermal temperature profiles given that we do not expect stratospheres for planets with such temperatures (e.g. Fortney et al., 2008), similar to previous work with transmission retrievals (e.g. Pinhas et al., 2019). We also include an additional free parameter for the reference pressure, P_{ref}, the point in the atmosphere where the radius of the planet is set. We model the atmosphere between 100-10^{-6} bar with 100 layers evenly spaced in log pressure, and model the spectrum with 4000 wavelength points between 0.39-0.9 µm. Our Bayesian analysis is carried out using the Nested Sampling algorithm MultiNest (Feroz & Hobson, 2008; Feroz et al., 2009; Buchner et al., 2014).

The retrieved constraints are shown in Table 4.5, and the posterior distribution is shown in Fig. 4.12. For their retrievals we considered two competing scenarios: a cloudy/hazy atmosphere and a relatively-clear atmosphere. The first case, where clouds mask atomic and molecular species in the transmission spectrum of HATS-46b, is statistically preferred to 3.0σ due to the relatively featureless spectrum, when using Bayesian model evidence comparisons (e.g., Benneke & Seager, 2013; Welbanks & Madhusudhan, 2021).

In the alternative, less statistically preferred scenario of a clear atmosphere, where clouds do not mask the atomic and molecular species, we can place constraints on the abundance of K and Na. There is no visible feature of Na in the spectrum, hence we place an upper limit on Na abundance of $\log(\mathrm{Na}) < -4.45$ to 3σ, i.e., less than 20×solar Na abundance for this cloud-free scenario.

This is a conservative upper limit, since the lack of features in the transmission spectrum drives the atmospheric temperatures in the model to the lower end of the prior, which decreases the atmospheric scale height and thereby the strength of features. There is therefore a degeneracy between temperature and abundance, and an atmospheric temperature closer to the equilibrium temperature would give a tighter limit on abundance.

Additionally, we assess the impact of unnoculted star spots and faculae in the transmission spectrum of HATS-46b using Aurora (Welbanks & Madhusudhan, 2021). We allow for the possibility of a contaminated stellar photosphere and retrieve for three additional parameters to the fiducial model described above. These are, the photospheric temperature (Gaussian prior centred at the effective temperature of the star and a width of 100 K), the fraction of unnoculted spots or faculae (uniform prior between 0 and 50 %), and the temperature of these inhomogeneities (uniform prior from 0.5 to 1.5 times the effective temperature of the star). Priors are in line with what is recommended by Pinhas et al. (2018). The retrieved properties stellar properties are in agreement with the possibility of a spotless star. The retrieved photospheric temperature of HATS-46 is consistent with the reported value in Table 4.1, with a relatively low fraction of spots (i.e., 2σ upper limit of $\lesssim 22\%$) with temperatures consistent with the photospheric stellar temperature at 2σ. The presence of stellar heterogeneities is not preferred since its Bayesian evidence value is lower relative to our fiducial model. Based on these observations and the models considered here, we find no evidence for stellar contamination affecting our observations.

4.5 Discussion & Conclusions

I presented the analysis and results of spectroscopic NTT/EFOSC2 data of HATS-46b in transmission. The inflated, Jupiter-sized exoplanet orbits its relatively faint ($V_{\mathrm{mag}} = 13.6$) G type host star in a 4.7-day period and has an equilibrium temperature of 1100 K (Louden & Hartman, 2021).

One transit was observed with NTT/EFOSC2 using the method of long-slit spectroscopy and a comparison star was used to conduct differential spectroscopy. A total of 93 spectral frames with exposure times of 240 s were acquired. The

Parameter	**Prior Range**	**Retrieval Constraint**
$\log(X_{\mathrm{H_2O}})$	-15 → -1	$-8.4^{+4.8}_{-4.2}$
$\log(X_{\mathrm{Na}})$	-15 → -1	$-10.1^{+3.5}_{-3.0}$
$\log(X_{\mathrm{K}})$	-15 → -1	$-8.6^{+3.3}_{-4.0}$
T_{top} / K	750 → 2500	1167^{+530}_{-300}
$\alpha_1\,/\,\mathrm{K}^{-\frac{1}{2}}$	0 → 1	$0.67^{+0.21}_{-0.23}$
$\alpha_2\,/\,\mathrm{K}^{-\frac{1}{2}}$	0 → 1	$0.61^{+0.25}_{-0.27}$
$\log(P_1/\mathrm{bar})$	-6 → 2	-1.7 ± 1.7
$\log(P_2/\mathrm{bar})$	-6 → 2	$-4.1^{+1.6}_{-1.3}$
$\log(P_3/\mathrm{bar})$	-2 → 2	$0.60^{+0.90}_{-1.35}$
$\log(P_{\mathrm{ref}}/\mathrm{bar})$	-4 → 2	$-2.51^{+1.02}_{-0.86}$
$\log(\alpha_{\mathrm{haze}})$	-4 → 6	$-0.0^{+2.8}_{-2.5}$
γ_{haze}	-20 → -1	$-11.3^{+6.3}_{-5.5}$
$\log(P_{\mathrm{cl}}/\mathrm{bar})$	-6 → 2	$-4.42^{+1.24}_{-0.94}$
ϕ_{cl}	0 → 1	$0.79^{+0.13}_{-0.19}$

Table 4.5: Parameters and uniform prior ranges for our retrieval. We retrieve the Na, K and H_2O abundances, temperature profile, and partial cloud/haze parameters. Our temperature profile includes 6 free parameters, and our cloud/haze parametrisation includes 4 free parameters (see Section 4.4.3).

resulting light curves did not show noise structures beyond a weak dependence on seeing, with fitted average amplitudes of 600 ppm for our best noise model, which included a linear detrend against FWHM.

I extracted the transmission spectrum in 26 bins, covering the wavelength range of $3900 - 9000\,\text{Å}$ with a median transit depth uncertainty of 357 ppm (compared to its calculated atmospheric scale height of 310 ppm) for the $\approx 200\text{Å}$ wide bins. Fringing effects resulted in noisier spectroscopic light curves and larger uncertainties for the fitted transit depths at wavelengths $> 7200\,\text{Å}$.

The measured transmission spectrum is relatively featureless, it does not show a sodium feature or a scattering slope. The fitted, relatively large transit depth at the wavelength of the potassium doublet was dismissed as an effect of the nearby strong telluric signal due to the O_2 *A*-band.

My collaborator's atmospheric retrieval analysis of the transmission spectrum

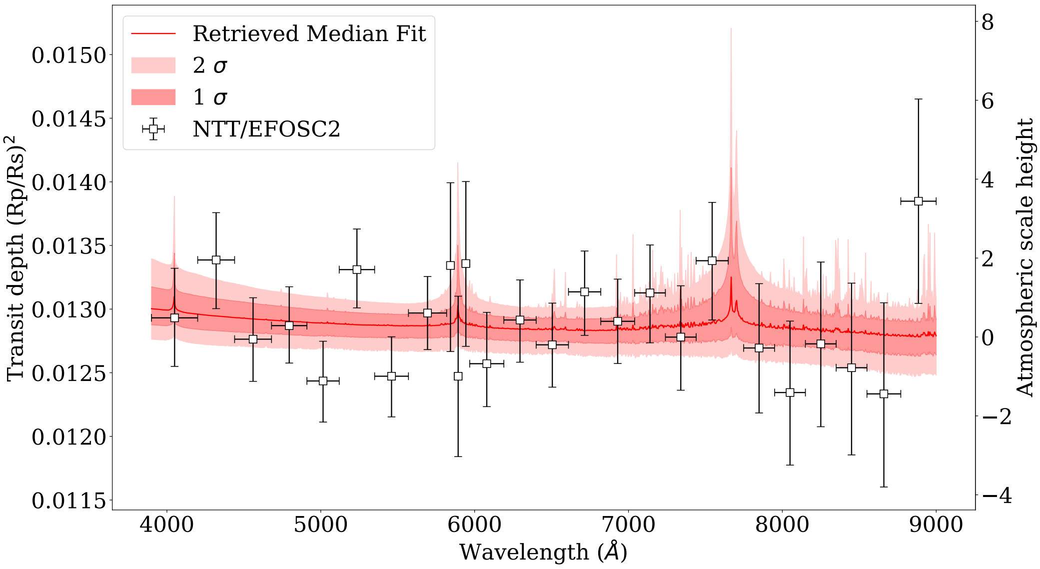

Figure 4.11: Transmission spectrum of HATS-46b as observed by NTT/EFOSC2 and using linear in FWHM detrending (black), and the median retrieved atmospheric model (red), including the respective 1σ and 2σ confidence intervals. It is shown that the retrieved transmission spectrum is relatively featureless, suggesting high-altitude clouds in the atmosphere. Note that narrower bins around the Na doublet (5890, 5895 Å) are used to probe for absorption and the bin centred on the K doublet (7665, 7699 Å) was disregarded due to the close strong O_2 telluric line.

of HATS-46b favours a cloudy atmosphere with 3.0σ confidence. In an alternative cloud-free model they place a conservative upper limit on the Na abundance of 20×solar (3σ confidence). Including stellar activity in our retrievals results in lower Bayesian evidence and no meaningful constraints on the additional parameters. If activity were to play a role in the shape in our transmission spectrum, we would expect to retrieve constraints on the spot coverage fraction or temperature of the spots. Thus this concludes that the cloudy atmosphere model without the additional stellar activity parameters is favoured for the atmosphere of HATS-46b.

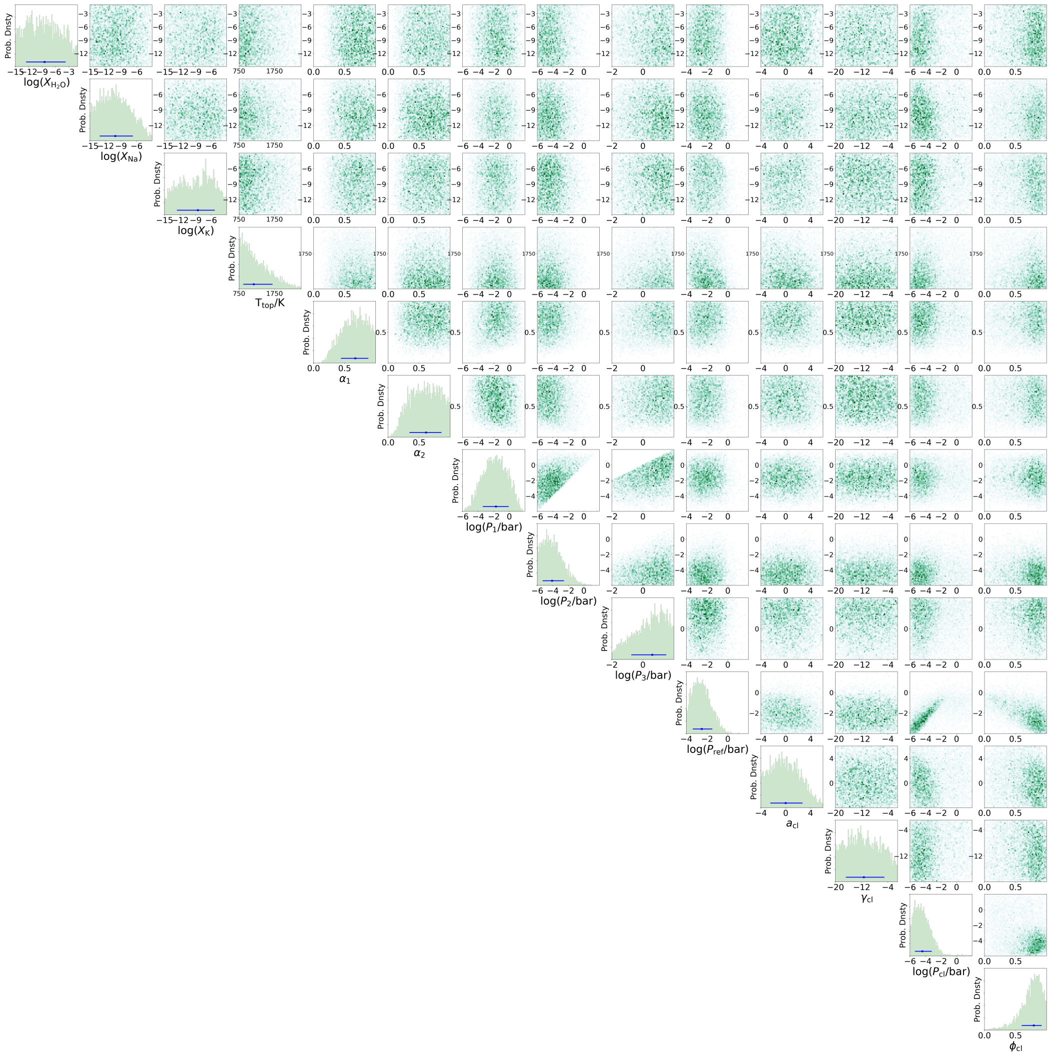

Figure 4.12: Posterior distribution of HATS-46b from the retrieval of the NTT/EFOSC2 observations of HATS-46b. We retrieved three chemical species, H_2O, Na and K, and parametrised the atmospheric temperature profile with six parameters, as discussed in Section 4.4.3. We also include additional parameters for the reference pressure and partial clouds/hazes.

Chapter 5

Transmission Spectroscopy of WASP-39 b

Declaration

This chapter is based on the paper published as Ahrer et al. (2023b), but adapted to make my contributions clear and included additional material. This paper was part of the *JWST* Transiting Exoplanet Community Early Release Science (ERS) program. I have led this paper and the analyis and interpretation on these data, including the writing of the majority of the text (not including the model and reduction specific sections). Specific contributions from my collaborators are made clear in the text since it was a large community effort. I added a section about my data reduction with the `Eureka!` pipeline (introduced in Section 2.3.3) to which I contributed major parts in the development and programming (in particular Stages 1&4&5). In addition, I have changed some of the structure of the text since the journal format did not fit the format of the thesis.

Specific contributions from my collaborators for the work described here: C. A. Murray (CAM), D. Petit dit de la Roche (DP), E. Schlawin (ES), K. B. Stevenson (KBS), M. Mansfield (MM), S. Zieba (SZ) reduced data, modelled the light curves, and/or produced the planetary spectrum presented in this chapter. N. Batalha, K. Ohno, S. E. Moran (SEM) and S. Mukherjee generated atmospheric grids with `PICASO, Vulcan & Virga`, J. Goyal prepared the `ATMO` grids and J. Lothringer the `PHOENIX` grids for comparison with data. CAM, KBS, MM, S. Gill, SEM, and Z. Berta-Thompson generated figures shown here. I will refer to their initials in brackets throughout the chapter to refer to individual collaborators.

5.1 Introduction

JWST has demonstrated the necessary precision and wavelength coverage to make bulk characterisation of hot exoplanet atmospheres routine (The JWST Transiting Exoplanet Community Early Release Science Team et al., 2023). The *JWST* Director's Discretionary Early Release Science (ERS) program provided the scientific community with observations of typical targets quickly enough to inform planning for the telescope's second cycle of scheduled observations. The primary goals of the Transiting Exoplanet Community ERS program (TEC ERS, #1366, led by N. M. Batalha, J. L. Bean, and K. B. Stevenson) are to demonstrate instrument capabilities, quickly build community experience, and seed initial discovery in transiting exoplanetary science (Stevenson et al., 2016a; Bean et al., 2018). The Panchromatic Transmission program (a part of the TEC ERS) observed a single exoplanet, WASP-39b, in transmission using four different instrument modes. It included overlapping wavelength coverage to cross-compare and validate all three near-infrared (NIR) instruments for time-series observations, see Section 2.3.2. The observations presented here form one quarter of this program, demonstrating the capacity of the Near-Infrared Camera (NIRCam) for transiting exoplanet atmospheric characterisation.

WASP-39b is a highly inflated exoplanet of roughly Saturn mass, orbiting its G7 main-sequence star with a 4.05 day period (Faedi et al., 2011). The *JWST* Transiting Exoplanet Community ERS team selected WASP-39b for its inactive host star and prominent spectroscopic features, which trace the atmospheric composition of the planet. The star's relative inactivity was confirmed through a photometric monitoring campaign using the Next-Generation Transit Survey (NGTS) (Wheatley et al., 2018) and Transiting Exoplanet Survey Satellite (TESS) (Ricker et al., 2015), presented in this chapter.

Reported atmospheric metallicities of WASP-39b span a wide range of possible values ($0.003 - 300\times$ solar) (Wakeford et al., 2018; Fischer et al., 2016; Tsiaras et al., 2018; Kirk et al., 2019; Pinhas et al., 2019; Welbanks et al., 2019) due to limits on wavelength coverage, lower signal-to-noise ratio data, and/or differences between analyses (Changeat et al., 2020; Mugnai et al., 2021; Swain et al., 2021; Libby-Roberts et al., 2022). If the Solar System trend for gas giants (Lodders & Fegley, 1998; Kreidberg et al., 2014b) also applies to exoplanets, WASP-39b should have an atmospheric metallicity comparable to that of Saturn ($10\times$ solar, Fletcher et al., 2009) and other Saturn-mass exoplanets.

This chapter is structured as follows: first, I describe the observations of

WASP-39b, the NGTS photometric monitoring and the *JWST* NIRCam observations. Then I describe the steps and pipelines that were used by collaborators and myself to reduce these *JWST* data, followed by the transit light curve fitting. Both of these sections are also split up into the analyses of the short-wavelength (SW, photometric) and long-wavelength (LW, spectroscopy) channel, see Section 2.3.2. Following the data results I describe our team's work on fitting grid models to the retrieved transmission spectrum of WASP-39b. The chapter ends with a discussion of the results and conclusions.

5.2 Observations

5.2.1 Photometric Monitoring of Host Star

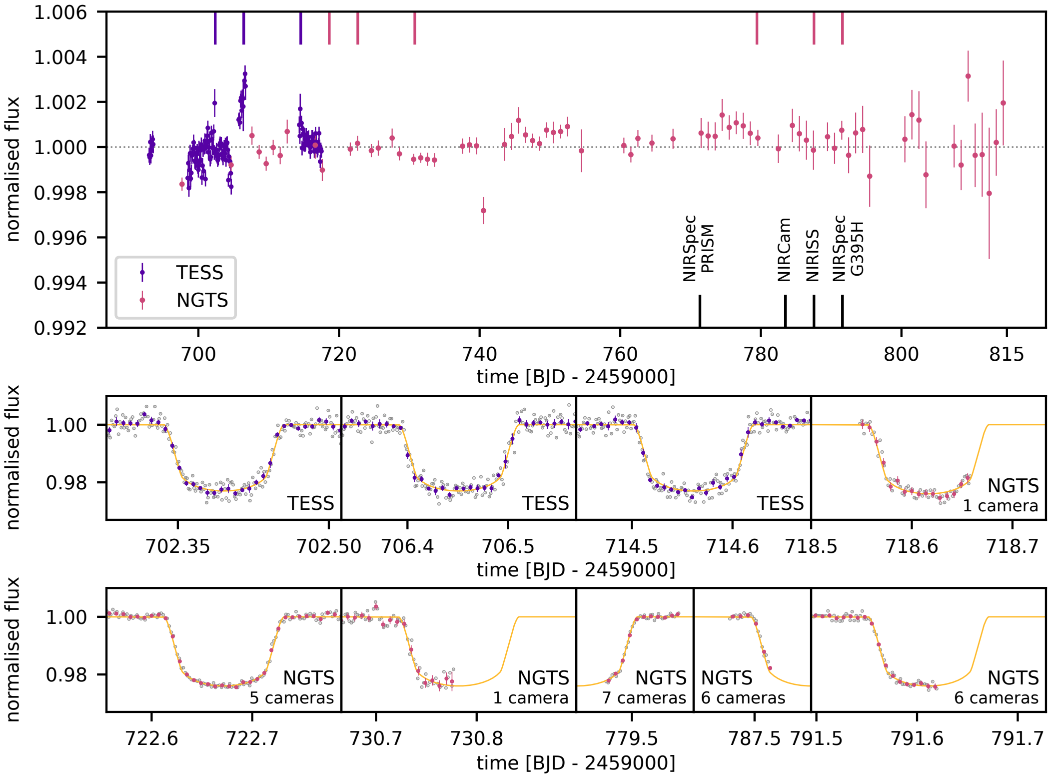

Figure 5.1: **Photometric monitoring of WASP-39 (top) and individual transit observations (bottom) using NGTS (magenta) and TESS (dark purple).** The black marks indicate the times of the four *JWST* ERS transit observations. The monitoring light curve shows evidence for optical variability, but with an RMS amplitude of only 0.06% in NGTS. The times of the individual transit observations are indicated on the top panel, and they are all consistent with transits free of starspot crossings or other features associated with stellar activity.

In order to confirm that WASP-39 is a relatively inactive star, and that the *JWST* observations were not adversely affected by stellar activity, photometric monitoring was carried out by collaborators with the ground-based Next Generation Transit Survey (NGTS) (Wheatley et al., 2018). Monitoring began at the end of April 2022 and continued until late August, spanning the *JWST* ERS transit observations of WASP-39b in July. They used one camera on most photometric nights to take a series of 10 s images lasting on average for 2 h.

The resulting monitoring light curve is plotted in Fig. 5.1 (top panel), showing one binned point for each night. Also included is the TESS sector 51 PDCSAP (Pre-search Data Conditioned Simple Aperture Photometry) light curve of WASP-39 (Ricker et al., 2015), which is binned to 2 h to be comparable with NGTS. Both light curves have been detrended against sky brightness. They show evidence for stellar activity, but only with a low amplitude of 0.06% in NGTS.

Also plotted in Fig. 5.1 (lower panels) are individual transit observations of WASP-39b with NGTS and TESS (the times of which are indicated on the monitoring light curve). For four of the NGTS transits, there were multiple cameras employed. This significantly improves the photometric precision (Bryant et al., 2020), which is otherwise limited by atmospheric scintillation (O'Brien et al., 2022). The transit models were generated from the system parameters listed in Table 5.5. Only the transit times and the mutual depth of the TESS transits were fitted, which were slightly shallower than expected. This is common for observations with TESS as the detector has large pixels and hence many light curves are diluted by additional sources.

The transit observations in Fig. 5.1 show no evidence for starspot-crossing events, which would be visible as bumps in the transit light curve. The absence of such events across multiple high-precision transits provides additional evidence that WASP-39 is a quiet star and that the *JWST* ERS transit observations are unlikely to be adversely affected by stellar variability.

5.2.2 ***JWST*** NIRCam Observation

JWST observed the 2.8-hour transit of WASP-39b over a span of 8.2 hours, providing a baseline before and after transit to measure transit depths accurately. A dichroic beam splitter allows NIRCam to simultaneously observe a target in both short wavelength (SW) and long wavelength (LW) channels (Rieke et al., 2005; Greene et al., 2017). The LW channel used the Grism R + F322W2 filter to observe a wavelength range of 2.420 – 4.025 µm with a spectroscopic resolving power of $R \simeq 1600$ at 4 µm (Fig. 5.2, top panel). The SW imaging channel used the WLP8 weak lens and F210M filter (2.0 – 2.2 µm) to produce the hexagonal pattern shown in the bottom panel of Fig. 5.2. Spreading the light prevents saturation, reduces variability due to image motion over an imperfect flat field, and allows monitoring of mirror-segment alignment. Both SW and LW channels used the SUBGRISM256 subarray mode (largest subarray) with four output amplifiers and the SHALLOW4 readout pattern to minimise data volume. With 12 groups per integration (82.17 s total), *JWST* NIRCam acquired 366 integrations for this transit observation. See Section 2.3.1 for a summary about groups, integration and readout patterns.

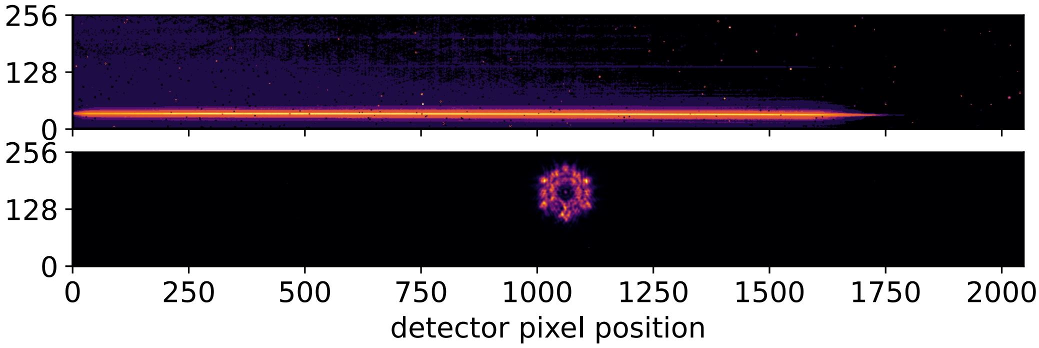

Figure 5.2: **Raw NIRCam image of the LW (top) and SW (bottom) channels.** The faint horizontal stripes seen in the LW channel originate from neighbouring objects. The SW channel is able to track changes in alignment for individual mirror segments. No impactful tilt events were noted in this observation. These tilt events, sudden tilts in the mirror segments, caused abrupt flux changes in the *JWST* commissioning observations of transiting exoplanet HAT-P-14b (Rigby et al., 2023) and were also observed during the WASP-39b transit captured by *JWST* NIRSpec/G395H (Alderson et al., 2023).

5.3 Data Reduction

Independent data analyses were conducted using multiple pipelines and fitting tools to ensure that the same transmission spectrum was obtained using different reduction pipelines. We also chose to investigate different transit light fitting methods within a given data reduction.

Many of the reductions presented below used intermediate data products from or made minor edits to the `jwst` pipeline. The default pipeline settings include a flux calibration step at Stage 2. In all data reductions presented below, we skipped that step, as it introduced scatter in the extracted spectral time series (the conversion factor from units of countrate to flux is not perfect and adds an error to the data uncertainties). This is justified because the transit depths computed are relative, rather than absolute, flux measurements.

Below I describe the independent data reductions applied to the SW photometry and LW spectroscopy, respectively. In each case I note where data reductions deviated from the standard `jwst` pipeline.

5.3.1 Short-Wavelength (SW) Photometry

Two collaborators performed independent short-wavelength (SW) data reductions using the open-source `Eureka!` (SZ) and `tshirt` (ES) pipelines.

Eureka! Short-Wavelength Reduction

`Eureka!` is an open-source pipeline designed to perform spectral extraction and fitting for *JWST* exoplanet time-series observations (Bell et al., 2022) that we, a team of 15 researchers, developed as part the *JWST* TEC ERS team and in preparation for our data. For further details about `Eureka!` and its individual stages see Section 2.3.3.

The `Eureka!` short wavelength data reduction used the default `jwst` settings for Stages 1 and 2, with the exception of increasing the rejection threshold during jump detection to 10σ (see Section 2.3.3, which improved the quality of the resulting light curve. In Stage 3, `Eureka!` first masks all pixels for which the "DO_NOT_USE" data quality flag was raised by the `jwst` pipeline. An outlier rejection was performed along the time axis for each individual pixel in a segment using a 7σ threshold, repeating this process twice. Next, the $1/f$ noise (or pink noise, where f is frequency), which describes the detector's correlated read noise (Schlawin et al., 2020), was corrected in each of the four amplifier regions by subtracting the median flux in each row calculated without pixels containing the star.

Finally, the image centre was determined and aperture photometry on the target was performed. Different target apertures and background annuli were explored, and the combination that minimised the root-mean-square variations was chosen, leading to a target aperture radius of 65 pixels and a background annulus from 70 to 90 pixels relative to the centre.

tshirt Short-Wavelength Reduction

`tshirt` is an open source pipeline[1] that has tools to modify `jwst` and performs photometric and optimal spectral extraction of light curves.

---

[1] https://tshirt.readthedocs.io/en/latest/

In the Stage 1 SW analysis, `tshirt` applied a row-by-row, odd/even-by-amplifier (`ROEBA`) subtraction algorithm that used background pixels to reduce the $1/f$ noise. In this procedure, background pixels are used to correct each group in a similar fashion as with reference pixel correction.[2] The `ROEBA` correction happens after the bias subtraction step. First, the median of all even columns' background rates is subtracted from all even columns and the median of all odd columns' background rates is subtracted from all odd columns to remove most pre-amp reset offsets and odd/even pixel effects. Next, the median of each column's background rate is subtracted from each row to remove the $1/f$ noise for timescales longer than a row read time (5.24 ms). The correction was applied to each group so that $1/f$ noise would not be detected as spurious jumps or cosmic rays by the pipeline. All pixels more than 201 pixels from the source were utilised to estimate the background and $1/f$ noise, then subtracted the median of each row from all pixels in that row. Stage 2 of `jwst` was skipped, as it only changes the rates from ADU per second to physical units and conducts flat fielding. This does not affect the relative measurements of the light curve (due to the high pointing precision) and allows for comparison to detector-level effects.

For the photometric extraction, ES used a source radius of 79 pixels and a background annulus of 79 to 100 pixels and performed a 2D Gaussian fit to determine the centre of the aperture.

5.3.2 Long-Wavelength (LW) Spectroscopy

Three independent long-wavelength data reductions were performed, using the `Eureka!` (KBS, MM, and I), `HANSOLO` (DP), and `tshirt` (ES) pipelines.

The reference files in the Calibration Reference Data System (CRDS) at the time of our analysis included a linear solution for wavelength as a function of x coordinate (the dispersion direction), but this is not strictly accurate at the blue end. To correct our wavelength solution for all methods, my collaborator and member of the NIRCam instrument team (ES) used the commissioning program 1076 to derive a third-degree polynomial wavelength solution that uses the Pfund and Bracket hydrogen series in the planetary nebula IRAS 05248-7007. We found the residuals in this solution are $\lesssim 0.1$ nm and the stellar absorption lines in WASP-39 agree with the solution to within 1 nm. The difference between the corrected wavelengths and the original wavelength solution is almost zero at the red end of the spectrum, but increases to about 50 nm at the blue end.

---

[2] https://jwst-pipeline.readthedocs.io/en/latest/jwst/refpix/index.html

Eureka! Long-Wavelength Reduction

My data reduction team and I investigated several variations of the `Eureka!` long-wavelength data reduction to minimise the median absolute deviation (MAD) of the final extracted light curves, with different settings for cosmic-ray jump detection, identifying the spectral trace, the aperture size for spectral extraction, the region for background subtraction, and limits for outlier rejection. Here I present details of the data reduction that I did and then the one from my collaborator K. B. Stevenson (KBS). In the final version of the paper we chose to only show one `Eureka!` reduction. Since we chose our final NIRCam transmission spectrum to be the one that was the most median between all submitted transmission spectra (see later in text) and that turned out to be KBS's `Eureka!` spectrum, it was then also the one shown as the only `Eureka!` spectrum in the published paper. Thus in this section I will describe my reduction as well as the one from KBS.

Stages 1 and 2 were identical to the `jwst` pipeline, with the exception of increasing the rejection threshold during jump detection to 6σ for both of our reductions and omitting the aforementioned flux calibration step in Stage 2.

In Stage 3, we both trimmed the data to a subarray extending from pixels $4-64$ in the cross-dispersion direction and $4-1704$ in the spectral direction. `Eureka!` then masks any pixels with NaN values for the flux or error. We fitted the spectral trace with a Gaussian profile and KBS corrected for the curvature of the trace to the nearest integer pixel, while I did not conduct curvature correction.

KBS and I excluded a region 14 and 12 pixels wide, respectively, on either side of the spectral trace from the background calculation and performed a column-by-column linear fit to subtract the background. I used a double-iteration 7σ threshold for outlier rejection of the sky background along the time axis during background subtraction. Additionally, KBS and I both used a 7σ threshold for outlier rejection during the polynomial fit to the background. To obtain the spectrum, both of us constructed a normalised spatial profile using the median of all data frames, then KBS and I used optimal extraction (Horne, 1986) on an aperture with a half-width of 9 pixels and 8 pixels, respectively. For the optimal extraction, KBS rejected outliers above a 10σ threshold, I used a 7σ threshold. Fig. 5.3 shows the curvature-corrected, background-subtracted, median frame with indicated background and aperture regions from KBS's reduction of the NIRCam LW data.

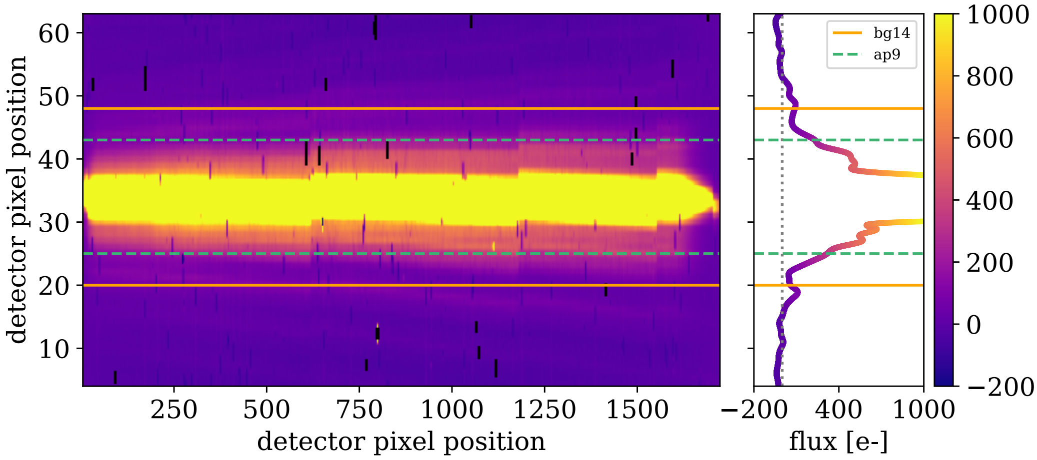

Figure 5.3: **Left: Curvature-corrected, background-subtracted, median frame.** KBS performed optimal spectral extraction on the pixels in between the green dashed lines. `Eureka!` uses the pixels outside of the two orange solid lines for background subtraction. The flux spans -200 – 1000 electrons, thus drawing attention to the residual background features. **Right: Vertical slice depicting the flux averaged over detector pixels 855 to 865.** The background region clearly demonstrates some low-level residual structure.

HANSOLO Long-Wavelength Reduction

The `HANSOLO` (atmospHeric trANsmission SpectrOscopy anaLysis cOde) pipeline was originally developed to analyse ground-based transmission spectra observed with 8m-class telescopes (Lendl et al., 2016, 2017) and was adapted by my collaborator (DP), to enable its use on NIRCam data. `HANSOLO` begins with the calibrated `rateints.fits` outputs of `jwst` Stage 1.

The `LACOSMIC` algorithm (van Dokkum, 2001) was used to remove cosmic ray effects from the two-dimensional images and identified the spectral trace using a Moffat function fit to each column. To remove the sky, a linear trend was fitted and subtracted from each column, excluding from the fit a region of 20 pixels on either side of the trace centre. Then the spectrum was extracted by summing over an aperture with a half-width of 3 pixels.

The spectra from different images were aligned with each other using cross correlation. To correct outlier pixels, each spectrum was normalised to account for the effect of the transit on the time series. Outliers $> 3\sigma$ away from the mean were removed from the time series of each wavelength point in the normalised spectra and replaced with the median value over time. Then DP rescaled the spectra to their original amplitudes.

`tshirt` Long-Wavelength Reduction

As with the short-wavelength reduction, a few modifications were made to the Stage 1 `jwst` ramps-to-slopes pipeline. `ROEBA` subtraction reduced $1/f$ noise (described above for photometry); however, only pixels 1847 to 2044, which are on the rightmost amplifier, are available as low-illumination background.

For Stage 3, `tshirt` performed optimal spectral extraction weighted by the covariance between pixels (Schlawin et al., 2020). A spectral aperture centered at pixel 34 in the spatial direction with a half-width of 5 pixels was used. The background region was selected to extend between pixels 5-24 and 44-65 in the spatial direction. The background was fit with a column-by-column linear trend with 3-sigma clipping. For the spectral extraction, the spatial profile was fitted with a cubic spline with 20 knots and an outlier rejection threshold of 30σ. If a pixel was deemed an outlier either by the "DO_NOT_USE" data quality flag or by the spatial profile outlier detection, the rest of the spatial profile was weighted by the reference profile to ensure that the flux was conserved. For the covariance weighting, a correlation of 8% was assumed between pixels as measured by background pixels' noise properties.

5.4 Light Curve Fitting

5.4.1 Short-Wavelength Data

Both `Eureka!` and `tshirt` were used to generate the short-wavelength light curves, as shown in Fig. 5.4. The light curves were then fit using both pipelines, with models that included both the transit and systematic noise. However, in order to investigate the effect of different systematic models on the resulting spectra, each fit used a slightly different noise model. Table 5.1 summarises the systematics models which were used in each short-wavelength fit.

5.4.2 Long-Wavelength Data

For the long-wavelength fits, the data were summed into 15 nm bins ($\simeq$ 15 pixels). We experimented with bins as small as 10 nm, but found that reducing the bin size below 15 nm led to poor constraints on the limb darkening and added additional scatter to the resulting spectrum. The resulting individual spectroscopic light curves from my reduction are shown in Fig. 5.5.

Fig. 5.6 shows that the noise is primarily Gaussian out to long time scales of order the length of ingress/egress. Additionally, each of us created a white light

Table 5.1: Details of the two methods used to fit the short-wavelength photometry. Abbreviations for priors are as follows: U=uniform prior, with numbers indicating lower and upper limits; N=normal prior, with numbers indicating mean and sigma; LN=log-normal prior, with numbers indicating mean and sigma. Period of the planet was fixed to 4.05527999 days from Fischer et al. (2016)

Fitting Method		
	`Eureka!`	`tshirt`
Noise Parameters and Priors		
Polynomial in time (c_0,c_1,etc.; unitless, days^{-1}, etc.)[3]	1st-order c_0: U,0.9,1.1 c_1: U,-0.1,0.1	2nd-order c_0: N,24,0.24 c_1: N,0,0.576 c_2: N,0,0.144
System Parameters and Priors		
Planet-to-star radius ratio ($R_\mathrm{p}/R_\mathrm{s}$, unitless)	U,0,0.3	LN,ln(0.08),0.5
Mid-transit time (T_c, BJD$-$2459783)	U,0.45,0.55	N,0.5005,0.0007
Inclination (i, $\circ$)	U,80,90	N,87.93,0.14 (Fischer et al., 2016)
Scaled semi-major axis (a/R_s, unitless)	U,2,20	N,11.55,0.13
Limb darkening law used	Kipping 2-parameter	Kipping 2-parameter
Limb darkening parameters (u_1,u_2)	U,0,1	Uninformative priors
Fit Results		
transit depth (ppm)	21103 ± 85	21177 ± 53

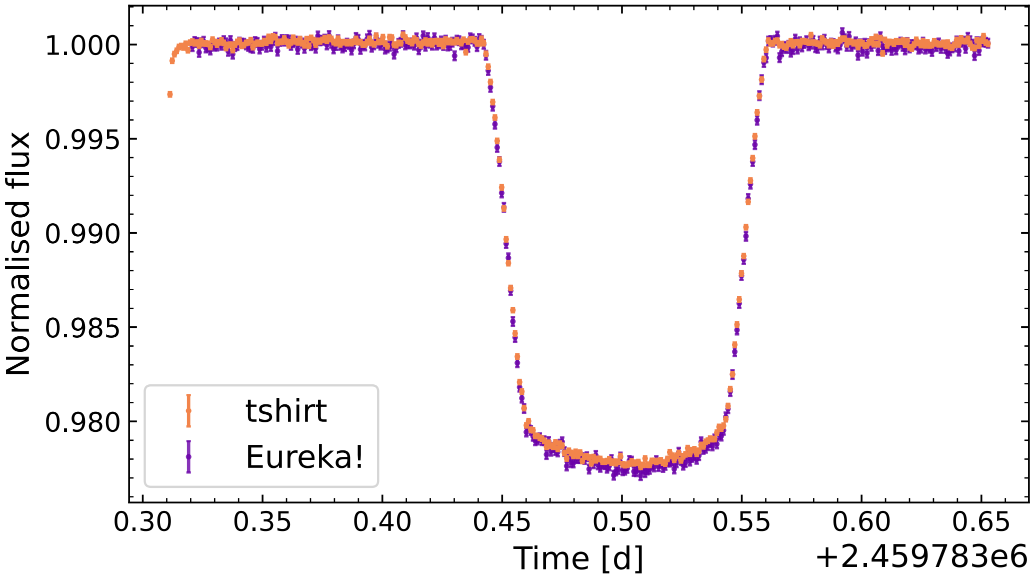

Figure 5.4: *JWST* NIRCam SW (photometry) light curves of the transit of WASP-39b as retrieved by the `Eureka!` and `tshirt` pipelines.

curve by summing the extracted spectra over the entire 2.420 – 4.025 µm wavelength region.

We experimented with different wavelength cut-offs but chose to extract spectra in this wavelength region because the low instrument throughput affected the quality of the extracted light curves beyond this region. Fig. 5.7 shows all reduced transmission spectra with one bin added on the blue end and two added on the red end, as well as the relative throughput at the wavelengths of these bins. This figure demonstrates the large error bars derived from data near the edges of the NIRCam/F322W2 bandpass. Therefore, we recommend that future works limit extracted spectra to the wavelength region between 2.420 – 4.025 µm.

The long-wavelength light curves were fitted using four independent pipelines: `chromatic-fitting`, `Eureka!`, `HANSOLO`, and `tshirt`. `chromatic-fitting` is an open-source[4] `Python` tool to perform light-curve fitting, built on the data visualiser `chromatic` (Berta-Thompson, in prep.[5]). Again here the `Eureka!` light curve fitting was the one from my collaborator K. B. Stevenson.

For this dataset, my collaborator C. A. Murray applied `chromatic-fitting` light-curve fitting to a `Eureka!` data reduction. As with the short-wavelength fits, the long-wavelength light curves were fitted with models that include different noise

---

[4] https://github.com/catrionamurray/chromatic_fitting/

[5] https://github.com/zkbt/chromatic/

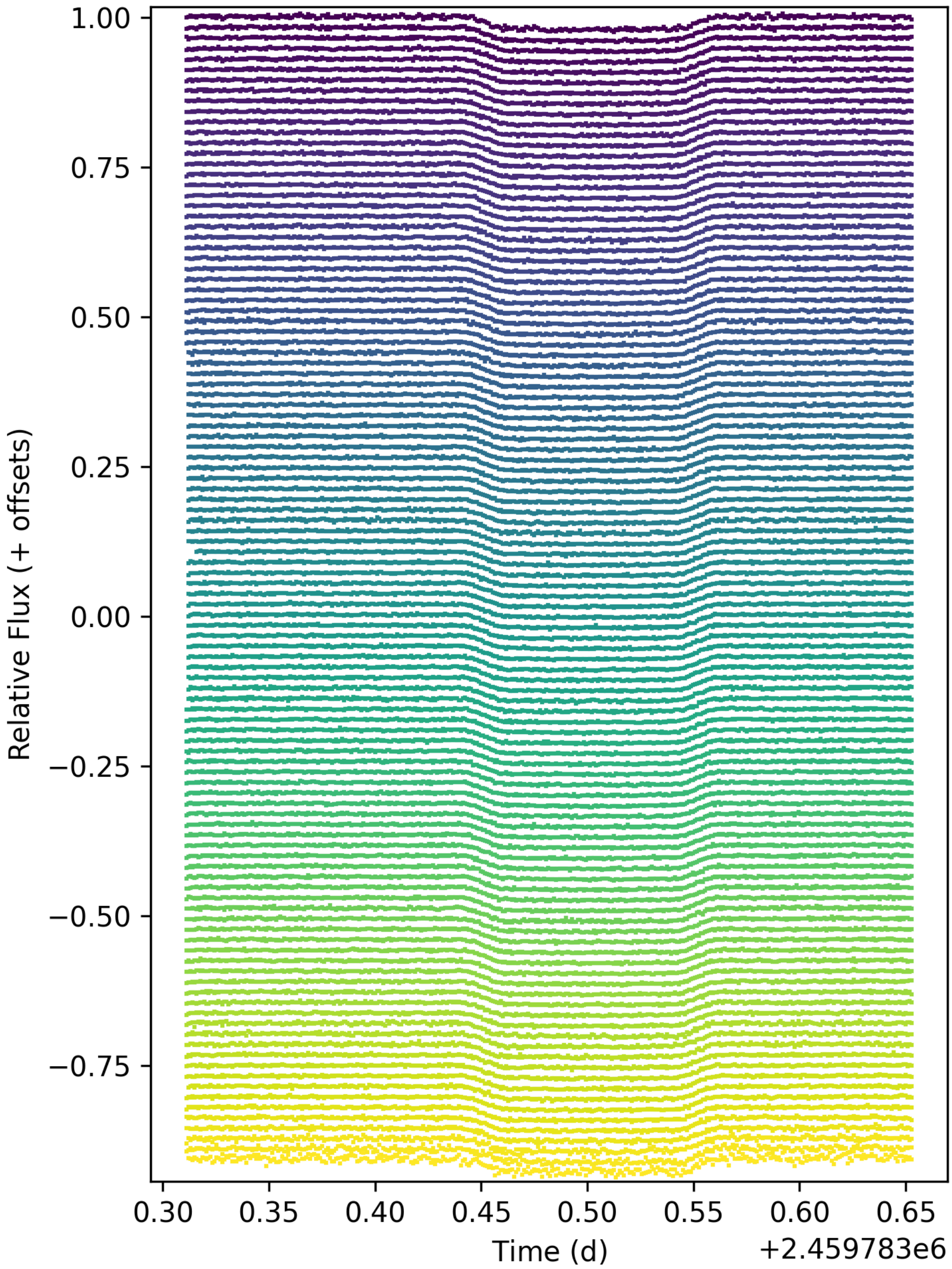

Figure 5.5: Retrieved spectroscopic light curves using my `Eureka!` reduction. The wavelength range is 2.420 – 4.025 µm, with bin sizes of 15 nm (blue to red from top to bottom).

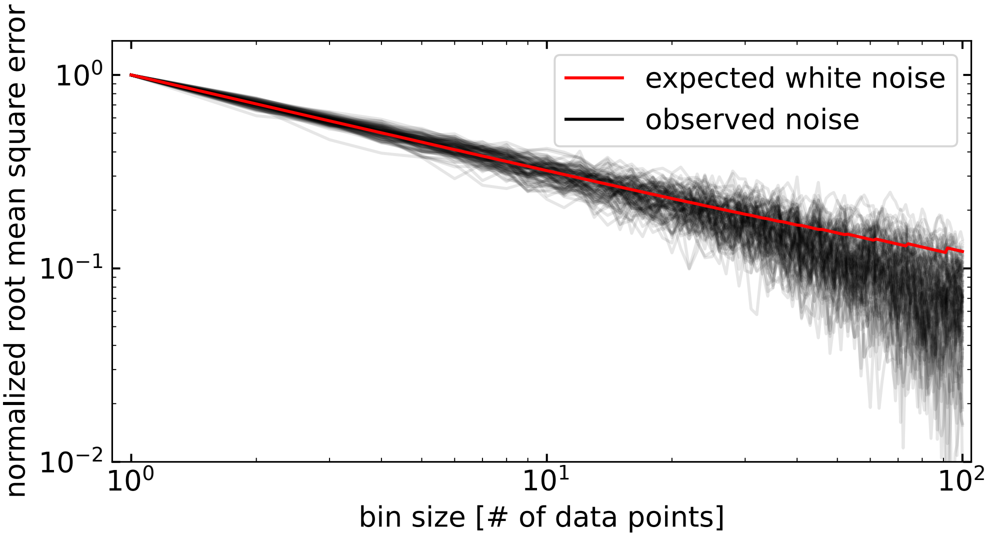

Figure 5.6: Normalised root mean square error as a function of bin size for all spectroscopic channels. The red line shows the expected relationship for perfect Gaussian white noise. The black lines show the observed noise from each spectroscopic channel for the `Eureka!` long wavelength reduction. Values for all channels are normalised by dividing by the value for a bin size of 1 in order to compare bins with different noise levels. The black lines closely follow the red line out to large bin sizes of ≈ 30 (≈ 0.5-hr time scales), which demonstrates that the residuals to the fit are dominated by white Gaussian noise.

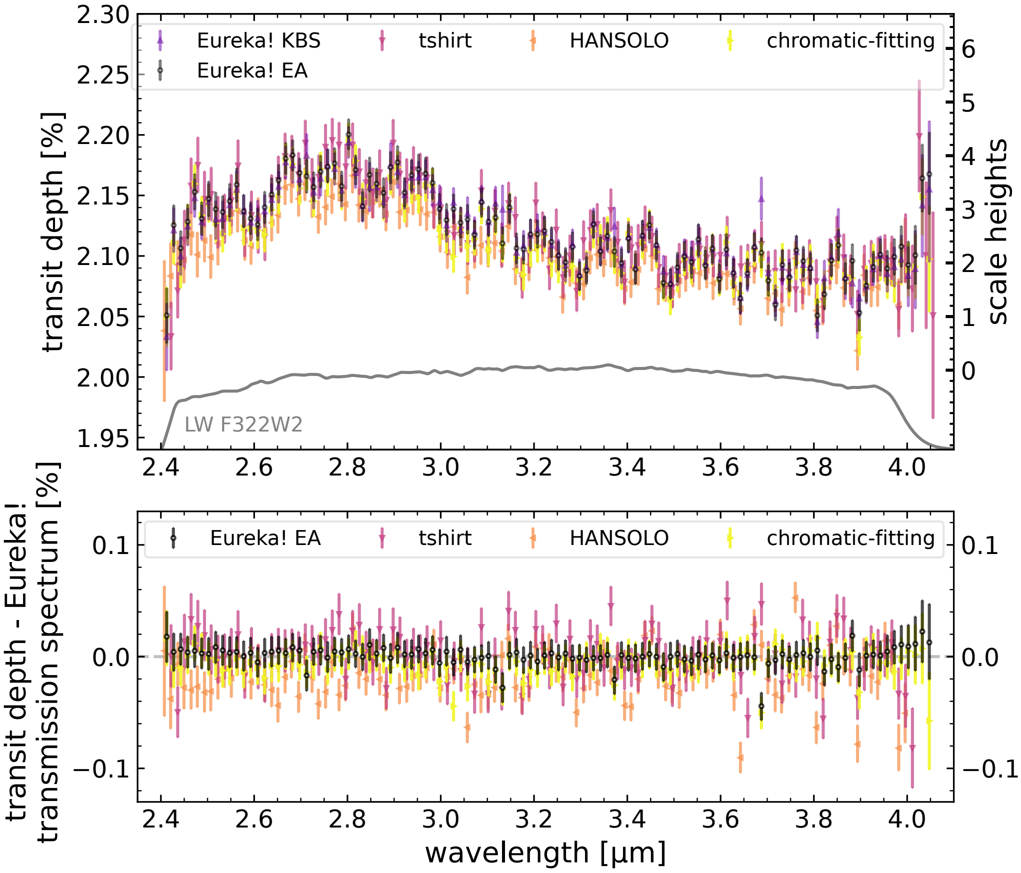

Figure 5.7: *Top panel:* Transmission spectra from our reductions (including mine, indicated by 'Eureka! EA') when including additional data on the blue and red edges (now spanning 2.405 – 4.055 µm), demonstrating the large error bars and diverging data points near the edges of the NIRCam bandpass in the LW spectroscopic channel.
Bottom panel: The differences in retrieved transmission spectra by subtracting the `Eureka!` spectrum from the other three reduced spectra shown in the top panel. This shows the strong agreement between the spectra; however, we do note minor disagreements at shorter wavelengths that were attributed to differences in the treatment of limb-darkening effects within the individual fitting methods.

parameterisations. Table 5.3 summarises the systematics models that were used in each long-wavelength fit.

For all fits, the parameters were estimated with a Markov Chain Monte Carlo (MCMC) fit, using either the `emcee` `Python` package (Foreman-Mackey et al., 2013) (for fits performed with `Eureka!`), the `pymc3` `Python` package (Salvatier et al., 2016) (implemented through the `Exoplanet` code (Foreman-Mackey et al., 2021; Luger et al., 2019), for fits performed with `chromatic-fitting` or `tshirt`), or the `CONAN` `Python` package (Lendl et al., 2016, 2017) (for fits performed with `HANSOLO`). The number of free parameters and the resulting differential MADs of the light curves from each fit are also listed in Tables 5.1 and 5.3. The best-fit parameters from the white light-curve fits are given in Table 5.5.

In the process of performing the fits to the long-wavelength data, we regularly found that the best-fit transmission spectra were shifted vertically for different limb-darkening parameterisations and, for some reductions, exhibited changes in the apparent size of the features in the transmission spectrum. In particular, it was found that light-curve fits with all limb-darkening coefficients fixed to outputs from ExoTiC-LD (Laginja & Wakeford, 2020b,a; Wakeford & Grant, 2022) could result in a biased planet spectrum and might present a higher level of time-correlated noise in the residuals. This was attributed to a combination of JWST's high-precision light curves and deficiencies in the stellar limb-darkening models to accurately represent WASP-39 (Morello et al., 2017, 2020). Therefore, the results presented here use the quadratic limb-darkening law, in its classical form or reparameterised by Kipping (2013) (see Table 5.3 for the law used by the individual fitting methods), with one or both coefficients as free parameters. Members of my data reduction and analysis team and I independently confirmed that these parameterisations produce transmission spectra that are consistent both with each other and with the spectra resulting from using more complex limb darkening parameterisations, such as a four-parameter law with either fixed or free parameters (Claret, 2000). We therefore recommend that future transmission spectrum analyses with NIRCam use similar methods. Limb-darkening conclusions from the full Transiting Exoplanet Community ERS program will be discussed further by Espinoza et al. (in prep.).

The final light curves are shown in Figure 5.8 and the LW transmission spectra are shown in Figure 5.7. Both the short wavelength and long wavelength datasets are also available in our Reproducible Research Compendium on Zenodo at `https://doi.10.5281/zenodo.7101283`. The median difference between each transmission spectrum and the `Eureka!` spectrum is 0.87σ (using the maximum error at each point), which demonstrates a remarkable level of agreement. Using

Table 5.3: Details of the four fitting methods used to fit the long-wavelength spectroscopy. Abbreviations for priors are as follows: U=uniform prior, with numbers indicating lower and upper limits; LU=log-uniform prior, with numbers indicating lower and upper limits; N=normal prior, with numbers indicating mean and sigma; LN=log-normal prior, with numbers indicating mean and sigma. The notation “spec-fixed” indicates that a value was fit in the white light curve and fixed to the best-fit value for the spectroscopic light curves. Periods were fixed or fitted for with respect to the value from Fischer et al. (2016).

	Fitting Method			
	`chromatic-fitting`	`Eureka!`	`HANSOLO`	`tshirt`
Noise Parameters and Priors				
Polynomial in time (c_0,c_1,etc.; unitless, days^{-1}, etc.)	2nd-order c_0: N,1.0,0.01 c_1: N,0.0,10^{-4} c_2: N,0.0,10^{-4}	1st-order c_0: N,1.0,0.001 c_1: N,0.0,0.01	0th-order c_0: U,0.8,1.2	2nd-order c_0: N,24,0.24 c_1: N,0,0.576 c_2: N,0,0.144
Polynomial with drift in y position (y_0,y_1,etc.; unitless, pixels^{-1}, etc.)	2nd-order y_0: fixed to 0.0 y_1: N,0,10^{-4} y_2: N,0,10^{-4}	N/A	N/A	N/A
Gaussian Process 3/2 Matern kernel model (amplitude A, correlation length L; unitless, days)	N/A	N/A	A: LU,10^{-20},10^{-5} L: LU,10^{-10},1	N/A
Multiplier to the expected noise level from Stage 3 (s, unitless)	N,1,0.1	N,1.1,0.1	N/A	N/A
System Parameters and Priors				
Planet-to-star radius ratio ($R_\mathrm{p}/R_\mathrm{s}$, unitless)	N,0.145,0.05	N,0.145,0.05	U,0,1	LN,ln(0.08),0.5
Period (P, days)	fixed to 4.05527999	fixed to 4.05527999	fixed to 4.05527999	N,4.05527999,7×10^{-7}
Mid-transit time (T_c, BJD−2459783)	N,0.5,0.02; spec-fixed	N,0.5,0.05; spec-fixed	U,0.45,0.55; spec-fixed	N,0.5005,0.0007
Inclination (i, $\circ$)	N/A	N,87.93,0.25; spec-fixed	N/A	N,87.93,0.14
Scaled semi-major axis (a/R_s, unitless)	N/A	N,11.55,1; spec-fixed	N/A	N,11.55,0.13
Impact parameter (b, unitless)	U,0,1.145; spec-fixed	N/A	U,0,1; spec-fixed	N/A
Limb darkening law used	Kipping 2-parameter	quadratic	quadratic	Kipping 2-parameter
Limb darkening parameters (u_1,u_2)	N, μ from ExoTiC-LD, 0.05	U,-1,1; u_1 spec-fixed	N, μ from ExoTiC-LD, 0.1; u_1 spec-fixed	Uninformative priors
Fit Statistics				
Median error bar on final spectrum (ppm)	121	135	137	180

Table 5.5: Best-fit orbital parameters from both short-wavelength (SW) and white-light long-wavelength (LW) fits.

Pipeline	$T_c - 2459783$ (BJD)	R_p/R_s	a/R_s	i ($\circ$)
`Eureka!` SW	0.50153 ± 0.00003	0.1453 ± 0.0003	11.43 ± 0.05	87.77 ± 0.06
`tshirt` SW	0.501540 ± 0.000017	0.14552 ± 0.00018	11.458 ± 0.026	87.79 ± 0.03
`chromatic-fitting` LW	0.501616 ± 0.000024	0.14531 ± 0.00019	11.43 ± 0.20	87.78 ± 0.52
`Eureka!` LW	0.501582 ± 0.000032	0.14588 ± 0.00030	$11.381^{+0.055}_{-0.054}$	$87.748^{+0.065}_{-0.063}$
`HANSOLO` LW	$0.501624^{+0.000072}_{-0.000080}$	$0.14482^{+0.00048}_{-0.00049}$	$11.407^{+0.059}_{-0.061}$	$87.802^{+0.071}_{-0.065}$
`tshirt` LW	0.501610 ± 0.000014	0.14563 ± 0.00016	11.44 ± 0.02	87.77 ± 0.02

the same calculation, my own `Eureka!` transmission spectrum differs from KBS's spectrum with a median of 0.23σ. Additionally, the residuals showed no evidence for time-correlated noise, as shown in Figure 5.6.

For ease of interpretation, it was decided to compare our atmospheric models to only one transmission spectrum. The `Eureka!` spectrum was selected, as it was on average nearest the median spectrum (the median transit depth at each bin).

5.5 Atmospheric Forward Modelling

To interpret the long-wavelength data from NIRCAM/F322W2, we performed χ^2 fits to the transmission spectra using three grids of radiative-convective equilibrium models: `ATMO` (Tremblin et al., 2015; Goyal et al., 2018, 2020), `PHOENIX` (Hauschildt et al., 1999; Barman et al., 2001; Lothringer & Barman, 2020), and `PICASO 3.0` (Batalha et al., 2019; Mukherjee et al., 2022). All models used a common set of planetary parameters, but had differing opacity sources, cloud treatments, and grid points, described in detail below. Each model was binned to the resolution of the data to perform the χ^2 fitting. We performed these three independent model grid fits to fully vet our inferences about the atmospheric metallicity and the presence of specific molecular features within the data.

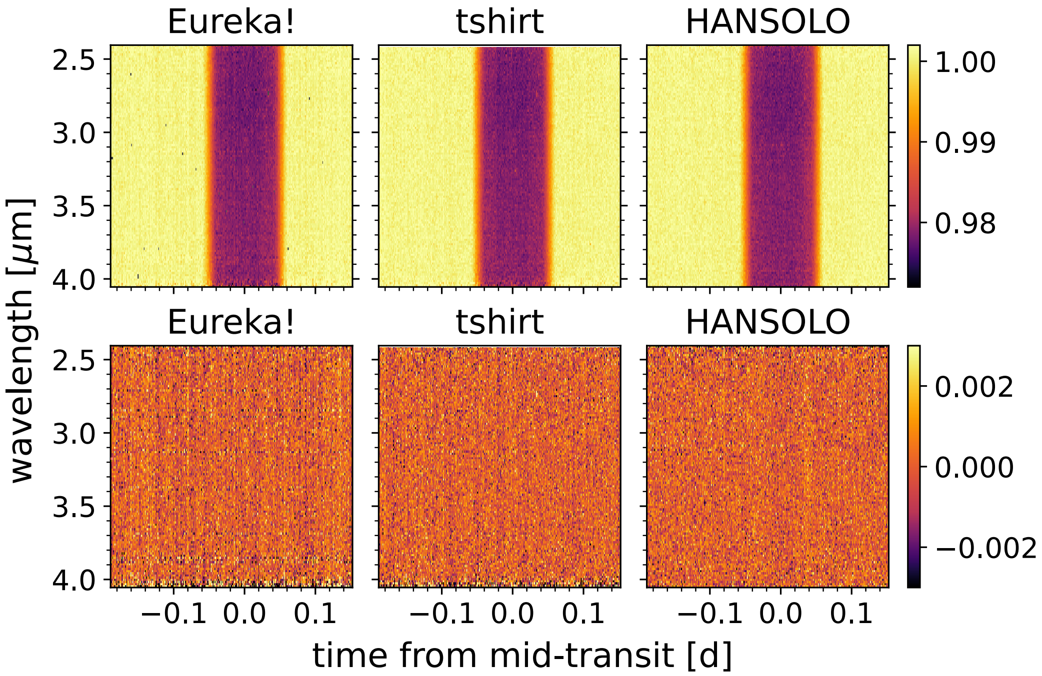

Figure 5.8: *Top Row:* Time-series NIRCam data for the WASP-39b system, from three independent spectral extractions. Color represents relative brightness at each time and wavelength, normalized by the median stellar spectrum. *Bottom Row:* Resulting residuals after fitting the time-series NIRCam data.

5.5.1 The `PICASO 3.0`, `Vulcan`, & `Virga` Model Grid

Our primary atmospheric model grid is built from the open-source radiative-convective equilibrium code `PICASO` (Planetary Intensity Code for Atmospheric Spectroscopy Observations) (Batalha et al., 2019), version 3.0 (Mukherjee et al., 2022), which was developed from the Fortran-based `EGP` (McKay et al., 1989; Fortney et al., 2005; Marley et al., 2021). We used `PICASO 3.0` to generate one-dimensional temperature-pressure profiles in thermochemical equilibrium. The base `PICASO 3.0` forward model grid computes atmospheric mixing ratios using variations of planetary intrinsic temperatures ($T_{\rm int}$) of 100 K, 200 K, and 300 K; C/O ratios of 0.229, 0.458, 0.687, 0.916; and atmospheric solar metallicity values of 0.1, 0.316, 1.0, 3.162, 10.0, 31.623, 50.119, and 100× solar. The `PICASO` grid assumes full day-night energy redistribution. To compute model transmission spectra from the atmospheric profiles, opacities described by Marley et al. (2021) were used (see in particular Table 2); which sources H_2O from Barber et al. (2006); Tennyson & Yurchenko (2018), CH_4 from Tennyson & Yurchenko (2012); Yurchenko et al. (2013); Yurchenko & Tennyson (2014), CO_2 from Huang et al. (2014), and H_2S from Tennyson & Yurchenko (2012); Rothman et al. (2013); Azzam et al. (2015).

We then used the one-dimensional CHON-based chemical kinetics code `VULCAN` (Tsai et al., 2021) and the cloud modeling code `Virga` (Rooney et al., 2022), which is the `Python` implementation of the `Eddysed` cloud code (Ackerman & Marley, 2001), to post-process disequilibrium chemistry from mixing and photochemical products as well as the effect of clouds. These additional post-processed grids also include vertically constant eddy diffusivities ($K_{\rm zz}$) of 10^5 – 10^{11} cm^2/s in steps of 2 dex, and both clear and cloudy models. For the `Vulcan` disequilibrium runs, we only computed model grid points for a select subset of metallicity values (1, 10, 50, and 100× solar) and C/O ratios (0.229, 0.458, 0.687). We found that neither the cloudy nor clear disequilibrium grids from `VULCAN` offered an improvement in the χ^2_ν value. Given the sparseness of these pre-computed disequilibrium grid models, we left rigorous quantification of self-consistent disequilibrium chemistry in the atmosphere of WASP-39b to future work.

Within `PICASO`, clouds are implemented both as grey absorbers and as Mie scatterers using temperature-relevant cloud condensate species from `Virga`. For the grey clouds, the grid specified a cloud optical depth ($\tau_{\rm cloud}$) between 1 and 0.1 bar ranging from $\tau_{\rm cloud} = 3.2\times10^{-6}$ to 1 in steps of 0.1 dex across all wavelengths. For clouds of specific condensates, the atmospheric modelling team used `Virga` to compute log-normal particle size distributions using sedimentation efficiency ($f_{\rm sed}$) values of 0.6 to 10 for MnS, Na_2S, and $MgSiO_3$ along the range of $K_{\rm zz}$. Smaller sedimentation efficiencies, f_{sed}, with larger eddy diffusivities, K_{zz}, generated more extended cloud decks and stronger cloud opacity.

5.5.2 The `PHOENIX` Model Grid

We also used a grid of atmosphere models from the `PHOENIX` radiative-convective equilibrium code to fit the data (Hauschildt et al., 1999; Barman et al., 2001; Lothringer & Barman, 2020). Similar to the `PICASO 3.0` grid, parameters including the day-night energy redistribution factors, interior temperature (200 K, 400 K), bulk atmospheric metallicity (0.1, 1, 10, 100× solar), and C/O ratio (136 grid points from 0.3 to 1) were varied. Aerosol properties were parameterized through a haze factor (0, 10× multi-gas Rayleigh scattering) and a grey cloud deck pressure level (0.3, 3, and 10 mbar). Models with molecular abundances quenched at 1 bar to simulate vertical mixing were also calculated. The grid also included rainout to account for species sequestered as condensates in the deep atmosphere. Opacities are described by Lothringer & Barman (2020); Lothringer et al. (2021) and taken from Rothman et al. (2013).

5.5.3 the `ATMO` Model Grid

Similar to the model grids described above, we compared the data to a grid of models from the `ATMO` radiative-convective-thermochemical equilibrium code (Tremblin et al., 2015; Drummond et al., 2016; Goyal et al., 2018, 2020). The `ATMO` grid used similar atmospheric and aerosol parameterisations to those used in the `PHOENIX` grid and also included rainout that accounts for species condensed in the deep atmosphere. Also included are day-night energy redistribution factors (0.25, 0.5, 0.75, and 1; with 1 as full redistribution), atmospheric metallicity (0.1, 1, 10, 100× solar), interior temperature (100, 200, 300, 400 K), C/O ratio (0.35, 0.55, 0.7, 0.75, 1.0, 1.5), cloud scattering factor (0, 0.5, 1, 5, 10, 30, 50× H_2 Rayleigh scattering at 350 nm between 1 and 50 mbar pressure levels), and a haze scattering factor (1, 10× multi-gas Rayleigh scattering). Opacities for H_2O, CO_2, and CH_4 are taken from Tennyson & Yurchenko (2012); Yurchenko et al. (2013); Yurchenko & Tennyson (2014); Tennyson & Yurchenko (2018) and H_2S from Rothman et al. (2013).

5.5.4 Grid Fits to *JWST*/ NIRCam Data

We applied each of our three grids – `ATMO`, `PHOENIX`, and `PICASO 3.0` – to fitting the NIRCam F322W2 spectrum (2.4 – 4.0 µm). In doing so, we found that the models strongly favoured a solar- or super-solar-metallicity atmosphere (1 – 100× solar), a sub-stellar C/O ratio ($\leqslant 0.35$), and substantial contribution from clouds, which are parameterised differently by each model grid (see each grid description above).

We show the best fits from each model grid in Fig. 5.9. This interpretation is in agreement with the results using JWST's NIRSpec/PRISM instrument from 3.0 – 5.0 µm (The JWST Transiting Exoplanet Community Early Release Science Team et al., 2023), improving on the wider spread from previous Hubble Space Telescope (*HST*) results (Tsiaras et al., 2018; Fischer et al., 2016; Pinhas et al., 2019; Welbanks et al., 2019; Kawashima & Min, 2021; Wakeford et al., 2018) or *HST* and ground-based optical interpretations (Kirk et al., 2019).

For the NIRCam-only fit, the `PICASO` grey-cloud scheme produced a slightly better best fit ($\chi^2_\nu = 1.16$) than the `PICASO + Virga` more realistic clouds ($\chi^2_\nu = 1.23$), both of which were preferred to the clear-model best fit (100× solar) with $\chi^2_\nu = 1.53$. The `Virga` best-fit grid resulted in an atmosphere of 1× solar metallicity, C/O = 0.229, $f_{\rm sed} = 0.6$, and $K_{\rm zz} = 10^9$ cm/s^2. This `Virga` best-fit model consists of clouds of MnS and MgSiO$_3$ with deep ($\geqslant 100$ bars) cloud bases and diminishing optical depth up to $\sim$ mbar pressures.

The best-fit equilibrium model from the `PHOENIX` grid had 100× solar metallicity, a C/O ratio of 0.3, and a cloud deck at 3 mbar. Cloudy models were generally preferred over clear models, but not with statistical significance (χ^2_ν of 1.25 compared to 1.22). The `PHOENIX` grid finds best fits with very high metallicity (100× solar), so this low confidence regarding clouds reflects the cloud-metallicity degeneracy inherent in data restricted to narrow wavelengths (e.g. Benneke & Seager, 2013), as well as potentially the sparseness of the model grid.

For the `ATMO` grid, the best-fit equilibrium model to the NIRCam spectrum was 1× solar metallicity, a C/O ratio of 0.35, a cloud factor of 5 and a haze factor of 1. As with the other two grids, strongly cloudy models (cloud factor of $\geqslant$5) were preferred to clear models (χ^2_ν of 1.1 vs 1.2).

5.5.5 *HST* +NIRCam

In Fig. 5.10, we show the comparison between the spectra of *HST* /WFC3 (G141 and G102, covering 0.8 – 1.65 µm) and *JWST*/ NIRCam (F210M+F322W2, 2.0 – 4.0 µm). We chose to only show Wide Field Camera 3 (WFC3) observations from *HST* , as these are of higher precision than observations from the Space Telescope Imaging Spectrograph (STIS) or ground-based data (Wakeford et al., 2018). Additionally, as *HST* /WFC3 has the most archival exoplanet data of any instrument on *HST* , future *JWST* exoplanet programs will primarily rely on this *HST* instrument for inter-telescope comparisons or extending the wavelength coverage of *JWST*

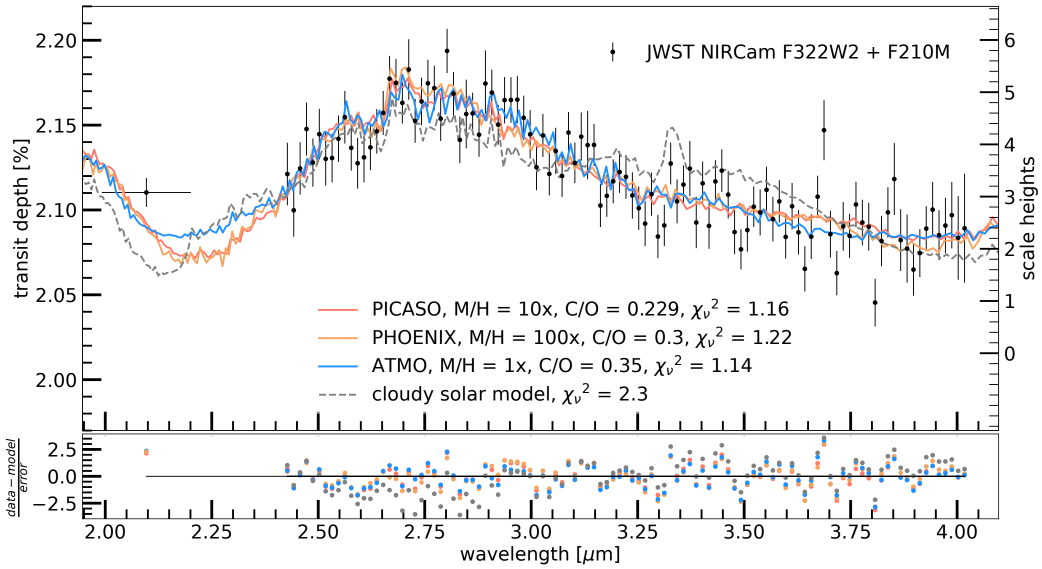

Figure 5.9: **Measured transmission spectrum compared to atmospheric forward model grids.** *Top:* The single best fit for each model grid (shown as solid colored lines; `PICASO 3.0`, `ATMO`, `PHOENIX`), fits the planet spectrum (`Eureka!` reduction) with $\chi_\nu^2 \leqslant 1.22$. All single best fits prefer at least solar metallicity and substantial cloud cover. Also shown as a grey dashed line is a solar metallicity, stellar C/O ratio atmospheric model, demonstrating the lack of methane absorption seen in the spectrum. Because we can put an upper limit on the CH_4 abundance, the preferred C/O ratio found by the model grids is sub-stellar. *Bottom:* Residuals of each best fit, shown as the model spectrum subtracted from the reduced spectrum and divided by the uncertainty in transit depth. The residuals show wavelength-dependent correlations, the origin of which are unknown and left for a future study.

data. For example, the addition of optical and shorter wavelength near-infrared data can help break metallicity degeneracies by better constraining the presence and extent of clouds (e.g. Benneke & Seager, 2013; Wakeford et al., 2018). High altitude clouds or hazes can be inferred by their particle sizes, where small particles scatter shorter wavelengths more efficiently (e.g. Pinhas & Madhusudhan, 2017; Kitzmann & Heng, 2018), thus enabling the disentanglement of a very cloudy, low metallicity atmosphere from a less cloudy, high metallicity atmosphere (Pinhas et al., 2019).

5.5.6 Molecular Detections

Once we found the "single best fit" for the `PICASO` grid to the NIRCam spectrum (10× solar, C/O = 0.229, grey cloud optical depth = 2.6×10^{-3} from 1 to 0.1 bar), we used this as a base model to explore the significance of specific molecular detections. The atmospheric modelling team performed the same Gaussian residual

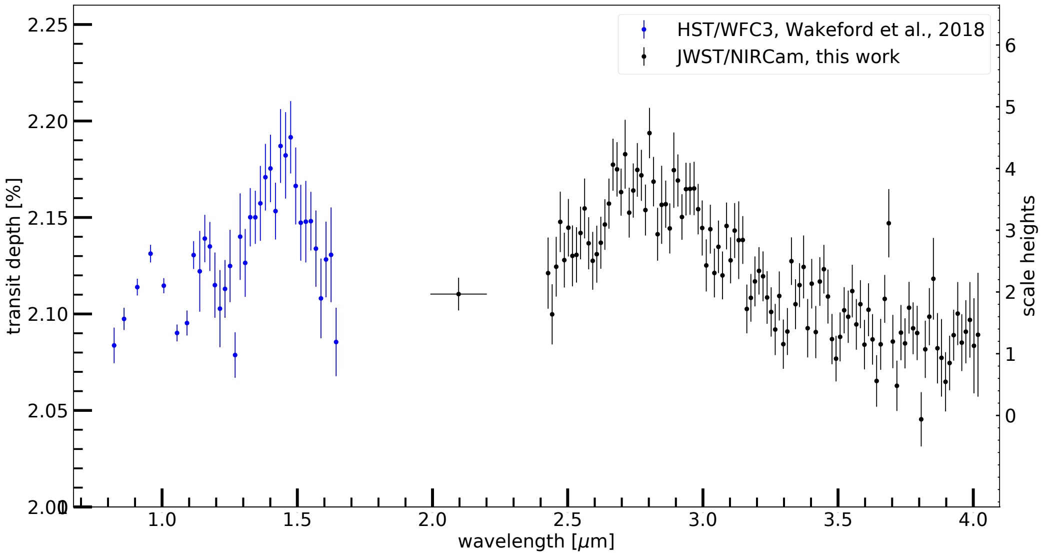

Figure 5.10: **Our *JWST*/ NIRCam spectrum compared to existing *HST* /WFC3 data.** As in Fig. 5.9, but with the addition of *HST* /WFC3 data from 0.8 to 1.65 μm, showing the comparable precision and complementary wavelength coverage offered by the combination of NIRCam and *HST* /WFC3

.

fitting, shown in Fig. 5.11, as for the detection of CO_2 in the NIRSpec/PRISM 3.0 - 5.0 µm analysis (The JWST Transiting Exoplanet Community Early Release Science Team et al., 2023).

First, we tested whether we could improve the best fit in the presence or absence of H_2O, CO_2, CH_4, or H_2S. We reran the best-fit base model by zeroing out each of these species in turn, shown in Fig. 5.14, and then repeating our χ^2 analysis.

We found that while the presence of H_2O, H_2S, and CH_4 resulted in a better χ^2_ν value, only H_2O and H_2S did so in a statistically meaningful way. Specifically, we find a Bayes factor, $\ln(B)$, of 123.2 between the Gaussian residual and constant models for H_2O over the whole NIRCam wavelength range, corresponding to 15.9σ, a strong detection. For CO_2 we find $\ln(B)$ of 0.82 between the Gaussian residual and constant models between 2.4 and 2.9 µm, or 1.9σ, which is a weak or non-detection (Trotta, 2008). CO_2 is strongly detected at 4.3 µm in the NIRSpec data for WASP-39b (The JWST Transiting Exoplanet Community Early Release Science Team et al., 2023; Alderson et al., 2023; Rustamkulov et al., 2023), but the strong overlapping H_2O band at 2.8 µm prevents NIRCam from making a significant CO_2 detection.

Since H_2S does not contain strong molecular features within the NIRCam wavelength range, the Gaussian residual fitting we perform for the detection significance of other molecules is not applicable, and we left its further quantification to more rigorous atmospheric retrieval analyses. Increasing the CH_4 abundance beyond that of the best-fit model also improved the χ^2_ν, though again not to high statistical significance (weak or non-detection at approximately 2σ).

Both WASP-39b NIRSpec datasets (The JWST Transiting Exoplanet Community Early Release Science Team et al., 2023; Alderson et al., 2023; Rustamkulov et al., 2023) observed evidence for a molecular feature near 4.0 µm, which is currently best explained by SO_2. The reddest data points (>4.025 µm) from NIRCam also show an increase that is consistent with this feature seen in the NIRSpec data. However, as shown in Fig. 5.7, these NIRCam data points have very large error bars because the detector throughput drops off dramatically past 4.0 µm. Future investigations to thoroughly explore the physicochemical likelihood of SO_2 in the atmosphere of WASP-39b must rely on wavelengths that can fully capture the complete absorption feature, which is beyond the reach of high fidelity NIRCam/F322W2 measurements.

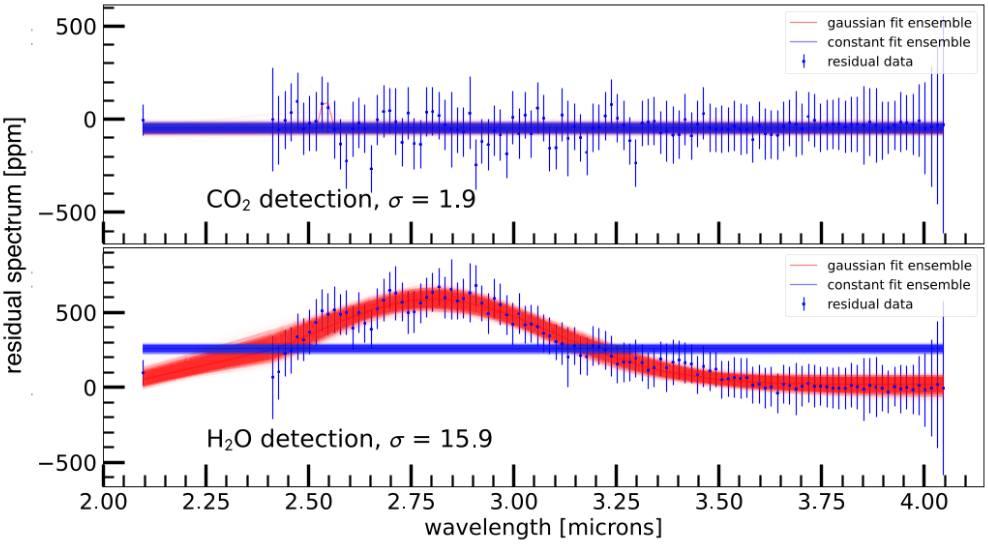

Figure 5.11: **Gaussian residual fitting of H_2O and CO_2.** The blue points show the residual features left after subtracting out the gas in question (CO_2, top, and H_2O, bottom) from the single best-fit model. The Gaussian model ensemble fit to the residual is shown in red; the best-fit Gaussian ensemble to a flat-line model is shown in blue. We strongly detect H_2O at nearly 16σ and show weak evidence for CO_2 (small feature at 2.6 µm) at 1.9σ.

5.6 Discussion and Conclusions

In this chapter I have described the analysis of *JWST* NIRCam observations of exoplanet wASP-39b as also described in the paper Ahrer et al. (2023b), which represent the work of a large team of people under my leadership and coordination.

5.6.1 Data Reduction and Analysis

The data reduction and analysis included three independent reductions of the NIRCam LW spectroscopic data and four independent transit light curve fits and analyses of the reduced data, as well as two independent analyses of the SW photometric data. For both data reductions (LW and SW), customising the *JWST* Science Calibration Pipeline `jwst` to allow for minor adaptions to default steps and values worked best. The wavelength solution available with the reference files provided by the *JWST* CRDS at the time of our analysis was inaccurate (particularly for the blue edge of the LW channel), so we redefined our wavelength values using a polynomial wavelength calibration derived from a planetary nebula observed as part of commissioning (Program 1076).

The team and I found no large systematic structures affecting the LW light curves and a minuscule ramp at the start of the SW light curve (Figure 5.12, panel d). The only other systematic identified was $1/f$ noise. For NIRCam, this manifests as weak structures in the dispersion direction, as shown in Figure 5.12c. We did not correct for $1/f$ noise in the final LW reduction because it did not impact the precision reached by individual spectroscopic light curves (compare `t-shirt` and `Eureka!` in Figure 5.13 for analyses with and without $1/f$ noise corrections). We found the need to remove structures due to $1/f$ noise in the SW reduction.

We found a linear model in time was sufficient to detrend the data, which produced uncertainties of 1.18× the photon noise limit (median of 135 ppm for the transit depths) at a binned spectral resolution of 15 nm ($\simeq$15 pixels). Similarly, the photometric transit-depth precision was 1.35× the noise limit at 53 ppm. The residuals are not time-correlated (see Figure 5.6).

Figure 5.13 displays the final independently derived transit spectra and photometry. Each reduction is consistent with our selected reduction (`Eureka!`) to better than 1σ, as is the broadband 3.6 µm *Spitzer* point (Wakeford et al., 2018). The overall shape of the spectrum is due primarily to absorption of water vapour (broad feature centred at 2.8 µm). The right-axis scale is in equivalent scale heights, where one scale height is approximately 800 km.

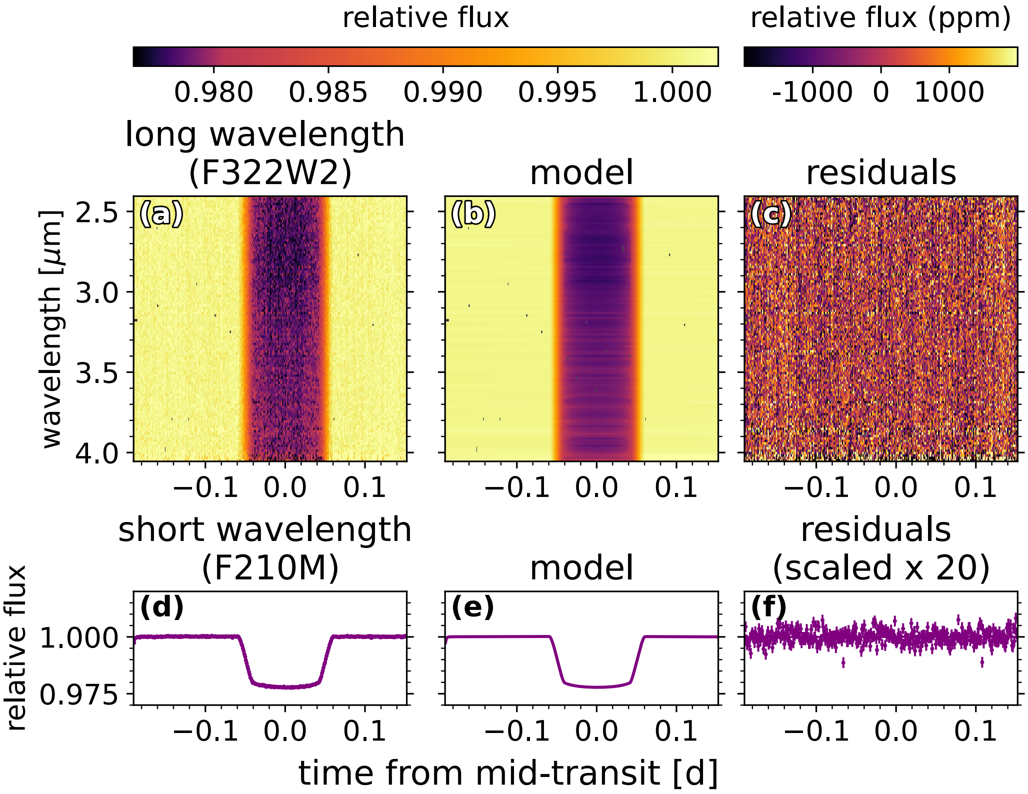

Figure 5.12: **The relative brightness of the WASP-39 planetary system as a function of time and wavelength, as measured by NIRCam.** Panels a, b, and c show the spectroscopic data while panels d, e, and f present the photometric (short wavelength) channel. The extracted flux normalised by the median stellar spectrum is shown in panels a and d, the best-fit transit and systematic models are shown in panels b and e, and the residuals are shown in panels c and f. The flux decrease results from the transit of exoplanet WASP-39b in front of its star. The subtle variation in transit depth around 2.8 µm is due primarily to water vapour in the planet's atmosphere. The vertical striping in the residuals is due to $1/f$ noise.

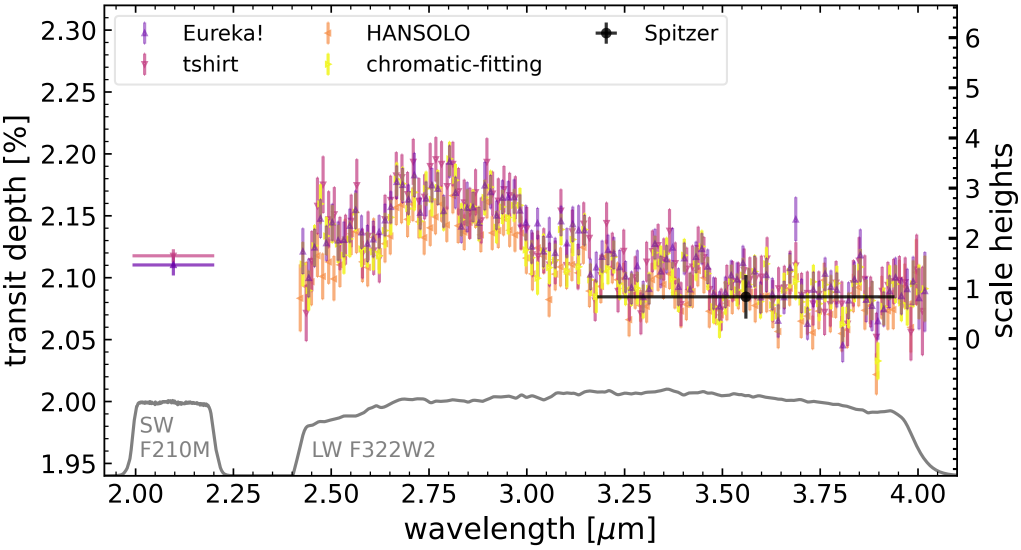

Figure 5.13: The transit spectrum of WASP-39b as measured from JWST's NIRCam instrument. The coloured points with 1σ uncertainties depict our independent analyses of the spectroscopic LW channel (2.420 – 4.025 µm) and photometric SW channel (2.0 – 2.2 µm) with their respective throughputs shown in grey. All analyses agree with the broadband *Spitzer* point (black circle, 3.2 – 4.0 µm). The broad feature centred at 2.8 µm spans 2.5 scale heights (∼2000 km) and is due primarily to water vapour within WASP-39b's atmosphere. We note the consistency between analyses in the fine structure.

5.6.2 Atmospheric grid model analysis

To interpret the presence of other molecules within the planetary atmosphere, we compared the (`Eureka!`) transit spectrum to a set of independently computed atmospheric model grids that spanned a range of cloud properties, metallicity values, and C/O ratios. Figure 5.14 shows a representative best-fit model highlighting the contributions of major molecular absorbers.

Our spectroscopic wavelength range covered by NIRCam/F322W2 includes absorption features due to prominent atmospheric molecules such as H_2O, CO_2, and CH_4. Following the team's model grid search, we definitively confirm the presence of H_2O at nearly 16σ. Water vapour was previously identified in the atmosphere of WASP-39b using Hubble WFC3 observations taken at shorter wavelengths ($[H_2O] = -1.37^{+0.05}_{-0.13}$) (Wakeford et al., 2018). We also see weak evidence for CO_2 absorption, which was also seen with high confidence using NIRSpec/PRISM at 4.3 µm (The JWST Transiting Exoplanet Community Early Release Science Team et al., 2023), but the overlap between the CO_2 feature at 2.8 µm and the broad H_2O feature (il-

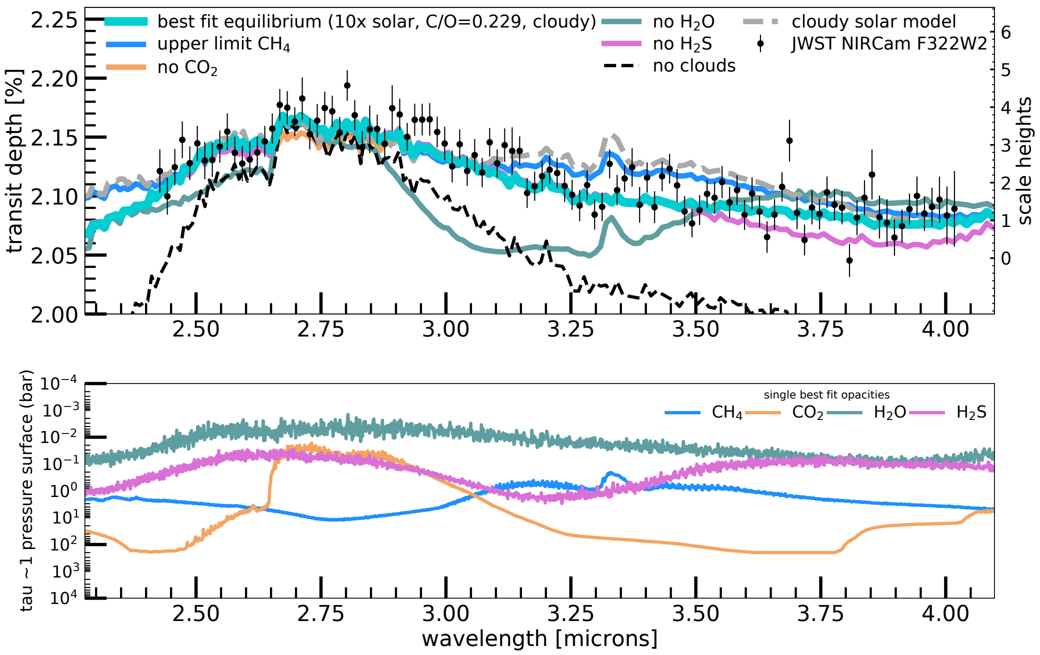

Figure 5.14: **Contributions of key absorbers impacting the spectrum.** Top: The best-fit `PICASO 3.0` equilibrium model (10× solar, C/O = 0.229, moderate grey clouds with cloud optical depth of 2.5×10^{-3}) is shown compared to the `Eureka!` reduction, along with models with individual molecular species removed to show its contribution to the spectrum. Each model is normalized to the data for illustration by offsetting each model to have the same transit depth at 2.8 µm. Water predominately sets the shape of the spectrum, followed by the influence of clouds. The grey dashed line shows a cloudy solar-metallicity and stellar-C/O atmospheric model, illustrating the lack of a strong CH_4 peak seen in the data. Bottom: The opacities of the dominant molecular species at an optical depth of 1 in the atmosphere. In the single best-fit model shown in the lower panel, the methane peak at 3.3 µm is blended out by water absorption. However, manual scaling of CH_4 gives an upper limit of CH_4 abundance (blue line) for the single best-fit model shown in the top panel.

lustrated in Figure 5.14) leads to a more tentative identification here. Each forward model grid prefers significant cloud coverage, which impacts the spectrum at ∼mbar pressures, despite differing cloud parametrisations between grids with varying levels of physical complexity.

5.6.3 Constraints on Metallicity and C/O ratio

In a hot (∼1000 K) solar-metallicity atmosphere with a stellar C/O ratio, CH_4 would be visible as a strong peak at 3.3 µm (grey dashed line in Figure 5.14, Figure 5.9) under thermochemical equilibrium. Such a peak is absent in the reduced spectrum. We quantified this using a residual fitting test. In a higher-metallicity and/or lower-C/O atmosphere, carbon is increasingly partitioned into CO and CO_2, and the CH_4 peak at 3.3 µm disappears. Therefore, the absence of a strong CH_4 peak at 3.3 µm in our data drives the metallicity to higher values and the C/O ratio to lower values.

We scaled the CH_4 volume mixing ratio (VMR) within their single best-fit `PICASO 3.0` model (10× solar metallicity; C/O ratio of 0.229) to determine an upper limit on the abundance of CH_4 at 1 mbar, where it contributes most strongly to the spectrum. Within their single best-fit model scaling, we find an upper limit on CH_4 abundance at 1 mbar of 5.5×10^{-5} (or 55 ppm) VMR, above which the goodness of fit per free parameter, χ^2_ν, gets increasingly worse (i.e., $\chi^2_\nu > 2$). We also tested whether other data reductions favoured best-fit models with stronger methane abundances, but found they did not have any statistical significance.

Driven by this CH_4 upper limit, the single best fit from each grid favours the lowest C/O ratio (0.229, 0.3, and 0.35 for `PICASO 3.0`, `PHOENIX`, and `ATMO`, respectively) within that grid. These best-fit point values for C/O from the three grids agree well with the value of $0.31^{+0.08}_{-0.05}$ found by Wakeford et al. (2018). We examined the effect of an even lower C/O grid point by computing the best-fit `PICASO 3.0` model with a C/O of 0.115, but found no discernible difference in the transit spectrum. Comparing our inferred C/O ratio for WASP-39b's atmosphere to that of its host star, we see that it is substellar ($\leqslant 0.35$, whereas WASP-39 is 0.46 ± 0.09, (Polanski et al., 2022)). Note that the C/O ratio shown here represents the carbon-to-oxygen fraction of the planet's upper atmosphere rather than that of the whole atmosphere, as these NIRCam observations probe approximately the 0.1 – 10 mbar pressure range. WASP-39b's temperature-pressure profile is cool enough for the formation of silicate (i.e., O-bearing) cloud species at depth, which would deplete oxygen from the upper atmosphere and actually *increase* the C/O ratio aloft compared to the bulk planetary envelope (Lodders et al., 2002; Woitke et al., 2018).

Figure 5.15 compares the best-fit metallicity values computed, shown as separate O and C abundances, and C/O ratios to previous studies using *HST* data, as well as results for exoplanets observed at high resolution and Solar System gas giants. The *JWST*/ NIRCam data rule out a super-stellar C/O ratio for WASP-39b. Additionally, Figure 5.15 demonstrates JWST's capability to measure the C/O ratios of giant planet atmospheres by observing both carbon- and oxygen-bearing species, which until now has only been achieved through high-resolution exoplanet observations (e.g. Gandhi et al., 2019; Line et al., 2021). Similar measurements have been difficult to achieve from *HST* alone. Even in the Solar System gas giants, such constraints have proved difficult from both remote sensing and in-situ missions, as the low temperatures of Jupiter, Saturn, Uranus, and Neptune lead to condensation of most oxygen-bearing species (e.g. H_2O, CO_2) at high altitudes, prohibiting accurate measurement of the oxygen abundance (e.g. Li et al., 2020; Atreya et al., 2022).

The apparent substellar C/O ratio inferred from chemical equilibrium models may trace photochemical processes in the planet's upper atmosphere. For example, photochemical destruction of CH_4 in the upper atmosphere could explain the absence of a CH_4 peak at 3.3 µm (e.g. Moses et al., 2011; Tsai et al., 2021). The most likely immediate products of CH_4 photolysis, such as HCN or C_2H_2, would be produced in abundances too small ($\lesssim$ a few parts-per-million (ppm) Moses et al., 2011; Tsai et al., 2021) to be robustly detected with a single NIRCam transit, even from complete CH_4 conversion.

Alternatively, much of the carbon available from CH_4 photolysis could have been oxidized by photodissociated H_2O to form CO and CO_2 (Moses et al., 2011; Agúndez et al., 2014; Hu, 2021; Tsai et al., 2021), though the absolute abundances of these two carbon reservoirs would not have been meaningfully altered since their abundances under chemical equilibrium are already higher than that of CH_4. Other proposed disequilibrium chemistry processes could reduce the CH_4 abundance at the terminator without also decreasing the C/O ratio (Cooper & Showman, 2006; Steinrueck et al., 2019; Molaverdikhani et al., 2019, 2020; Drummond et al., 2020).

We defer the exploration of complex disequilibrium models to atmospheric retrieval analyses using the full set of data provided by the Transiting Exoplanet Community ERS program. That dataset will also constrain the presence of additional oxygen- and carbon-bearing species to provide a more robust constraint on the C/O ratio than we can obtain here. However, the C/O ratio estimate we report from NIRCam is broadly consistent with the C/O ratio found from the other individual ERS WASP-39b datasets, which range from best-fits that are sub-solar (NIRISS/SOSS Feinstein et al., 2023), (NIRSpec/PRISM 3.0 - 5.0 µm The JWST Transiting Exoplanet Community Early Release Science Team et al., 2023) and (NIRSpec/G395H Alderson et al., 2023); to a slightly super-solar upper limit (NIRSpec/PRISM 0.5 - 5.5 µm, Rustamkulov et al., 2023).

If disequilibrium chemistry is not prevalent in the planet's upper atmosphere, the inferred high metallicity and low C/O ratio can be tied back to WASP-39b's formation. The most prominent scenario is that WASP-39b formed via core accretion exterior to the water-ice line and accreted low-C/O solid material in situ and/or

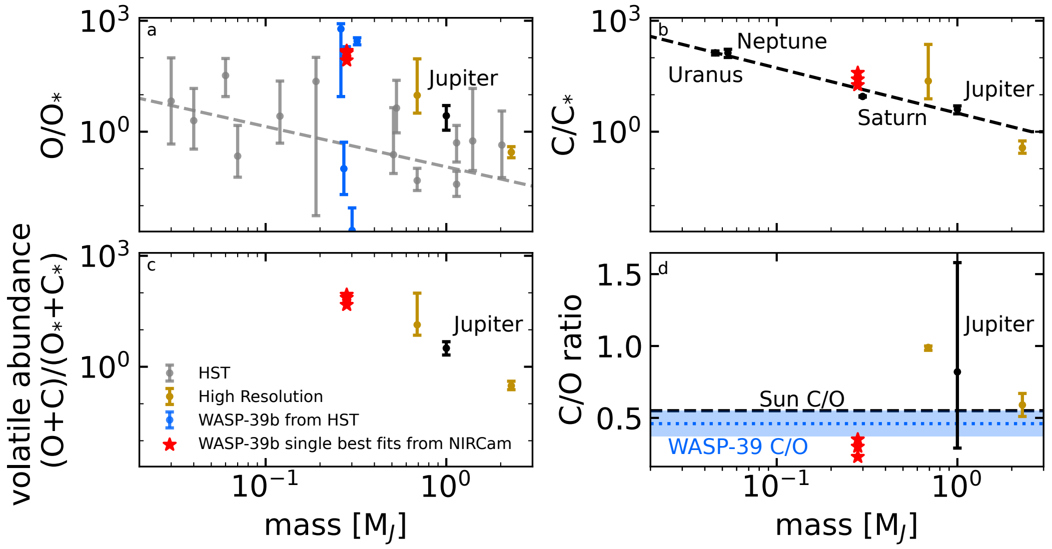

Figure 5.15: Trends in elemental abundances and C/O ratio with planet mass. Panels a, b, and c show the abundances of oxygen, carbon, and net volatiles (oxygen + carbon), respectively, scaled to stellar values. Grey points in panel (a) show *HST* constraints based on $\geqslant 2\sigma$ H_2O detections, with the grey dashed line showing the best-fit trend from Welbanks et al. (2019). Blue points show all previous estimates of the metallicity of WASP-39b from *HST* data, offset in mass for clarity(Welbanks et al., 2019; Wakeford et al., 2018; Pinhas et al., 2019; Tsiaras et al., 2018; Kirk et al., 2019). The black points and dashed line in panel (b) show a fit based on CH_4 abundances of Solar System giant planets (Wong et al., 2004; Fletcher et al., 2009; Karkoschka et al., 2011; Sromovsky et al., 2011). Of the Solar System planets, only Jupiter has a constrained oxygen abundance (from Juno observations of H_2O, Atreya et al., 2022)). Gold points indicate high-resolution observations of H_2O and CO in exoplanets (Gandhi et al., 2019; Line et al., 2021), and red stars show the best-fit values for WASP-39b as measured by *JWST*/ NIRCam for each of the three model grids described in this paper. The black dashed line in panel (d) depicts the solar C/O ratio of 0.55 (Asplund et al., 2009) and the blue dotted line with a shaded 1σ uncertainty region indicates the measured C/O ratio of the star WASP-39 (Polanski et al., 2022). Our results for WASP-39b favour a super-stellar volatile abundance and substellar C/O ratio. However, we emphasise that a full retrieval will be necessary to determine accurate means and 1σ error bars for the NIRCam results.

while migrating inward within the protoplanetary disk (Ali-Dib & Ali-Dib, 2017; Espinoza et al., 2017; Cridland et al., 2019). Taken as such, *JWST* observations could offer important clues regarding the degree to which hot Jupiter atmospheres undergo solid accretion during their early evolution.

5.6.4 Conclusions

Here, we have demonstrated the excellent performance of NIRCam for exoplanet transmission spectroscopy. We conducted independent data reduction and analyses for both the long-wavelength spectroscopy and short-wavelength photometry data. The data showed low systematic noise and our reductions demonstrated remarkable consistency.

We fitted grid models to retrieve the atmospheric properties and we find strong evidence (nearly 16σ) for water vapour in WASP-39b's atmosphere and the absence of a CH_4 feature drives the model fit to low C/O values and high metallicity values. This may be caused by disequilibrium processes in the atmosphere or indicate significant accretion of solid materials during planet formation and migration.

Full retrieval analysis of this NIRCam data is required to fully understand the constraints on the above findings. In addition combined analysis of NIRCam and all other ERS *JWST* transmission spectra of WASP-39b (Alderson et al., 2023; Feinstein et al., 2023; Rustamkulov et al., 2023) in Carter & May et al. (submitted), as well as the retrieval analysis on the full data set (Welbanks et al., in prep.) will provide a clearer picture of WASP-39b's atmosphere.

In summary, with the first *JWST* exoplanet spectra now comparable to the first near-infrared Jupiter spectra (Danielson et al., 1966), the future promises many exciting discoveries and major advancements in the formation, evolution, and atmospheric chemistry of hot Jupiters.

Chapter 6

Conclusions and Future Work

6.1 Summary

In this thesis I discussed the methods for the detection and characterisation of exoplanets and their atmospheres, with a focus on hot Jupiters. These are of particular interest as their formation and migration mechanisms are not fully understood (see Section 1.3.3). In addition, hot Jupiters are the ideal targets for studying a collection of molecular and atomic species in their atmospheres as well as clouds and hazes using transmission spectroscopy (see Section 1.4.5).

I presented the methods used in the data reduction and analysis of transmission spectroscopy data for three hot gaseous exoplanets (see Chapter 2). For two of them, I used data gathered with the EFOSC2 spectrograph mounted on the ground-based telescope NTT, located at the La Silla Observatory in Chile. For the third exoplanet I used the space observatory *JWST* and its instrument NIRCam. I discussed the differences as well as their similarities and how they complement each other in Section 2.6. This is followed by the individual Science chapters.

In Chapter 3 I presented the study of WASP-94Ab, a hot Jupiter, orbiting its host star in an orbit with a 4-day period, published by Ahrer et al. (2022). I used NTT/EFOSC2 observations of one transit and a modified LRG-BEASTS pipeline to extract the time-series spectra from the raw frames and generate the spectroscopic light curves. These light curves were then all fitted simultaneously using nested sampling and a transit model in combination with GPs, where the hyperparameters were linked across all light curves, to derive the transit depth for each wavelength bin. The retrieved transmission spectrum showed significant sodium absorption as well as a steep slope at the bluer end of the spectrum. There were no signs of stellar contamination as the star appears to be inactive, however, it cannot be ruled out entirely. The best-fitting model suggested a super-Rayleigh slope and a relatively clear atmosphere with sodium absorption.

Chapter 4 describes my published study of hot Saturn-sized exoplanet HATS-46b (Ahrer et al., 2023a), which has a 5-day orbit around its host star. Similar to Chapter 3, I reduced and analysed NTT/EFOSC2 data using a modified LRG-BEASTS pipeline. The extracted light curves showed little systematic noise, but were fitted using multiple detrending methods and compared to make sure the errors were not underestimated. The final transmission spectrum appeared almost flat, it did not show any strong variations or features. The best-fitting model was a cloudy atmosphere.

Chapter 5, based on Ahrer et al. (2023b), is different to the two previous ones as I presented observations from the NIRCam instrument on *JWST*. This work was part of a series of four papers, all studying the same exoplanet WASP-39b with different *JWST* instruments or modes as part of the *JWST* Transiting Exoplanet Community Early Release Science (*JWST* TEC ERS) team.

I also utilised a different data reduction and analysis code. The `Eureka!` pipeline was developed by collaborators and myself to be able to reduce data from any *JWST* instruments for exoplanet observations and also fit light curves, essentially including all steps from raw frames to the final transmission spectrum. With this pipeline I extracted the transmission spectrum of WASP-39b and compared it to my collaborators' retrieved spectra. We found a strong water vapour absorption in the atmosphere of WASP-39b which overpowers any other features e.g. we did not find evidence for methane, leading to the result of a low value for the C/O ratio and a high value for the metallicity in WASP-39b's atmosphere.

With the work in this thesis I added three atmospheric characterisation studies of hot Jupiters to the research literature (Ahrer et al., 2022, 2023a,b) using transmission spectroscopy from the ground and from space. Transmission spectroscopy allows us to study exoplanet atmospheres and characterise their composition, learning about their atomic and molecular abundances, constraining clouds and hazes, and testing our physical and chemical models. All of this with the goal to inform our understanding of planet formation and migration of hot Jupiters, to advance our models and methods, and to fulfill our curiosity about extrasolar worlds.

6.2 Conclusions

While the main conclusions of the atmospheric studies of each exoplanet are discussed in detail in each chapter, here I discuss my conclusions about the telescopes, instruments and differences between the observations.

6.2.1 Capabilities of NTT/EFOSC2 and *JWST*/NIRCam

With my work in this thesis I demonstrated the capabilities of NTT/EFOSC2 to observe transmission spectra. I discussed NTT/EFOSC2's systematics for two different grisms and showed that it can successfully be used to identify absorption features (Chapter 3), as well as scattering slopes and clouds (Chapters 3&4) in exoplanet atmospheres.

I also presented the first *JWST* NIRCam transmission spectrum as part of the Early Release Science Transiting Exoplanet Community. I discussed data reduction and analysis methods by comparing independent pipelines and showed NIRCam's capabilities with regards to exoplanet transmission spectroscopy with our findings of water vapour in the atmosphere and lack of methane.

6.2.2 Optical versus infrared observations

The infrared wavelength ranges allow for observations of key molecular bands, including carbon- and oxygen-bearing species such as H_2O and CO_2 and photochemical products such as SO_2. These are needed to gain insights into planet formation and migration mechanisms of hot Jupiters by probing for mass-metallicity relations and C/O ratios, as discussed in Section 1.4.5.

The optical waveband on the other hand probes for atomic absorptions such as sodium and potassium, but most importantly constrains the presence or absence of clouds and hazes as well as stellar contamination (see Sections 1.4.5 & 2.6.2). These are crucial for understanding the cloud and haze levels, which are crucial atmospheric properties that influence the atmospheric abundances retrieved in the infrared wavelength ranges. Similarly, the lack of information on the stellar contamination level can cause degeneracies in retrieved models as features might be attributable to both planet and star (e.g. in the case of Moran et al., 2023).

In summary, transmission spectroscopy observations in both optical and infrared wavelength ranges are needed to gain an accurate picture of the composition of exoplanet atmospheres.

6.2.3 Ground-based versus space observations

Observing from the ground has a major disadvantage in that the Earth's own atmosphere complicates inferences about exoplanet atmospheres. For example as discussed in Chapter 4, where a telluric absorption line of O_2 caused confusion over the origin of a feature observed in the transmission spectrum. It could have been attributed to potassium in the atmosphere of HATS-46b, however, due to the strong, nearby telluric signal of O_2 A-band I chose to dismiss this data point in the following atmospheric analysis. In addition to that, a lot of awarded ground-based observing nights are lost due to bad weather.

On the other hand, observations with space telescopes do not have to deal with Earth's atmosphere, however, they have their own drawbacks e.g. the competitiveness of the observations, and the long planning and building time scales for launch which also leads to instruments being behind with the current technology.

Both ground-based and space observations have limitations when it comes to the observability of targets e.g. ground-based telescopes are limited by the nighttime and seasons, while space telescopes are limited by their orbits and pointing.

In the end, both ground-based and space telescopes have their place in exoplanet atmospheres. Ground-based provide easier access to data and thus larger sample sizes, can confirm space observations and often have a faster turnaround. In addition, they can also be repaired and updated with new and improved instruments. Space observations provide a more limited sample of observations and limited in capabilities, however, they are not affected by Earth's atmosphere, allowing more reliable results in particular in the infrared wavelength ranges.

6.3 Ongoing and Future Work

6.3.1 LRG-BEASTS

The LRG-BEASTS survey has gathered a large sample of observations of hot Jupiters in the last few years, including > 20 nights of past and upcoming NTT/EFOSC2 observations that I am the PI of, that have not been fully analysed to date.

A couple of these observations show strong systematics, e.g. due to cloud coverage during the night, and require another transit to achieve the precision necessary to draw conclusions from the retrieved transmission spectrum. Most of these will have extra transit observations taken in the upcoming semester in order to fully understand systematics in our data.

Thus future work of mine will include the reduction and analysis of these data sets, focusing on the ones that have been or are scheduled to be observed in the infrared to provide complementary wavelength information.

6.3.2 WASP-94Ab

HARPS observations that were used in Chapter 3 to derive the stellar activity indicator $\log R'_{\rm HK}$ are part of a high-resolution transmission spectroscopy program (Hot Exoplanet Atmospheres Resolved with Transit Spectroscopy; HEARTS) to look for absorption features in exoplanet atmospheres (PI: Ehrenreich, ESO programme 097.C-1025(B)). I started working on these data recently in collaboration with the PI and Co-Is of this program to see whether we can confirm the sodium detection at high resolution, run combined low and high resolution retrieval analysis, as well as constrain WASP-94Ab's projected angle of its misaligned orbit further using the Rossiter-McLaughlin effect (see Section 1.2.2).

In addition, a *JWST* proposal for Cycle 2 (ID 3154, PI Ahrer) has been accepted to observe WASP-94A b in transmission with NIRSpec/G395H. Due to its misaligned and retrograde orbit, it is expected to have undergone high-eccentricity (disk-free) migration (see Section 1.3.3 for migration processes), predicting a value for C/O ratio between 0.5 and 0.7, which is higher compared to planets with similar metallicity that migrated via disk migration, as shown in Fig. 6.1.

WASP-94Ab also ties in well with another program that was approved in *JWST* cycle 2 which targeted the question of whether atmospheric composition actually traces formation by observing aligned and misaligned hot Jupiters as a testbed (ID 3838, PI Kirk, Co-PI Ahrer).

6.3.3 WASP-39b

My collaborators and I are now working on providing a transmission spectrum of WASP-39b including all instruments and modes observed with *JWST*, using one reduction code and consistent light curve fitting (Carter & May et al., submitted). Collaborators are also working on running multiple different retrieval codes and setups on all data sets simultaneously (Welbanks et al., in prep).

In addition to the original ERS observations of WASP-39b with NIRSpec/PRISM, NIRSpec/G395H, NIRCam/F322W2 and NIRISS/SOSS our team was also awarded observing time to take data of a transit with MIRI/LRS. This took place in February 2023 with the aim of confirming the ERS findings of sulfur dioxide in the atmosphere (Alderson et al., 2023; Rustamkulov et al., 2023), which is known to also exhibit a feature in MIRI wavelength range (Tsai et al., 2023). My collaborators and I

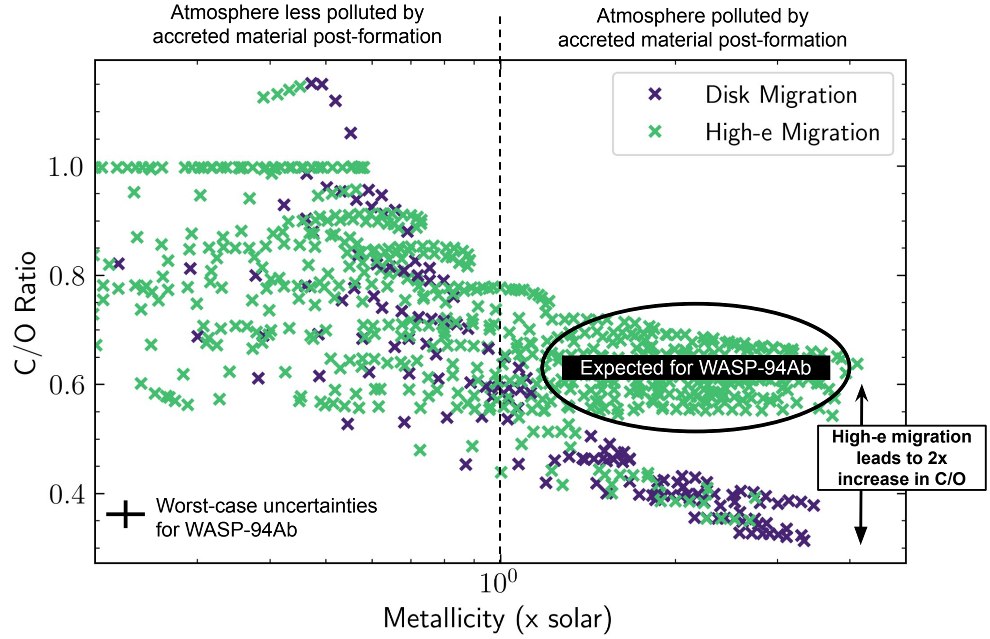

Figure 6.1: Figure from the *JWST* proposal, accepted to be observed in Cycle 2 (ID 3154, PI Ahrer). It shows the effect of disk-driven and high-eccentricity migration on the C/O ratio and metallicity in the atmosphere of hot Jupiters, adapted from Booth et al. (2017). WASP-94Ab is predicted to have undergone migration via the high-eccentricity mechanism and its metallicity was suggested to be super-solar, see Chapter 3. Thus I show here the expected values of the C/O (indicated by the circle) which we can determine using our observations with *JWST* NIRSpec/G395H. Figure Credit: I computed this based on code from my collaborator and Co-I J. Kirk who reconstructed it from a figure in Booth et al. (2017).

reduced and analysed the data recently and this is ongoing work (Powell et al., in prep).

6.3.4 Eureka! pipeline

With every *JWST* data set that is being analysed using our `Eureka!` pipeline we make new additions, find new bugs and/or it has to be adapted due to updates in utilised packages such as the default `jwst` pipeline.

In *JWST* proposal Cycle 2 our `Eureka!` team had an Archival Research (AR) program accepted (ID 3273, PI K. B. Stevenson and Co-PI T. Bell), which will provide the necessary funds to build on `Eureka!` by (1) expanding to other time-series instrument modes that have not been previously supported, (2) adding more flexibility for the user in the light curve fitting, (3) improving and/or adding to our supported algorithms, (4) solving user issues and problems brought to us by `Eureka!` users. The aim is to make `Eureka!` a more stable, robust and reliable pipeline for all future *JWST* (and *HST*) exoplanet observations.

6.4 Outlook

6.4.1 *JWST*

At the time of writing this thesis *JWST* has only been conducting less than one year of science observations. There will be a lot of data and studies published using *JWST* data in the next decade (the mission is expected to last for 20 years).

While I am excited about the insights we will gain from C/O ratios and metallicity in terms of understanding the origins of hot Jupiters, I am also particularly looking forward to studies of limb asymmetries (e.g. GO #3969, PI: Espinoza). Both morning and evening contribute to the measured transit depth in transmission spectroscopy, but the two are predicted to inherit different properties (temperature, clouds, molecular abundances, etc.) due to atmospheric circulation (e.g. Dobbs-Dixon et al., 2011; Von Paris et al., 2016; Powell et al., 2019; Espinoza & Jones, 2021). This leads to asymmetric transit light curves and with *JWST* this effect will be used to study the properties of morning and evening side of hot Jupiters and test the model predictions.

Within the exoplanet community there is also a push towards smaller, terrestrial planets and the Trappist-1 system has gotten a lot of time in both *JWST* cycles 1 and 2 to observe and characterise the planets in the system. I am looking forward to seeing the results of these studies and what atmospheric constraints the teams can achieve with *JWST*.

Director's Discretionary program

Exoplanet science was listed as a key science area for the 2020s in the Astro2020 Decadal Survey (National Academies of Sciences Engineering and Medicine, 2021) and as a result, it was announced that there will be a large-scale Director's Discretionary exoplanet program starting in *JWST*'s cycle 3 (1 July 2024). At the date of writing this thesis a working group of senior scientists has been formed to identify and formulate a program. I am looking forward to seeing which exoplanets will be observed as part of this program and which science cases will be targeted.

Meetings within the exoplanet community have emerged to discuss ideas for this large-scale program, including within the ERS TEC team which I joined.

Programs suggested include large transmission and/or emission spectroscopy surveys of gas giants e.g. filling in gaps of hot Jupiters or hot Neptune-sized planets to provide statistics and study populations. There is also discussion about doing ‘easy’ Science cases versus doing ‘risky’ observations (too risky for the normal proposal calls) that might not work out e.g. looking for exomoons. In the end, it is up to the working group to formulate a proposal but I expect a couple of white papers to voice their ideas before deciding.

6.4.2 Synergies between high and low resolution exoplanet spectra

I expect that there will be an increase in studies that use low and high resolution observations, e.g. by combined atmospheric retrieval studies of transmission spectra. But there are also other synergies I expect will be relevant in the future. For example, as *JWST* will be used to resolve the terminator region in transmission spectroscopy (see Section 6.4.1), this has also been studied recently in the high resolution transmission spectroscopy regime (e.g. Ehrenreich et al., 2020; Kesseli & Snellen, 2021; Gandhi et al., 2022). It will be exciting to see whether the atmospheric constraints found by limb asymmetries studies using low and high resolution observations are consistent and what type of constraints we can achieve.

6.4.3 Exoplanet Detection

While new atmospheric studies of already known exoplanets are planned and undergoing, we cannot forget that the number of exoplanets discovered is increasing as well e.g. with TESS (Transiting Exoplanet Survey Satellite; Ricker et al., 2015). In addition new ground-based transit surveys e.g. ASTEP (Antarctic Search for Transiting ExoPlanets; Crouzet et al., 2010) on Antarctica access new planet populations and with amateur astronomers help classify transits (e.g. TESS Planet Hunters; Eisner et al., 2020, 2021) I expect a continous flow of newly detected exoplanets, especially smaller planets as we improve our telescopes/instruments and our methods. I also look forward to a larger sample of Jupiter-sized planets at larger distances, ‘warm Jupiters’, so we can study their atmospheres and composition e.g. to measure the C/O ratio and metallicity of planets that have not migrated.

6.4.4 Missions and Telescopes

The field of exoplanets is ever-growing and a lot of exciting new telescopes, instruments and space missions are planned. This includes *PLATO* (PLAnetary Transits and Oscillations of stars; Rauer et al., 2014) and *Ariel* (Tinetti et al., 2018) within the next decade, or planned missions like *LIFE* (Large Interferometer For Exoplanets; Quanz et al., 2022) and *HWO* (Habitable Worlds Observatory). While *PLATO*'s mission focuses on the detection of terrestrial planets, *Ariel* will observe the atmospheres of one thousand exoplanets in the infrared wavelength ranges. *LIFE*'s objective is to obtain emission spectra of tens of terrestrial exoplanets to determine their habitability using interferometry. HWO was listed as one of NASA's top priorities in their Astro2020 Decadal report (National Academies of Sciences Engineering and Medicine, 2021) and its goal is to directly image terrestrial planets and characterise their atmosphere.

Large ground-based telescopes, which are currently expected to have first light by the end of this decade, ESO's Extremely Large Telescope (ELT), Giant Magellan Telescope (GMT) and the Thirty Meter Telescope (TMT) are going to expand our capabilities in the high resolution as well as the direct imaging regime. For example, ELT's instrument METIS will cover the infrared wavelength ranges 3–5 µm in high resolution spectroscopy, as well as allows for exoplanet imaging down to 14µm[1].

6.4.5 Conclusions

In conclusion, all of these telescopes and instruments will be working in tandem to further understand exoplanet atmospheres and their processes. I am particularly excited about seeing new findings about hot Jupiters and their formation and migration mechanisms – this hopefully includes my own studies! I am also looking forward to scientific advances in bringing atmospheric 3D structures and observations together e.g. by modelling asymmetric light curves and working in synergy with high resolution spectroscopy.

Finally, with more exoplanet missions and new telescopes to come online within the next decade, I expect/hope that we will find unexpected results that surprise us. For example, as happened within the ERS team when we first saw the 'mystery' absorber in the atmosphere of WASP-39b (The JWST Transiting Exoplanet Community Early Release Science Team et al., 2023), now identified as SO_2 (Alderson et al., 2023; Rustamkulov et al., 2023) as a product of photochemistry (Tsai et al., 2023).

Working in this field, contributing by studying exoplanet atmospheres with ground-based and space telescopes, and looking ahead is incredibly exciting. I cannot wait to see what new discoveries are next and I am thrilled to be a part of this.

---

[1] `https://elt.eso.org/instrument/METIS/`, accessed 01/06/2023

Bibliography

Ackerman A. S., Marley M. S., 2001, The Astrophysical Journal, 556, 872

Addison B. C., et al., 2014, arXiv, p. arXiv:1403.0652

Agúndez M., Parmentier V., Venot O., Hersant F., Selsis F., 2014, Astronomy & Astrophysics, 564, A73

Ahrer E., Wheatley P. J., Kirk J., Gandhi S., King G. W., Louden T., 2022, Monthly Notices of the Royal Astronomical Society, 510, 4857

Ahrer E., Wheatley P. J., Gandhi S., Kirk J., King G. W., Louden T., Welbanks L., 2023a, Monthly Notices of the Royal Astronomical Society

Ahrer E. M., et al., 2023b, Nature, 614, 653

Aigrain S., Pont F., Zucker S., 2012, Monthly Notices of the Royal Astronomical Society, 419, 3147

Aigrain S., Parviainen H., Pope B. J., 2016, Monthly Notices of the Royal Astronomical Society, 459, 2408

Akeson R. L., et al., 2013, Publications of the Astronomical Society of the Pacific, 125, 989

Alam M. K., et al., 2021, The Astrophysical Journal Letters, 906, L10

Albrecht S., et al., 2012, Astrophysical Journal, 757, 18

Albrecht S. H., Dawson R. I., Winn J. N., 2022, Publications of the Astronomical Society of the Pacific, 134, 082001

Alderson L., et al., 2020, Monthly Notices of the Royal Astronomical Society, 497, 5182

Alderson L., et al., 2023, Nature, 614, 664

Ali-Dib M., Ali-Dib M., 2017, Monthly Notices of the Royal Astronomical Society, 467, 2845

Ambikasaran S., Foreman-Mackey D., Greengard L., Hogg D. W., O'Neil M., 2014, IEEE Transactions on Pattern Analysis and Machine Intelligence, 38, 252

Arcangeli J., et al., 2019, Astronomy and Astrophysics, 625, A136

Asplund M., Grevesse N., Sauval A. J., Scott P., 2009, Annual Review of Astronomy and Astrophysics, 47, 481

Atreya S. K., Crida A., Guillot T., Li C., Lunine J. I., Madhusudhan N., Mousis O., Wong M. H., 2022, arXiv, p. arXiv:2205.06914

Azzam A. A., Lodi L., Yurchenko S. N., Tennyson J., 2015, Journal of Quantitative Spectroscopy and Radiative Transfer, Volume 161, p. 41-49., 161, 41

Bachelet E., Penny M., 2019, The Astrophysical Journal Letters, 880, L32

Baeyens R., Decin L., Carone L., Venot O., Agúndez M., Mollière P., 2021, Monthly Notices of the Royal Astronomical Society, 505, 5603

Baeyens R., Konings T., Venot O., Carone L., Decin L., 2022, Monthly Notices of the Royal Astronomical Society, 512, 4877

Bailer-Jones C. A. L., Rybizki J., Fouesneau M., Mantelet G., Andrae R., 2018, The Astronomical Journal, 156, 58

Bakos G., Noyes R., Kovács G., Stanek K., Sasselov D., Domsa I., 2004, Publications of the Astronomical Society of the Pacific, 116

Bakos G. A., et al., 2013, Publications of the Astronomical Society of the Pacific, 125, 154

Balan S. T., Lahav O., 2009, Monthly Notices of the Royal Astronomical Society, 395, 1936

Baranne A., et al., 1996, Astronomy and Astrophysics Supplement Series, 119

Barber R. J., Tennyson J., Harris G. J., Tolchenov R. N., 2006, Monthly Notices of the Royal Astronomical Society, 368, 1087

Barclay T., Kostov V. B., Colón K. D., Quintana E. V., Schlieder J. E., Louie D. R., Gilbert E. A., Mullally S. E., 2021, The Astronomical Journal, 162

Barman T. S., Hauschildt P. H., Allard F., 2001, The Astrophysical Journal, Volume 556, Issue 2, pp. 885-895., 556, 885

Barragán O., et al., 2019, Monthly Notices of the Royal Astronomical Society, 490, 698

Barstow J. K., 2020, Monthly Notices of the Royal Astronomical Society, 497, 4183

Barstow J. K., Aigrain S., Irwin P. G. J., Sing D. K., 2017, The Astrophysical Journal, 834, 50

Batalha N. E., Marley M. S., Lewis N. K., Fortney J. J., 2019, The Astrophysical Journal, 878, 70

Batygin K., Bodenheimer P. H., Laughlin G. P., 2016, The Astrophysical Journal, 829, 114

Bean J. L., et al., 2018, Publications of the Astronomical Society of the Pacific, 130, 114402

Bean J. L., et al., 2023, Nature, pp 1–2

Beaulieu J. P., et al., 2006, Nature, 439, 437

Bell T. J., et al., 2021, Monthly Notices of the Royal Astronomical Society, 504, 3316

Bell T. J., et al., 2022, JOSS, 7, 4503

Bell T. J., et al., 2023, arXiv, p. arXiv:2301.06350

Benedict G. F., et al., 2002, The Astrophysical Journal, 581

Benedict G. F., et al., 2006, The Astronomical Journal, 132

Benedict G. F., McArthur B. E., Nelan E. P., Wittenmyer R., Barnes R., Smotherman H., Horner J., 2022, The Astronomical Journal, 163

Benneke B., Seager S., 2013, Astrophysical Journal, 778

Bennett D. P., et al., 2014, Astrophysical Journal, 785

Bento J., et al., 2014, Monthly Notices of the Royal Astronomical Society, 437, 1511

Birkby J. L., de Kok R. J., Brogi M., de Mooij E. J. W., Schwarz H., Albrecht S., Snellen I. A. G., 2013, Monthly Notices of the Royal Astronomical Society: Letters, 436, L35

Birkby J. L., Kok R. J. d., Brogi M., Schwarz H., Snellen I. A. G., 2017, The Astronomical Journal, 153, 138

Bixel A., et al., 2019, The Astronomical Journal, 157, 68

Bond I. A., et al., 2004, The Astrophysical Journal, 606, L155

Bond I. A., et al., 2017, Monthly Notices of the Royal Astronomical Society, 469, 2434

Bonomo A. S., et al., 2017, Astronomy and Astrophysics, 602, 107

Booth R. A., Clarke C. J., Madhusudhan N., Ilee J. D., 2017, Monthly Notices of the Royal Astronomical Society, 469

Borsa F., et al., 2021, Astronomy and Astrophysics, 645, A24

Borsato N. W., Hoeijmakers H. J., Prinoth B., Thorsbro B., Forsberg R., Kitzmann D., Jones K., Heng K., 2023, A&A, 673, A158

Borucki W. J., et al., 2010, Science, 327

Boss A. P., 1997, Science, 276

Bowens R., et al., 2021, Astronomy & Astrophysics, 653

Brahm R., et al., 2018, The Astronomical Journal, 155, 112

Brogi M., Snellen I. A. G., de Kok R. J., Albrecht S., Birkby J., de Mooij E. J. W., 2012, Nature, 486, 502

Brogi M., De Kok R. J., Birkby J. L., Schwarz H., Snellen I. A., 2014, Astronomy and Astrophysics, 565, A124

Brogi M., et al., 2023, The Astronomical Journal, 165, 91

Brown T. M., 2001, The Astrophysical Journal, 553, 1006

Bryant E. M., et al., 2020, Monthly Notices of the Royal Astronomical Society, 494, 5872

Buchner J., et al., 2014, Astronomy and Astrophysics, 564

Buzzoni B., et al., 1984, The Messenger, 38, 9

Carleo I., et al., 2022, The Astronomical Journal, 164, 101

Carone L., et al., 2021, Astronomy and Astrophysics, 646, A168

Carter J. A., Winn J. N., 2009, Astrophysical Journal, 704, 51

Carter A. L., et al., 2020, Monthly Notices of the Royal Astronomical Society, 494, 5449

Cartier K. M. S., et al., 2016, The Astronomical Journal, 153, 34

Casasayas-Barris N., et al., 2017, A&A, 608, A135

Casasayas-Barris N., et al., 2020, Astronomy and Astrophysics, 635, A206

Casasayas-Barris N., et al., 2021, Astronomy & Astrophysics, 647, A26

Chachan Y., et al., 2019, The Astronomical Journal, 158, 244

Chachan Y., Knutson H. A., Lothringer J., Blake G. A., 2023, The Astrophysical Journal, 943

Chang S.-H., Gu P.-G., Bodenheimer P., 2009, The Astrophysical Journal, Volume 708, Issue 2, pp. 1692-1702 (2010)., 708, 1692

Changeat Q., Edwards B., Al-Refaie A. F., Morvan M., Tsiaras A., Waldmann I. P., Tinetti G., 2020, The Astronomical Journal, 160, 260

Charbonneau D., Brown T. M., Latham D. W., Mayor M., 2000, The Astrophysical Journal, 529, L45

Charbonneau D., Brown T. M., Noyes R. W., Gilliland R. L., 2002, The Astrophysical Journal, 568, 377

Chauvin G., Lagrange A. M., Dumas C., Zuckerman B., Mouillet D., Song I., Beuzit J. L., Lowrance P., 2004, A&A, 425, L29

Chen G., et al., 2018, Astronomy and Astrophysics, 616, A145

Chen G., Casasayas-Barris N., Pallé E., Welbanks L., Madhusudhan N., Luque R., Murgas F., 2020, Astronomy and Astrophysics, 642, A54

Chen G., et al., 2021, Monthly Notices of the Royal Astronomical Society, 500, 5420

Chen G., Wang H., van Boekel R., Pallé E., 2022, The Astronomical Journal, 164, 173

Christie D. A., et al., 2021, Monthly Notices of the Royal Astronomical Society, 506, 4500

Cieza L., et al., 2007, The Astrophysical Journal, 667

Claret A., 2000, Astronomy and Astrophysics, v.363, p.1081-1190 (2000), 363, 1081

Cooper C. S., Showman A. P., 2006, The Astrophysical Journal, 649

Coulombe L.-P., et al., 2023, Nature, 620, 292

Cridland A. J., Pudritz R. E., Alessi M., 2016, Monthly Notices of the Royal Astronomical Society, 461

Cridland A. J., Van Dishoeck E. F., Alessi M., Pudritz R. E., 2019, Astronomy & Astrophysics, 632, A63

Crossfield I. J. M., Kreidberg L., 2017, The Astronomical Journal, 154, 261

Crossfield I. J. M., Knutson H., Fortney J., Showman A. P., Cowan N. B., Deming D., 2012, The Astrophysical Journal, 752, 81

Crossfield I. J. M., et al., 2022, The Astrophysical Journal Letters, 937

Crouzet N., et al., 2010, Astronomy and Astrophysics, 511, A36

Csizmadia S., Pasternacki T., Dreyer C., Cabrera J., Erikson A., Rauer H., 2013, Astronomy and Astrophysics, 549, A9

Damasso M., et al., 2020, Astronomy and Astrophysics, 642, A133

Damiano M., et al., 2022, The Astronomical Journal, 164, 225

Danielson R. E., Danielson E. R., 1966, ApJ, 143, 949

Dawson R. I., Johnson J. A., 2018, Origins of Hot Jupiters, doi:10.1146/annurev-astro-081817-051853

De Kok R. J., Brogi M., Snellen I. A., Birkby J., Albrecht S., De Mooij E. J., 2013, Astronomy and Astrophysics, 554

De Wit J., Gillon M., Demory B. O., Seager S., 2012, Astronomy and Astrophysics, 548, A128

Delrez L., et al., 2016, Monthly Notices of the Royal Astronomical Society, 458, 4025

Deming D., et al., 2015, Astrophysical Journal, 805, 132

Dobbs-Dixon I., Agol E., Burrows A., 2011, The Astrophysical Journal, 751, 87

Dorval P., et al., 2020, Astronomy and Astrophysics, 635

Doyon R., et al., 2012, SPIE, 8442, 84422R

Drummond B., Tremblin P., Baraffe I., Amundsen D. S., Mayne N. J., Venot O., Goyal J., 2016, Astronomy and Astrophysics, 594

Drummond B., et al., 2020, Astronomy & Astrophysics, 636, A68

Ehrenreich D., et al., 2020, Nature

Einstein A., 1936, Lens-like action of a star by the deviation of light in the gravitational field, doi:10.1126/science.84.2188.506

Eisner N. L., et al., 2020, Monthly Notices of the Royal Astronomical Society, 494, 750

Eisner N. L., et al., 2021, Monthly Notices of the Royal Astronomical Society, 501, 4669

Eistrup C., Walsh C., Van Dishoeck E. F., 2018, Astronomy and Astrophysics, 613

Espinoza N., Jones K., 2021, The Astronomical Journal, 162, 165

Espinoza N., Jordán A., 2015, Monthly Notices of the Royal Astronomical Society, 450, 1879

Espinoza N., Fortney J. J., Miguel Y., Thorngren D., Murray-Clay R., 2017, The Astrophysical Journal, 838, L9

Espinoza N., et al., 2019, Monthly Notices of the Royal Astronomical Society, 482, 2065

Evans T. M., Aigrain S., Gibson N., Barstow J. K., Amundsen D. S., Tremblin P., Mourier P., 2015, Monthly Notices of the Royal Astronomical Society, 451, 680

Evans T. M., et al., 2016, ApJL, 822, L4

Evans T. M., et al., 2017a, Nature, 548, 58

Evans T. M., et al., 2017b, Nature, 548, 58

Evans T. M., et al., 2018, The Astronomical Journal, 156, 283

Faber J. A., Rasio F. A., Willems B., Faber J. A., Rasio F. A., Willems B., 2005, Icarus, 175, 248

Fabrycky D. C., Winn J. N., 2009, Astrophysical Journal, 696, 1230

Faedi F., et al., 2011, Astronomy and Astrophysics, 531, A40

Faria J. P., Haywood R. D., Brewer B. J., Figueira P., Oshagh M., Santerne A., Santos N. C., 2016, Astronomy and Astrophysics, 588, 31

Feinstein A. D., et al., 2023, Nature, 614, 670

Feroz F., Hobson M. P., 2008, Monthly Notices of the Royal Astronomical Society, 384, 449

Feroz F., Hobson M. P., Bridges M., 2009, Monthly Notices of the Royal Astronomical Society, 398, 1601

Ferruit P., Birkmann S., Böker T., Sirianni M., Giardino G., de Marchi G., Alves de Oliveira C., Dorner B., 2014, Space Telescopes and Instrumentation 2014: Optical, Infrared, and Millimeter Wave, 9143, 91430A

Fischer P. D., et al., 2016, The Astrophysical Journal, 827, 19

Fisher C., Heng K., 2018, Monthly Notices of the Royal Astronomical Society, 481, 4698

Fletcher L. N., Orton G. S., Teanby N. A., Irwin P. G., Bjoraker G. L., 2009, Icarus, 199, 351

Flower P. J., Flower J. P., 1996, ApJ, 469, 355

Foreman-Mackey D., Hogg D. W., Lang D., Goodman J., 2013, Publications of the Astronomical Society of the Pacific, 125, 306

Foreman-Mackey D., et al., 2021, Journal of Open Source Software, 6, 3285

Fortney J. J., Sudarsky D., Hubeny I., Cooper C. S., Hubbard W. B., Burrows A., Lunine J. I., 2003, The Astrophysical Journal, 589

Fortney J. J., Marley M. S., Lodders K., Saumon D., Freedman R., 2005, The Astrophysical Journal, 627, L69

Fortney J. J., Lodders K., Marley M. S., Freedman R. S., Fortney J. J., Lodders K., Marley M. S., Freedman R. S., 2008, ApJ, 678, 1419

Fortney J. J., Dawson R. I., Komacek T. D., 2021, Journal of Geophysical Research: Planets, 126, e06629

Fossati L., Ayres T. R., Haswell C. A., Bohlender D., Kochukhov O., Flöer L., 2013, Astrophysical Journal Letters, 766, L20

Fu G., Deming D., Knutson H., Madhusudhan N., Mandell A., Fraine J., 2017, The Astrophysical Journal, 847, L22

Fu G., et al., 2022, The Astrophysical Journal Letters, 925, L3

Gaia Collaboration Brown A. G. A., Vallenari A., Prusti T., de Bruijne J. H. J., Babusiaux C., Bailer-Jones C. A. L., 2018, Astronomy and Astrophysics, 616, A1

Gammie C. F., 2001, The Astrophysical Journal, 553

Gandhi S., Madhusudhan N., 2018, Monthly Notices of the Royal Astronomical Society, 474, 271

Gandhi S., Madhusudhan N., 2019, Monthly Notices of the Royal Astronomical Society, 485, 5817

Gandhi S., Madhusudhan N., Hawker G., Piette A., 2019, The Astronomical Journal, 158

Gandhi S., et al., 2020, Monthly Notices of the Royal Astronomical Society, 495

Gandhi S., Kesseli A., Snellen I., Brogi M., Wardenier J. P., Parmentier V., Welbanks L., Savel A. B., 2022, Monthly Notices of the Royal Astronomical Society, 515, 749

Gao P., Powell D., 2021, The Astrophysical Journal Letters, 918

Gao P., et al., 2020, Nature Astronomy, 4

Garcia L. J., Moran S. E., Rackham B. V., Wakeford H. R., Gillon M., De Wit J., Lewis N. K., 2022, Astronomy and Astrophysics, 665, A19

Gardner J. P., et al., 2006, Space Science Reviews, 123, 485

Garhart E., et al., 2020, The Astronomical Journal, 159, 137

Giacobbe P., et al., 2021, Nature, 592, 205

Gibson N. P., Pont F., Aigrain S., 2011, Monthly Notices of the Royal Astronomical Society, 411

Gibson N. P., Aigrain S., Roberts S., Evans T. M., Osborne M., Pont F., 2012a, Monthly Notices of the Royal Astronomical Society, 419, 2683

Gibson N. P., et al., 2012b, Monthly Notices of the Royal Astronomical Society, 422, 753

Gibson N. P., Aigrain S., Barstow J. K., Evans T. M., Fletcher L. N., Irwin P. G., 2013, Monthly Notices of the Royal Astronomical Society, 436, 2974

Gibson N. P., et al., 2020, Monthly Notices of the Royal Astronomical Society

Gillon M., et al., 2017, A&A, 601, A117

Goldreich P., Tremaine S., 1980, The Astrophysical Journal, 241, 425

Goyal J. M., et al., 2018, Monthly Notices of the Royal Astronomical Society, 474, 5158

Goyal J. M., et al., 2020, Monthly Notices of the Royal Astronomical Society, 498, 4680

Greene T., et al., 2007, Techniques and Instrumentation for Detection of Exoplanets III, 6693, 66930G

Greene T. P., et al., 2017, jwst, p. 5001

Grunblatt S. K., Huber D., Gaidos E., Hon M., Zinn J. C., Stello D., 2019, The Astronomical Journal, 158, 227

Guilluy G., et al., 2022, Astronomy and Astrophysics, 665, A104

Hadden S., Lithwick Y., 2014, Astrophysical Journal, 787

Handley W. J., Hobson M. P., Lasenby A. N., 2015a, Monthly Notices of the Royal Astronomical Society: Letters, 450, L61

Handley W. J., Hobson M. P., Lasenby A. N., 2015b, Monthly Notices of the Royal Astronomical Society, 453, 4384

Haswell C. A., et al., 2020, Nature Astronomy, 4, 408

Hauschildt P. H., Allard F., Baron E., 1999, The Astrophysical Journal, Volume 512, Issue 1, pp. 377-385., 512, 377

Hawker G. A., Madhusudhan N., Cabot S. H. C., Gandhi S., Hawker G. A., Madhusudhan N., Cabot S. H. C., Gandhi S., 2018, ApJL, 863, L11

Haynes K., Mandell A. M., Madhusudhan N., Deming D., Knutson H., 2015, Astrophysical Journal, 806, 146

Haywood R. D., et al., 2014a, International Journal of Astrobiology, 13, 155

Haywood R. D., et al., 2014b, Monthly Notices of the Royal Astronomical Society, 443, 2517

He C., et al., 2018, The Astrophysical Journal Letters, 856, L3

Helling C., et al., 2016, Monthly Notices of the Royal Astronomical Society, 460, 855

Henry G. W., Marcy G. W., Butler R. P., Vogt S. S., 2000, The Astrophysical Journal, 529

Hirano T., et al., 2016, The Astrophysical Journal, 820, 41

Hoeijmakers H. J., et al., 2018a, Nature, 560, 453

Hoeijmakers H. J., Schwarz H., Snellen I. A., De Kok R. J., Bonnefoy M., Chauvin G., Lagrange A. M., Girard J. H., 2018b, Astronomy and Astrophysics, 617, A144

Hoeijmakers H. J., et al., 2019, Astronomy and Astrophysics, 627, A165

Hoeijmakers H. J., et al., 2020, Astronomy and Astrophysics, 641, A123

Holman M. J., et al., 2010, Science, 330

Horne K., 1986, Publications of the Astronomical Society of the Pacific, Vol. 98, p. 609-617 (1986), 98, 609

Hörst S. M., et al., 2018, Nature Astronomy 2018 2:4, 2, 303

Hu R., 2021, The Astrophysical Journal, 921, 27

Huang X., Gamache R. R., Freedman R. S., Schwenke D. W., Lee T. J., 2014, Journal of Quantitative Spectroscopy and Radiative Transfer, 147, 134

Hubbard W. B., Fortney J. J., Lunine J. I., Burrows A., Sudarsky D., Pinto P. A., 2001, The Astrophysical Journal, Volume 560, Issue 1, pp. 413-419., 560, 413

Huitson C. M., Sing D. K., Vidal-Madjar A., Ballester G. E., Lecavelier des Etangs A., Désert J. M., Pont F., 2012, Monthly Notices of the Royal Astronomical Society, 422, 2477

Huitson C. M., et al., 2013, Monthly Notices of the Royal Astronomical Society, 434

Huitson C. M., Désert J.-M., Bean J. L., Fortney J. J., Stevenson K. B., Bergmann M., 2017, The Astronomical Journal, 154, 95

Husser T. O., Wende-Von Berg S., Dreizler S., Homeier D., Reiners A., Barman T., Hauschildt P. H., 2013, Astronomy and Astrophysics, 553

Ikoma M., Nakazawa K., Emori H., Ikoma M., Nakazawa K., Emori H., 2000, ApJ, 537, 1013

Inaba S., Wetherill G. W., Ikoma M., 2003, Icarus, Volume 166, Issue 1, p. 46-62., 166, 46

International Astronomical Union 2006, in International Astronomic Union.

Jeffreys H., 1983, Theory of Probability. International series of monographs on physics, Clarendon Press, Oxford, `https://books.google.co.uk/books?id=EbodAQAAMAAJ`

Kaeufl H.-U., et al., 2004, in Ground-based Instrumentation for Astronomy. , doi:10.1117/12.551480

Kama M., Folsom C. P., Pinilla P., 2015, Astronomy and Astrophysics, 582

Karkoschka E., Tomasko M. G., Karkoschka E., Tomasko M. G., 2011, Icarus, 211, 780

Kass R. E., Raftery A. E., 1995, Journal of the American Statistical Association, 90

Kataria T., et al., 2016, ApJ, 821, 9

Kawashima Y., Ikoma M., 2019, The Astrophysical Journal, 877, 109

Kawashima Y., Min M., 2021, Astronomy and Astrophysics, 656, A90

Kempton E. M., et al., 2018, Publications of the Astronomical Society of the Pacific, 130

Kendrew S., et al., 2015, Publications of the Astronomical Society of the Pacific, Volume 127, Issue 953, pp. 623 (2015)., 127, 623

Kesseli A. Y., Snellen I. A. G., 2021, The Astrophysical Journal, 908

Keyte L., et al., 2023, Nature Astronomy, 7

Khalafinejad S., et al., 2021, Astronomy and Astrophysics, 656

Kipping D. M., 2013, Monthly Notices of the Royal Astronomical Society, 435, 2152

Kirk J., 2018, PhD thesis, University of Warwick, Coventry, `https://wrap.warwick.ac.uk/111014/`

Kirk J., Wheatley P. J., Louden T., Littlefair S. P., Copperwheat C. M., Armstrong D. J., Marsh T. R., Dhillon V. S., 2016, Monthly Notices of the Royal Astronomical Society, 463, 2922

Kirk J., Wheatley P. J., Louden T., Doyle A. P., Skillen I., McCormac J., Irwin P. G. J., Karjalainen R., 2017, Monthly Notices of the Royal Astronomical Society, 468, 3907

Kirk J., Wheatley P. J., Louden T., Skillen I., King G. W., McCormac J., Irwin P. G., 2018, Monthly Notices of the Royal Astronomical Society, 474, 876

Kirk J., López-Morales M., Wheatley P. J., Weaver I. C., Skillen I., Louden T., McCormac J., Espinoza N., 2019, The Astronomical Journal, 158, 144

Kirk J., et al., 2021, The Astronomical Journal, 162, 34

Kitzmann D., Heng K., 2018, Monthly Notices of the Royal Astronomical Society, 475, 94

Knudstrup E., Albrecht S. H., 2022, Astronomy and Astrophysics, 660, A99

Knutson H. A., et al., 2007, Nature, 447, 183

Knutson H. A., et al., 2012, Astrophysical Journal, 754, 22

Komacek T. D., Showman A. P., 2020, The Astrophysical Journal, 888, 2

Konacki M., Wolszczan A., 2003, The Astrophysical Journal, 591, L147

Kozai Y., 1962, The Astronomical Journal, 67

Kreidberg L., 2015, Publications of the Astronomical Society of the Pacific, 127, 1161

Kreidberg L., et al., 2014a, Nature, 505, 69

Kreidberg L., et al., 2014b, Astrophysical Journal Letters, 793, L27

Kreidberg L., Line M. R., Thorngren D., Morley C. V., Stevenson K. B., 2018, The Astrophysical Journal Letters, 858, L6

Kurucz R. L., Bell B., 1995, Atomic Line Data. Smithsonian Astrophysical Observatory, Cambridge, MA

Laginja I., Wakeford H., 2020a, ExoTiC-ISM v2.0.0, doi:10.5281/ZENODO.3923986, `https://zenodo.org/record/3923986`

Laginja I., Wakeford H. R., 2020b, Journal of Open Source Software, 5, 2281

Lally M., Vanderburg A., 2022, The Astronomical Journal, 163, 181

Langeveld A. B., Madhusudhan N., Cabot S. H., 2022, Monthly Notices of the Royal Astronomical Society, 514, 5192

Lecavelier Des Etangs A., Pont F., Vidal-Madjar A., Sing D., 2008a, Astronomy and Astrophysics, 481, 83

Lecavelier Des Etangs A., Vidal-Madjar A., Désert J. M., Sing D., 2008b, Astronomy and Astrophysics, 485, 865

Lee E. J., Chiang E., 2016, The Astrophysical Journal, 817, 90

Lee E. J., Chiang E., Ormel C. W., 2014, Astrophysical Journal, 797, 95

Lee E., Dobbs-Dixon I., Helling C., Bognar K., Woitke P., 2016, Astronomy and Astrophysics, 594, A48

Leleu A., et al., 2021, Astronomy and Astrophysics, 649, 14

Lendl M., et al., 2016, A&A, 587, A67

Lendl M., Cubillos P. E., Hagelberg J., Müller A., Juvan I., Fossati L., 2017, Astronomy and Astrophysics, 606, A18

Li G., Naoz S., Kocsis B., Loeb A., 2014, Astrophysical Journal, 785

Li C., et al., 2020, Nature Astronomy 2020 4:6, 4, 609

Libby-Roberts J. E., et al., 2022, The Astronomical Journal, 164, 59

Lidov M. L., 1962, Planetary and Space Science, 9

Lienhard F., et al., 2020, Monthly Notices of the Royal Astronomical Society, 497, 3790

Lin D. N. C., Papaloizou J., 1986, Astrophysical Journal v.309, p.846, 309, 846

Lin D. N., Bodenheimer P., Richardson D. C., 1996, Nature, Volume 380, Issue 6575, pp. 606-607 (1996)., 380, 606

Line M. R., et al., 2021, Nature, 598, 580

Lines S., et al., 2018, Astronomy and Astrophysics, 615, A97

Llop-Sayson J., et al., 2021, The Astronomical Journal, 162

Lodders K., Fegley B., 1998, The planetary scientist's companion. Oxford University Press, `https://ui.adsabs.harvard.edu/abs/1998psc..book.....L/abstract`

Lodders K., Fegley B., Lodders K., Fegley B., 2002, Icarus, 155, 393

Lothringer J. D., Barman T. S., 2020, The Astronomical Journal, 159, 289

Lothringer J. D., Rustamkulov Z., Sing D. K., Gibson N. P., Wilson J., Schlaufman K. C., 2021, The Astrophysical Journal, 914, 12

Louden E. M., Hartman J. D., 2021, Monthly Notices of the Royal Astronomical Society, 501, 5393

Louden T., Wheatley P. J., Irwin P. G. J., Kirk J., Skillen I., 2017, Monthly Notices of the Royal Astronomical Society, 470, 742

Lovis C., et al., 2011, arXiv e-prints, p. arXiv:1107.5325

Luger R., Agol E., Foreman-Mackey D., Fleming D. P., Lustig-Yaeger J., Deitrick R., 2019, The Astronomical Journal, 157, 64

Luque R., et al., 2020, Astronomy and Astrophysics, 642, A50

MacDonald R. J., Goyal J. M., Lewis N. K., 2020, The Astrophysical Journal, 893, L43

Madhusudhan N., 2019, Annual Review of Astronomy and Astrophysics, 57, 617

Madhusudhan N., Seager S., 2009, Astrophysical Journal, 707

Madhusudhan N., Amin M. A., Kennedy G. M., 2014, Astrophysical Journal Letters, 794, 12

Madhusudhan N., Bitsch B., Johansen A., Eriksson L., 2017, Monthly Notices of the Royal Astronomical Society, 469

Magic Z., Chiavassa A., Collet R., Asplund M., 2015, Astronomy & Astrophysics, 573, A90

Maimone M. C., et al., 2022, A&A, 667, A106

Majeau C., Agol E., Cowan N. B., 2012, Astrophysical Journal Letters, 747, L20

Mamajek E. E., 2009, in AIP Conference Proceedings. pp 3–10, doi:10.1063/1.3215910

Mamajek E. E., Hillenbrand L. A., 2008, The Astrophysical Journal, 687, 1264

Mandel K., Agol E., 2002, The Astrophysical Journal, 580, L171

Mansfield M., et al., 2020, Monthly Notices of the Royal Astronomical Society, 499, 5151

Mao S., Paczynski B., 1991, The Astrophysical Journal, 374

Marley M. S., et al., 2021, The Astrophysical Journal, 920, 85

Marois C., Macintosh B., Barman T., Zuckerman B., Song I., Patience J., Lafrenière D., Doyon R., 2008, Science, 322, 1348

Mayor M., Queloz D., 1995, Nature, 378, 355

Mayor M., et al., 2003, The Messenger, 114, 20

McArthur B. E., et al., 2004, The Astrophysical Journal, 614

McArthur B. E., Benedict G. F., Henry G. W., Hatzes A., Cochran W. D., Harrison T. E., Johns-Krull C., Nelan E., 2014, Astrophysical Journal, 795

McCullough P. R., Crouzet N., Deming D., Madhusudhan N., 2014, Astrophysical Journal, 791, 55

McGruder C. D., et al., 2020, The Astronomical Journal, 160, 230

McGruder C. D., et al., 2022, AJ, 164, 134

McKay C. P., Pollack J. B., Courtin R., 1989, Icarus, Volume 80, Issue 1, p. 23-53., 80, 23

McLaughlin D. B., 1924, The Astrophysical Journal, 60

Middelkoop F., 1982, Astronomy and Astrophysics, 107, 31

Mikal-Evans T., et al., 2023, The Astrophysical Journal Letters, 943, L17

Moehler S., Freudling W., Møller P., Patat F., Rupprecht G., O'Brien K., 2010, Publications of the Astronomical Society of the Pacific, 122

Molaverdikhani K., Henning T., Mollière P., 2019, The Astrophysical Journal, 883, 194

Molaverdikhani K., Henning T., Mollière P., 2020, The Astrophysical Journal, 899, 53

Mollière P., Van Boekel R., Bouwman J., Henning T., Lagage P. O., Min M., 2017, Astronomy and Astrophysics, 600, A10

Mollière P., Wardenier J. P., Van Boekel R., Henning T., Molaverdikhani K., Snellen I. A., 2019, Astronomy and Astrophysics, 627, A67

Moran S. E., et al., 2023, The Astrophysical Journal Letters, 948, L11

Mordasini C., van Boekel R., Mollière P., Henning T., Benneke B., 2016, The Astrophysical Journal, 832

Morello G., Tsiaras A., Howarth I. D., Homeier D., 2017, The Astronomical Journal, 154, 111

Morello G., Claret A., Martin-Lagarde M., Cossou C., Tsiaras A., Lagage P.-O., 2020, The Astronomical Journal, 159, 75

Moses J. I., et al., 2011, Astrophysical Journal, 737

Mugnai L. V., et al., 2021, The Astronomical Journal, 161, 284

Mukherjee S., Batalha N. E., Fortney J. J., Marley M. S., 2022, The Astrophysical Journal, 942, 71

National Academies of Sciences Engineering and Medicine 2021, Pathways to Discovery in Astronomy and Astrophysics for the 2020s. The National Academies Press, Washington, DC, doi:10.17226/26141

Neveu-Vanmalle M., et al., 2014, Astronomy and Astrophysics, 572

Nikolov N., et al., 2014, Monthly Notices of the Royal Astronomical Society, 437, 46

Nikolov N., et al., 2015, Monthly Notices of the Royal Astronomical Society, 447, 463

Nikolov N., Sing D. K., Gibson N. P., Fortney J. J., Evans T. M., Barstow J. K., Kataria T., Wilson P. A., 2016, The Astrophysical Journal, 832, 191

Nikolov N., et al., 2018, Nature, 557, 526

Nortmann L., Pallé E., Murgas F., Dreizler S., Iro N., Cabrera-Lavers A., 2016, Astronomy and Astrophysics, 594

Nowak G., et al., 2020, Astronomy and Astrophysics, 642, A173

Noyes R. W., Hartmann L. W., Baliunas S. L., Duncan D. K., Vaughan A. H., 1984, The Astrophysical Journal, 279, 763

Nugroho S. K., et al., 2021, The Astrophysical Journal Letters, 910, L9

Öberg K. I., Murray-Clay R., Bergin E. A., 2011, Astrophysical Journal Letters, 743, 16

Ohno K., Kawashima Y., 2020, ApJL, 895, L47

Olmschenk G., et al., 2022, AJ, 165, 175

Oshagh M., Santos N. C., Ehrenreich D., Haghighipour N., Figueira P., Santerne A., Montalto M., 2014, Astronomy and Astrophysics, 568

O'Brien S. M., et al., 2022, Monthly Notices of the Royal Astronomical Society, 509, 6111

Palle E., et al., 2017, Astronomy & Astrophysics, 602, L15

Panwar V., Desert J. M., Todorov K. O., Bean J. L., Stevenson K. B., Huitson C. M., Fortney J. J., Bergmann M., 2022a, Monthly Notices of the Royal Astronomical Society, 510, 3236

Panwar V., Désert J.-M., Todorov K. O., Bean J. L., Stevenson K. B., Huitson C. M., Fortney J. J., Bergmann M., 2022b, Monthly Notices of the Royal Astronomical Society, 515, 5018

Park C., et al., 2014, Ground-based and Airborne Instrumentation for Astronomy V, 9147, 91471D

Parmentier V., Showman A. P., Lian Y., 2013, Astronomy and Astrophysics, 558, A91

Parviainen H., 2018, in Deeg H. J., Belmonte J. A., eds, Springer Nature 2018, Handbook of Exoplanets. Springer International Publishing, Cham, pp 1567–1590, doi:10.1007/978-3-319-55333-7_149

Parviainen H., Aigrain S., 2015, Monthly Notices of the Royal Astronomical Society, 453, 3821

Pearson K. A., Griffith C. A., Zellem R. T., Koskinen T. T., Roudier G. M., 2019, The Astronomical Journal, 157, 21

Pepe F., et al., 2014, Astronomische Nachrichten, 335, 8

Perryman M., 2018, The Exoplanet Handbook Second Edition, 2nd edn. The Cambridge University Press, `http://weekly.cnbnews.com/news/article.html?no=124000`

Perryman M., Hartman J., Gásp´ G., Gáspár´ G., Bakos G., Lindegren L., 2014, The Astrophysical Journal, 797, 14

Petit Dit De La Roche D. J., Hoeijmakers H. J., Snellen I. A., 2018, Astronomy and Astrophysics, 616, A146

Piaulet C., et al., 2023, Nature Astronomy, 7

Pinhas A., Madhusudhan N., 2017, Monthly Notices of the Royal Astronomical Society, 471, 4355

Pinhas A., Rackham B. V., Madhusudhan N., Apai D., 2018, Monthly Notices of the Royal Astronomical Society, 480

Pinhas A., Madhusudhan N., Gandhi S., MacDonald R., 2019, Monthly Notices of the Royal Astronomical Society, 482, 1485

Pino L., et al., 2018, Astronomy & Astrophysics, 612

Pinte C., et al., 2019, Nature Astronomy, 3, 1109

Plate M. B. J. t., Holota W., Posselt W., Koehler J., Melf M., Bagnasco G., Marenaci P., 2005, https://doi.org/10.1117/12.620772, 5904, 185

Polanski A. S., Crossfield I. J. M., Howard A. W., Isaacson H., Rice M., 2022, Research Notes of the AAS, 6, 155

Pollacco D., et al., 2006, Publications of the Astronomical Society of the Pacific, 118, 1407

Pollack J. B., et al., 1996, Icarus, 124, 62

Polyansky O. L., Kyuberis A. A., Zobov N. F., Tennyson J., Yurchenko S. N., Lodi L., 2018, Monthly Notices of the Royal Astronomical Society, 480

Pont F., Knutson H., Gilliland R. L., Moutou C., Charbonneau D., 2008, Monthly Notices of the Royal Astronomical Society, 385, 109

Pont F., Sing D. K., Gibson N. P., Aigrain S., Henry G., Husnoo N., 2013, Monthly Notices of the Royal Astronomical Society, 432, 2917

Powell D., Zhang X., Gao P., Parmentier V., 2018, The Astrophysical Journal, 860, 18

Powell D., Louden T., Kreidberg L., Zhang X., Gao P., Parmentier V., 2019, The Astrophysical Journal, 887

Prinoth B., et al., 2022, Nature Astronomy, 6, 449

Quanz S. P., et al., 2022, Astronomy and Astrophysics, 664, A21

Queloz D., Eggenberger A., Mayor M., Perrier C., Beuzit J. L., Naef D., Sivan J. P., Udry S., 2000, Astronomy and Astrophysics, 359

Rackham B. V., de Wit J., 2023, arXiv, p. arXiv:2303.15418

Rackham B., et al., 2017, The Astrophysical Journal, 834, 151

Rackham B. V., Apai D., Giampapa M. S., 2018, The Astrophysical Journal, 853, 122

Rackham B. V., Apai D., Giampapa M. S., 2019, The Astronomical Journal, 157, 96

Rafikov R. R., 2005, The Astrophysical Journal, 621, L69

Rajpaul V., Aigrain S., Osborne M. A., Reece S., Roberts S., 2015, Monthly Notices of the Royal Astronomical Society, 452, 2269

Rajpaul V., Aigrain S., Roberts S., 2016, Monthly Notices of the Royal Astronomical Society, 456, L6

Rajpaul V. M., et al., 2021, Monthly Notices of the Royal Astronomical Society, 507, 1847

Rasmussen C. E., Williams C. K. I., 2006, Gaussian Processes for Machine Learning. MIT Press, Cambridge, MA

Rauer H., et al., 2014, Experimental Astronomy, 38, 249

Rauscher E., Menou K., Seager S., Deming D., Cho J. Y.-K., Hansen B., 2006, The Astrophysical Journal, Volume 664, Issue 2, pp. 1199-1209., 664, 1199

Redfield S., Endl M., Cochran W. D., Koesterke L., 2008, The Astrophysical Journal, 673, L87

Rice W. K. M., Armitage P. J., Hogg D. F., 2007, Monthly Notices of the Royal Astronomical Society, 384, 1242

Richard C., et al., 2012, Journal of Quantitative Spectroscopy and Radiative Transfer, 113

Ricker G. R., et al., 2015, Journal of Astronomical Telescopes, Instruments, and Systems, Volume 1, id. 014003 (2015)., 1, 014003

Rieke M. J., Kelly D., Horner S., 2005, Cryogenic Optical Systems and Instruments XI, 5904, 590401

Rieke G. H., et al., 2015, Publications of the Astronomical Society of the Pacific, 127, 584

Rigby J., et al., 2023, PASP, 135, 048001

Robberto M., 2009, Technical Report JWST-STScI-001721, p. 1721

Roberts S., Osborne M., Ebden M., Reece S., Gibson N., Aigrain S., 2013, Philosophical Transactions of the Royal Society A: Mathematical, Physical and Engineering Sciences, 371

Roman M., Rauscher E., 2019, The Astrophysical Journal, 872, 1

Rooney C. M., Batalha N. E., Gao P., Marley M. S., 2022, The Astrophysical Journal, 925, 33

Rossiter R. A., 1924, The Astrophysical Journal, 60

Rothman L. S., et al., 2013, Journal of Quantitative Spectroscopy and Radiative Transfer, Volume 130, p. 4-50., 130, 4

Rustamkulov Z., et al., 2023, Nature, 614, 659

Salvatier J., Wiecki T. V., Fonnesbeck C., 2016, PeerJ Computer Science, 2016, e55

Santerne A., et al., 2016, ApJ, 824, 55

Santerne A., et al., 2018, Nature Astronomy, 2, 393

Schlawin E., Leisenring J., Misselt K., Greene T. P., McElwain M. W., Beatty T., Rieke M., 2020, The Astronomical Journal, 160, 231

Schlawin E., Challener R., Mansfield M., Rauscher E., Adams A. D., Lustig-Yaeger J., 2023, The Astronomical Journal, 165, 210

Schlichting H. E., 2014, Astrophysical Journal Letters, 795, L15

Schwarz G., 1978, Annals of Statistics

Seager S., Sasselov D. D., 2000, The Astrophysical Journal, 537, 916

Segura-Cox D. M., et al., 2020, Nature, 586, 228

Seidel J. V., et al., 2019, Astronomy and Astrophysics, 623

Seidel J. V., et al., 2020, Astronomy and Astrophysics, 641, L7

Sheppard K. B., Mandell A. M., Tamburo P., Gandhi S., Pinhas A., Madhusudhan N., Deming D., 2017, The Astrophysical Journal, 850

Sheppard K. B., et al., 2021, The Astronomical Journal, 161, 51

Showman A. P., Guillot T., 2002, Astronomy and Astrophysics, 385, 166

Silvotti R., et al., 2007, Nature, 449, 189

Silvotti R., et al., 2014, A&A, 570, A130

Sing D. K., 2018, arXiv, pp 3–48

Sing D. K., et al., 2011, Astronomy and Astrophysics, 527, 73

Sing D. K., et al., 2012, Monthly Notices of the Royal Astronomical Society, 426, 1663

Sing D. K., et al., 2015, Monthly Notices of the Royal Astronomical Society, 446, 2428

Sing D. K., et al., 2016, Nature, 529, 59

Snellen I., Brown A., 2018, Nature Astronomy, 2, 883

Snellen I. A., Albrecht S., De Mooij E. J., Le Poole R. S., 2008, Astronomy and Astrophysics, 487, 357

Snellen I. A., De Kok R. J., De Mooij E. J., Albrecht S., 2010, Nature, 465, 1049

Snellen I. A. G., et al., 2014, Nature, 509, 63

Spake J. J., et al., 2021, Monthly Notices of the Royal Astronomical Society, 500, 4042

Speagle J. S., 2020, Monthly Notices of the Royal Astronomical Society, 493, 3132

Spyratos P., et al., 2021, Monthly Notices of the Royal Astronomical Society, 506, 2853

Spyratos P., Nikolov N. K., Constantinou S., Southworth J., Madhusudhan N., Sedaghati E., Ehrenreich D., Mancini L., 2023, Monthly Notices of the Royal Astronomical Society, 521, 2163

Sromovsky L. A., Fry P. M., Kim J. H., 2011, Icarus, 215, 292

Steinrueck M. E., Parmentier V., Showman A. P., Lothringer J. D., Lupu R. E., 2019, The Astrophysical Journal, 880, 14

Stevenson K. B., 2016, The Astrophysical Journal, 817, L16

Stevenson K. B., et al., 2012, Astrophysical Journal, 754, 136

Stevenson K. B., et al., 2016a, Publications of the Astronomical Society of the Pacific, 128, 094401

Stevenson K. B., et al., 2016b, AJ, 153, 68

Suárez Mascareño A., et al., 2018, Astronomy and Astrophysics, 612, 41

Swain M. R., Vasisht G., Tinetti G., Swain M. R., Vasisht G., Tinetti G., 2008, Nature, 452, 329

Swain M. R., et al., 2021, The Astronomical Journal, 161, 213

Taylor J., Parmentier V., Line M. R., Lee E. K., Irwin P. G., Aigrain S., 2021, Monthly Notices of the Royal Astronomical Society, 506

Temmink M., Snellen I. A., 2023, Astronomy and Astrophysics, 670, A26

Tennyson J., Yurchenko S. N., 2012, Monthly Notices of the Royal Astronomical Society, 425, 21

Tennyson J., Yurchenko S. N., 2018, Atoms, 6, 26

Tennyson J., et al., 2016, Journal of Molecular Spectroscopy, 327

Teske J. K., Khanal S., Ramírez I., 2016, The Astrophysical Journal, 819, 19

The JWST Transiting Exoplanet Community Early Release Science Team et al., 2023, Nature, 614, 649

Tinetti G., et al., 2007, Nature, 448, 169

Tinetti G., et al., 2018, ExA, 46, 135

Todorov K. O., et al., 2019, A&A, 631, A169

Toomre A., 1964, The Astrophysical Journal, 139

Tremblin P., Amundsen D. S., Mourier P., Baraffe I., Chabrier G., Drummond B., Homeier D., Venot O., 2015, Astrophysical Journal Letters, 804, 6

Triaud A. H., et al., 2010, Astronomy and Astrophysics, 524, 25

Trilling D. E., Benz W., Guillot T., Lunine J. I., Hubbard W. B., Burrows A., 1998, The Astrophysical Journal, 500, 428

Trotta R., 2008, Contemporary Physics, 49, 71

Tsai S.-M., Malik M., Kitzmann D., Lyons J. R., Fateev A., Lee E., Heng K., 2021, The Astrophysical Journal, 923, 264

Tsai S. M., et al., 2023, Nature, 617, 483

Tsiaras A., et al., 2018, The Astronomical Journal, 155, 156

Udalski A., et al., 2005, The Astrophysical Journal, 628, L109

Veitch-Michaelis J., Lam M. C., 2019, arXiv e-prints, 1912.05883

Visscher C., Lodders K., Fegley B., 2010, Astrophysical Journal, 716, 1060

Von Paris P., Gratier P., Bordé P., Leconte J., Selsis F., 2016, Astronomy and Astrophysics, 589, A52

Wakeford H., Grant D., 2022, Exo-TiC/ExoTiC-LD: ExoTiC-LD v2.1 Zenodo Release, doi:10.5281/ZENODO.6809899, `https://zenodo.org/record/6809899`

Wakeford H. R., Sing D. K., 2015, Astronomy and Astrophysics, 573, A122

Wakeford H. R., et al., 2013, Monthly Notices of the Royal Astronomical Society, 435, 3481

Wakeford H. R., et al., 2017a, Science, 356, 628

Wakeford H. R., et al., 2017b, The Astrophysical Journal, 835, L12

Wakeford H. R., et al., 2018, The Astronomical Journal, 1, 29

Wakeford H. R., et al., 2019, The Astronomical Journal, 157

Wang J. J., et al., 2020, The Astronomical Journal, 159, 263

Wang J. J., et al., 2021, The Astronomical Journal, 162, 148

Weaver I. C., et al., 2020, The Astronomical Journal, 159, 13

Welbanks L., Madhusudhan N., 2021, The Astrophysical Journal, 913

Welbanks L., Madhusudhan N., Allard N. F., Hubeny I., Spiegelman F., Leininger T., 2019, The Astrophysical Journal Letters, 887, L20

Wheatley P. J., et al., 2018, Monthly Notices of the Royal Astronomical Society, 475

Williams P. K. G., Charbonneau D., Cooper C. S., Showman A. P., Fortney J. J., 2006, The Astrophysical Journal, Volume 649, Issue 2, pp. 1020-1027., 649, 1020

Wilson J., et al., 2020, Monthly Notices of the Royal Astronomical Society, 497, 5155

Wilson J., Gibson N. P., Lothringer J. D., Sing D. K., Mikal-Evans T., De Mooij E. J., Nikolov N., Watson C. A., 2021, Monthly Notices of the Royal Astronomical Society, 503, 4787

Winn J. N., Winn N. J., 2010, arXiv, p. arXiv:1001.2010

Woitke P., Helling C., Hunter G. H., Millard J. D., Turner G. E., Worters M., Blecic J., Stock J. W., 2018, Astronomy and Astrophysics, 614, A1

Wolszcan A., Frail D. A., 1992, Nature, 355, 145

Wong M. H., et al., 2004, Icarus, 171, 153

Wong I., et al., 2022, The Astronomical Journal, 164

Wyttenbach A., Ehrenreich D., Lovis C., Udry S., Pepe F., 2015, Astronomy and Astrophysics, 577

Yu X., et al., 2021, Nature Astronomy, 5

Yurchenko S. N., Tennyson J., 2014, Monthly Notices of the Royal Astronomical Society, 440, 1649

Yurchenko S. N., Tennyson J., Barber R. J., Thiel W., 2013, Journal of Molecular Spectroscopy, Volume 291, p. 69-76., 291, 69

Zamyatina M., et al., 2023, Monthly Notices of the Royal Astronomical Society, 519, 3129

Zhang M., et al., 2018, The Astronomical Journal, 155, 83

Zhang M., Chachan Y., Kempton E. M., Knutson H. A., 2019, Publications of the Astronomical Society of the Pacific, 131, 034501

Zhang M., Chachan Y., Kempton E. M., Knutson H. A., Chang W., 2020, ApJ, 899, 27

Zhou G., et al., 2019, The Astronomical Journal, 158

van Sluijs L., et al., 2023, Monthly Notices of the Royal Astronomical Society, Volume 522, Issue 2, pp.2145-2170, 522, 2145

van Dokkum P., 2001, Publications of the Astronomical Society of the Pacific, 113, 1420